Advanced Control Functionalities for

Photovoltaic and Energy Storage Converters

by

Emanuel Serban

B.Sc., Polytechnic University of Timisoara, 1994
M.Sc., Polytechnic University of Timisoara, 1995

A THESIS SUBMITTED IN PARTIAL FULFILMENT OF
THE REQUIREMENTS FOR THE DEGREE OF

DOCTOR OF PHILOSOPHY

in

The Faculty of Graduate Studies and Postdoctoral Studies

(Electrical & Computer Engineering)

THE UNIVERSITY OF BRITISH COLUMBIA

(Vancouver)

June 2017

Abstract

Power conversion systems including grid-connected photovoltaic (PV) and electrical energy storage (EES) stages open the prospects for new opportunities to improve the system's performance in energy production and standards compliance.

This dissertation proposes a completely revised state-of-the-art architecture with functionalities integrated within a unified system, which extracts more solar energy, provides safety compliance and grid stability.

The first improvement of the power conversion system is focused on inverters' dc voltage extension range, which leads to increased PV energy harvesting. A proposed technique provides a lower voltage limit in the dc-bus utilization with the employment of the new voltage-reactive power control strategy accompanied with a modified zero-sequence modulation. Then, a higher dc-bus voltage limit is obtained by maximizing the utilization of power semiconductors. A graphical comparative analysis approach using I-V and P-V characteristics reflects remarkable PV-converter system behavior, which illustrates the advantages of the wide dc-bus range in 1500V systems. As a result, the maximum power point tracking (MPPT) dc voltage range is extended by an additional 30% improving the systems energy capture capabilities under extreme temperatures beyond the performance of traditional 1000V single-stage inverters. Furthermore, the single-stage conversion was extended to two-stages, with mini-boost rated for a fraction of the nominal power of the converter. Thus, the proposed design concept delivers significantly higher performance whilst reducing system cost at component level.

The next proposed improvement of the system focuses on grid fault detection for standards compliance, using a search sequence function. This proposed technique is integrated within the active-reactive power control, MPPT algorithm, and phase-locked loop routine. In addition, the islanding search sequence is synchronized and incorporated within the MPPT (designed with an adaptive strategy to achieve system stability and minimum impact on power quality).

Finally, the system's control functionalities advances into grid support strategies, designed with frequency- and voltage-assist features for network stability. The change in active-reactive power flow is achieved using a responsive gradient to command the transitions between grid-feeding and grid-loading.

The proposed system's combined methods result in a cohesive PV/EES conversion architecture whose improved performance has been confirmed through electronic simulation and experimental results.

Lay Summary

Solar photovoltaic (PV) energy and energy storage systems require innovative solutions to improve performance, efficiency, and safety compliance. In this thesis, three critical approaches to optimization of solar power converters were covered.

The first approach is giving the converter a wider, more flexible, input voltage range which results in increased energy harvest. The proposed system architecture allowing this, results in improved performance at a reduced hardware cost.

The second strategy provides enhanced safety by using a smart algorithm to detect grid faults and conditions such as blackouts in a fraction of a second.

The third and final approach provides the ability to use the solar converter to support the grid and significantly increase its stability beyond existing standards.

The combination of these three approaches allow for the development high performance, efficient, safe and grid friendly power converters ready for the next generation of solar power solutions.

Preface

This thesis contains research and development with contributions that have been published in the form of four academic IEEE journal and one conference scientific papers, proposed and investigated by lead author, Emanuel Serban, under the supervision of Dr. Martin Ordonez.

Chapter 2 contains passages covered in the following publications:

[1] E. Serban, M. Ordonez, and C. Pondiche, "DC-bus voltage range extension in 1500 V photovoltaic inverters," *IEEE J. Emerg. Sel. Topics Power Electron.*, vol. 3, no. 4, pp. 901–917, June 2015.

[2] E. Serban, F. Paz, and M. Ordonez, "Improved PV Inverter Operating Range Using a Miniboost," accepted for publication at IEEE Transactions in Power Electronics*,* Dec. 2016.

[3] E. Serban, F. Paz, and M. Ordonez, "PV Array Voltage Range Extension for Photovoltaic Inverters Using a Mini-Boost," in *Energy Conversion Congress and Exposition (ECCE),* 2016, pp. 1-8.

Chapter 3 contains passages covered in the following publication:

[4] E. Serban, C. Pondiche, and M. Ordonez, " Islanding Detection Search Sequence for Distributed Power Generators Under AC Grid Faults*, "IEEE Trans. in Power Electron.,* vol. 30, no. 6, pp. 3106–3121, Jun. 2014.

Portions of chapter 4 have been published in the following publication:

[5] E. Serban, M. Ordonez, C. Pondiche, "Voltage and Frequency Grid Support Strategies Beyond Standards*," IEEE Trans. Power Electron.,* vol. 32, no. 1, pp. 298–309, Jan. 2017.

As first author of the afore-mentioned publications, the author of this thesis identified the research topics, developed the theoretical system concepts and models, wrote the manuscripts, performed the analysis and conducted the simulation, experimental validation of the proposed advancements in power electronics. The author was supervised, received technical advice, and writing and editorial modifications from Dr. Martin Ordonez. As well, co-authors Cosmin Pondiche and Francisco Paz provided some support for analysis and experimental testing.

Table of Contents

List of Tables

List of Figures

List of Symbols

$\alpha\beta$ Axis Clarke transformation.

β_I, β_V PV cell temperature coefficients ($\%/\,^{\circ}C$).

dq Axis Park transformation.

f Instantaneous grid frequency (Hz).

f_n Nominal grid frequency (Hz).

f_s Converter switching frequency (Hz).

G Solar irradiance (W/m^2).

I_{ac} Converter output ac current (A).

I_d Active current component aligned along d-axis (A).

I_{MPP} PV current operation at maximum power point (A).

I_{pv} PV array dc current (A).

I_q Reactive current component aligned along q-axis (A).

k Boltzmann constant ($1.380648 \cdot 10^{-23}\ J/K$).

L, L_f Converter filter inductor (H).

m Modulation index.

m_P, m_r Gradient of active power with frequency (W/Hz).

PF Power factor.

P Active power generated or received (W).

P_n Nominal active power (W).

P_m Momentary active power operation (W).

$P(f)$	Active power-frequency control strategy.
$P(SoC)$	Active power generation from SoC reserve.
P_{lim}	Active power limit threshold (W).
P_{MPP}	PV power operation at maximum power point (W).
ρ_a	Air density (kg/m^3).
P_r	Active power received from the grid port (W).
R	Resistance (Ω).
q_e	Electron charge ($1.602 \cdot 10^{-19} C$).
q, Q	Reactive power (VAr).
$Q(v)$	Reactive power-voltage control strategy.
S	Apparent power (VA).
SoC	State of charge (%).
SoC_{min}	Minimum (critical) level of SoC (%).
SoH	State of health (%).
V	Instantaneous voltage (V).
v, V_{ac}	Instantaneous grid ac voltage (V).
v_w	Wind velocity (m/s).
V_d	Grid phase voltage component aligned along d-axis $V_d = V\sqrt{2}$, (V).
V_{dc}	DC-link voltage (V).
V_e	Converter phase output voltage magnitude (V).
V_H	RMS ac voltage high limit (V).
V_{Hmin}	RMS ac voltage maximum limit (V).
V_{Lmin}	RMS ac voltage minimum limit (V).

V_{LL}	RMS line to line voltage (V).
V_{LN}	RMS line to neutral voltage (V).
$\hat{V}_{LN}$	Line to neutral voltage magnitude (V).
V_{MPP}	PV voltage operation at maximum power point (V).
V_n	Nominal grid ac voltage (V).
V_{oc}	PV open-circuit voltage (V).
V_{pv}	PV array dc voltage (V).
V_q	Grid phase voltage component aligned along q-axis (V).
V_{ref}	Reference voltage (V).
X	Reactance (Ω).
X/R	Line impedance ratio: ac system reactance to resistance ratio.
φ	Power factor angle (rad).
θ_v	Grid phase angle (rad).
ω	Fundamental angular line frequency (rad/s).

Prefixes for SI Units

p	Pico (10^{-12}).
p	Nano (10^{-9}).
μ	Micro (10^{-6}).
m	Milli (10^{-3}).
k	Kilo (10^3).
M	Mega (10^6).

SI Units

A	Ampere.
$°C$	Degree Celsius.
C	Coulomb.
F	Farad.
H	Henry.
Hz	Hertz.
J	Joule.
K	Kelvin.
s	Second.
V	Volt.
W	Watt.
°	Degree.
Ω	Ohm.

List of Abbreviations

AC   Alternating Current.

AI   Anti-islanding.

BW   Bandwidth.

CM   Common-mode.

CPU   Central Processing Unit.

CB-PWM   Carrier-based pulse-width modulation

D   Duty-ratio.

DC   Direct Current.

DG   Distributed Generation.

DoD   Depth of Discharge.

DPG   Distributed Power Generator.

DSP   Digital Signal Processing.

EES   Electrical Energy Storage.

EMC   Electromagnetic Compliance.

GaN   Gallium Nitride (power semiconductor devices).

GC   Grid Code.

GMS   Global Maxima Scan.

GRF   Generator Reference Frame.

ID   Islanding Detection.

IGBT   Insulated Gate Bipolar Transistor.

ISS	Islanding Search Sequence.
LV	Low Voltage.
MOSFET	Metal Oxide Semiconductor Field Effect Transistor.
MPP	Maximum Power Point.
MPPT	Maximum Power Point Tracking.
MV	Medium Voltage.
NDZ	Non-detection Zone.
NOCT	Nominal Operating Cell Temperature.
NP	Neutral-Point.
NPC	Neutral-point Clamped.
NPS	Neutral-point Shorted.
P&O	Perturb and Observe.
PCC	Point of Common Coupling.
PD	Phase Disposition.
PE	Protective Earth.
PLL	Phase-locked Loop.
PMSG	Permanent Magnet Synchronous Generator.
PS	Phase Shift.
p.u.	Per Unit value.
PV	Photovoltaic.
PWM	Pulse-width Modulation.
QSV	Quasi-space Vector.
RMS	Root Mean Square.

SiC	Silicon Carbide (power semiconductor devices).
SRF	Synchronous Reference Frame.
SPWM	Sinusoidal Pulse-width Modulation.
STC	Standard Test Condition.
SVM	Space Vector Modulation.
THD	Total Harmonic Distortion.
THI	Third Harmonic Injection.
TOU	Time-of-use.
TSOs	Transmission System Operators.
TNPC	T-type Neutral-point Clamped.
UPS	Uninterruptible Power Supply.
VQ	Voltage-Reactive power.
WT	Wind Turbine.
WBG	Wide Bandgap.
ZS	Zero-sequence.
3H-ZS	Third-harmonic Zero-sequence.

Acknowledgements

The contemplation of the world's complexity is an everlasting inspiration, purpose and motivation in my daily life.

I would like to thank my supervisor Dr. Martin Ordonez for his encouragement, dedication and support during this work.

I am missing the shared moments that I spent with my three daughters during the time I served in this work, as well as the other moments that I missed with my family while completing this work.

I would like to thank my parents for their perpetual encouragement towards education and providing the Christian values that greatly contributed to my life. I acknowledge the support in prayers and fellowship credited to the Romanian Orthodox Church, New Westminster and Negru Voda Monastery, Campulung. Psalm 92:5 & Luke 6:31.

To my beloved wife Helmine,

my wonderful children Christa, Maria, Alissa,

and my precious parents Adriana and Aurelian Serban.

Chapter 1. Introduction and Overview [1]

1.1. Motivation

Utility grid integration with modern renewable distributed power generators requires safety with grid code compliance, advanced features and controls for power conversion, high power quality and high performance system operation.

The penetration of distributed renewable generators in power grids is a rapidly increasing technology, driven by steep declines in system cost and policies favoring renewable energy. Economic analysis of solar photovoltaic (PV) can be clearly distinguished from conventional electrical power generation models. First, the radiant light from the Sun is free and solar technology can be developed due to purposeful research and development activities. Second, increasing the level of installed PV capacity, leads to a reduction in the use of fossil fuels, thereby mitigating the negative effects of emissions and pollutants. Third, solar electricity generation from PV systems is variable and intermittent. The variability of the solar production can be predicted from the daily and seasonal weather forecast.

The intermittency in solar production is as a result of the unpredictable nature of transient cloud fields. This application presents a variety of new issues since the existing power distribution networks were not initially designed to adopt a high share of variable renewable energy. The issue of balancing between load and generation must be addressed in order to maintain grid stability. Therefore, the line frequency and voltage are required being maintained at close to nominal values to ensure the grid stability for the customer loads.

This thesis investigates a system development employing high performance control functionalities, integrated within grid-connected converters, and designed to achieve higher PV energy harvesting for grid power production, safety compliance with redundancy and ac grid network stability. Within this context, this thesis focuses on new opportunities to improve a power system performance with the following three main integrated functionalities of grid-connected converters:

1) Voltage DC-bus extension strategies for converters operation in PV energy harvesting for improved system utilization.

2) Grid-interconnect islanding detection strategies of PV converters for safety and utility grid codes system compliance.

3) Advanced grid support system operation of grid-connected converters for network stabilization with power balancing.

The proposed control strategies combined, aim to enhance the system functionalities into a comprehensive solution, designed for grid-connected converters, in renewable and energy storage power conversion applications.
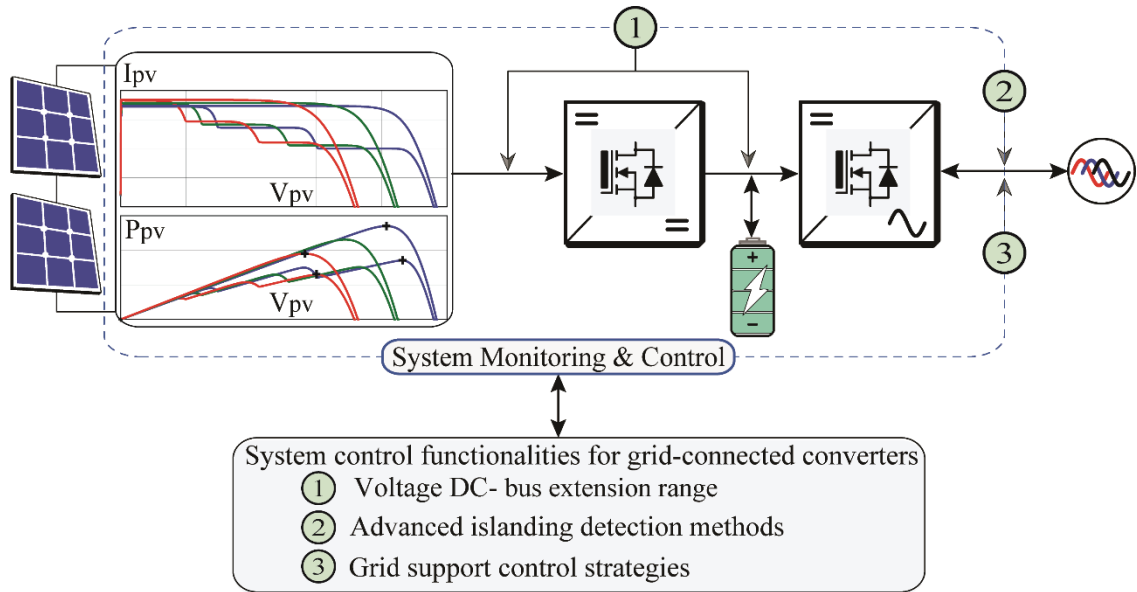
Figure 1.1: Conceptual system block diagram of the proposed control functionalities featured in PV and EES grid-connected converters.

Fig. 1.1 illustrates the conceptual system block diagram of the proposed control strategies contained in three integrated functionalities, designed for high performance and standards compliance of PV and EES grid-connected converters.

1.2. Literature Review

1.2.1. DC-bus Voltage Utilization for Energy Harvesting in PV Converters Application

The study of energy harvest methods is evaluated based on geographies with high potential for generation (e.g. in the mountains and central regions of the US and Canada). Unfortunately, these locations are subject to extreme PV-cell surface temperatures throughout the year, ranging from -20°C to 70°C. This affects both the open circuit voltage (V_{oc}) and the maximum power point voltage (V_{mp}) of the power plant [1]. This makes solar inverter design a complex task, since it has to accommodate a large voltage dc-bus range.

The most common single stage conversion PV systems are designed for operation under 1000V open-circuit voltage and may experience a wide dc bus variation. For example, a 1000V solar inverter may operate from 575V (e.g. lower dc-bus limit for standard $230V_{LN}/400V_{LL}$ grid) to 850V (upper dc-bus limit) at full nominal power, and extend the range up to 1000V with reduced power operation due to limited voltage blocking of power devices [2] - [4]. The inclusion of zero-sequence triple harmonics components provides improved dc-bus voltage utilization, up to 15% in the linear modulation range [5]. The minimum dc-bus range is improved since the inverter is allowed to operate at a lower dc-bus voltage ($V\sqrt{3}$, with V = peak-phase grid voltage) which provides an advantage for renewable power conversion. Three-phase neutral point-clamped (NPC) inverters [6] are widely used in renewable applications, which require special attention to the modulation strategy implementation. The type of modulation strategy used has a significant impact on the dc-bus utilization, conversion losses, power quality, and system performance characteristics (e.g. circulating currents, leakage current). System integration for multiple paralleled connected inverters requires analysis and solutions to avoid circulating currents between the inverters [7] - [10]. Modulation strategies for the 3-level NPC type topology have been proposed in the form of carrier-based pulse-width modulation (CB-PWM) [11], [12], space-vector modulation (SVM) [13] - [16] and selective harmonic elimination [17] - [19]. In the past literature, the third-harmonic injection PWM (THI-PWM) has been reported as being difficult to implement due to the triple-harmonic generation [20]. However, the advancements of phase-locked loop (PLL) techniques [21] - [25] provide real time accurate, robust and fast estimation of angular frequency and phase angle of the fundamental sinusoidal components. With the third-harmonics zero-sequence (3H-ZS) type modulators [26], [27], the minimum dc-bus voltage utilization range of the inverter design is limited at the ac grid peak-line voltage.

The research described in [28], [29] provided interesting and important contributions in the area of control and modulation strategies to improve dc-bus utilization.

Over time, PV inverter technology, without an MPPT boost stage, has settled for installations under 1000V (open-circuit) and a typical MPPT bus range covers from 575V (e.g. lower dc-bus limit for standard 230 V_{LN}/400V_{LL} grid) to 850V (upper bus limit at rated power). The power semiconductors voltage ratings availability and optimized for high efficiency (e.g. 600/650V, NPC topology) and cost, the inverter starts to curtail the power at 850V, where the inverter operates in power limit mode. An important objective of this dissertation is to extend both the lower dc-bus and upper dc-bus limit ranges to significantly increase the power operating area.

The need for increasing both the lower and higher system dc-bus limits is based on fundamental motivations: 1) Solar inverters operating at higher dc bus voltage (i.e., 1500V) have the potential to save copper and switchgear when adequate ac and dc conductors are selected [30], [31], leading to cost-effective installations; 2) Lower dc-bus limit extension allows energy capture under high PV temperatures (e.g. 70˚C) and low irradiation; 3) The extension of the upper dc-bus voltage allows for greater energy extraction under low temperatures (e.g., -20˚C) and high irradiation conditions.

Modern PV power plants have been studied in the literature including energy production maximization, control strategies related to reduced irradiance and PV modules orientation [32] - [37]. The PV module manufacturer specification is given at standard test conditions (STC, 1 kW/m^2, 25 C cell temperature, and air mass of 1.5). In real applications, these ideal conditions are almost non-existent simultaneously.

The negative factors which impact the PV power harvesting are related to low irradiance conditions, non-optimal tilt angles, PV cell soiling/dust, PV modules aging, and partial shading of the modules resulting in power harvesting degradation.

Maximum Power Point Tracking (MPPT) is one essential part of any PV application. These algorithms ensure the PV array operates at the most efficient condition harvesting as much energy as possible, even under changing environmental conditions [38] - [40]. One of the main problems with MPPT algorithms is related to local maxima created by partial shading conditions [41] - [43]. Although many solutions have been proposed that tackle the issue of local maxima [44] - [48], a problem still remains: the global maximum can be located at a voltage that is much lower than the overall voltage of the array. Single-stage PV inverters (no boost stage) will not be able to operate at such low voltages, making the inverter useless or significantly reducing the harvested energy below what is available. This problem is increased when the PV string array becomes bigger, leading to the presence of more operation points at local maxima.

In this dissertation, methods to extend the dc bus will be investigated in order to increase energy harvesting with PV plants operating at 1000V and 1500V open circuit voltage (Fig. 1.2).
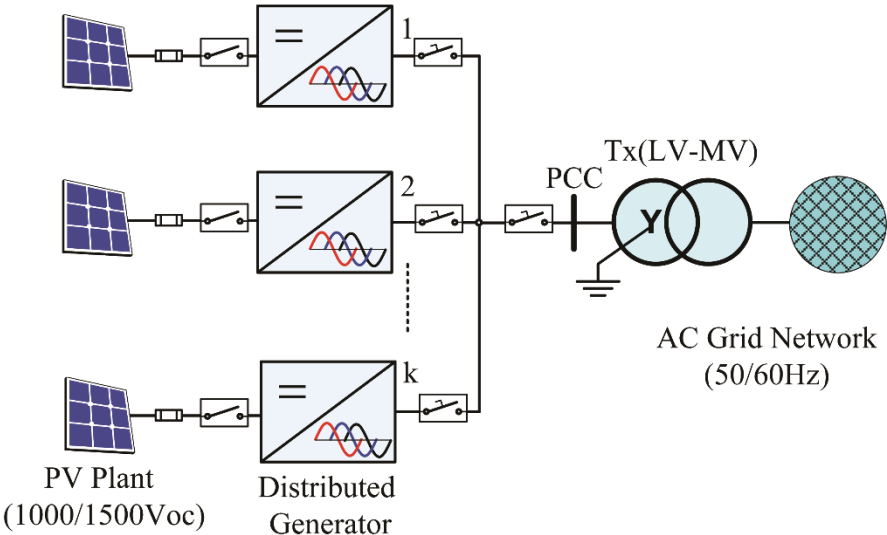
Figure 1.2: Single line diagram PV plant example with grid-connected distributed generators.

In the past two decades, the operating voltage of PV installation has increased in order to reduce current ratings and system installation costs. Such a large number of PV panels in series (e.g. 600 - 1500V systems) lead to wide variations of PV voltage due undesirable effects such as shading, soiling/dust, aging, and hot surface temperature. A partial shade would normally shut down solar inverters, unless a boost stage is added to the system input to ensure a proper dc link operating voltage for the inverter. A boost input stage can double the input voltage operating range to extract maximum power under any possible shading and temperature condition.

In Fig. 1.3 is shown a typical representation of PV module energy production over time used by manufacturers to provide required warranty or to differentiate their performance. The power loss (ΔP_{loss}) over time is inherent and the standard boost becomes evidently an overdesign. In contrast, the proposed PV string mini-boost design leads to an improvement in energy production over time in terms of both initial cost and return of investment.
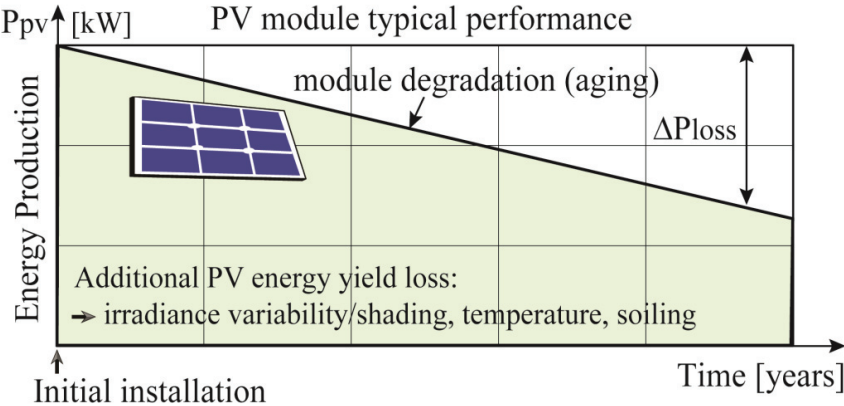
Figure 1.3: Typical representation of PV energy production over time.

In this work, a new string boost architecture arrangement is proposed in the form of a mini-boost used for three-phase PV string inverters. The string mini-boost increases the dc voltage range to extend power extraction under shading and low irradiance conditions and only requires to process a fraction of the rated power. The proposed cost effective solution is further

improved by using the inverter peak power envelope at boundary operation, resulting in expanded energy extraction beyond existing techniques. A design procedure to optimally size the mini-boost and the peak-power envelope is presented along with a comparative analysis, under different irradiance levels, to illustrate the advantages in energy extraction obtained with the proposed PV string mini-boost solution under low voltage and boundary operation. The improved efficiency operation schemes and safety issues of common-mode (leakage) current with three mitigation design techniques intended for three-phase three-level inverter transformer-less topology will be discussed.

1.2.2. Grid-interconnect Requirements for Distributed Generators

Grid-interactive based converters must meet stringent requirements to comply with standards. An important safety grid network protection is required for islanding detection (ID) for distributed power generators (DPGs). The DPG must detect the grid fault and cease power production to the ac grid within the voltage and frequency limits imposed by country-specific standards [5].

Islanding detection methods can be implemented that are external to the DPG, for example through power line communication supervisory control and data acquisition [49], [50]. However, the external solutions have disadvantages related to additional complexity, cost and communication-based protection. An internal solution at the DPG level is preferred, since the anti-islanding (AI) protection is embedded within the controls of the power generator source. Since the anti-islanding is embedded within the control block level, the methods would enable a greater degree of freedom for implementing algorithms.

Passive AI methods are based on the monitoring of variations to grid parameters (voltage, frequency, phase and harmonics of voltage and current), which might occur during an islanding event. In general, the passive methods have a blind area, i.e. a non-detection zone of operation

due to the nature of the *RLC* load at the moment of islanding [51] - [54]. Passive methods with harmonic detection and monitoring without non-detection zone (NDZ) for islanding detection have been investigated [55], [56]. These methods are sensitive to nuisance trips causing loss of renewable (e.g. solar, wind) power production.

Active islanding detection (ID) methods are based on positive feedback from at least one of the following grid perturbation parameter: frequency, phase, harmonics, active and reactive power. The active AI based on the frequency and voltage drift methods are very popular for single-phase converters due to straightforward implementation: active frequency drift [57], [58] slip-mode frequency and phase shift [59], [60]. Sandia frequency and voltage shift [61]. These methods can achieve NDZ to zero, but at the same time, special attention must be paid to the current waveform injected into the grid, as periodic step variations can cause the current controlled reference to contain harmonics.

The islanding detection with grid impedance estimation can use harmonic injection [62] or active/reactive power variation [63], [64]. An anti-islanding method implemented at the phase-locked loop (PLL) control structure [65], [66] has the advantage of using the existing current reference with grid synchronization. An optimum operating point of the ratio between the current level of distortion and the efficacy of the method must be found, and from this point of view the methods using harmonic injection have an intrinsic disadvantage.

Active and reactive power variation can be implemented at the dq-transformation structure, and represent another attractive method for islanding detection [67], [68]. Different approaches have been reported [69] where the output of reactive power controller is added to the combination of active power and detected frequency mismatch. Another approach is to periodically vary the reactive power with a constant disturbance amount [70] or the reactive

power variation is based on resonant frequency of ac loads [71]. A summary of positive feedback based anti-islanding (AI) schemes and design guidelines have been reported in [72].

While the focus of these methods is strictly on anti-islanding, the research and developments presented in this thesis describe the details of a unified control, where interestingly, other algorithms are suggested for integration with the islanding detection methods: maximum power point tracking (MPPT) and grid fault safety redundancy for islanding detection.

1.2.3.   Grid Support Requirements for Grid-connected Systems

In recent years, with a higher penetration of renewable distributed generators into the ac grid network, the risk of grid instabilities and vulnerabilities has increased. Distributed generation systems are designed to supply power for utility ac grid networks within specific voltage and frequency limits. The power generators must cease energizing the ac grid when operating outside of the voltage, frequency and time limits imposed by country-specific standards (e.g. UL, CSA, VDE, BDEW) [5].

The transmission system operators (TSOs) responsible for power dispatch management and, develop grid codes (GCs) [73] - [77] that are necessary in order to adopt and integrate renewable power systems.

The GCs are continuously revised, and new supplements (e.g. California Public Utilities Commission: Rule 21, Hawaii Electric Companies: transient over-voltage, frequency-voltage ride-through, requirements) are issued to ensure the compliance of grid inter-connection power generators. The most important grid connection requirements for renewable power systems are related to the low- voltage and medium-voltage grids. The new design platforms of power converters must be designed with grid support features, which operate cohesively while

managing anti-islanding [5], [78] protections, voltage/frequency ride through [79] - [82] and active/reactive power controls [83] - [87] under grid faults [88] - [90].

The utility GCs have specific grid support requirements for grid-connected power generators [73] - [75]. The GC requirements normally addresses one active feature at a time. The requirements include:

1) Response to frequency variation to reduce the active power for over-frequency and increase active power for under frequency. For example, the power generator must reduce its active power by a certain power gradient when the line frequency increases over a specified value (e.g. 60.2 for 60Hz or 50.2Hz for 50Hz grid system).

2) Static grid support, where the power generator is required to have configurable reactive power set-points. The power factor (PF) or reactive power (Q) are set to a constant value; reactive power value is a function of the grid voltage variation, $Q(v)$; power factor is variable, with the active power operation, $cos\varphi(P)$.

3) Dynamic grid support (e.g. low and high voltage ride through) in which the power generator delivers reactive current on a pre-determined voltage transient profile.

Compliance with the relevant national and local codes is mandatory for renewable energy systems. The standard grid connection requirements for distributed generation impose configurable grid support features [91]. For example, the main factors that cause ac network grid frequency deviations are loss of main power generation (e.g. due to an old power system), lack of grid support capability in PV power generators, and sudden interruptions in the productivity of PV generator caused by high dynamics in irradiance [92]. The renewable energy PV/wind sources and electrical energy storage (EES) elements (e.g. batteries) are grid-interfaced through

distributed power converters [93]. The power converters' systems can be integrated in islanded (off-grid) and grid-connected ac networks.

Different control approaches are available for driving the power converter in specific modes of operations. The system controller can be designed to address a wider range of single- and three-phase converter applications, including at least one of following control modes of operation:

a) grid-forming stand-alone (UPS mode)

b) grid-supporting (islanded mode and grid-connected)

c) grid-feeding (grid-connected)

d) grid-loading (active rectifier or charge mode)

The integration of the aforementioned control modes into the system controller enables versatile power converter operation in both islanded and grid-connected ac networks.

a) In grid-forming mode, the controller is designed to emulate the converter into an ideal ac voltage-controlled source (Fig. 1.4). The dc input source (V_{dc}) used is an electrical energy storage element. A typical practical example is a line-interactive uninterruptible power supplies application, due to its high-fidelity voltage and frequency regulation. Power sharing by parallel multi-converters can be achieved through the implementation of accurate synchronization between the converters [94]. The advantage resides in the fact that the ac bus voltage and frequency are well regulated due to low-output impedance. Through communication, the multi-converter system easily controls the main transfer switch for stand-alone UPS (back-up) and grid-connected modes. The major disadvantage is the need of hardware communication between converters, and more attractive solutions have been proposed to avoid the communication signals [95].
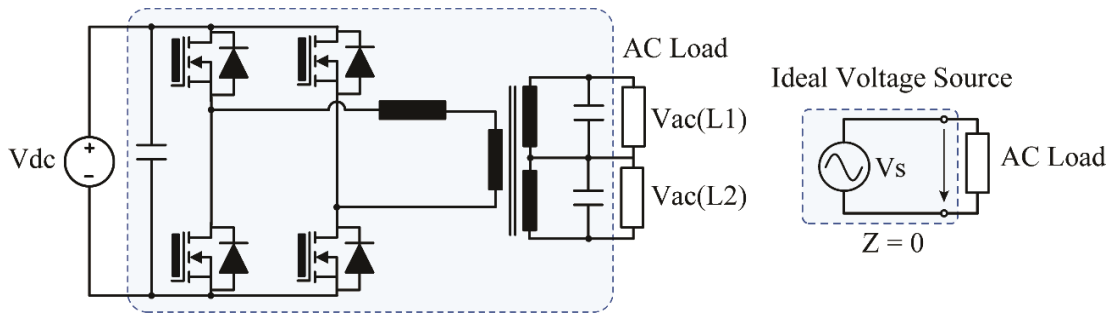
Figure 1.4: Two-level full bridge topology example for single phase (e.g. $120V_{LN}/240V_{LL}$) transformer-based voltage-forming converter.

b) In grid-supportive mode, the controller is designed to emulate the converter into combined voltage- and current-controlled source (Fig. 1.5) with typical applications in micro-grids. A commonly used dc source (V_{dc}) is a PV or EES generator. The controller's main purpose is to participate in ac voltage and frequency regulation by controlling the active power (P) and reactive power (Q) delivered from the converter. The power sharing control between the paralleled converters within a micro-grid system is implemented using droop and virtual output voltage controllers [96] - [103]. Low-voltage micro-grid-support has been proposed in the form of voltage-based droop using P/V-droop characteristic to control the active power depending on the grid voltage variation range [104]. Control strategies for seamless transfer between islanded and grid-connected modes of operation have been proposed in [105] - [107].
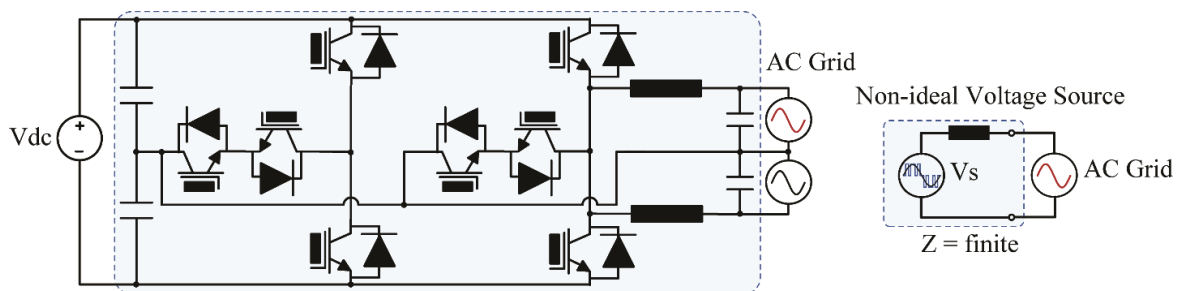
Figure 1.5: Three-level topology example for single phase (e.g. $120V_{LN}/240V_{LL}$) transformer-less grid-supportive converter.

c) In grid-feeding mode, the controller is designed to emulate the converter into an ideal current-controlled source (Fig. 1.6), with a wide applicability in utility-grid interactive distributed generation. A common dc input source (V_{dc}) used is a PV or EES generator. Grid-feeding based converters must meet stringent requirements to comply with standards and certifications (e.g. IEEE1547, CSA107.1-01, DIN EN 50438, VDE-AR-N 4105, AS4777, JEAC9701).
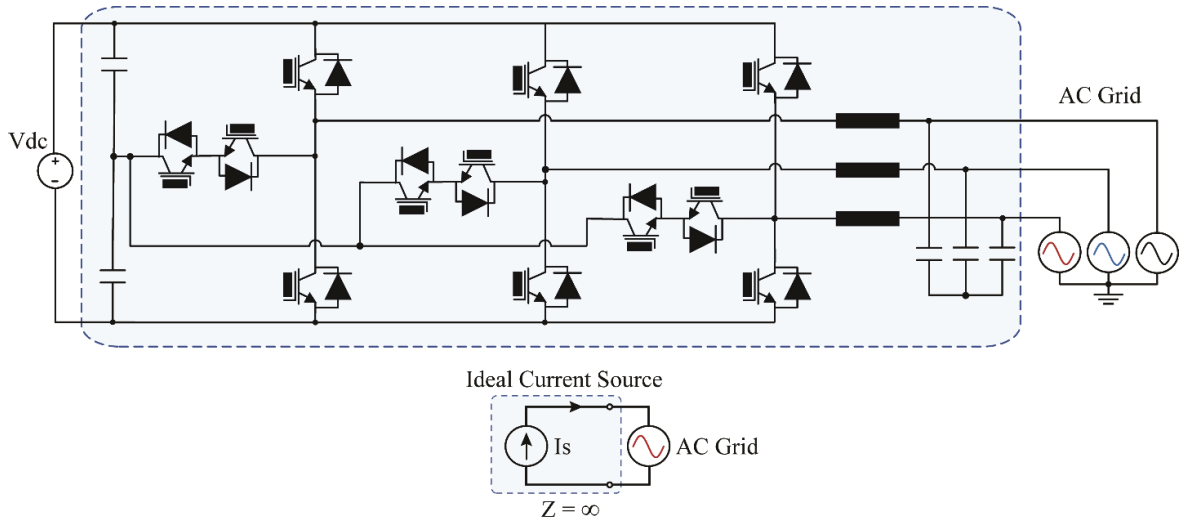
Figure 1.6: Three-level TNPC topology example for three phase transformer-less grid-feeding converter.

The primary low-level controller for current regulation is designed with high bandwidth and performance, to ensure fast and stable control [108]. The higher-level control layers are designed to access the current reference loop in order to perform slower tasks (e.g. maximum power point tracking, temperature compensated P/Q reference set-points). Transmission system operators (TSOs) require access of communication with grid-feeding converters' P/Q set-points for flexible power dispatch. Solutions for the integration of renewable energy sources, PV and wind, with battery energy storage, have been investigated with energy management with multiple energy storage systems [109] - [112]. However, the integration of PV and battery EES for grid-support controls with extended capabilities, beyond GC standards have not been investigated. Specific GC requirements are imposed on PV inverters for the supply curtailment and the cease

of operating beyond a certain frequency limit. The existing inverter power curtailment method, and sudden cease of power production induce a local perturbance to the ac grid network. Furthermore, this effect could be amplified in cases where there is high renewable PV/wind penetration in the grid network. In contrast, the proposed controller transitions the power flow from grid-feeding to force charge, using a grid-loading mode for ac network power balancing.

d.) A new control method (described in Chapter 4) is proposed in the form of grid-loading mode (energy storage charge phase), where the controller is designed to receive active power and transfer to an energy storage element. The controller commands the EES converter to transition from operating in grid-feeding, to operating in force charge for achieving grid-loading. The transition is implemented with adjustable ramps for overall power smoothing/balancing, which results in improvements to grid stability.
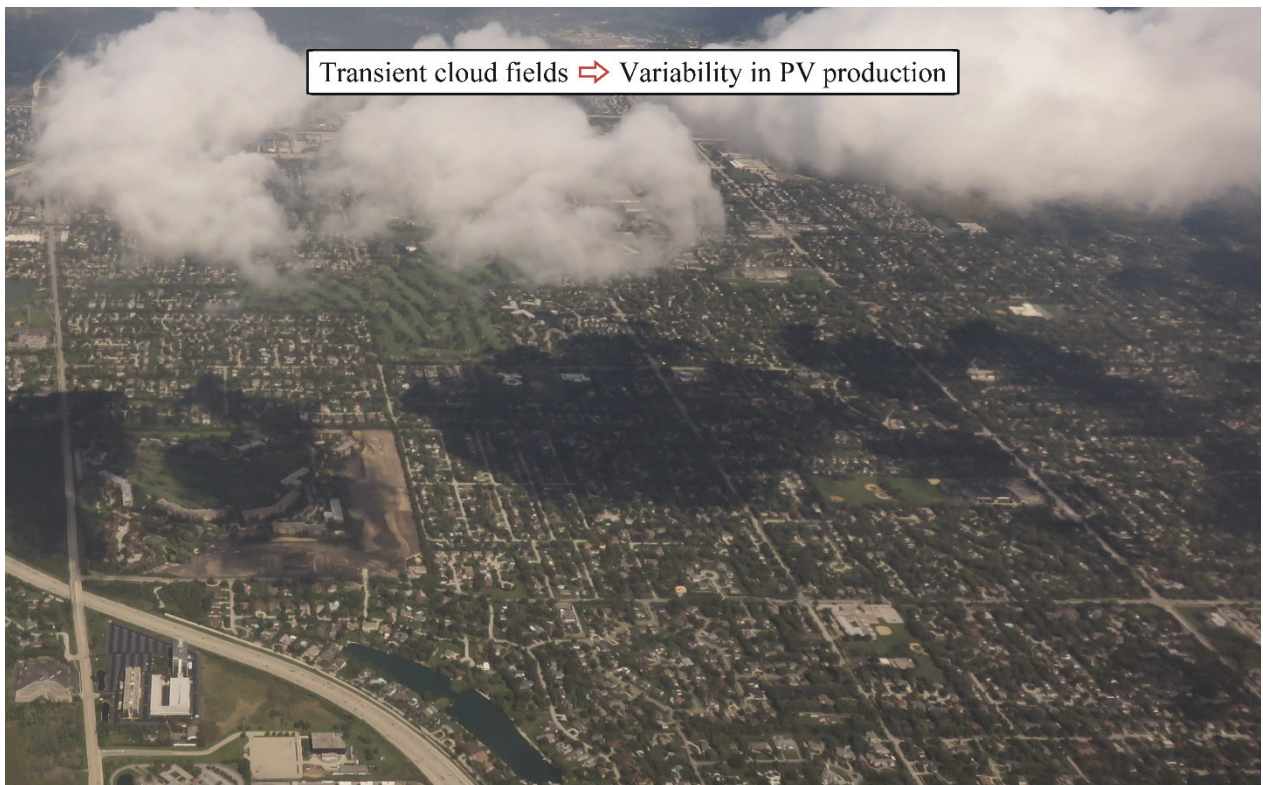
Figure 1.7: An aerial view example of transient clouds which significantly attenuate ground-level solar irradiance intensity with impact of variability in PV generation (Source: E. Serban, 2016).

In Fig. 1.7 is shown an aerial view example of transient cloud fields, causing variability in PV energy production. The impact of transient clouds to the sudden change in PV production is perceived to be a major concern for transmission system grid operators.

The typical application for the proposed grid-support controller relates to variable renewable PV/wind generation, which markedly affects the stability of the operation of utility-grid systems. The end result aims to a system contribution of the grid network stability, using the proposed controls implemented locally, at every distributed generator, which collectively will improve the ac network stability.

1.2.4. Photovoltaic Cell Characteristics

The photovoltaic effect is related to the generation of voltage and current from a material (e.g. p-n type, semiconductor diode) upon exposure to sunlight. A consequence of photons absorbed by the charge carriers (e.g. electrons) is an excitation of the carriers to a higher-energy state (e.g. free electrons from their bonds). This generates an electromotive force and part of the light energy is converted into electric energy. The most common models of PV cell used as equivalent circuits [113] - [116] with physical and current-voltage characteristics are illustrated in Fig. 1.8, (a) - (g).

The model of PV cell provides an estimation I-V and P-V characteristic curves, and thus emulates the cell behavior under various environmental and loading conditions. The simplest model is the basic single-diode shown in Fig. 1.8 (a), and the output cell current I is given by four-parameter equation:

$$I = I_{ph} - I_{D1}\left(e^{\frac{V}{V_{t1}}} - 1\right).$$ (1.1)
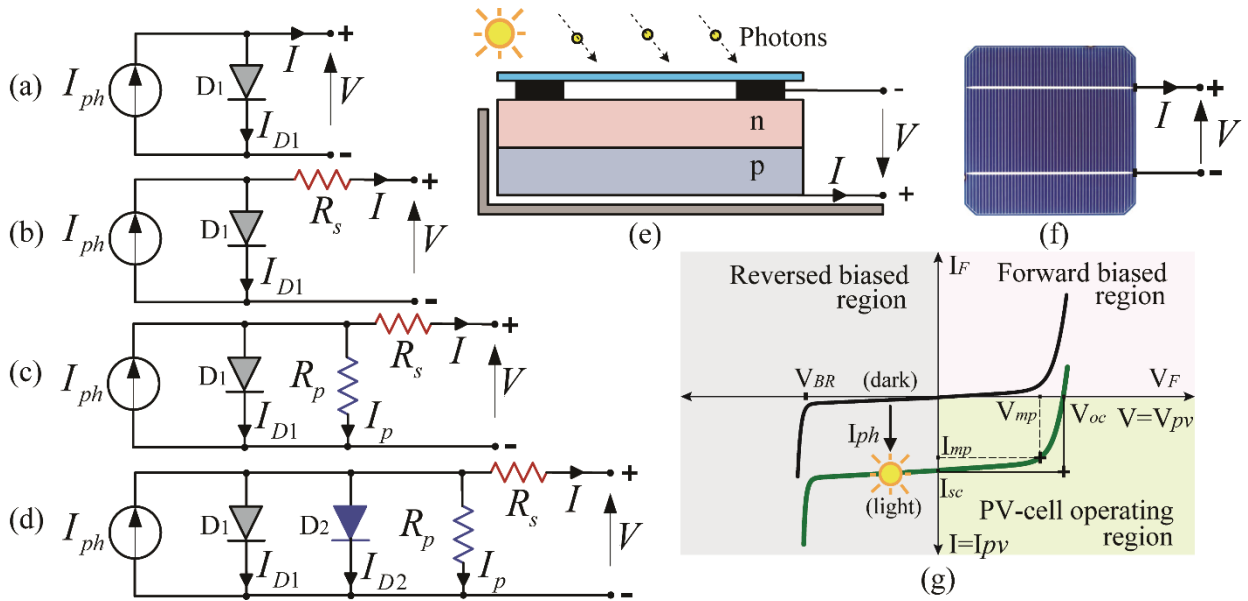
Figure 1.8: Photovoltaic cell models.

(a) Single-diode ideal model

(b) Single-diode and series resistance model

(c) Single-diode, series and parallel (shunt) resistance model

(d) Double-diode, series and parallel resistance model

(e) PV cell simplified cross section

(f) PV cell physical structure

(g) Current-voltage (I – V) characteristics.

The current-voltage expression considering the series resistance R_s (Fig. 1.8 (b), e.g. due to internal cell resistance, grid contacts), (1.1) becomes a five-parameter model expression:

$$I = I_{ph} - I_{D1}\left(e^{\frac{V + I \cdot R_s}{V_{t1}}} - 1 \right).$$
(1.2)

The PV cell crystal imperfections with leakage current across the junction and within the cell, lead to parallel resistance (R_p) addition, as shown in Fig. 1.8 (c) and (1.2) becomes:

$$I = I_{ph} - I_{D1}\left(e^{\frac{V + I \cdot R_s}{V_{t1}}} - 1 \right) - \frac{V + I \cdot R_s}{R_p}.$$
(1.3)

The double-diode model shown in Fig. 1.8 (d) further improves the cell model, including other undesired effects of losses due to carrier recombination in space charge region and surface recombination. Finally, the seven-parameter model of the cell output current is given by:

$$I = I_{ph} - I_{D1}\left(e^{\frac{V+I\cdot R_s}{V_{t1}}} - 1\right) - I_{D2}\left(e^{\frac{V+I\cdot R_s}{V_{t2}}} - 1\right) - \frac{V+I\cdot R_s}{R_p}, \tag{1.4}$$

where:

- I_{ph} - photo-generated current
- I_{D1}, I_{D2} – reverse (dark) saturation current of diodes D_1, D_2
- R_s - cell series equivalent resistance
- R_p - cell parallel equivalent resistance
- V_{t1}, V_{t2} - cell equivalent junction thermal voltage, $V_{t1} = \frac{A_1 k T_c}{q_e}, V_{t2} = \frac{A_2 k T_c}{q_e}$, with diode quality (ideality) factors typical use $A_1 = 1, A_2 = 2$. Other parameters: T_c - cell p-n junction temperature, k - Boltzmann constant, q_e - electron charge.

The PV cell photo-generated current is influenced by the instantaneous light intensity G (i.e. solar irradiance), cell temperature T_c, and cell current temperature coefficient β_I with respect to a specified reference standard test conditions (Table 1.1), as per the following expression:

$$I_{ph} = I_{ph.ref} \frac{G}{G_{ref}}\left[1 + \beta_I (T_c - T_{ref})\right]. \tag{1.5}$$

An estimation of the cell temperature (T_c) can be determined using Nominal Operating Cell Temperature (NOCT, Table 1.1) methodology:

$$T_c = T_a + \frac{G}{G_{ref}}\left[(T_{NOCT} - T_{ref})\right]. \tag{1.6}$$

The PV cell (module) data specification (e.g. ratings: $V_{mpp}, I_{mpp}, V_{oc}, I_{sc}, P_{max}$) is provided based on specific test conditions, as shown in Table 1.1. The associated performance parameters are the nameplate product ratings provided by the module manufacturer.

Table 1.1: PV cell (module) test conditions under Standard Test Conditions (STC) and Nominal Operating Cell Temperature (NOCT).

Parameter	Solar irradiance G_{ref}	PV cell reference temperature	Ambient reference temperature	Spectrum air mass	Wind speed
STC	$G_{STC} = 1000 \, W/m^2$	$T_{ref} = 25 \,°C$	-	1.5	-
NOCT	$G_{NOCT} = 800 \, W/m^2$	-	$T_{ref} = 20 \,°C$	1.5	$1 \, m/s$

The PV cell I-V and P-V characteristics can be developed using equations (1.1) - (1.6), depending of desired model accuracy, under the following circuit conditions:

$$I = \begin{cases} I_{sc}\big|_{V=0} & \text{short-circuit condition} \\ I_{oc}\big|_{V=V_{oc}} = 0 & \text{open-circuit condition} \\ I_{mpp}\big|_{V=V_{mpp}} & \text{maximum power point} \\ \dfrac{dP}{dV}\bigg|_{\substack{V=V_{mpp} \\ I=I_{mpp}}} = 0. \end{cases} \tag{1.7}$$

Results of I-V and P-V characteristics are reported in literature [117] for cells made from different semiconductor materials (e.g. crystalline, polycrystalline and thin film).

In practical applications, a number of individual PV cells (e.g. 72 cells) are interconnected in a sealed, waterproof package forming a PV module (panel). To further increase their utility, the modules are in series and/or parallel connected for an array configuration. Complementarily, power converter systems are designed to harvest direct current (dc) electric energy from a solar PV array, convert it to useful alternating current (ac), and generate the harvested solar electricity into ac power grid. The purpose of this research work is to investigate and develop new high

performance solutions for a power conversion system, the link between PV, electrical energy storage and ac power grid.

1.3. Contributions of the Work

The main goal of this work is to introduce a power conversion system which makes use of new control strategies, implemented in three interdependent control mechanisms, integrated within grid-connected converters. When all three interdependent control mechanisms are combined, a set of advanced system functionalities will be enabled. First, the limitation in performance for energy harvesting of pre-existing PV systems is addressed with voltage extended novel strategies. A new architecture approach using a string mini-boost for high performance and cost optimization is investigated in detail. Second, the research objective for system safety compliance in grid faults detection is investigated with new methods, namely islanding search sequence and with MPPT unified controls. Third, the grid stability improvement under variability of renewable energy sources, is investigated with active and power balancing controller for voltage and frequency grid support.

Fig. 1.9 shows the conceptual system block diagram in the area of major improvement that will be investigated in this thesis. Once the control functionalities are established, designed and implemented, the grid-connected converter system becomes enabled for high performance operation.
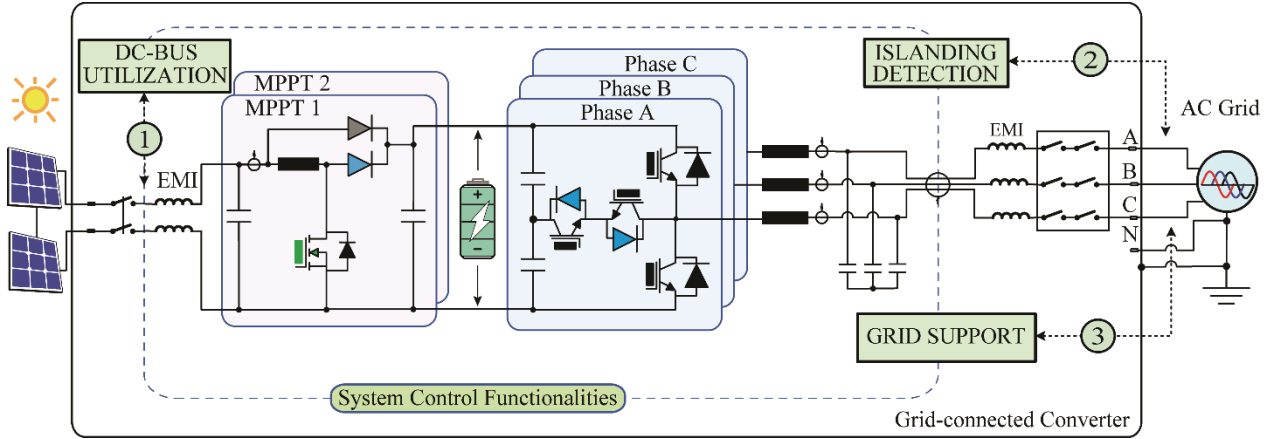
Figure 1.9: Conceptual system block diagram of the proposed control strategies featured in PV and EES grid-connected converters.

The proposed power conversion system with advanced control functionalities for grid-connected PV and EES converters are summarized in Table 1.2. A brief description of the advantages of using the proposed system solutions is illustrated in the following table:

Table 1.2: Advantages of proposed system control strategies featured in grid-connected PV converters.

Proposed system functionality	Advantage examples of the proposed strategies
① Voltage DC-bus extension range operation for PV systems (System performance).	▪ Expanded energy harvesting and inverter operational dc range. ▪ New modified modulation technique for 15% dc-bus extension gain and robust behavior under dynamic operation conditions. ▪ PV-converter system optimization with high performance cost-effective design. ▪ PV inverter with string mini-boost stage design for improved energy harvesting with low expense of system components.
② Safety methods and advanced grid fault (islanding) detection methods (Safety system compliance).	▪ Leakage circulation current reduction methods for safety and standards compliance. ▪ Enhanced islanding search sequence for safety and redundancy of the system. ▪ System integrated controls with MPPT and islanding detection for reduced ac grid perturbation. ▪ System redundancy in grid fault islanding detection solution.
③ Grid support control strategies (Grid stability).	▪ Grid frequency- and voltage-assist flexible controls designed to achieve grid stability with power balancing, under high penetration of PV/wind into ac networks.

The important contributions described in the following chapters include:

1.3.1. High Performance Power Conversion System with DC-bus Extension for Improved Energy Harvesting

The first area of contributions is related to the system's performance of dc voltage extension range, which leads to increased energy harvesting:

A) The introduction of a graphical I-V and P-V analysis approach, which reveals important insights of PV-converter system behavior, which identify the advantages in 1500V voltage systems to expand the dc-bus voltage utilization range using typical available power devices (e.g. 1200V) within three-phase grid-connected converters.

B) Converter operation with lower dc-bus limit, using the proposed VQ-controller with reactive power injection technique, where the minimum voltage level is reduced to achieve an advantageous dc-bus voltage extension (below the peak ac grid line voltage, $< V\sqrt{3}$).

C) The introduction of Quasi Space Vector (QSV) modified modulation to comply with 15% lower dc-bus extension while providing an accurate and robust Zero-Sequence for transients and paralleling of power converters.

D) A new architecture for photovoltaic grid-connected inverters based on a string mini-boost stage to increase the operating region of the inverter, without the losses and cost of a full-size boost stage. The proposed peak power envelope inverter operation provides design optimization for energy harvesting maximization. Three methods for leakage current reduction for safety and standard compliance are presented.

1.3.2. Grid-connected Inverters with Islanding Detection Control Strategies

The next advanced system's control functionality contribution is in the concept of four islanding detection (ID) methods development, with an islanding search sequence (ISS) integrated within PV converter at the following control levels: reactive power control (ISS-P), active power control

(ISS-Q), integrated MPPT and ID control structure (ISS-MPPT), integrated PLL ID control structure (ISS-PLL). The main contributions related to safety standards compliance and combined/integrated algorithms, are:

A) The introduction of islanding search sequence (ISS) applied to P, Q, and PLL islanding detection and the introduction of a new integrated MPPT detection method.

B) The proposal of using a combination of two or more methods simultaneously with a safety redundancy feature to provide fault tolerant system compliance.

C) Principles and practical system design guidelines are provided on the topic of search sequences in islanding detection for an integrated control.

1.3.3.   Grid Support Control Strategies

The third system's functionality advances into grid support functions, designed for distributed generators (DGs) relates to variable renewable PV/wind generation, which markedly affects the stability of the operation of utility-grid systems. The main contributions are listed below:

A) Extended $P(f)$ utility-grid support strategy: the converter's capacity to actively generate/receive power in response to frequency variation. The controller features a storage converter that operates in grid-feeding mode, while outside of the permissible GC frequency-voltage limits, commands the transition to force charge grid-loading in an attempt to gain stability through frequency-assist. The transition between grid-feeding and grid-loading is achieved using an adjustable power gradient, for smooth network power balancing.

B) Combined $P(f) - Q(v)$ grid support strategy: the converter's active/reactive power manipulation for frequency- and voltage-assist in response to signs of grid instability.

C) The $P - Q$ decoupled set-points are calculated from flexible pre-configured values of SoC_{min}, power gradient, energy shifting for time of use, voltage and frequency limits for immediate grid frequency- and voltage-assist in a network of DGs to achieve grid stabilization.

1.4. Dissertation Outline

The goals of this thesis involve investigation of a power conversion system employed with control strategies for high performance functionalities advancements in power electronics, using new advanced control methods and design techniques for grid-connected power converters. This work is organized in the following structure:

In Chapter 2, improved system energy harvesting methods for grid-connected converters are investigated, using dc-bus voltage range extension design considerations in 1000V and 1500V open-circuit voltage solar inverters. A comparison between two voltage systems is provided, revealing the advantages of 30% higher dc bus utilization for improved energy harvesting of 1500V PV systems. The concept of the proposed voltage-reactive power (VQ) controller is introduced, with design and implementation details for MPPT dc-bus voltage extension optimization. The proposed model is accompanied with the details of a new modified quasi-space vector (QSV) pulse-width modulation system implementation. Simulation and experimental verification of the VQ controller and QSV modified modulation applicable for MPPT dc-bus voltage range extension are performed using a three-phase 3-level, transformer-less inverter. Chapter 2 continues with concepts of improved PV energy production and design optimization methodology, using a string mini-boost stage for photovoltaic grid-connected inverters, to increase the operating at the boundary region of the inverter without the losses and cost of a full-size boost stage. The design optimization maximizes the utilization of the power components by

using the proposed peak power envelope inverter operation. Furthermore, improved string mini-boost efficiency operation schemes and safety issues of common-mode current with three mitigation design techniques intended for three-phase three-level inverter transformer-less topology are presented.

In Chapter 3, the system grid-interconnect requirements are addressed, with the characteristics of islanding detection elements and the parameters within which the islanding detection schemes can be implemented. This chapter describes the overall system architecture and the implementation of the control structures of the proposed islanding search sequence methods within the converter controls. The combined algorithms of MPPT, ID and safety redundancy leads to a novel integrated control solution for grid-connected PV converters.

The experimental verification uses a three-phase, multi-level, transformer-less converter developed for robust and rapid islanding detection for converter grid interconnect compliance.

Chapter 4 investigates system control functionalities implemented in a grid-connected energy storage architecture, in order to prevent ac grid network instabilities. It presents a control architecture and the description for implementation of $P(f)$ - $Q(v)$ strategies beyond standard grid support requirements. Simulations and experimental verification of the proposed $P(f)$ and $Q(v)$ grid support strategies are provided at the end of this chapter.

Chapter 5 presents an outlook related to future research in the field of PV and electrical energy storage interfaced with power electronic converters.

Chapter 2. DC-bus Voltage Range Extension in PV Inverters for Higher Energy Harvesting[2]

This chapter investigates development of a system with the objectives of higher PV energy production and system design optimization, by applying novel advanced control methods and techniques in grid-connected converters.

Solar plants based on single-stage conversion photovoltaic (PV) inverters have gained popularity due to their simplicity, high efficiency, and cost-effectiveness. Existing PV plants mostly operate under 1000V and are subject to wide dc-bus voltage variations due to the effect of PV cell temperature and the voltage of the maximum power point (well below the open circuit voltage). In particular, attractive locations such as US-Canada mountain/central regions are subject to extreme PV surface temperatures, making the dc-bus voltage variation a challenge for single-stage solar inverters.

Transformer-less single-stage power inverters present the merits of cost-effectiveness, simplicity in hardware design, and high efficiency to perform renewable power conversion. Typical (< 1000V) PV installations are subject to reduced dc-bus voltage utilization due to the effect of PV cell temperature and Maximum Power Point (MPPT) available voltage range.

---

[2] Part of this chapter has been published in [E. Serban, M. Ordonez, and C. Pondiche, "DC-bus voltage range extension in 1500 V photovoltaic inverters," IEEE Journal of Emerging and Selected Topics in Power Electronics, vol. 3, no. 4, pp. 901–917, June 2015.], [E. Serban, F. Paz, and M. Ordonez, "Improved PV Inverter Operating Range Using a Miniboost," accepted at IEEE Transaction in Power Electronics, Dec. 2016.] and [E. Serban, F. Paz, and M. Ordonez, "PV Array Voltage Range Extension for Photovoltaic Inverters Using a Mini-Boost," in *Energy Conversion Congress and Exposition (ECCE)*, 2016, pp. 1-8.].

2.1. System Analysis and Control Strategy for DC-bus Voltage Range Extension in PV Inverters for Higher Energy Harvesting

a) 1000V system   b)1500V system
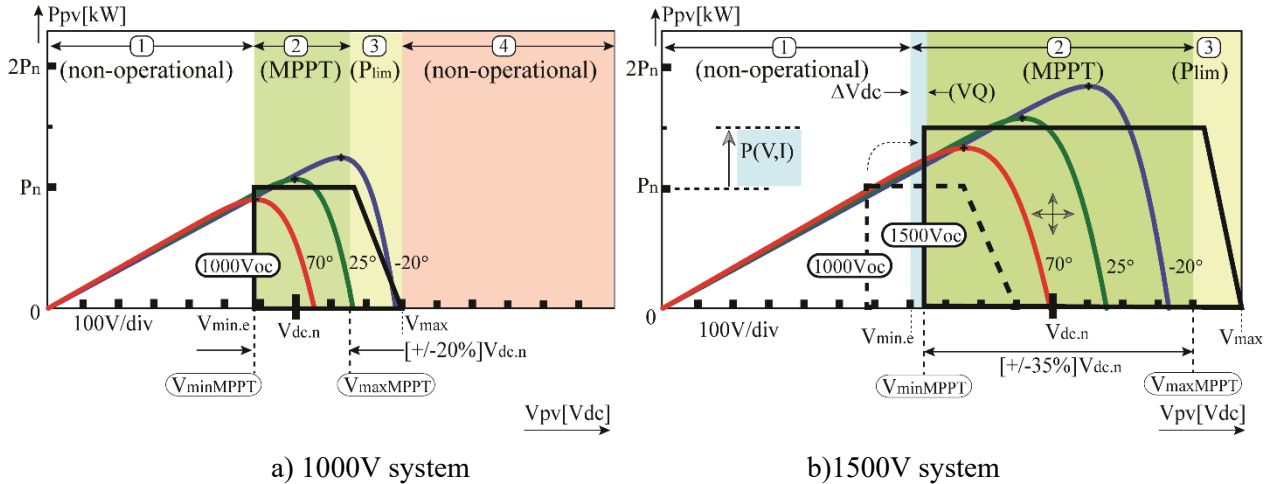
Figure 2.1: Power versus dc-bus voltage utilization characteristic: a) bus limitations (+/-20%$V_{dc.n}$) in traditional 1000V PV systems, and b) significant bus utilization extension (+/-35%$V_{dc.n}$) in 1500V PV systems under the same irradiance of 1000W/m2.

① Non-operational low voltage shutdown range

② MPPT region covered by the inverter

③ Power limit/derating mode

④ Over-voltage non-operational

(VQ) lower dc-bus limit extension (ΔVdc).

The dc-bus operation utilization range is in direct relation to the PV modules characteristics: voltage, current and temperature, as shown in Fig. 2.1 (a). The PV modules operation with the ambient temperature has an impact on the voltage maximum power point (MPP) characteristics. For instance, as illustrated in Fig. 2.1 (a), at higher ambient temperature the PV modules operate with lower MPP voltage (70˚C, I-V power curve), which require an extremely low dc-bus limit. On the other hand, the inverter upper dc-bus limit must be designed to withstand the maximum PV open-circuit voltage at high irradiance and low ambient temperature. The position of the power curves, as shown in Fig. 2.1 (a), are well outside the inverter dc-bus voltage operating

area, compromising the inverter ability to secure the maximum power extraction. Therefore, through the graphical investigation, Fig. 2.1 (a) clearly shows that the MPP can get outside the power area covered by the inverter, thus leading to undesirable energy waste.

2.1.1. PV systems Comparison: 1000V and 1500V

As will be seen, the MPPT dc-bus voltage operation for the solar inverter is preferably selected at the ratio of 2:1 between the maximum MPPT voltage ($V_{maxMPPT}$) and the minimum MPPT voltage ($V_{minMPPT}$) operation in full power (i.e. $V_{maxMPPT}:V_{minMPPT} = 2:1$). This suggested design ratio permits a better dc-bus voltage utilization to produce higher energy conversion and lower PV plant system cost. Further insight can be gained from the comparison (Fig. 2.1) between 1000V and 1500V open-circuit voltage systems. The design adaptation for 1500V system presents a significant advantage for dc-bus utilization energy yield and additional inverter rated power can be installed at the same dc and ac currents (same conductor size), in comparison with 1000V system. Therefore, the medium power (e.g. 10 - 100kVA) and large utility-scale central inverters (e.g. > 500kVA) are anticipated to increase the voltage ratio.

For clarity, in the 1000V versus 1500V comparison, the dc and ac inverter currents are considered constant, in order to use the same size conductors and related balance of systems (e.g. combiner boxes with fuses, circuit breakers, surge arrestors) - the difference resides only in the insulation voltage ratings. The 1000V system is shown in Fig. 2.1 (a), where the MPPT voltage range varies within +/-20% from the nominal dc-bus voltage (e.g. $V_{dc.n}$= 710V) with standard 3-phase grid connection (230/400V, $V_{maxMPPT}:V_{minMPPT} = 1.7:1$). Due to the power semiconductors voltage ratings availability and optimization for high efficiency (e.g. 600/650V, NPC topology), the inverter starts to curtail the power at 850V, where the inverter operates in power limit (P_{lim}) mode. Another system limitation is the open-circuit voltage of 1000V due to

some of present safety standards. The higher open-circuit voltage must be avoided (voltage range 4, Fig. 2.1 (a)) otherwise the inverter may be irreversibly damaged due to internal component ratings. Instead, the 1500V system illustrated in Fig. 2.1 (b), presents several major advantages. The first advantage is the extended MPPT dc-bus voltage of +/-35% from its nominal (e.g. $V_{dc.n}=$ 1125V), with a total of 30% wider than 1000V systems. This advantage translates to a higher energy harvesting for grid power production from the solar array. The 1500V system allows connecting a higher number of PV modules in series (>50% more than 1000V systems) and, with conversion operation at higher PV voltage, the system produces more power. Therefore, an immediate advantage it results to a wider MPPT dc-bus utilization (Fig. 2.1 (b)), while eliminating the need of an additional dc-dc boost converter stage. Since common power semiconductors availability jumps from 600/650V to 1200V voltage rating, NPC and active-NPC topologies can be optimized for 1500V systems.

The inverter power curtailment may start at 1500V or higher, with proper safe-operating area characterization and considering the safety standards. Another advantage is the increased inverter power module for a PV plant installation, with the advantage of less numbers of inverters installed (time and system cost are reduced).

The 1000V and 1500V PV system comparison summary is provided in Table 2.1.

The abnormal non-operation mode at dc overvoltage levels (V_{max}, Table 2.1) is typically doubled for 1500V systems comparing with 1000V system, due to the component ratings (e.g. power semiconductors, capacitors). However, the practical operational voltage range is less (e.g. < 1600V) due to certified component ratings and the necessary deratings for increased reliability: the higher the device voltage rating the higher derating factor is required, due to terrestrial cosmic radiation.

Table 2.1: 1000V and 1500V PV system comparison summary.

Criterion	1000V system	1500V system
MPPT range (dc-ratio)	+/- 20% $V_{dc.n}$	+/- 35% $V_{dc.n}$
DC overvoltage (V_{max})	> 1000-1200	> 2000-2400
Power curtailment	> $850 V_{dc}$	> $1500 V_{dc}$
Nominal inverter power	P_n	> 1.3 P_n
Operation at high/low PV cell temperature (MPP locus)	Restricted (e.g. < V_{MPP}, P_{lim})	Improved (e.g. V_{MPP}, P_{MPP})
PV plant design flexibility due to extreme temperature conditions	Restricted	Improved
System cost/W	Standard	Reduced
PV plant: installation & commissioning time	Standard	Reduced
Available certified components and safety standards for system design	Common	Less common
Power semiconductors voltage deratings subject to terrestrial cosmic radiation	Standard	Requires higher design margin

Note: 1000V: $V_{dc.n} = 710V$ and 1500V: $V_{dc.n} = 1125V$ ($V_{dc.n}$ selection value is function of the nominal grid voltage. The grid voltage establishes the minimum DC-bus voltage operation.)

(a)
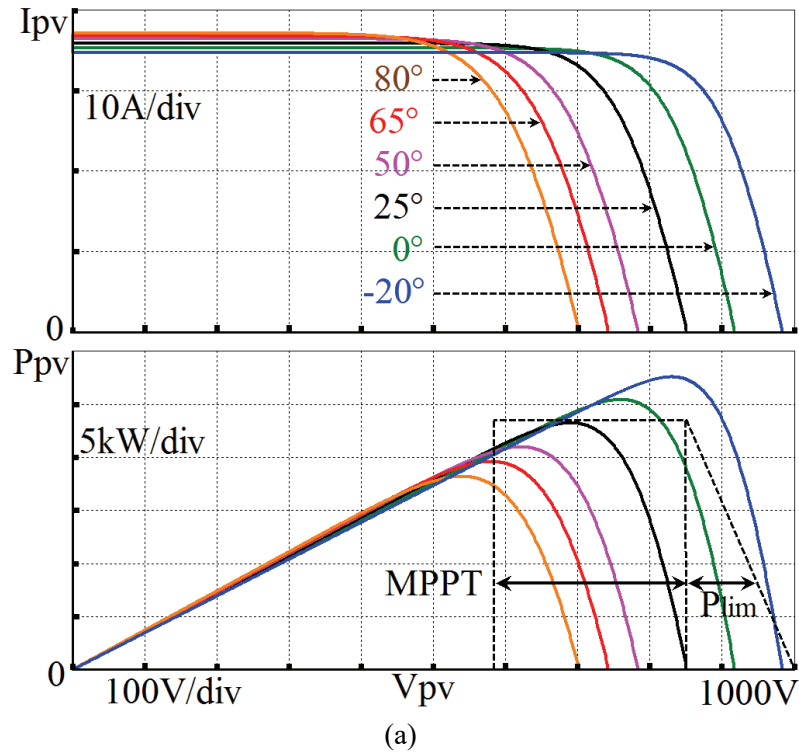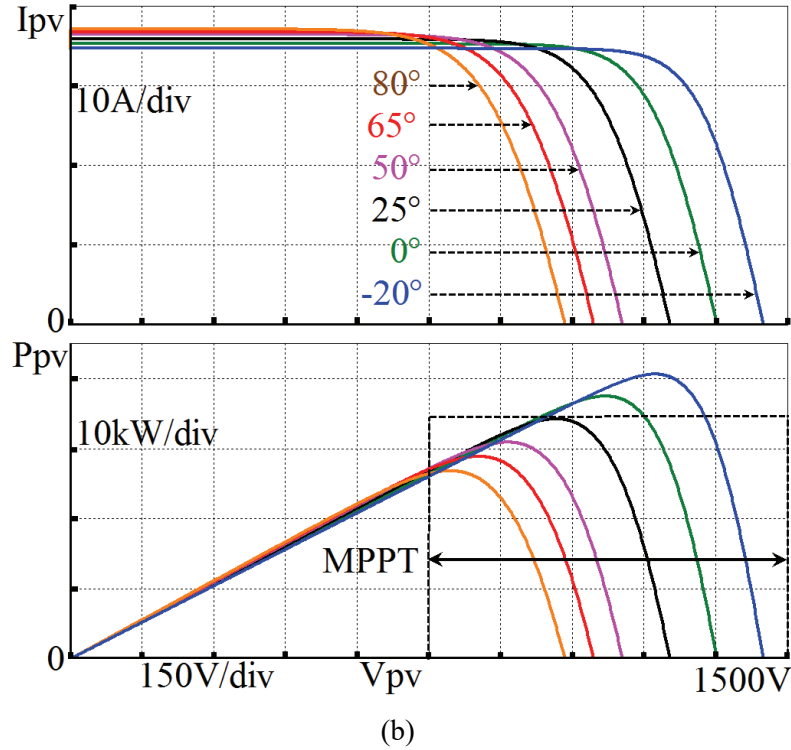
Figure 2.2: DC-bus voltage utilization comparison between 1000V and 1500V systems (I-V and P-V characteristics):

(a) The 1000V PV system MPPT range is limited to 575-850V (1.45:1 ratio) for $400V_{LL}$/50/60Hz grid.

(b) The 1500V PV system MPPT range is extended to 750-1500V (2:1) for $480V_{LL}$/50/60Hz grid.

PV module employed has $V_{oc.stc}$=44.8V, $V_{mp.stc}$=36.3V, β=-0.34%/˚C, P_{max}=305W (Canadian Solar CS6X-305P) with surface cell temperatures T_c= -20, 0, 25, 50, 65, 80˚C at $1kW/m^2$. The 1000V system has 4 parallel strings of 19 PV modules in series and the 1500V system has 4 parallel strings of 28 PV modules in series.

Fig. 2.2 shows a more detailed and direct comparison between 1000V and 1500V systems under different PV cell temperature conditions. The typical temperature specification range for PV modules is -40˚C to +85˚C and the analysis in Fig. 2.2 considers a maximum of +80˚C cell surface temperature. The high temperature operation conditions severely limit the energy production from the 1000V PV array, where the MPP voltage falls outside of the inverter dc-bus operation range in Fig. 2.2 (a) for temperatures greater than 65˚C. Unlike the 1000V systems, the 1500V PV inverter provides maximum energy yield with high PV cell temperatures (Fig. 2.2 (b)), where the MPP voltage is within the inverter operational lower dc-bus range. At low temperature

range and high irradiation, the PV array finds its operation at its best, capable to deliver high energy. For operation under very low PV cell temperatures (e.g., -20˚C), the 1000V system (Fig. 2.2 (a)) is unable to capture the power curve. The 1000V solar inverter is forced to operate at the upper dc-bus limit, where it is not able to capture the available power, due to derated/curtail power mode (P_{lim}) as shown in Fig. 2.2 (a). Instead, the 1500V system operates optimally at both, lower and upper dc-bus limit, as illustrated in Fig. 2.2 (b).

From the discussion about Fig. 2.1, it can be concluded that the input voltage ratio ($V_{maxMPPT}/V_{minMPPT}$) between the maximum and minimum MPPT voltage solar inverter operation plays an important role in harvesting energy under any environmental operating condition. Figs. 2.1 and 2.2 clearly indicate that the MPP locus (relation between voltage and current of PV module at MPP) of a 1500V system has a much larger exposure operational area than 1000V system, under different irradiance and temperature of MPP family curves.

The analysis suggests that beside the utility-scale centralized inverters, the next generation of medium power solar inverters will likely shift towards 1500V PV plant installations to achieve a larger input voltage range ratio ($V_{maxMPPT}/V_{minMPPT}$), preferably higher than 2:1 MPPT dc ratio. The medium power inverter is suggested for design with the weight for maximum of two people lifting for installation (e.g. $m < 70kg$). Medium power inverters for decentralized PV plants present advantages over large-utility central inverters in the form of redundancy with reduced downtime, reduced cost and time of installation, and easier maintenance. The extension of the PV voltage to a wider range (e.g. 1500V) provides a greater economic value, as long the power converter is designed closer to standard ac grid voltages (e.g. $480\,V_{LL}$, $600\,V_{LL}$). In addition, it is preferable that the system components selected are classified for 'low voltage' ($<1000\,V_{LL}$) applications. The benefits are related to the availability of cost-effective components.

Table 2.2: Solar inverters parallel connected in PV applications with standard/custom grid transformer.
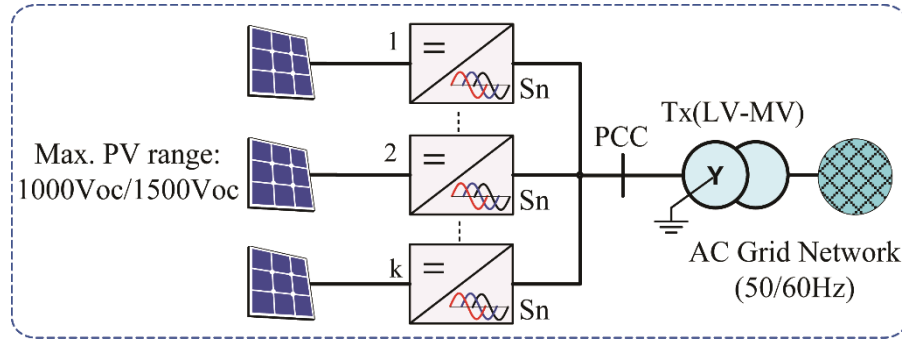
PV Voltage system	PCC Grid Voltage V_{LN}/V_{LL} [V_{rms}]	P_n [pu]	MPPT range [V_{dc}] (dc-bus ratio)
1000Voc	Custom: 202/350	0.88	500-850 (1.7:1 ratio)
	Standard: 230/400	1	575-850 (1.48:1 ratio)
1500Voc	Standard: 277/480	1.2	700-1500 (2.14:1 ratio)
	Custom: 300/520	1.3	750-1500 (2:1 ratio)

Table 2.2 shows the typical PV plant characteristics, where 'n' inverters are connected in parallel at the point of common coupling (PCC) and interfaced to the ac grid network through low-voltage (LV) to medium-voltage (MV) transformers. It should be noted that the PCC-LV grid could be customized from standard LV grid (e.g. $230V_{LN}/400V_{LL}$) by simply changing the transformer turns-ratio. This simple procedure enables higher dc-bus utilization, especially for 1000V system, where for a custom $202V_{LN}/350V_{LL}$ LV grid the dc-ratio is increased from 1.48:1 to 1.7:1. The disadvantage of this approach becomes the reduced inverter rated power with 12% as shown in Table 2.2. In this case, the PV plant cost increases (higher numbers of combiner boxes) with the benefit of increasing the dc-bus for higher energy yield. The 1500V system eliminates such constraints where the PCC-LV grid can be either with standard or custom LV-

MV transformer. As shown in Table 2.2, the MPPT range is similar for the custom or standard LV grid.

The discussion and study presented in this section provides evidence and insight about the advantages of 1500V PV systems and the importance of dc-bus ratio selection. The dc-bus extension range in 1500V systems is able to capture more energy from the PV arrays under a wide range of PV cell temperature (unlike the 1000V PV system) and improve the MPPT dc-bus ratio (greater than 2:1 ratio). The trend for higher voltage operation (e.g. > 1500V) will continue as long the all-inclusive technology is enabled to support the system application: safety standards, component ratings (e.g. PV modules, power semiconductors, dc and ac switch gears).

2.2. VQ-control Strategy for MPPT DC-bus Voltage Extension

The objective of this section is to develop the VQ reactive injection technique, so the minimum voltage level is reduced to achieve an advantageous dc-bus voltage extension (below the peak ac grid line voltage). A major limitation for the inverter dc-bus voltage-operation is the reduced available MPPT range over the realistic ambient temperature range. As a result, the energy harvest is reduced due to the limitation of threshold voltage ($V_{minMPPT}$), therefore a loss of PV plant production efficiency. The solar plant PV array is selected to operate from minimum to maximum ambient temperature due to extreme weather climate conditions (e.g. US-Canada higher elevation regions). For example, considering the environmental ambient temperature range of (-30 to +50)℃ the PV module can reach to the cell surface temperature in the range of ($T_{c.min}$ to $T_{c.max}$) -20 to +80℃. The PV array maximum open-circuit voltage is selected at the lowest daily minimum temperature (with PV module voltage and current temperature coefficients, β_V, β_I) and is related to the safety standards rated voltage (e.g. $V_{oc.max}$=1000V). The minimum

open-circuit voltage (V_{oc}) and maximum-power point voltage (V_{mp}) for the PV array string is determined at the daily maximum cell temperature (T_c), with the consideration of standard test conditions (STC) of 1000W/m^2 irradiance and T_{stc}=25˚C reference temperature, as per the following relation:

$$\begin{cases} V_{\text{oc}}(T_c) = V_{\text{oc.stc}}(T_c) \cdot \left[1 + \beta_{V_{oc}}(T_\text{c} - T_\text{stc})\right] \\ V_{\text{mp}}(T_c) = V_{\text{mp.stc}}(T_c) \cdot \left[1 + \beta_{V_{mp}}(T_\text{c} - T_\text{stc})\right] \\ I_{\text{sc}}(T_c) = I_{\text{sc.stc}}(T_c) \cdot \left[1 + \beta_{I_{mp}}(T_\text{c} - T_\text{stc})\right] \\ I_{\text{mp}}(T_c) = I_{\text{mp.stc}}(T_c) \cdot \left[1 + \beta_{I_{mp}}(T_\text{c} - T_\text{stc})\right] \\ P_{\text{mp}}(T_c) = V_{\text{mp}}(T_c) \cdot I_{\text{mp}}(T_c). \end{cases} \tag{2.1}$$
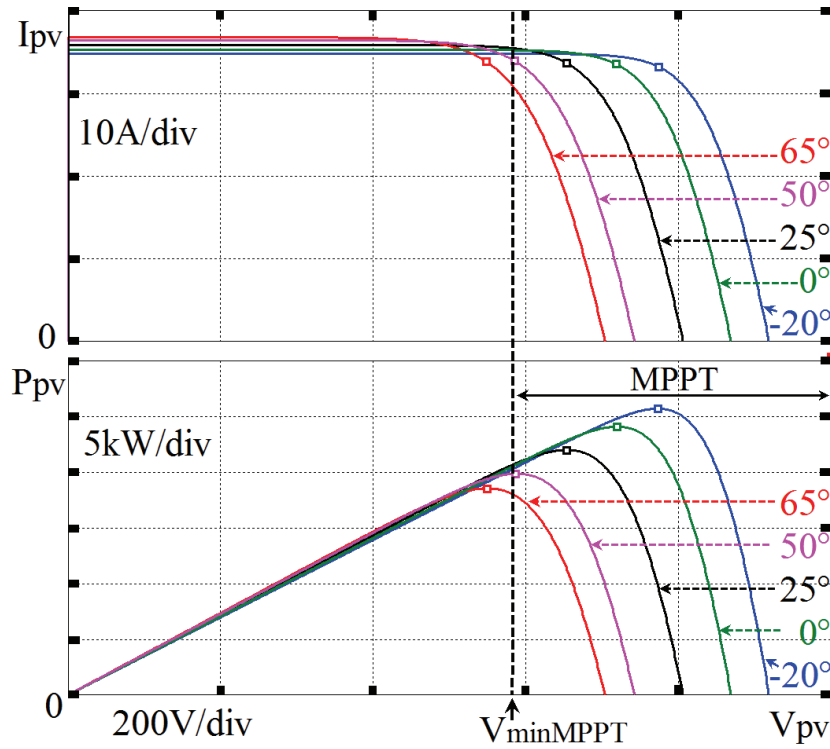
(a)
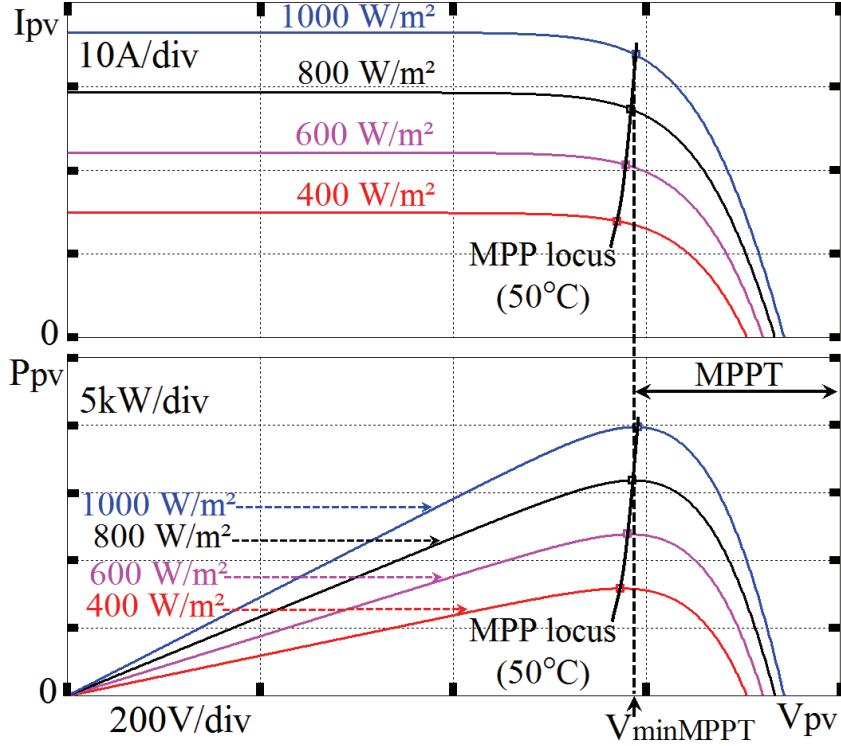
(b)

Figure 2.3: DC-bus voltage utilization limitation example (1000V system), using 4 parallel strings of 18 modules in series: significant decrease of MPP voltage level at high temperature and low insolation.

(a) I-V and P-V characteristics of PV array with different surface cell temperature levels (T_c=-20, 0, 25, 50, 65°C) at 1kW/m^2.

(b) I-V and P-V characteristics of PV array with different solar irradiation levels (G=400, 600, 800, 1000 W/m^2) at T_c=50°C.

PV module: $V_{oc.stc}$=44.8V, $V_{MPP.stc}$=36.3V, $\beta_V = -0.34\%/°C$, β_I=0.065%/°C, P_{max}=305W (Canadian Solar CS6X-305P).

Fig. 2.3 shows four parallel module-strings with crystalline silicon modules connected in series. The energy loss associated with inverter minimum voltage ($V_{minMPPT}$) is evident as the PV cell temperature increases (Fig. 2.3 (a)) or with the decrease of solar irradiation (Fig. 2.3 (b)). The MPPT dc-bus voltage available for the inverter operation at higher ambient temperature (>40°C) is severely limited, since the $V_{minMPPT}$ has to be greater than the peak ac grid line voltage (e.g. at grid line to line voltage $400V_{LL}$, $\hat{V}_{LL} = V\sqrt{3} = 564 \, V_{pk}$). Under these conditions, the inverter cannot operate in MPPT mode and the energy harvesting is reduced, with operation

in power limit mode. It is concluded that the MPP voltage point goes below the inverter lower operating range (e.g., minus 20% from nominal $V_{dc.n}$=710V). Clearly, further bus extension to lower limits benefits the ability of the inverter to capture energy. To overcome this detrimental low voltage issue, two steps are taken in this dissertation to push the lower dc-bus limit range: 1) an extension to minus 35% from nominal voltage (e.g. $V_{dc.n}$=1125V) using a 1500V system (already discussed in Section 2.1) and 2) VQ controller technique to extend the MPPT range further as explained below.

2.2.1. VQ Controller Structure and Inverter System

The proposed VQ controller technique provides the advantage of extending the MPPT range beyond the existing aforementioned limitation. The VQ controller calculates the minimum level required for the voltage reference and when $V^*_{min.e} \leq \max{(v_{an}, v_{bn}, v_{cn})_{rms}}\sqrt{6}$ it adjusts the reactive power in order to maintain the inverter in MPPT mode. The VQ controller maintains the modulation in the linear range, while the power quality remains unchanged. The VQ methodology provides the dc-bus extension regardless of the PV plant maximum operation voltage (e.g. 1000V or 1500V). From Fig. 2.3 (b) it can be noted that the dc-bus can be further extended towards the lower voltage range by employing the VQ controller.

The inverter is desired to operate in the linear modulation range to avoid the low-frequency baseband distortion of output phase currents, hence the minimum dc bus voltage ($V_{dc.min}$) is greater or equal to the grid phase voltage magnitude component (V) as per the following relation:

$$V_{dc.min} \geq \begin{cases} V \cdot \sqrt{3} & \text{with 3H-ZS modulation} \\ V \cdot 2 & \text{with SPWM}. \end{cases} \qquad (2.2)$$
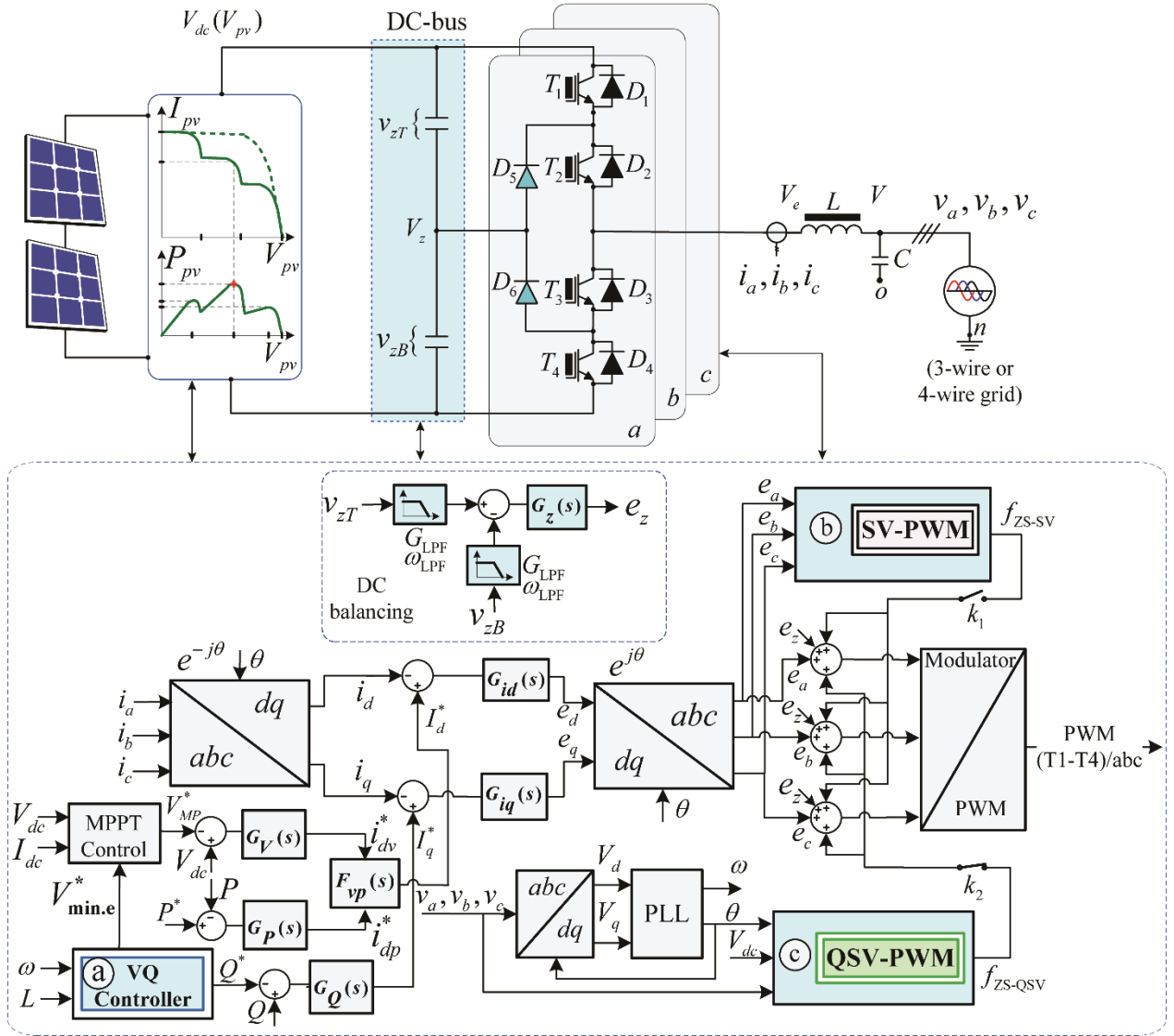
Figure 2.4: Three-level grid-connected inverter control structure: (a) VQ controller for MPPT dc-bus extension voltage utilization operation with carrier-based modulation for maximum dc-bus voltage utilization with (b) SV-PWM and c) proposed 3H-ZS QSV modulation.

Fig. 2.4 represents the conceptual block diagram of a three-phase grid-connected inverter with the modulation and control structures for the three-level NPC topology used for the analysis and implementation of the proposed techniques. The simplified 3-phase inverter power stage represented in a single-line diagram (Fig. 2.4), with inverter phase magnitude voltage V_e, grid phase magnitude voltage V, LC filter (o is the floating common point of filter capacitors) connected to a 3-wire or 4-wire grid system. The inverter current regulators are implemented in

synchronous reference frame voltage-oriented with zero phase and magnitude error controller design. The grid phase voltage magnitude component V_d detected by the PLL is considered aligned along d-axis and on q-axis the voltage component $V_q=0$. The dc-bus voltage V_{dc} regulation and its optimization are performed through the MPPT algorithm and active/reactive power controllers. The selection function F_{vp} arbitrates the inverter functionality: the priority is given to MPPT control and only in events of power derating (e.g. due to thermal limit) the power controller G_P is accessed. In normal operation, the inverter operates with the voltage G_V or active power G_P controllers to command the active current reference I_d^*, with the alignment on d-axis. The 3-level inverter active power regulation is achieved by using the active current controller G_{id}. The 3-level inverter reactive power regulation is achieved by the reactive current controller G_{iq} which is, for example, enabled to achieve dc-bus voltage extension ($V_{min.e}^*$).

In this research, the neutral-point compensation is performed by manipulating the common mode injection signal at the modulator level [118]. The dc balancing response under transient conditions is achieved at the fundamental line cycle (Fig. 2.4), and in order to achieve a faster dc balancing effect, the neutral-point control can be added at each switching cycle of the modulator [119], [120]. In the case that SVM strategy is used, the neutral-point balancing is typically implemented using the nearest three vector schemes without any extra switching state, for lower commutation losses. In the typical three-level inverters application, the load current (active and reactive) is well controlled by the inverter, which avoids causing an immediate imbalance at the switching cycle level by not impacting the neutral-point. The neutral-point proportional-integral controller G_z performs the top voltage side V_{zT} and bottom voltage side V_{zB} balancing by introducing the compensated signal e_z as a dc common-mode voltage injection to the modulator. The dc common-mode voltage injection method has been selected due to strong

balancing regulation [121] necessary for dc-bus voltage utilization maximization. The sensing signals to the neutral-point controller are filtered with the cut-off frequency (ω_{LPF}) selected below the line frequency (ω) for dc component top and bottom voltage regulation. As illustrated in Fig. 2.4, the 3H-ZS injection can be provided from the traditional carrier-based SV-PWM (k_1=on) or from the proposed QSV-PWM (k_2=on). The VQ controller becomes active only on demand, when the MPPT controller requires lower dc voltage range operation ($V_{min.e}^*$) with the details as follows.

2.2.2. MPPT DC-Bus Voltage Utilization with VQ
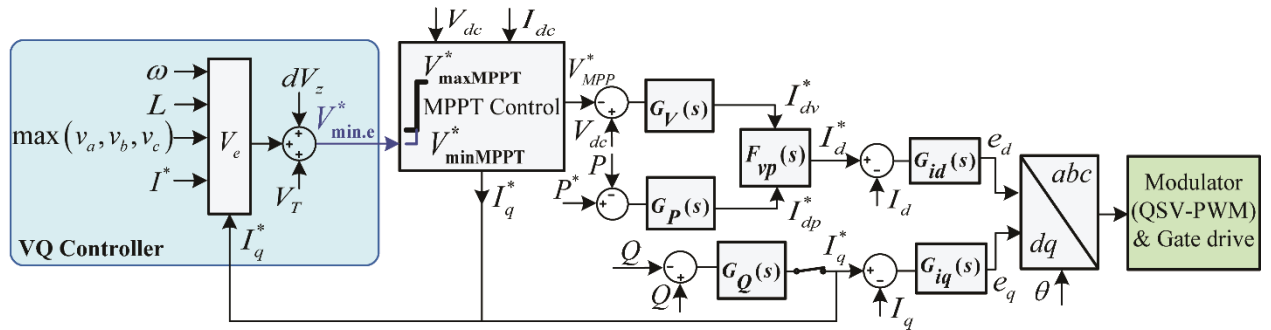
Figure 2.5: VQ controller for MPPT dc-bus voltage utilization extension.

The inverter operation over wider dc-bus voltage utilization is desired in order to allow a higher energy yield from the renewable sources. Fig. 2.5 shows the inverter control structure implementation of the proposed VQ controller, applicable for 1500V systems (as well as 1000V system). The MPPT control block represents the master controller which programs the voltage reference V_{MPP}^* for PV array global maxima determination, using $dP - P\&O$ technique [122], [123]. The selection function F_{vp} arbitrates the inverter active power in the following fashion: G_V becomes active if the PV power is less than the inverter nominal (rated) power ($P_{MPP} < P^* = P_n$), otherwise, when the active power set-point is less than the PV available power, ($P^* <$

P_{MPP}), the active power controller G_P is selected. The reactive power controller G_Q becomes active only under the reactive power commands (Q^*) of grid support functions (e.g. power factor lead/lag commands). For simplicity, the inverter filter inductor (L) and devices voltage drop (V_T) are considered constant. The rest of the parameters (e.g. ω-angular frequency, dV_z neutral-point deviation) are dynamically measured and calculated. At low dc bus range, the MPPT algorithm commands the reactive current reference (I_q^*), while the VQ controller updates the minimum value of dc bus ($V_{min.e}^*$), which after is provided to the MPPT controller (Fig. 2.5). The VQ controller calculates and updates the MPPT algorithm with the minimum admissible dc-bus voltage for linear modulation operation. The minimum dc-bus reference ($V_{min.e}^*$) regulation level is dynamically controlled in linear modulation by the VQ and MPPT controllers and must satisfy the following expression:

$$V_{min.e}^* = dV_z(I,m,\phi) + V_T(I) + k_m V_e \,, \tag{2.3a}$$

where:

- V_e represents the magnitude phase inverter voltage and k_m is dependent of the modulation control law (e.g. $k_m = \sqrt{3}$ with 3H-ZS injection).

- dV_z represents the neutral-point dc bus ripple deviation and its magnitude level is dependent of capacitance value between positive, negative and neutral-point, load current ($I = \sqrt{I_d^2 + I_q^2}$), modulation index (m), power factor angle (φ) and neutral-point controller (G_z) bandwidth. The neutral-point voltage deviation represents a loss in dc-bus utilization and the dc-balancing controller must be designed to regulate ($< 0.5\%$) the dc component top and bottom voltages in order to obtain dc-bus voltage maximization.

- m represents the modulation index and is given by:

$$\begin{cases} m = \dfrac{\sqrt{2}V_{LNrms}}{\dfrac{V_d}{2}} = \dfrac{2\sqrt{2}}{\sqrt{3}}\dfrac{V_{LLrms}}{V_d} \qquad m \in [0, m_{max}] \\[4mm] m_{max} = \begin{cases} 1 \quad \text{for} \quad \text{SPWM} \\[2mm] \dfrac{2}{\sqrt{3}} \cong 1.15 \quad \text{for} \quad \text{3H-ZS PWM.} \end{cases} \end{cases} \qquad (2.3b)$$

- $V_T(I)$ represent the power devices on-state voltage drop under phase current I.

Moreover, the dc bus voltage can be further reduced with the reactive power engagement, while the inverter continues to export constant active power to the grid. The dc voltage utilization range extension represents an important advantage since the inverter is able to operate at a wider dc input range. The particular case of 3-phase balanced and sinusoidal voltage system is discussed as follows.
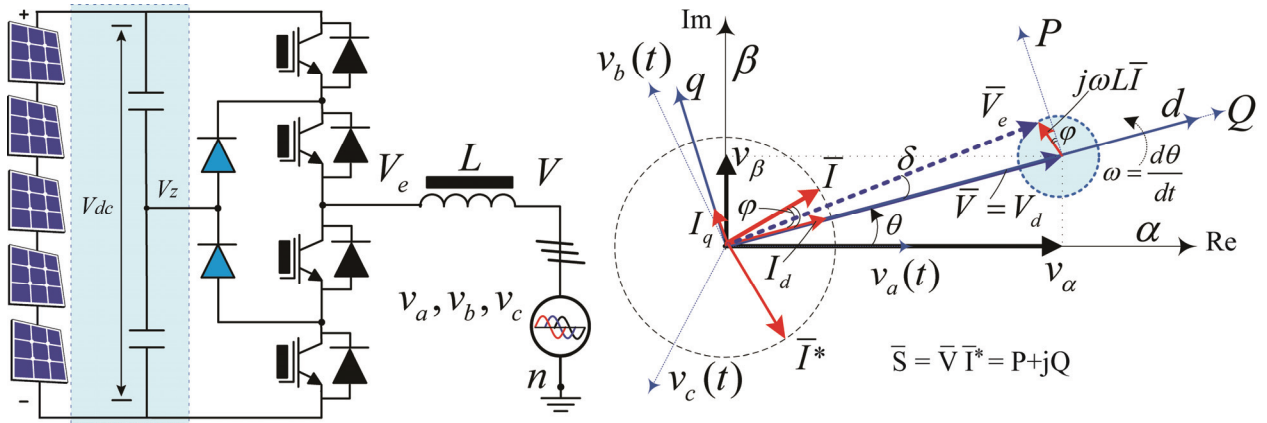
Figure 2.6: Three phase 3- level inverter vectorial diagram: abc natural coordinates, stationary $\alpha\beta$ and rotating dq-reference frame.

Fig. 2.6 illustrates the vector transformation diagram from a symmetrical balanced three-phase grid voltage system $v_a(t), v_b(t), v_c(t)$ to synchronous rotating dq-reference frame voltages V_d, V_q and the current vector I with its dq components I_d, I_q which are synchronously rotating with the angular grid frequency ω. The grid phase voltage magnitude $(\bar{V} = V_d)$ is aligned along the d-axis with the load angle $\varphi = \sphericalangle(\bar{I}, \bar{V})$ with respect to the inverter current vector $\bar{I} = (\bar{V}_e - \bar{V})/jX_L$, $j = \sqrt{-1}$. The inverter three-phase currents from natural a-b-c coordinates

i_a, i_b, i_c are transformed to stationary αβ-reference frame, i_α, i_β, which are then converted to synchronously rotating reference dq-frame I_d, I_q as shown in Fig. 2.6. The power transfer between the inverter and grid ($\bar{S} = \bar{V}\bar{I}^* = P + jQ$), considering a highly inductive filter (X_L) is given by the following active (P) and reactive (Q) expression [96], [124]:

$$
\begin{cases}
P = \dfrac{V_e V}{X_L} \sin \delta \\[2mm]
Q = \dfrac{V(V - V_e \cos \delta)}{X_L}.
\end{cases}
\tag{2.4}
$$

The inverter active power (P) injection to the grid is predominantly dependent on the power angle $\theta_v = \delta = \sphericalangle(\bar{V}_e, \bar{V})$. In practice, the power angle is a small angle formed by the inverter fundamental components V_e and the grid voltage V. The inverter output voltage magnitude can be controlled using the reactive power variation [125], [126]. The inverter magnitude voltage (before filter inductor L as per Fig. 2.4) can be determined from the vector diagram in Fig. 2.6 and the relation (2.4), as following:

$$
V_e = \sqrt{V^2 + \underbrace{\left(\frac{2\omega L}{3V}\right)^2 (P^2 + Q^2)}_{V_S} + \underbrace{\frac{4}{3}\omega L Q}_{V_Q}}.
\tag{2.5}
$$

As shown in relation (2.5), the inverter voltage (V_e) revolves around the grid voltage (V) with two terms, where in practical cases is found that V_Q is more dominant than V_S term. As evidenced in relation (2.5), the inverter voltage can be controlled according to the following two cases:

a) $V_e > V$ if $V_S + V_Q > 0$: this case corresponds to the inverter operation at unity and lag power factor.

b) $V_e < V$ if $V_S + V_Q < 0$: due to this property, the inverter can operate with an available dc-bus voltage below the magnitude of the grid voltage, hence extending the dc utilization range.

The dominant term $\omega L Q$ can be used for the dc bus extension, with three theoretical degree of freedom: angular frequency, inductor value and reactive power injection ($Q < 0$). In practice, the first two parameters (ω and L) are constant while the only the reactive component can become the control reference set point (I_q^* or Q^*, figs. 2.4 and 2.5). The inverter voltage can be lower than the grid voltage when the following condition is satisfied:

$$Q^2 + \frac{3V^2}{\omega L}Q + P^2 < 0. \tag{2.6}$$

From expression (5) and (6) it can be observed that the inverter voltage can operate with $V_e < V$ when the inverter reactive power is controlled within the following range:

$$Q = \left[-Q_{max}; \left(-\frac{3V^2}{2\omega L} + \sqrt{\left(\frac{3V^2}{2\omega L}\right)^2 - P^2} \right) \right]. \tag{2.7}$$

The reactive power (power factor lead, $Q < 0$, up to the maximum value Q_{max}) is controlled by the inverter in order to extend the dc-bus voltage utilization. The active and reactive power controlled by the inverter have the form:

$$\begin{cases} P = \dfrac{3}{2}V_d I_d \\[2mm] Q = -\dfrac{3}{2}V_d I_q, \end{cases} \tag{2.8}$$

where the measured voltage and currents from the abc/dq transformations are:

- V_d is practically the magnitude phase grid voltage, $V = V_d$

- I_d, I_q represent the inverter active and reactive components (magnitude) of phase currents.

With the expression manipulation (5) and (8) the inverter magnitude output phase voltage is obtained:

$$V_e = \sqrt{V_d{}^2 + \left(\frac{2\omega L}{3V_d}\right)^2 \left[\left(\frac{3}{2}V_d I_d\right)^2 + \left(\frac{3}{2}V_d I_q\right)^2\right] - \left(\frac{4}{3}\omega L\right)\left(\frac{3}{2}V_d I_q\right)}. \tag{2.9}$$

With further simplification, the relation (2.9) becomes:

$$\begin{cases} V_e = V_d \sqrt{1 + \left(\dfrac{\omega L I}{V_d}\right)^2} - \dfrac{2\omega L}{V_d} I_q \\ I = \sqrt{I_d^2 + I_q^2}. \end{cases} \tag{2.10}$$

From the relation (2.10) it can be observed that the dc-bus utilization extension is mainly dependent of line frequency (ω), ac inductance value (L) and reactive current component (I_q). The first two parameters (ω, L) are selected as part of the initial inverter design, while the reactive current component is manipulated on-line, at the time when the dc-bus becomes insufficient for linear modulation inverter operation.

When the solar inverter operates at nominal power, its apparent power rating (S_n) must be increased while the reactive power is injected for dc-bus extension range. If the apparent power (S_n) is kept constant (by design, due to power devices safe operating area of operation and thermal limits) then the VQ controller is enabled only when the $I_d < I_n$ ($I = I_n$ represents the nominal inverter current) and $P < S_n$ conditions are satisfied. In this case, the maximum reactive current is calculated $I_q = \sqrt{I_n^2 - I_d^2}$ and used in relation (2.10) for determining the minimum dc-bus voltage at which the solar inverter can operate in linear modulation. It should be noted that the dc-bus extension range is performed on an increased power losses expense, since the power devices operate at the nominal current (I_n), including both active and reactive currents. In conclusion, the VQ control strategy has the ability to extend the minimum dc-bus voltage utilization by employing the reactive power injection control for higher overall energy yield.
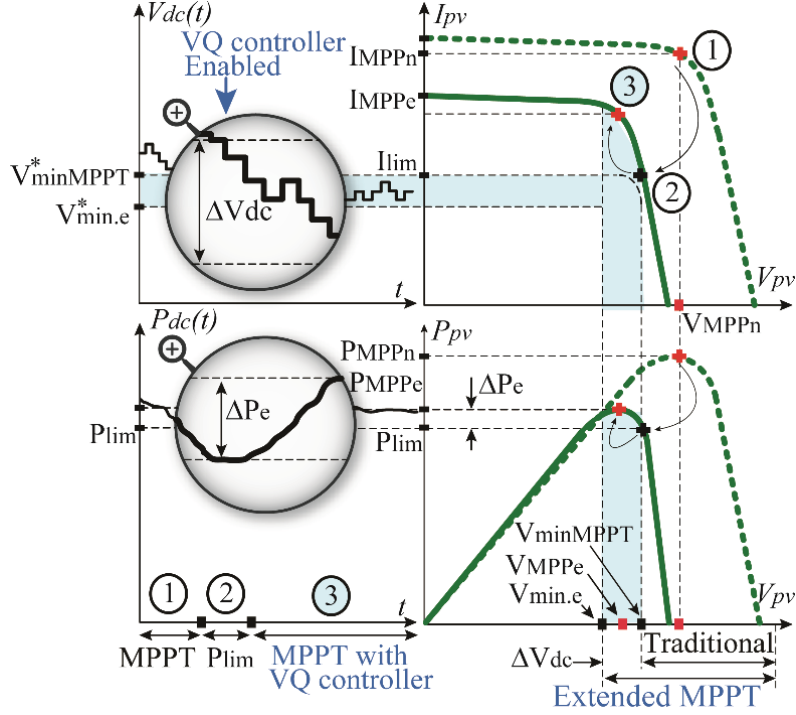
Figure 2.7: PV Inverter modes of operation example for the illustration of VQ controller mechanism: 1) MPPT, 2) power limit mode and 3) proposed VQ-controller with MPPT dc-bus extension.

Fig. 2.7 illustrates the solar inverter operation example under the following cases:

- Case 1: the inverter operates at the global maxima by harvesting the maximum available power P_{MPP} at $V_{MPP.n}$.

- Case 2: the inverter operates in dc power limit P_{lim} caused by insufficient dc bus voltage V_{minMPP}, due to higher PV cell temperature or lower insolation conditions. This case represents a limitation of MPPT operation using the existing control methods.

- Case 3: the VQ controller is enabled for MPPT dc-bus voltage utilization extension. The solar inverter is capable of operating at the global maxima (P_{MPPe}) and lower dc-bus voltage levels (V_{MPPe}). In this case the proposed inverter controls (Fig. 2.5) is using relation (2.9) to re-calculate the new minimum admissible dc-bus voltage ($V_{min.e}$) used by the MPPT algorithm. The dc-bus voltage utilization is extended with the reactive power

injection control, while the inverter continues to supply the active power to the grid. The MPPT algorithm is now capable of maintaining the inverter in MPPT mode for an increase (ΔP_e) in power production, while satisfying the $V_{min.e} < V_{MPPe}$ condition. In the particular case when the grid voltage rises above the configured level (e.g. $> +10\%$ from nominal), the VQ controller changes its priority from maximum energy harvesting to grid stabilization mode with $Q > 0$. In case when the grid voltage falls below the configured level (e.g. $< -10\%$ from nominal) then the VQ controller may satisfy the two requirements: grid support and dc-bus extension with maximum energy harvesting.

With the proposed control strategy, the minimum dc-bus voltage control reference is optimally calculated by the MPPT algorithm for inverter efficiency improvement and maximization of available power transfer for 1500V systems (as well as 1000V systems).

2.3. Quasi-Space Vector Modulation Strategy for DC-bus Utilization in 3-phase PV inverters - An alternative to Space Vector Modulation

The classical sinusoidal pulse-width modulation (SPWM) in 3-phase systems contains no zero-sequence components and is the simplest for implementation. However, in order to increase the dc-bus utilization, zero-sequence methods have been proposed in the literature [5], [127] in the following simplest form of third-harmonic zero-sequence (3H-ZS) injection signal:

$$f_{\text{ZS-THI}}(t) = \gamma \sin 3\left(\omega t\right). \tag{2.11}$$

The 3H-ZS with the amplitude of γ=1/6 provides the maximum linear modulation index and with $\gamma = 1/4$ would reduce the harmonic distortion in inverter output voltage [127], [128]. One of the most used modulation strategy with the use of 3H-ZS, is traditionally done in the form

of a carrier-based space-vector PWM (SV-PWM) to improve the dc-bus utilization. The conceptual schematic of the inverter presented in Fig. 2.4 shows this classic carrier-based SV-PWM implemented in block (b) and coupled to the control signals dq/abc.

In this chapter a quasi-space vector PWM (QSV-PWM) is proposed to maintain a 15% maximization of dc-bus utilization while providing an additional important benefit: 3H-ZS signal is decoupled from the control signals, instead being derived from the grid voltage phase angle (θ) of phase-locked loop (PLL) control structure. As will be demonstrated, this strategy provides accurate and robust zero sequence (ZS) that allows improved paralleling of decentralized inverters while maintaining wide dc-bus extension.

With the use of 3H-ZS, the magnitude of each inverter phase voltage control signal is reduced allowing the modulation index (m) to increase beyond unity, while the linear modulation is maintained ($m_{max} \leq 1.15$). The carrier-based space-vector zero-sequence function is expressed by relation (2.12), derived from the control signals e_a, e_b, e_c,

$$f_{\text{ZS-SV}}(t) = -\frac{1}{2}\Big[\min\big(e_a(t), e_b(t), e_c(t)\big) + \max\big(e_a(t), e_b(t), e_c(t)\big)\Big]. \qquad (2.12)$$

These control signals are, in fact, the output of the synchronous frame current regulators transformed to the three-phase coordinates (dq/abc). During transient conditions, the perturbations may be propagated through the ZS, which temporarily affects the power quality and the dc-bus neutral-point deviation. Instead, the proposed carrier-based quasi-space vector ZS function is derived from the phase-locked loop (PLL) control structure to provide a clean and robust signal, as illustrated in block (c) of Fig. 2.4. The ZS function for the QSV-PWM is implemented with third-order harmonics, and is expressed with the following general expression:

$$f_{3ZS}(t) = \frac{1}{\pi\sqrt{3}} \sum_{k=0}^{n} \left(\frac{(-1)^k}{\left[(2k+1)^2 - \frac{1}{9} \right]} \sin\left[3\omega(2k+1)t \right] \right). \qquad (2.13)$$

The 3H-ZS injection components expressed in relation (2.13) do not affect the fundamental output voltages, since the common mode voltages cancel between the phases in a three-phase system. The inclusion of the 3H-ZS components provides improved dc-bus voltage utilization, up to 15% in a direct comparison with sinusoidal PWM (SPWM). In this way, the ZS component derivation is decoupled from the instantaneous control signals (less stable) as follows. For simplicity and practical implementation, relation (2.13) is reduced to the following two terms of third-order harmonics expression:

$$f_{ZS}(t) = \gamma_1 \left(\sin 3(\omega t) + \gamma_2 \sin 9 \cdot (\omega t) \right). \qquad (2.14)$$

The γ_1, γ_2 coefficients are selected and approximated the with space vector similarity for the QSV zero-sequence injection,

$$f_{QSV}(t) = \frac{1}{4} \left(\sin(3\omega t) - \frac{1}{10} \sin\left(9\omega t\right) \right). \qquad (2.15)$$
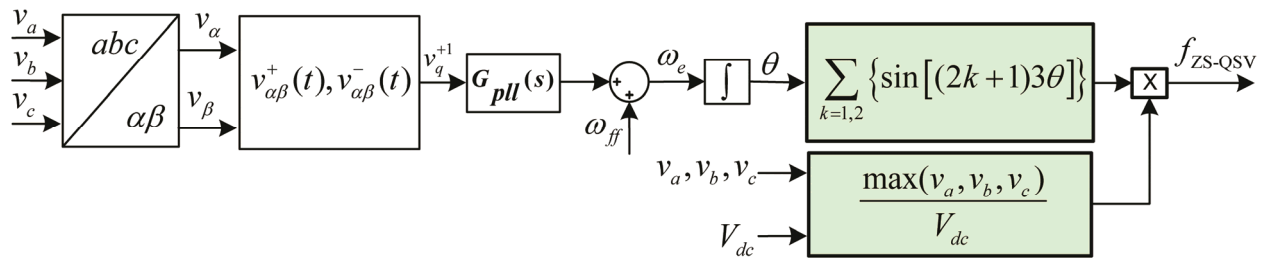
Figure 2.8: QSV 3H-ZS injection implementation and derivation from PLL control structure with ac-to-dc bus voltage scaling factor.

Fig. 2.8 shows the QSV control structure implementation and its derivation from the PLL control structure with positive and negative voltage components decomposition designed to operate under unbalanced and distorted grid conditions [5]. As can be seen, the control structure from

Fig. 2.8 provides an accurate and robust ZS determination for inverters while maintaining the 15% bus extension. The ZS derivation from the PLL structure is not sufficient for a complete solution, thus a scaling factor is introduced in order to respond automatically under different modulation factors (dc and ac variations) as shown in Fig. 2.8. The ZS signal is scaled with respect to the dc-bus voltage and available grid voltage per the following final ZS expression:

$$f_{\text{ZS-QSV}}(t) = \frac{1}{4}\left(\sin(3\omega t) - \frac{1}{10}\sin(9\omega t)\right)\cdot\left(\frac{\max(v_a, v_b, v_c)_{rms}}{V_{dc}}\sqrt{6}\right). \tag{2.16}$$

The 3H-ZS derivation augmented with the dc-ac factor ratio, as shown in relation (2.16) used by the QSV modulation, provides an adaptive behaviour under all dc and ac operation conditions. The final expression of the reference control signals to the modulator block from Fig. 2.4 is dependent of the control signals (e_a, e_b, e_c) and two common mode signals: 3H-ZS (f_{ZS-QSV}) and neutral-point (e_Z) for dc balancing:

$$\begin{cases} e_a^*(t) = e_a(t) + f_{\text{ZS-QSV}}(t) + e_z(t) \\ e_b^*(t) = e_b(t) + f_{\text{ZS-QSV}}(t) + e_z(t) \\ e_c^*(t) = e_c(t) + f_{\text{ZS-QSV}}(t) + e_z(t). \end{cases} \tag{2.17}$$

In summary, Fig. 2.9 shows the comparison between continuous carrier-based modulation strategies: SPWM (e_S), THI-PWM (e_{THI}), SV-PWM (e_{SV}) and QSV-PWM (e_{QSV}) alternative method, given by the following phase control signals equations:

$$\begin{cases} e_S(t) = \sin(\omega t) \\ e_{\text{THI}}(t) = e_S(t) + f_{\text{ZS-THI}}(t) \\ e_{\text{SV}}(t) = e_S(t) + f_{\text{ZS-SV}}(t) \\ e_{\text{QSV}}(t) = e_S(t) + f_{\text{QSV}}(t). \end{cases} \tag{2.18}$$

The QSV modulation is comparable to SV modulation, with similar ZS injection signal $(f_{ZS-QSV} \cong f_{ZS-SV})$ and control signals $(e_{QSV} \cong e_{SV})$, with the advantage of a decoupled ZS derivation from the instantaneous control signals. Since the dc-bus range extension target

decentralized 1500V inverters, what follows is a detailed explanation of the paralleling advantages of the proposed QSV-PWM.
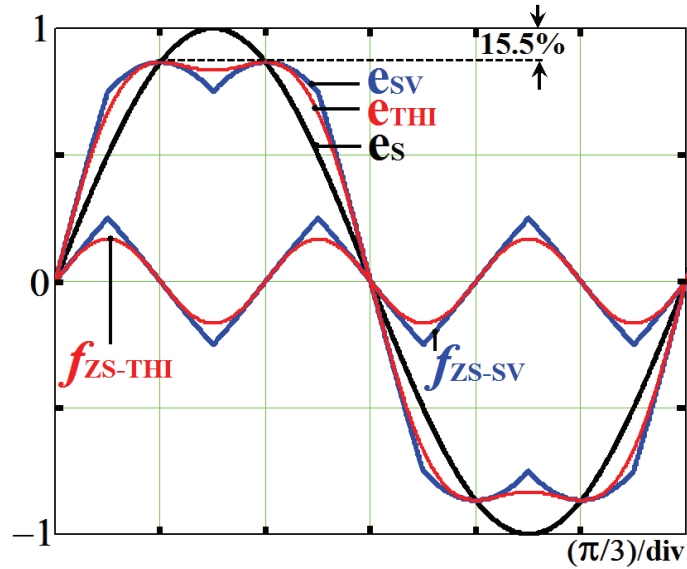
(a)
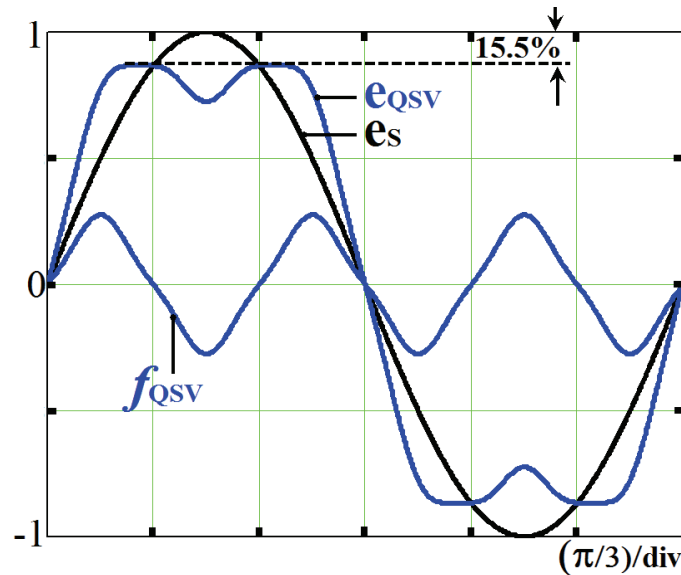
(b)

Figure 2.9: Continuous carrier-based modulation strategies comparison.

(a) Phase control signals: SPWM (e_S), SV-PWM (e_{SV}) and THI-PWM (e_{THI}) with 3H-ZS injection signals f_{ZS-THI} (equation (2.11), $\gamma=1/6$) and f_{ZS-SV} (equation (2.12)).

(b) Phase control modulation signals with SPWM (e_S) and the alternative strategy QSV-PWM (e_{QSV}) with ZS injection signal f_{QSV} (equation (2.15)).

2.3.1. Parallel Operation Structure: QSV-PWM and SV-PWM Comparison

Grid-connected inverters parallel connected (decentralized inverters), sharing the same dc and ac buses, offer advantages of system redundancy and power scalability for PV plants. The proposed QSV modulation and control strategy is developed without communication signals between the paralleled inverters.

The circulation current between paralleled inverters must be addressed, since it leads to negative impacts on the system losses and system stability. The circulating current is mainly affected by the modulator zero vectors of each PWM cycle [129].
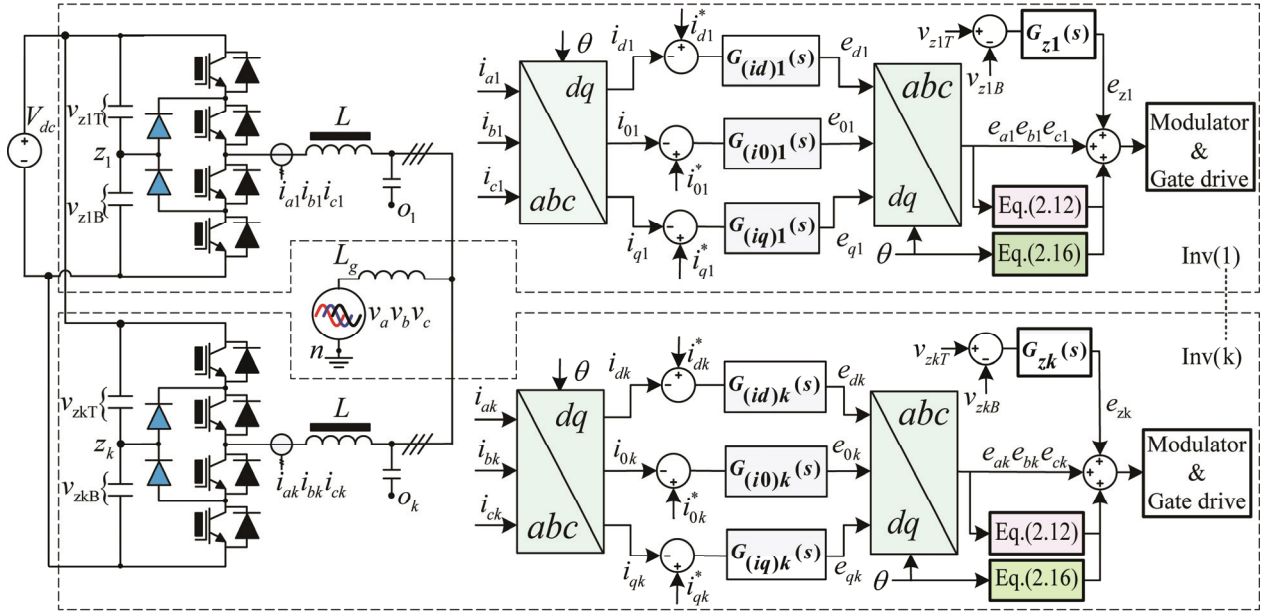
Figure 2.10: Example of three-phase paralleled connected inverters using QSV modified modulation (Eq.2.16) with current regulators control structure designed for circulation current elimination.

In Fig. 2.10 is shown a number (k) of 3-level inverters parallel connected at the same dc and ac bus in a simplified block diagram version with the current regulators designed in synchronous rotating $dq0$-reference frame control structure.

The inverter (k) phase currents transformed from a-b-c natural coordinates to α-β stationary frame, with the homopolar-sequence current (i_{0k}) consideration, are given by:

$$\begin{cases} i_{ak} = i_{\alpha k} + i_{0k} \\[2mm] i_{bk} = -\dfrac{1}{2}i_{\alpha k} + \dfrac{\sqrt{3}}{2}i_{\beta k} + i_{0k} \\[2mm] i_{ck} = -\dfrac{1}{2}i_{\alpha k} - \dfrac{\sqrt{3}}{2}i_{\beta k} + i_{0k}, \end{cases} \qquad (2.19\ \text{a})$$

$$\begin{cases} i_{\alpha k} = \dfrac{1}{3}\left(2\,i_{ak} - i_{bk} - i_{ck}\right) \\[2mm] i_{\beta k} = \dfrac{1}{\sqrt{3}}\left(i_{bk} - i_{ck}\right) \\[2mm] i_{0k} = \dfrac{1}{3}\left(i_{ak} + i_{bk} + i_{ck}\right). \end{cases} \qquad (2.19\ \text{b})$$

The inverter phase currents are controlled in synchronous rotating $dq0$-reference frame by the $G_{(id)k}(s), G_{(iq)k}(s), G_{(i0)k}(s)$ regulators, with the inverter control voltages expresses as:

$$\begin{cases} e_{dk} = \left[i_{dk}^{*} - \left(i_{\alpha k}\cos(\theta) + i_{\beta k}\sin(\theta)\right)\right]G_{idk} \\[2mm] e_{qk} = \left[i_{qk}^{*} + \left(i_{\alpha k}\sin(\theta) - i_{\beta k}\cos(\theta)\right)\right]G_{iqk} \\[2mm] e_{0k} = (i_{0k}^{*} - i_{0k})G_{i0k}. \end{cases} \qquad (2.20)$$

The following relation expresses the inverse transformation from synchronous rotating dq0-reference frame to $a - b - c$ natural coordinates with the ZS component:

$$\begin{cases} e_{ak} = e_{\alpha k} + e_{0k} \\[2mm] e_{bk} = -\dfrac{1}{2}e_{\alpha k} + \dfrac{\sqrt{3}}{2}e_{\beta k} + e_{0k} \\[2mm] e_{ck} = -\dfrac{1}{2}e_{\alpha k} - \dfrac{\sqrt{3}}{2}e_{\beta k} + e_{0k}. \end{cases} \qquad (2.21)$$

The conventional carrier-based SV-PWM using the relations (2.12), (2.21) and the standard control structure from Fig. 2.10 should be avoided since the common-mode third-

harmonic voltage injection is not kept centered at zero reference, due to the presence of common mode homopolar-sequence component in the dq/abc inverse-transformation.

Modified SV-PWM and other control methods have been proposed to address the circulating currents issue between parallel inverters [10], [129], [130]. The QSV-PWM presents an advantage with respect to conventional carrier-based SV-PWM since the common-mode third-harmonic voltage injection is always centered in zero, decoupled from the control signals e_{ak}, e_{bk}, e_{ck}. Fig. 2.10 shows the control with ZS loop regulator (G_{i0k}) designed to eliminate the current circulation between the inverters.

The power devices gate drive is controlled by the modulator, which is designed to process the control signals e_{ak}, e_{bk}, e_{ck}, neutral-point voltage (e_{zk}) for dc balancing (z_k) compensation.

The proposed QSV modulation integrated with the dq and homopolar-sequence control loops provide a simple and effective solution for 3H-ZS injection in parallel inverters operation. As can be noted, the communication between the inverter modules is not necessary. The 1500V parallel-connected inverters (decentralized PV plants) will likely take an important role due to modularity (which leads to redundancy and reduced down time) and the enhanced dc-bus utilization to achieve higher overall energy production. Decentralized inverters are designed in a compact and lightweight format to simplify the PV plant installation.

2.4. Simulation and Experimental Results

The experimental dc-bus voltage utilization methodology evaluation has been verified on a three-phase solar inverter platform as shown in Fig. 2.11, interfaced with 50/60Hz grid.

The three-level NPC type inverter has been used, with switching frequency $f_s = 20kHz$, the equivalent dc link capacitance of 2000µF, ac reactor inductance 4.3% per unit (p.u.) and filter capacitance values at 3% p.u. range.
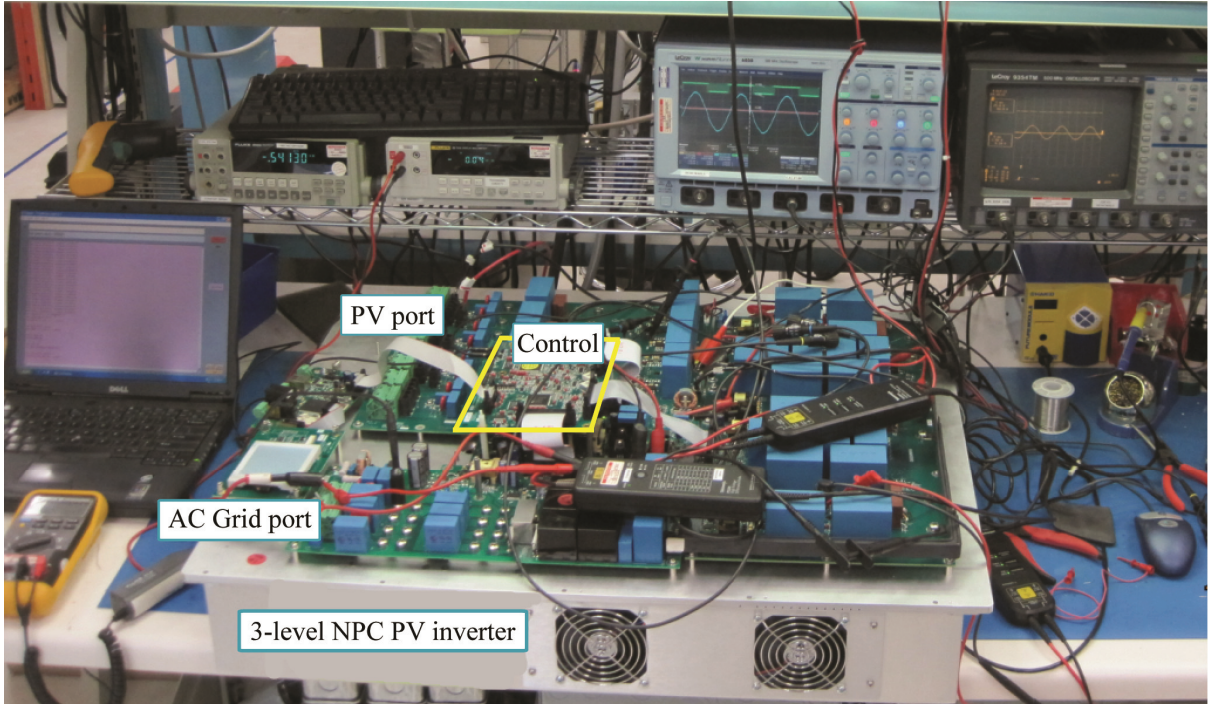
Figure 2.11: Grid-connected inverter and laboratory setup for dc-bus voltage utilization testing and evaluation.

2.4.1. Comparative Results of DC-bus Voltage Utilization with 1000V and 1500V PV Systems

In the comparative analysis below, the nominal current has been considered the same for both inverter systems ($31.8A_{rms}$), in order to maintain consistency with the analysis in Section 2.1. The nominal power is P_n=22kVA for the 1000V system and P_n=28.6kVA for 1500V system by using the 1.3 factor shown in Table 2.2.
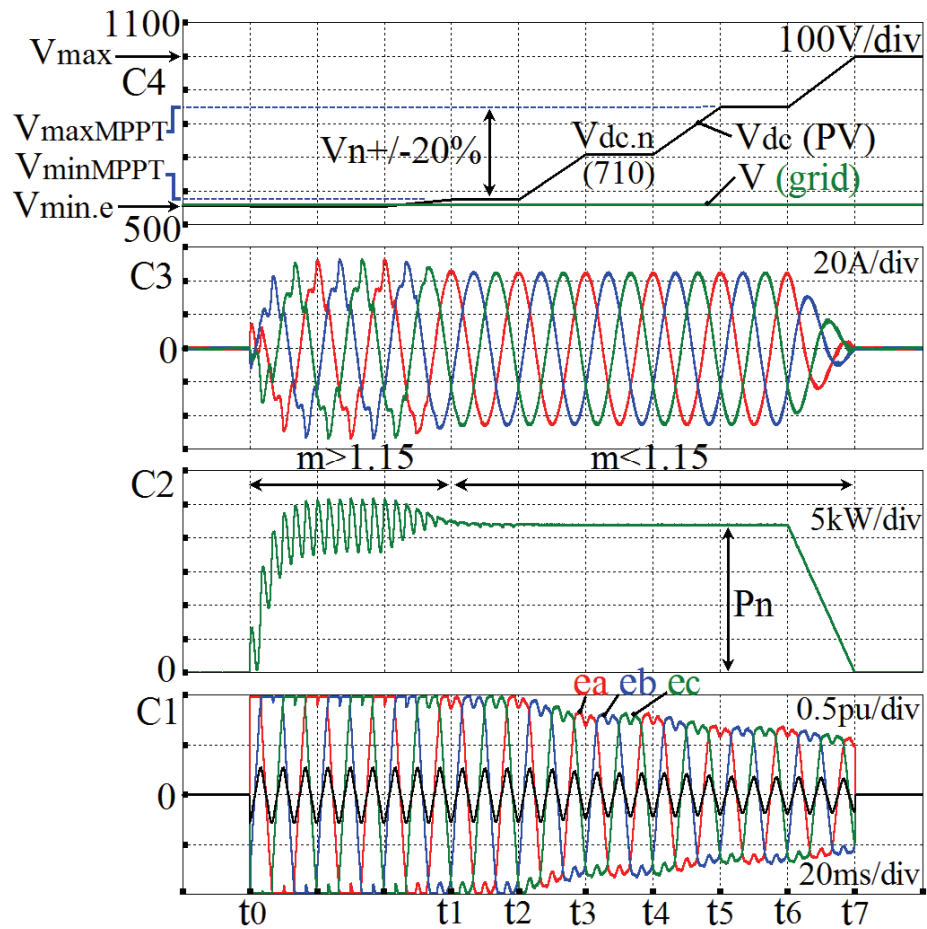
(a) 1000V system: $230 V_{LN}/400 V_{LL}$-50Hz.
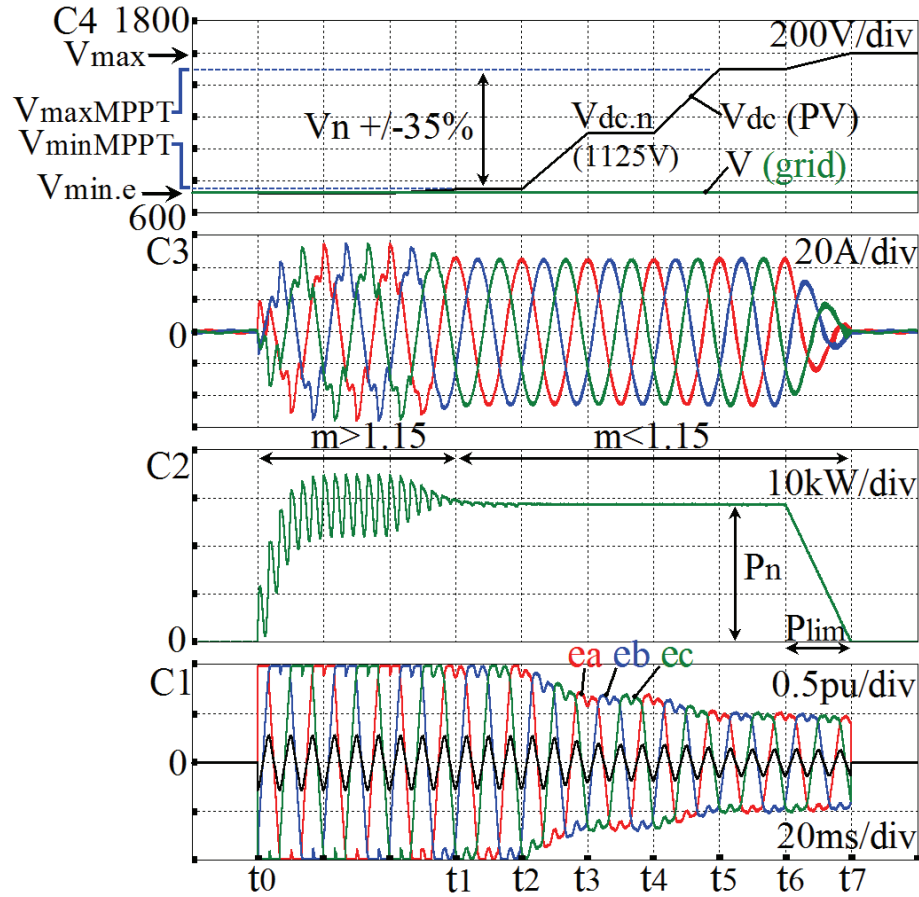
(b) 1500V system: $300V_{LN}/520V_{LL}$-50Hz.

Figure 2.12: Simulation results: solar inverter dc-bus dynamic range evaluation from $V_{min.e}$ to V_{max}: comparison between (a) 1000V (only +/-20 range) and (b) 1500V (extended +/-35%) systems.

Y-axis: C1- 3-level 3-phase control signals e_a, e_b, e_c and zero sequence ZS, 0.5 p.u./div, C2-Inverter active power, C3- Inverter phase currents I_a, I_b, I_c, 20A/div.C4- DC-bus voltage V_{dce} and grid line magnitude voltage V.

X-axis: 20ms/div.

Fig. 2.12 shows a comparative analysis with the solar inverters operating at nominal power (P_n) while the DC-bus ramps-up from minimum ($V_{min.e}$) to maximum (V_{max}) dc-bus voltage. During the $t_0 - t_1$ interval, the converter operates at minimum voltage level ($V_{min.e}$) with inverter currents distorted due to over-modulation. This mode of operation is not desired, and by enabling the VQ controller this situation is avoided under the same operation conditions. At instant t_1, the dc-bus voltage reaches the minimum MPPT level ($V_{minMPPT}$) and the current

distortion is eliminated owed to linear modulation ($m < 1.15$). From t_2, the dc-bus continues to increase and within the $t_3 - t_4$ interval the inverter attains the nominal dc-bus ($V_{dc.n}$). The inverter continues to operate at nominal power (P_n) while the dc-bus increases ($t_4 - t_5$). At the moment t_6 the inverter starts to derate/limit the power from $V_{maxMPPT}$ to V_{max}. The inverter ceases to operate from moment t_7 in order to avoid components operation outside the design data specification.

The typical NPC inverter design for 1000V system is optimized for performance, cost and standards compliance with $V_{max} = 1000V$. By keeping the same design considerations for 1500V system, the maximum operation voltage is selected at $V_{max} = 1600V$ which provides dc-bus utilization in the range of +/-35%$V_{dc.n}$ (i.e. $V_{maxMPPT}:V_{minMPPT} = 2:1$) in comparison to 1000V of +/-20%$V_{dc.n}$ (i.e. $V_{maxMPPT}:V_{minMPPT} = 1.7:1$). The additional 30% dc-bus voltage for 1500V translates into an increased overall energy production and proves the dc-bus extension concept proposed in this dissertation.

2.4.2. Lower DC-bus Limit Extension with VQ Reactive Power Injection

Fig. 2.13 illustrates the inverter reactive power control (Q) influence on the output fundamental component voltage (V_e), which demonstrated the validity of relation (2.10). The inverter is controlling the reactive power and maintaining an active power level of $P_n/2$ (14.3kW). Prior to instant t_1, the inverter operates with power factor lag ($Q = +24.7kVAr$) and the dc-bus utilization range is reduced due to the need of increasing the inverter output voltage V_e.
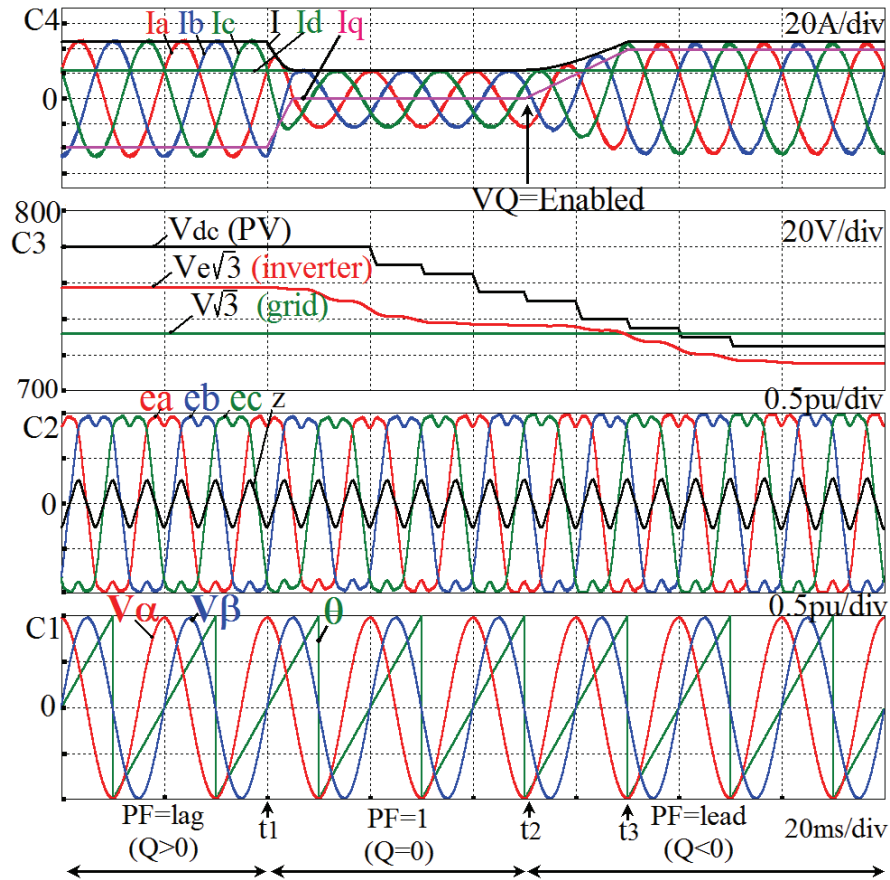
Figure 2.13: Simulation results: three-level VQ reactive power injection waveforms with constant active power ($P_n/2$), $300V_{LN}/520V_{LL}$-50Hz, 1500V system).

Y-axis: C1 - PLL phase angle θ stationary frame grid voltage V_α, V_β 0.5 p.u./div, C2 - 3-level 3-phase control signals e_a, e_b, e_c 0.5 p.u./div, C3 - Inverter output peak voltage V_e (fundamental component), DC-bus voltage V_{dc} and grid line magnitude voltage V 20V/div, C4 - Converter phase currents I_a, I_b, I_c, I_d, I_q 20A/div.

X-axis: 20ms/div.

The power factor lag represents a scenario when the utility plant controller commands the PV plant for grid support. In this particular case, the necessary dc-bus is increased, as it shown prior to moment t_1, the inverter voltage V_e is higher. At instant t_1, the inverter operates at unity power factor ($Q = 0$) and the dc-bus voltage utilization range is practically increased.

At the moment t_2, the available dc-bus voltage reduces (e.g. due to the PV array characteristics) while the inverter pursues the energy capitalization by enabling the VQ controller.

At this moment, the inverter provides the power factor lead ($Q = -24.7\text{kVAr}$, $S = 28.6\,\text{kVA}$) and the inverter fundamental voltage component V_e is reduced from 780V to 725V. As a result, the dc-bus can be reduced closer to V_e, considering the compensation factors of dc-bus neutral-point variation and devices voltage drop per relation (2.3).

Therefore, the energy maximization algorithm is maintained and power limit is not necessary due to the additional 3% dc-bus voltage extension. It should be noted that the dc-bus extension range can be found between 2 to 5% as being function of the filter inductance and angular frequency (relation (2.10)). The dc-bus is regulated at the minimum level and in linear-modulation to achieve high efficiency conversion and power quality, even in cases where the PV modules operates at high ambient temperature conditions with severe reduction of MPP voltage level.

Fig. 2.14 shows the inverter operation under the test conditions from Table 2.3. The traditional control constraints the inverter operation to $V_{minMPPT}$ voltage level in power limit mode. With the VQ controller enabled, the dc-bus minimum operation is extended to $V_{MPP.e}$ voltage level, and in consequence the gain power (ΔP_e) is increased resulting in higher energy yield from the PV array to the ac grid.
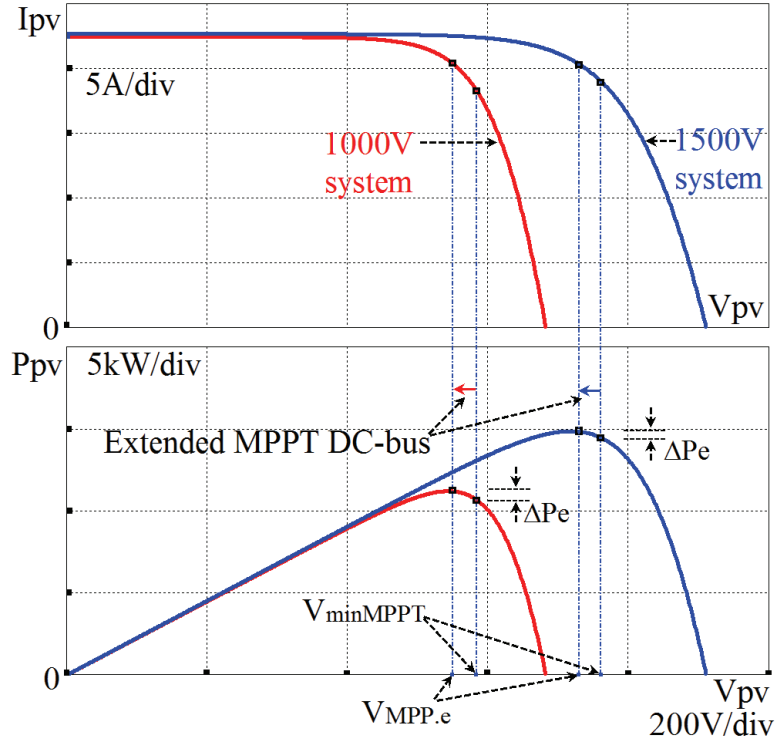
Figure 2.14: Simulation results: MPPT DC-bus extension with QV-controller enabled: the inverter operates from power limit mode (P_{lim}) to MPPT ($P_{MPPT.e}$) mode with a net gain (ΔP_e) of about 3% of available power harvesting.

1000V system: G=600W/m2, T_c=65°C, 4 parallel strings of 18 series, 1500V system: G=600W/m2, T_c=75°C, 4 parallel strings of 25 series, PV module: $V_{oc.stc}$=44.8V, $V_{mp.stc}$=36.3V, β=-0.34%/°C, P_{max}=305W.

Table 2.3: Solar inverter operation conditions for DC bus voltage utilization extension.

Inverter system	P [kW]	Q [kVA_r]	S [kVA]	PF [-]	I_{phase} [A]	$V_e\sqrt{3}$ [V_{dc}]	$\Delta V_Z + V_T$ [V_{dc}]	$V_{min.e}^*$ [V_{dc}]	$V_{min.e}$ [V_{dc}]	V_{max} [V_{dc}]
1000V	11.0	0	11	1	16	565	5	≥570	575	1000
	11.4	-19	22	0.51	31.8	545	10	≥555	555	
1500V	14.4	0	14.4	1	16	735	5	≥740	750	1600
	14.7	-24.7	28.6	0.51	31.8	714	10	≥724	725	

Fig. 2.15 shows the grid current distortion effect if the VQ controller is disabled. Prior to instant t_1, the inverter operates with reactive power generation under the test conditions from Table 2.3 (Q = -24.7kVA). At t_1, the VQ controller is disabled and the inverter continues to

operate with constant active power, while the phase currents are distorted since it is not operating in the linear modulation region anymore. Since this mode of operation is not desired, the VQ controller is re-enabled at instant t_2, where the VQ reactive power injection achieves a dc-bus extension range of 3%, in addition to the 3H-ZS modulation injection of 15%.
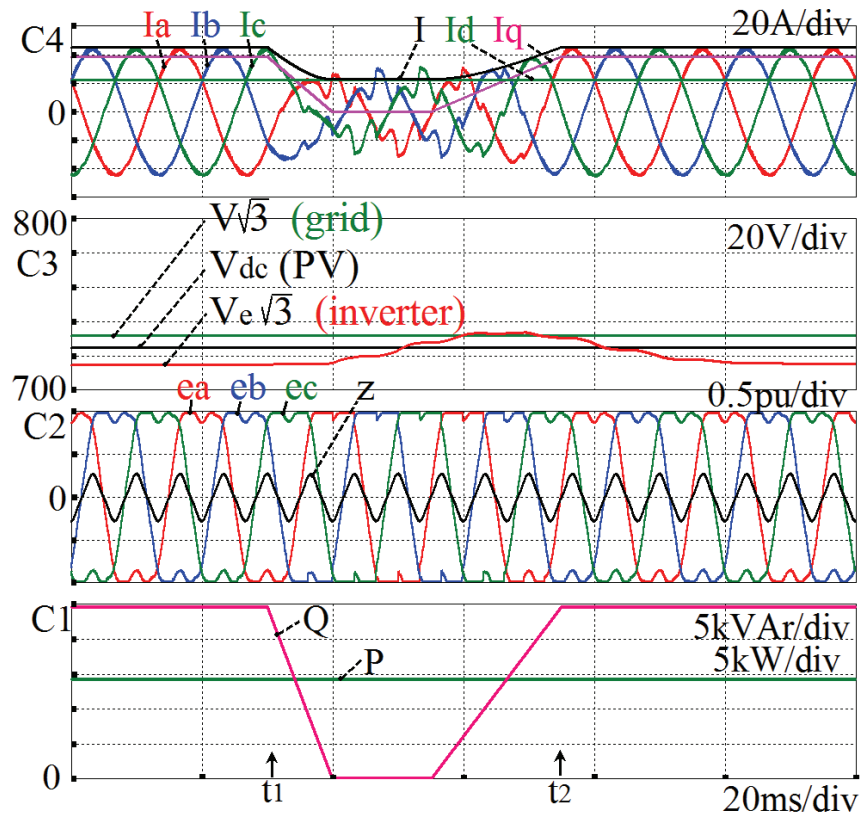
Figure 2.15: Simulation results: VQ controller temporarily disabled shows the effect on the grid current ($300V_{LN}/520V_{LL}$-50Hz) at minimum dc-bus inverter operation.

Y-axis: C1 - Active and reactive power, 5kW/div, 5kVAr/div, C2 - 3-level 3-phase control signals e_a, e_b, e_c and zero sequence ZS, 0.5 p.u./div, C3 - Inverter output peak voltage V_e (inverter fundamental component, 50Hz), DC-bus voltage V_{dc} and grid line magnitude voltage V 20V/div, C4 - Converter phase currents I_a, I_b, I_c, I_d, I_q 20A/div.

X-axis: 20ms/div.
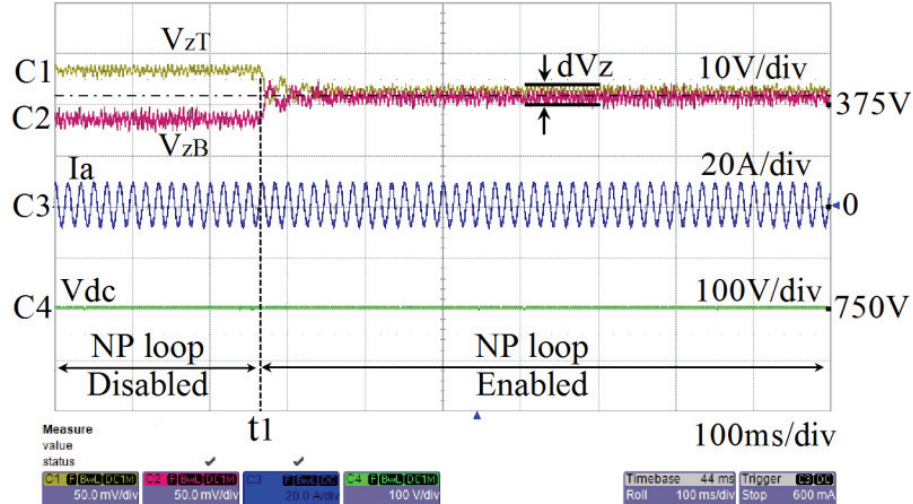
Figure 2.16: Experimental results: neutral-point balancing and regulation.

Y-axis: C1 - Top side dc-bus V_{zT} 10V/div, C2 - Bottom side dc-bus V_{zB} 10V/div, C3 - Inverter output phase A current I_a (PF=1) 20A/div, 50Hz), C4 - DC-bus voltage $V_{dc} = V_{zT} + V_{zB}$ 100V/div.

X-axis: 100ms/div.

Fig. 2.16 shows the neutral-point controller regulation for 3-level NPC topology: prior to moment t_1, the active dc-balancing mechanism is disabled. The test was performed in the linear modulation region at m=0.87. The difference in voltage between the top and bottom dc sides results in undesired effects, for example poor dc-balancing regulation leads to range loss of dc bus utilization. Moreover, at low dc-bus voltage scenarios, the inverter may be driven to operate in over-modulation, producing undesired distorted current to the ac grid (e.g. Fig. 2.15, C4, interval $[t_1 - t_2]$). At the moment t_1 the neutral-point controller is enabled with two immediate benefits: dc-bus balancing stable operation and the possibility of inverter to operate in linear modulation for the maximum system dc-bus voltage utilization.

The experimental test employing carrier-based space vector modulation is shown in Fig. 2.17 and Fig. 2.18.
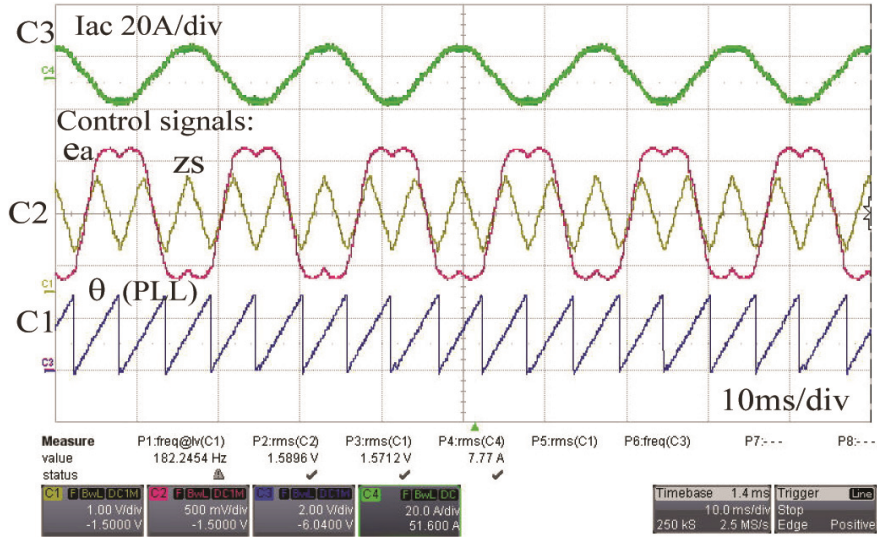
Figure 2.17: Experimental results with carrier-based space vector modulation with Zero-Sequence using relation (2.12), with test conditions: dc-bus V_{dc}=785V, grid voltage system $277V_{LN}/480V_{LL}$ /60Hz.

Y-axis: C1 - PLL phase angle θ, C2 - ZS 0.3125 p.u./div, Control phase signal e_a 0.67 p.u./div, C3 - Phase (a) grid current I_a 20A/div.

X-axis: 10ms/div.
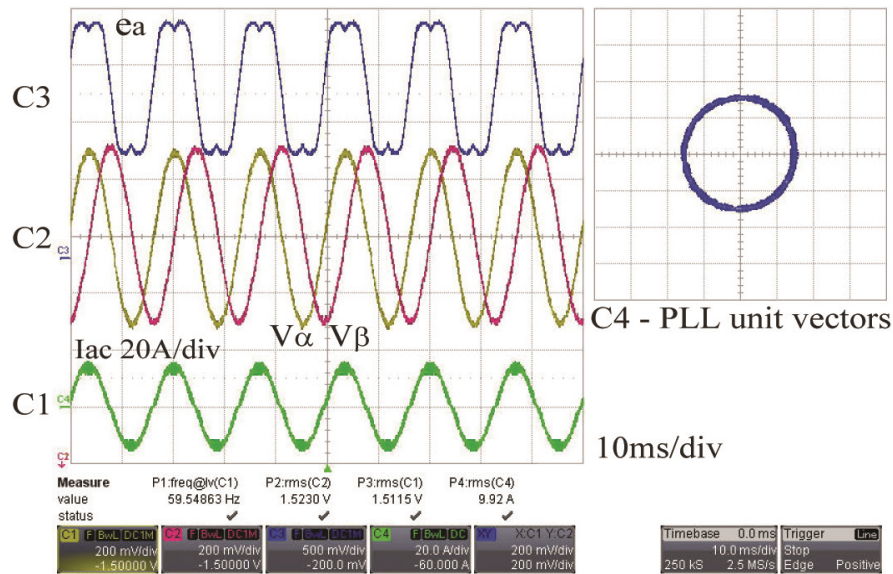
Figure 2.18: Experimental results using carrier-based space vector modulation strategy.

Y-axis: C1 - Phase grid current I_a 20A/div, C2 - Stationary frame grid voltage vectors, V_α, V_β, 0.67 p.u./div, C3 - Phase control modulator signal e_a, 0.65 p.u./div, C4 - Grid voltage unit vectors 0.67 p.u./div.

X-axis: 10ms/div.

2.4.3. Dynamic Behaviour Using QSV-PWM with Low DC-bus Voltage (15% Extension)

Fig. 2.19 shows the proposed QSV-PWM modulation under low dc-bus voltage and a dynamic load step transient. The experimental test was performed as shown in Fig. 2.20, with the third-harmonic ZS signal derived from the PLL phase angle. It is interesting to note that the QSV strategy complies with the 15% lower dc-bus extension while providing an accurate and robust ZS for transients and paralleling.
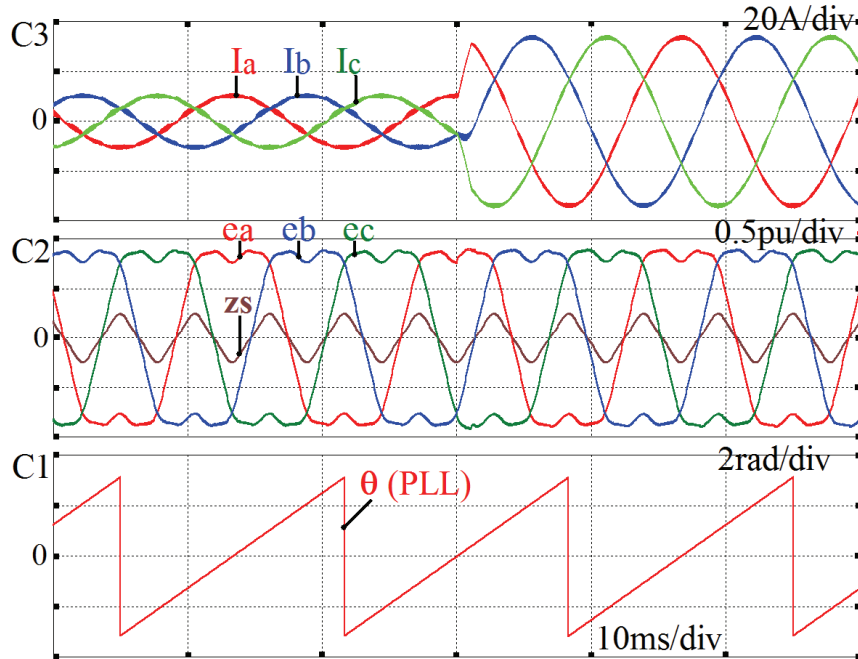
Figure 2.19: Simulation results with proposed QSV-PWM modulation strategy under low dc-bus voltage (785V) and load step transient.

Y-axis: C1 - PLL phase angle θ, C2 - 3H-ZS QSV signal, three-phase control signals e_a, e_b, e_c 0.5 p.u./div, C3 - Phase grid current I_a, I_b, I_c, 10A/div; grid voltage system $277V_{LN}/480V_{LL}/60$Hz.

X-axis: 10ms/div.
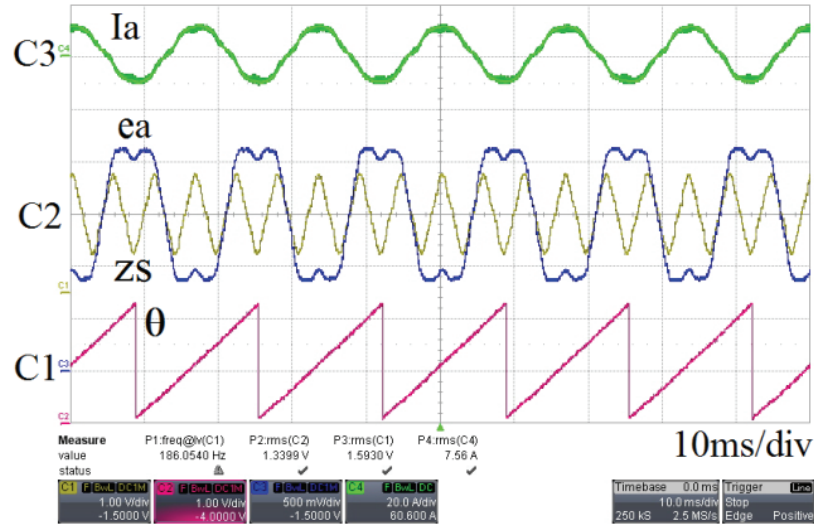
Figure 2.20: Experimental results with the proposed QSV-PWM with Zero-Sequence derived from the PLL (dc-bus V_{dc}=785V, grid voltage system $277V_{LN}$/$480V_{LL}$/60Hz).

Y-axis: C1 - PLL phase angle θ, C2 - ZS 0.3125 p.u./div, Control phase signal e_a 0.67/div, C3 - Phase (a) grid current I_a 20A/div.

X-axis: 10ms/div.
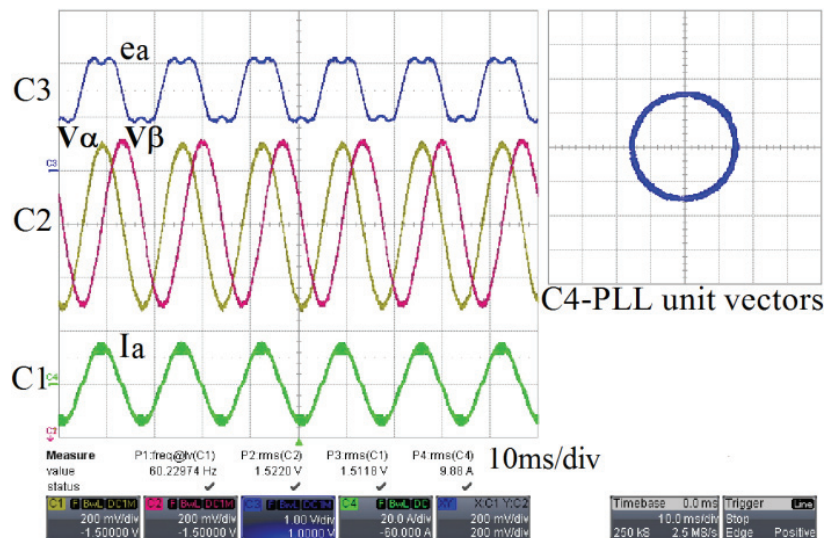
Figure 2.21: Experimental results using the proposed QSV-PWM strategy (dc-bus V_{dc}=785V, grid voltage system $277V_{LN}$/$480V_{LL}$/60Hz).

Y-axis: C1 - Phase grid current I_a 20A/div C2 - Stationary frame grid voltage vectors, V_α, V_β 0.67 p.u./div, C3 - Phase control modulator signal e_a 1.3 p.u./div, C4 - Grid voltage unit vectors 0.67 p.u./div.

X-axis: 10ms/div.

Fig. 2.21 shows the inverter current signals with low dc-bus voltage and the PLL control used for QSV-PWM: α-β stationary frame voltage vectors and their trajectory described by the PLL unit vectors. The PLL is designed to reject high-order voltage harmonics and to detect 3-phase voltage space vector positive and negative sequence components of the fundamental, irrespective of the transient and dc-link situation. The PLL phase angle (θ) detected is used for the derivation of 3H-ZS QSV modulation strategy. The following description explains a severe transient situation and the superior performance of QSV over SV.
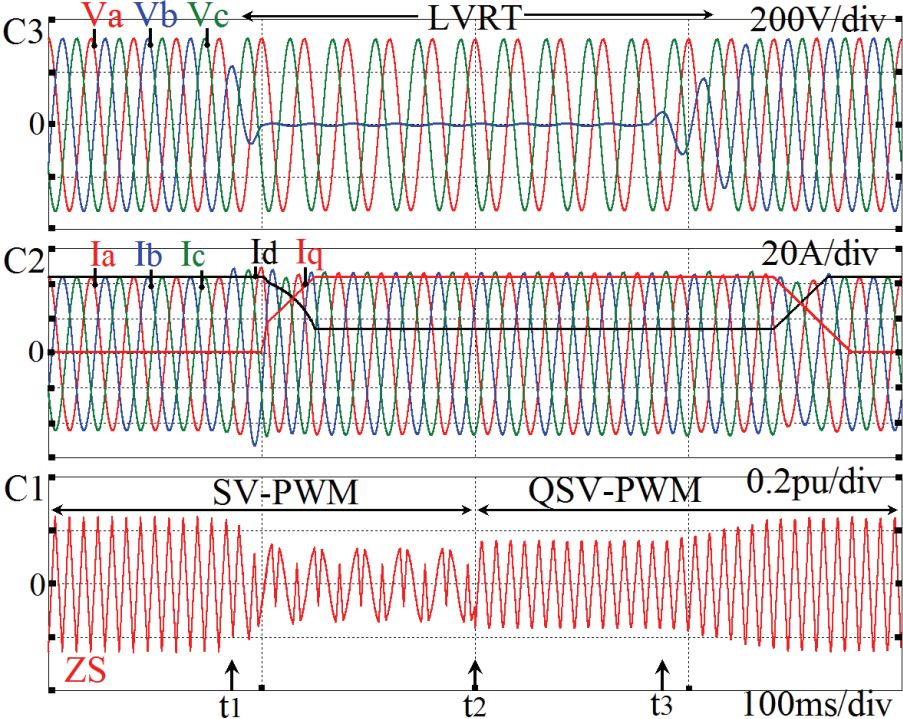
Figure 2.22: Simulation results: comparison results performed with carrier-based a) SV-PWM and b) QSV-PWM alternative modulation strategy (dc-bus V_{dc}=650V, grid voltage system $230V_{LN}/400V_{LL}/50$Hz).

Y-axis: C1 - Zero sequence 0.2 p.u./div, C2 - Phase grid currents I_a, I_b, I_c, d-q current components I_d, I_q 20A/div, C3 - Grid phase voltages V_a, V_b, V_c 200V/div.

X-axis: 100ms/div.

To further validate the effectiveness of QSV-PWM, the inverter performance has been evaluated with respect to one of the most demanding tests: dynamic grid support under asymmetrical grid fault with inverter low-voltage ride-through (LVRT). Fig. 2.22 demonstrates the performance comparison between QSV-PWM and SV-PWM. At the moment t_1, the one-phase (V_b) to ground phase fault is simulated and the inverter supports the grid with full rated reactive current $(I_q$ with power factor lead) while the active component (I_d) decreases.

It can be observed that with carrier-based SV-PWM enabled during the interval $t_1 - t_2$, the ZS cannot be maintained anymore as a triangular waveform, due to its derivation from the distorted modulator control signals (e_a, e_b, e_c). At instant t_2, the QSV-PWM is enabled where the 3H-ZS becomes quasi-triangular, since its derivation is not from the control signals but from the PLL phase angle. During the grid fault period, the inverter successfully supports the grid with balanced reactive currents. At instant t_3, the grid recovers and the inverter resumes transferring active power from the PV modules.

In addition to the dc-bus voltage extension, the reactive power control of PV plants represents an important feature for the utility grid stability, where each inverter automatically is enabled in the LVRT mode for the ac grid network support. What follows is a comparative evaluation of inverters operating in parallel with low dc-bus voltage

Fig. 2.23 shows the evaluation of two inverters parallel connected at dc and ac ports with conventional SV-PWM and QSV-PWM using the control structure from Fig. 2.10. The second inverter turns on at the moment t_1 and the grid current is shared equally between the inverters. However, the circulating currents i_{01}, i_{02} begin to flow between the parallel connected inverters and the dc source V_{dc}. The ZS control is enabled on each inverter at the moment t_2 in order to eliminate the average circulating current components - in a normal case, the ZS controller is

always enabled. Both modulation strategies are tested under the same conditions: the conventional carrier-based SV-PWM is not able to eliminate the undesired circulating current, instead, it is further aggravated as shown in Fig 2.23 (a). This issue is due to the derivation of 3H-ZS from the control signals, which contain the homopolar-sequence component (relation (2.21)) as discussed in Section 2.3.1. Instead, QSV-PWM is with decoupled 3H-ZS derivation from the control signals and the homopolar-sequence loop is able to regulate the average circulating current to zero. At the instant t_3 the dc-bus changes from 1500V to 750V and circulating current are seen for carrier-based SV-PWM while the proposed QSV-PWM is proven stable under this dc-bus transient situation.

(a)
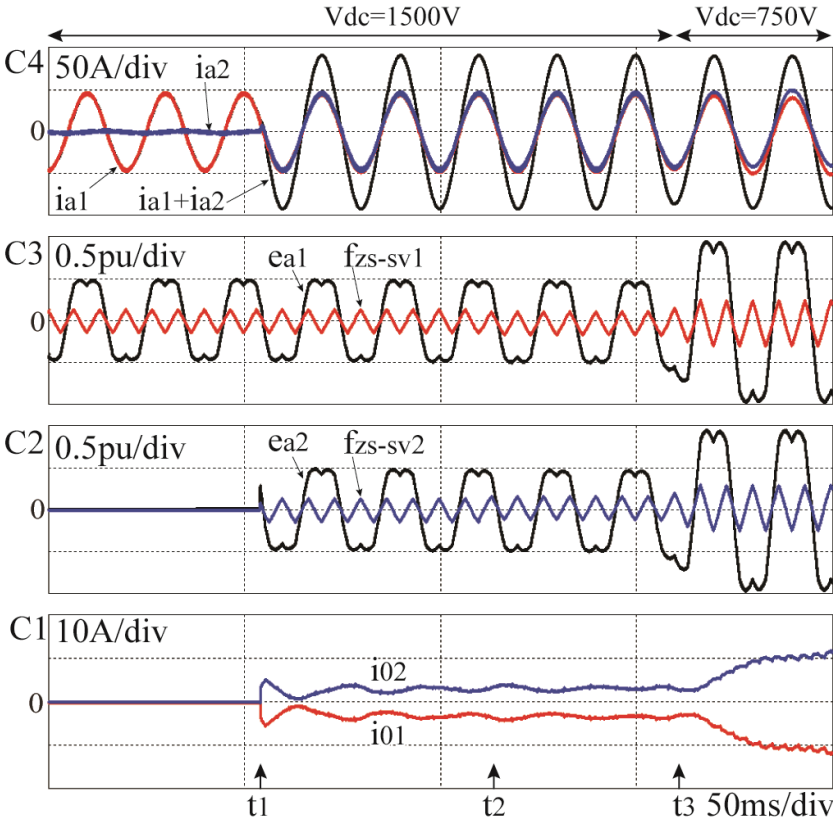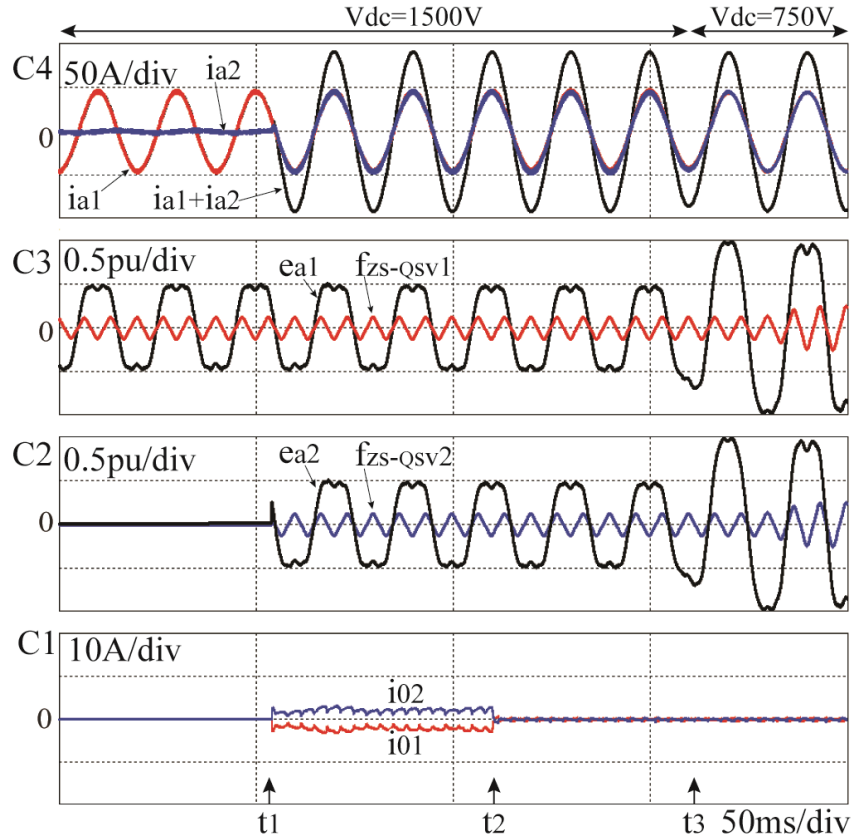
Figure 2.23: Simulation results: solar inverters parallel operation performed with (a) conventional carrier-based SV-PWM (circulating current issues) and (b) proposed QSV-PWM strategy with robust current sharing (grid voltage system $277V_{LN}/480V_{LL}$-50Hz with grid inductance L_g=1mH).

Y-axis: C1 - Average circulating currents between the inverters: i_{01}, i_{02} 10A/div, C2, C3 - Control phase signals and ZS injection voltage 0.5 p.u./div, C4 - Phase (a) grid currents i_{a1}, i_{a2} and total current I.

X-axis: 50ms/div.

2.5. Improved PV Inverter Operating Range Using a String Mini-Boost

The operating region of the typical single-stage PV grid-connected inverter is illustrated in Fig. 2.24 (a). It is delimited by V_{dcMin}, below which the inverter enters in non-operational mode; above V_{dcMin}, the inverter can operate at full P_{dcN} until V_{dcMax}, and after that power is curtailed

to extend the range to V_{ov}; above V_{ov}, the inverter is non-operational. This range can be extended (indicated by (t)) by using a transformer to interface the grid, but the weight, volume, and the efficiency is penalized.

In Fig. 2.24 (b) the two-stage power conversion PV operating region is presented. The boost power converter follows the slope (m_b) that is reduced until new minimum voltage (V_{uv}) is achieved. Unfortunately, since the PV array will not always operate at nominal power (due to shading or other problems cause it to operate at the lower voltage, the boost converter is overdesigned causing the cost to be unnecessary high.

In this work, a new architecture and design methodology is proposed in the form of a string based boost for grid-connected converters. In Fig. 2.24 (c), an improved PV inverter operational range for power extraction and design optimization is presented using a mini-boost. The mini-boost stage converter is designed to operate only when the voltage is lower than V_{dcMin} and becomes disengaged when PV voltage exceeds V_{dcMin}, for an increase in system conversion efficiency and the operation at rated power.

The proposed mini-boost is designed to process only a fraction of the PV inverter nominal power P_{dcN}, leading to the use of smaller, and therefore lower cost components. The inverter sizing is further optimized based on a proposed peak power envelope at the boundary of the operating area. This technique allows for extra room in the operating region, to transfers more power to the grid than previously possible.

Figures 2.24 (a) and 2.24 (b) show the operating region of the two traditional photovoltaic grid-connected inverter topologies. In the following paragraphs, the details of the design and operating boundaries will be presented along with the resulting advantages and disadvantages comparison. The proposed mini-boost topology is presented in Section 2.5.3.
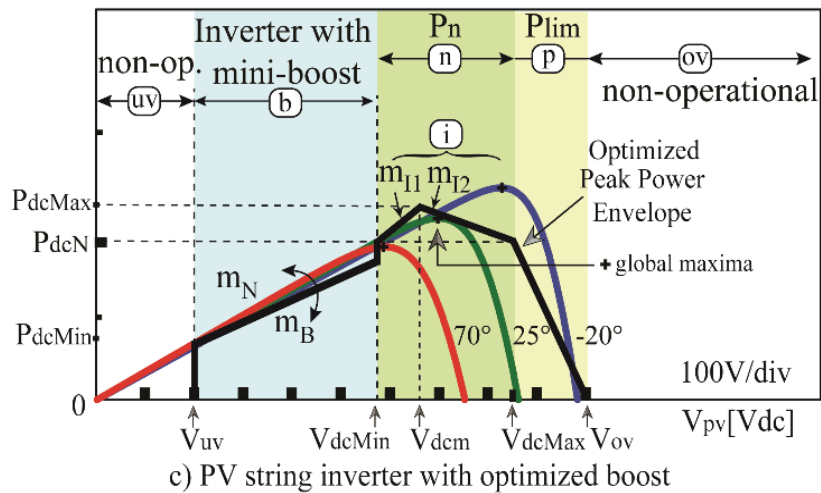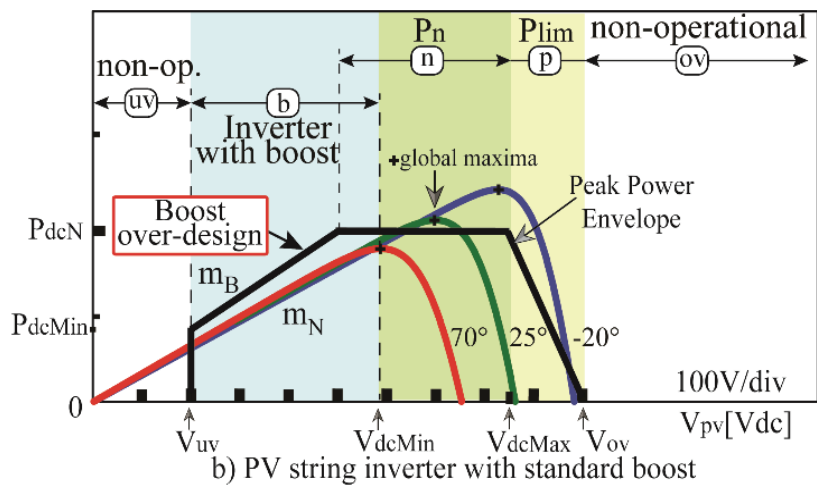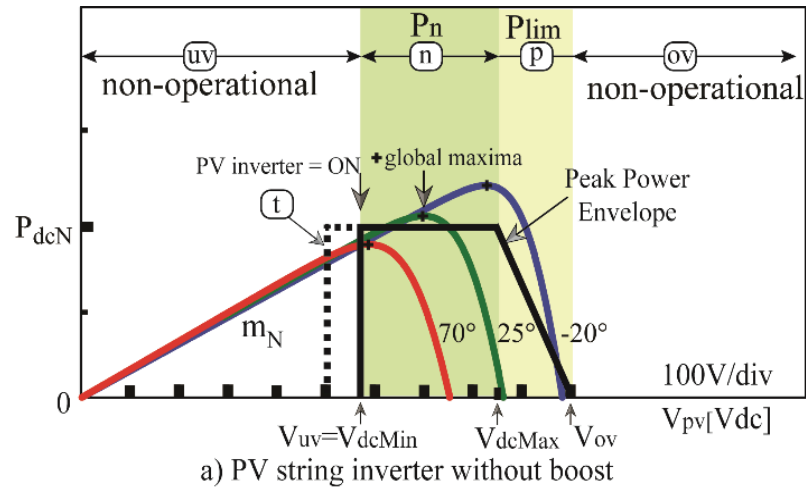
Figure 2.24: PV power versus dc-bus voltage utilization characteristics for: (a) Inverter without boost stage (b) Inverter with standard boost stage, and (c) Proposed optimized inverter with mini-boost and peak-power envelope at boundary conversion operation solution.

Fig. 2.24 notations:

(uv): Non-operational under dc voltage shutdown range

(b): Operation with boost converter

(n): Nominal power operation (MPPT)

(p): Power limit/curtailing mode

(ov): Over-voltage dc non-operational

(t): grid interfaced with line transformer for increased operational voltage (optional)

(i): increased converter power, optimization for constant input PV current and constant power losses operation.

2.5.1.   PV Inverter with Single-stage Power Conversion (no Boost Converter)

The single-stage PV inverter operating area is presented in Fig. 2.24 (a). This single-stage inverter is simple and efficient, since it does not include a second stage, but the operation is limited at the minimum operating voltage (V_{dcMin}) that is required to synchronized to the grid voltage. The region below V_{uv} represents the under voltage (uv) region, where the inverter is non-operational.

A single-stage inverter may operate from $V_{dcMin} = 575V$ (lower dc-bus limit) to $V_{dcMax} = 850V$ (upper dc-bus limit) at P_{dcN}, and extend the range up to $1000V$ with reduced power operation due to limited voltage blocking of commercially available power devices. The V_{dcMin} is dependent of the modulation strategy used as per

$$\begin{cases} V_{dcMin} = 2 \cdot \hat{V}_{LN} + V_{dcComp} & \text{(SPWM)} \\ V_{dcMin} = \sqrt{3} \cdot \hat{V}_{LN} + V_{dcComp} & \text{(ZS-PWM)}. \end{cases} \tag{2.22}$$

The minimum dc voltage is selected considering the compensation voltage V_{dcComp}, in addition to grid phase voltage magnitude $\hat{V}_{LN}$, ensuring the inverter operation in linear modulation. The zero-sequence pulse-width modulation (ZS-PWM) is used in this work, and provides an advantage over sinusoidal pulse-width modulation (SPWM) with an extension of $2/\sqrt{3}$ for the dc

input voltage utilization. If a line transformer is interfaced between the output of converter and grid for lower ac grid voltage inverter operation, (e.g. 15% lower) then the minimum voltage can be extended to lower PV input voltage. However, adding a line transformer to the system does not provide a cost-effective solution since it increases weight, volume and reduces efficiency [131].

2.5.2.   PV Inverter with Two-stage Power Conversion (with Boost Converter)

The operating region for the PV inverter with boost stage is presented in Fig. 2.24 (b). In this case, the operating region is extended (although not at full nominal power). This topology design allows more energy to be extracted, however, its components are over-sized and the efficiency is reduced. For uniform irradiance, the voltage will rarely drop below (V_{dcMin}) and for partial shading, the available power is less than the rated power. At lower voltage levels the inverter is able to extract the available power from the PV modules. The rated boost power at lower PV voltage is limited by the current ratings of power devices, current sensors and magnetics. As shown in Fig. 2.24 (b), the boost power stage is not optimized since the boundary of the operating region boot power ($P_B = V_{dc}I_{dc}$) is greater than the available power from PV-string modules (P_{pv}). It can be noted that the boundary power gradient of the boost stage (m_B),

$$m_B = \frac{dP_B}{dV_{pv}} \tag{2.23}$$

is greater than the gradient determined by the series/parallel combination of PV modules (m_N)

$$m_N = \frac{dP_{pv}}{dV_{pv}}. \tag{2.24}$$

From (2.24), the derivative of PV output power P_{pv} with respect to its voltage V_{pv} can be further expanded as

$$\frac{dP_{pv}}{dV_{pv}} = \frac{d(V_{pv}I_{pv})}{dV_{pv}} = I_{pv} + V_{pv}\frac{dI_{pv}}{dV_{pv}}. \tag{2.25}$$

The converter's target is to operate at MPP global maxima, when $dP_{pv}/dV_{pv} = 0$ ($P_{pv} = P_{MPP}$) and (2.25) can be expressed as a piece-wise function of incremental conductance (dI_{pv}/dV_{pv}) and instantaneous conductance (I_{pv}/V_{pv}) with respect to the MPP ($I_{pv} = I_{MPP}, V_{pv} = V_{MPP}$) operating point:

$$\begin{cases} \dfrac{dI_{pv}}{dV_{pv}} > -\dfrac{I_{pv}}{V_{pv}}, V_{pv} < V_{MPP} \\[2ex] \dfrac{dI_{pv}}{dV_{pv}} = -\dfrac{I_{pv}}{V_{pv}}, V_{pv} = V_{MPP} \\[2ex] \dfrac{dI_{pv}}{dV_{pv}} < -\dfrac{I_{pv}}{V_{pv}}, V_{pv} > V_{MPP}. \end{cases} \tag{2.26}$$

Substituting (2.24) to (2.25) and with a linear approximation of the piecewise function at $V_{pv} < V_{MPP}$, since the current variation is negligible, $dI_{pv} \approx 0$, leads to the property of selecting the boost nominal power at the boundary level impressed by the $P_{pv} - V_{pv}$ characteristics:

$$m_N = I_{pv} + V_{pv}\underbrace{\frac{dI_{pv}}{dV_{pv}}}_{\approx 0} \approx I_{pv}. \tag{2.27}$$

Another important observation is that, even when considering a wide temperature of PV junction cell variation (e.g.-20°C, +70°C), the slope can be considered constant at lower PV voltage operation as it can be seen in Fig. 2.24 as well. As a result, the criterion of using (2.27) for determining the boost's nominal power stage becomes sufficient for an optimized design. Furthermore, considering the shading effect, the available PV power decreases further, therefore the traditional boost power stage is not optimized which leads to an over-cost design.

The maximum recommendable design sizing criteria for PV voltage and current (I_{pvMax}, V_{pvMax}) are given by:

$$\begin{cases} I_{pvMax} = N_p I_{scTmax} \leq I_{maxAdm} \\ V_{pvMax} = N_s V_{ocTmin} \leq V_{maxAdm}, \end{cases} \quad (2.28)$$

where N_p and N_s are the number of parallel strings in the array and the number of series cells in each string respectively, I_{scTmax} and V_{ocTmin} are the short-circuit current at the maximum temperature (T_{Max}) and open-circuit voltage respectively at the minimum temperature (T_{Min}), I_{maxAdm} is the maximum admissible current given by the ratings of the power devices, inductors, switch-gear and cables, and V_{maxAdm} is the maximum admissible voltage given by the components ratings.

It can be argued that connecting more PV stings in parallel would increase the power gradient, beyond m_N. However, an important cost-effective design criterion is the maximum short-circuit current that the switch gear and the cables can handle, which leads to selection of maximum number of PV strings parallel (N_p) and series (N_s) connected is given by

$$\begin{cases} N_p \leq \dfrac{I_{maxAdm}}{I_{scTmax}} \\ N_s \leq \dfrac{V_{maxAdm}}{V_{ocTmin}}. \end{cases} \quad (2.29)$$

In this context, it is clear that the boost stage has been dimensioned for the full rated power P_{dcN}, although it will ever process a fraction if it. Therefore, the implementation through the traditional approach results in an overdesigned solution.

The PV module's energy production reduction is attributed to several factors, including irradiance variability, partial shading, soiling, cells delamination and discoloration, increased

operation temperature. The use of the standard boost design would lead excess of materials (e.g. magnetics, electronic components) while not being able to benefit of its full rated power capability.

2.5.3. PV Inverter with Proposed String Mini-Boost and Peak-Power Envelope Operation

A novel approach solution is presented in Fig. 2.24 (c): the mini-boost stage with peak power envelope boundary operation. In this case, a boost stage is included that is designed for a fraction of the rated power of the PV inverter and that can be bypassed if the PV array can provide the voltage by itself. This solution offers a trade-off between the single-stage and the two-stage converter architecture, offering the benefits of both parts without the additional losses and cost of a full-size boost. When large PV plants are considered, the mini-boost stages can be distributed to each string and rated for a fraction of each strings power.

A schematic of the proposed architecture is included in Fig. 2.25. In this schematic, two strings are included in the PV array and each string is assigned to a mini-boost, dc-dc conversion stage. The dc-ac power stage conversion is implemented using a 3-level Neutral-Point Clamped (NPC) PV inverter. Each dc-dc mini-boost stage is built using an inductor, a capacitor, a switch (Q_1, Q_2) and a diode (D_{b1}, D_{b2}) while the stage can be bypassed using diode D_{p1}, D_{p2} when the boosting is not needed. Conversely, if D_{p1}, D_{p2} are not implemented, the current flows through two series elements: a boost inductor (L_{b1}/L_{b2}) and a boost diode $(D_{b1}/D_{b2}$ - silicon carbide) which leads to additional losses. Instead, the by-pass diodes D_{p1}, D_{p2} are selected with a low voltage-drop and low cost standard recovery silicon type rectifiers. Furthermore, the replacement of the by-pass diode with an even lower on-resistance switch (k_{p1}, k_{p2}, e.g. low cost relay) will result in lower losses and heat dissipation. A simple control signal between k_{p1}, k_{p2} and Q_1, Q_2 is

implemented with a mutually exclusive logic. Therefore, the proposed re-design of the by-pass

boost switch provides an opportunity for higher-efficiency operation, as will be demonstrated in

Section 2.6.
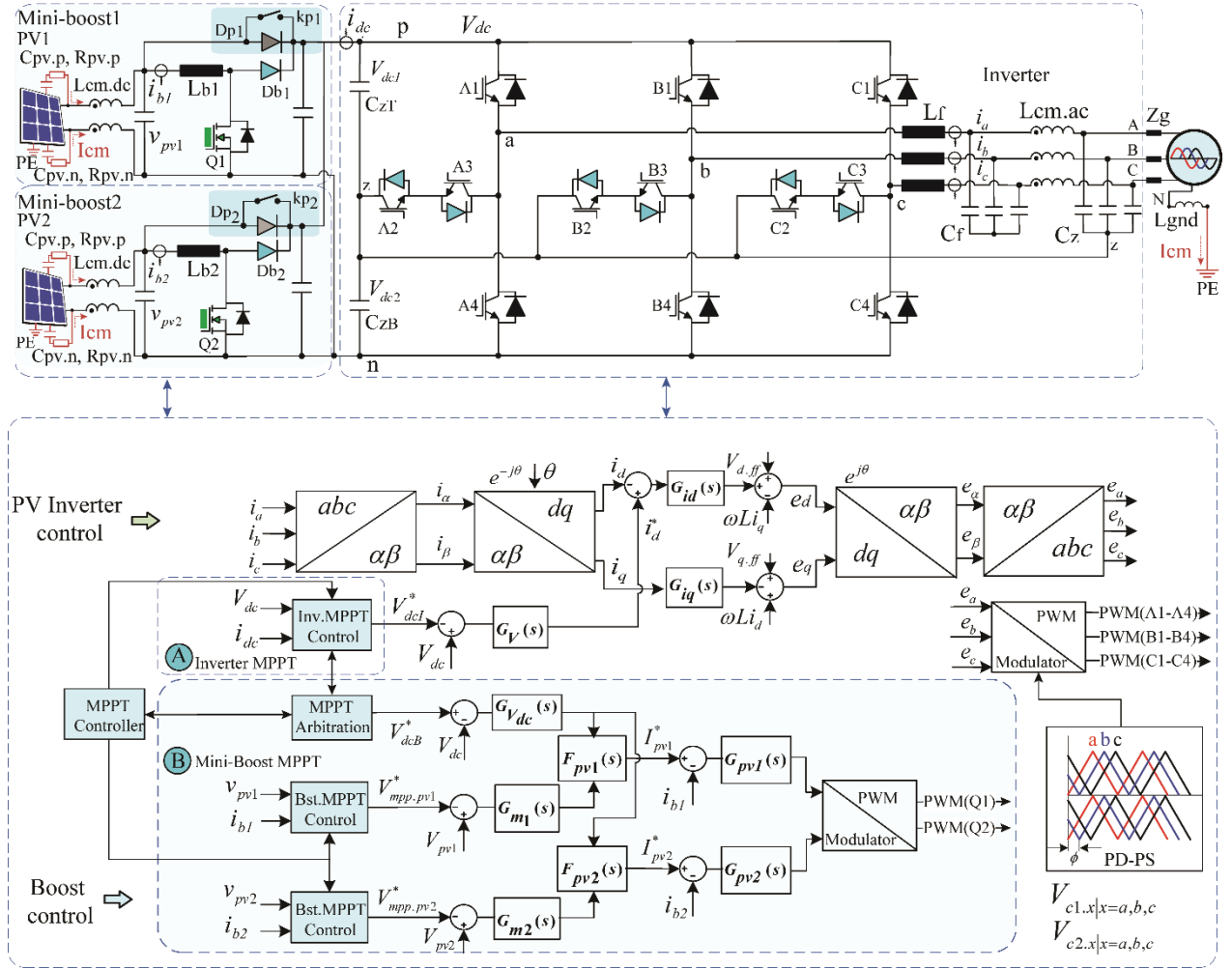
Figure 2.25: Power conversion stage and control block diagram with mini-boost engagement at low PV voltage operation. The maximum power point is determined by the MPPT block algorithm, that shifts control from the PV inverter to the mini-boost stages under different operating conditions.

The combined output of the mini-boost stages is connected to dc-link V_{dc}, which

represents the input voltage for the dc-ac inverter power stage. The three-phase inverter topology

selection is a three-level T-type NPC as shown in Fig. 2.25.

The inverter three-phase currents in natural abc coordinates i_a, i_b, i_c are transformed to stationary $\alpha\beta$-frame, i_α, i_β, which are then converted to synchronously rotating reference dq-frame i_d, i_q, as shown in Fig. 2.25. The grid-connected converter (mini-boosts and inverter) MPPT active power is achieved by the active current controller G_{id} with feedforward grid voltage d-axis component $\hat{V}_{LN} = V_d$ and decoupling from d-axis with the cross-coupling term $\omega L i_q$. The peak power envelope inverter operation is determined by the active current component (i_d) generated to the grid network. The active current reference i_d^* is obtained from the dc link voltage regulator G_V:

$$i_d^* = (V_{dc} - V_{dcI}^*)G_V.$$ (2.30)

The inverter dc link voltage reference V_{dcI}^* is a programmed value determined by the MPPT controller. The inverter MPPT active power is controlled by the equivalent inverter output average voltage e_d given by

$$\begin{cases} e_d = V_d - \omega L i_q + (i_d^* - i_d)G_{id} \\ e_q = V_q + \omega L i_d - i_q G_{iq}. \end{cases}$$ (2.31)

Figure 2.25 also shows the proposed control and MPPT implementation of the system. As it can be observed, the MPPT algorithm block is not only in charge of determining the MPP but also of moving back and forth between the single-stage and two-stage topologies. The arbitration of MPPT algorithm-control between the string mini-boosts and inverter power stages is performed as follows:

$$\begin{cases} \text{a. MPPT is performed by the inverter} & if & (V_{pv1}\ and\ V_{pv2}) > V_{dcMin} \\ \text{b. MPPT is performed by each mini} - \text{boost} & if & (V_{pv1}\ and\ V_{pv2}) < V_{dcMin} \\ \text{c. MPPT is performed by one mini} - \text{boost and inverter} & if & (V_{pv1}\ or\ V_{pv2}) < V_{dcMin}. \end{cases}$$ (2.32)

The MPPT controller (Fig. 2.25) selects the execution of maximum power tracking according to (2.32). In addition, the selection functions F_{pv1}, F_{pv2} determine the boost current references I_{pv1}^*, I_{pv2}^*, where in normal operation these functions use the output of G_{m1}, G_{m2} control blocks. However, in a grid fault case scenario, the selection functions use the output of the G_{Vdc} controller which must regulate the dc-link voltage V_{dc} at the reference voltage established by V_{dcB}^*.

A comparison summary is presented for a grid-tie inverter with standard boost, without and with mini-boost power stage in Table 2.4. It can be seen that the proposed PV string mini-boost topology introduces improvements in almost all the aspects compared in the table, which represent the main concerns when designing a power inverter for PV applications.

Table 2.4: Grid-connected inverter with- and without boost PV system comparison summary.

Criterion	Inverter without boost	Inverter with standard boost	Inverter with PV string mini-boost
MPPT range (dc-ratio)	Reduced	Improved	Optimized
System cost/W	Reduced	High	Medium/Optimized
System weight/power density	Reduced	Standard	Medium/Optimized
PV system power harvesting at low irradiance levels	Restricted (e.g.$< V_{MPP}, P_{lim}$)	Improved (e.g. V_{MPP}, P_{MPP})	Optimized (e.g. V_{MPP}, P_{MPP})
Operation voltage at high PV cell temperature (MPP locus)	Restricted (e.g.$< V_{MPP}, P_{lim}$)	Improved (e.g. V_{MPP}, P_{MPP})	Optimized (e.g. V_{MPP}, P_{MPP})
PV string design flexibility due to extreme temperature conditions	Restricted	Improved	Optimized
PV power system application: ground mounted, residential/commercial roof-top, car-ports	Restricted	Optimized	Optimized
PV inverter design	Reduced	Complex	Complex

2.5.4. Design of the Mini-Boost Stage with Peak Power Envelope Optimization

The renewable power that can be used and delivered to the ac grid, using an inverter with an optimized mini-boost power stage, is illustrated in Fig. 2.26. This design adds two major new features: the PV string mini-boost topology and the peak power envelope optimization. The design procedure for the proposed architecture will be outlined in the following paragraphs.
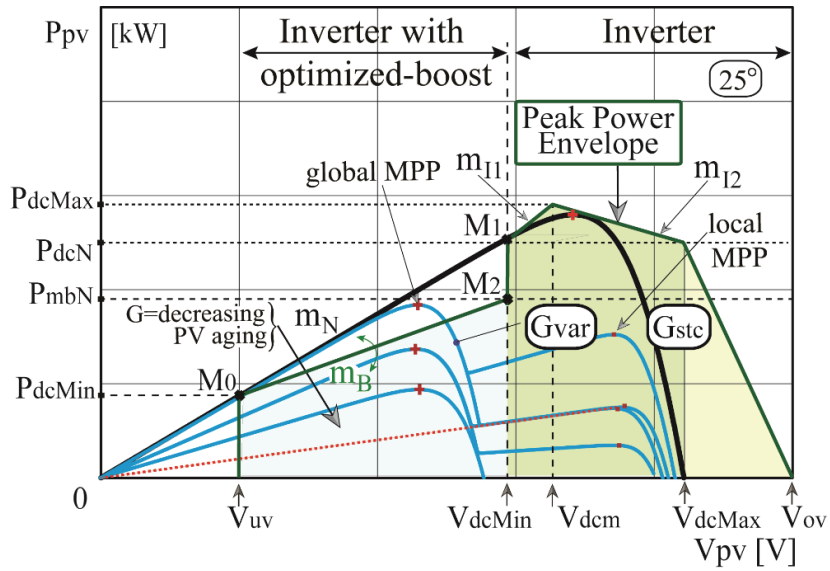
Figure 2.26: Peak power envelope and P-V characteristics under STC uniform insolation (G_{stc}) and two-step partially shaded (G_{var}) operating conditions for boost design optimization. This shading profile is used to analyse the mini-boost characteristics under different real operating conditions and design requirements.

A. PV String Mini-Boost Stage Design

The design of the mini-boost converter is based on selecting a power rating and gradient (m_b) that will be enough to tackle the power of the inverter at when the voltage has dropped below V_{dcMin} and no more. The boost boundary power gradient (m_B) is designed to be less than or equal to the gradient of the PV-string (m_N), considered at standard test conditions (STC). A convenient design consideration is that the m_N of the PV modules is practically independent of the operating

cell temperature, as can be seen from Fig. 2.24. The linearity of P-V characteristics and the close matching curves below MPP voltage determines the sizing boost selection criteria

$$m_B \leq m_N. \tag{2.33}$$

The minimum dc (P_{dcMin}) power is less than the MPP voltage at the same power gradient

$$P_{dcMin} = m_B V_{uv} < I_{MPP} V_{MPP}, \tag{2.34}$$

and this power level is less than the power at MPP voltage, at the same power gradient, where in a practical design, the minimum mini-boost start-up voltage (V_{uv}) is correlated with the internal auxiliary supply

$$V_{uv} = V_{auxMin} + V_{offset}. \tag{2.35}$$

The string boost is designed for the power size considering (2.28) - (2.29), (2.31) - (2.33). At low irradiance levels, the boost extracts the available energy from the PV string modules. The PV string boost sizing design optimization methodology is proposed as follows:

1) N_p, N_s: select the number of series and parallel PV modules (e.g. using equation (2.29)).

2) m_N: determine power gradient of the PV modules given by the equation of the line (M_0, M_1). The maximum boost size is less or equal to the nominal inverter rated power. (e.g. $P_{mbN} < P_{dcN}$).

3) m_B: calculate the boost boundary power gradient using equation (2.34).

4) P_{mbN}: the selection of mini-boost boundary power is suggested within a range, with a maximum power selected at $M_1(V_{dcMin}, P_{dcN})$, Fig. 2.26. However, the mini-boost maximum power can be selected at a lower value, $M_2(V_{dcMin}, P_{mbN})$, Fig. 2.26. This is selected based on the shading profile, components cost design optimization and PV modules aging-degrading prediction.

The boost component cost reduction aims for design optimization in cooling, magnetics, current sense transducer and power semiconductor devices.

The PV voltage variation with the MPPT control arbitration between the boosts and inverter power stages between the inverter, mini-boost and hybrid cases is shown in Fig. 2.27. The proposed mini-boost provides an advantage over the standard solution, in the optimization for cost, size, power density.

During the tracking process, when the PV voltage ramps above V_{dcInv}, the PV inverter transitions to operate without the mini-boost stage (boost disengaged) and the MPPT control moves to the inverter stage (n-region). When the operating voltage drops below V_{dcInv}, the boost is turned on again and the MPPT is transferred to the mini-boost stage (b-region).
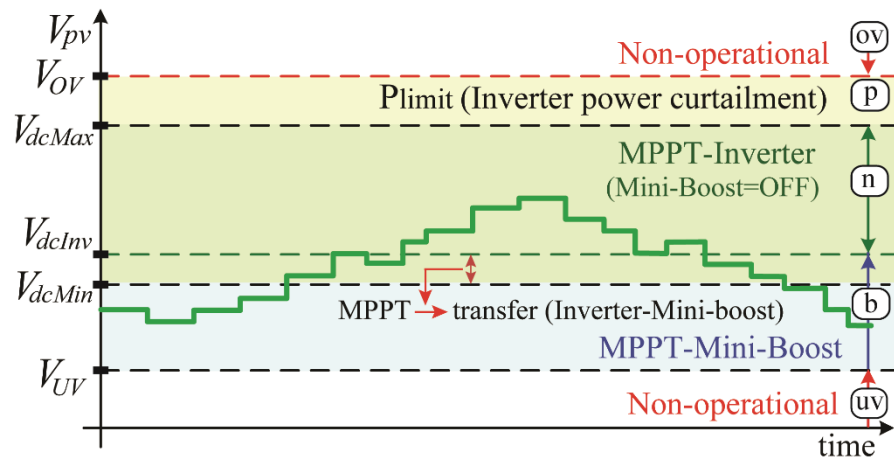
Figure 2.27: Inverter input dc voltage control by the MPPT algorithm; when the PV voltage is lower than the minimum voltage of the single-stage PV inverter, the boost stage is engaged and the MPPT control shifts to the mini-boost stage with peak power envelope operation.

Fig. 2.27 notations:

V_{UV} : Non-operational dc under voltage (uv, e.g. 200Vdc)

V_{dcMin}: Minimum dc link voltage for inverter operation in linear modulation range ($V\sqrt{3}$, where V is peak-phase grid voltage).

V_{dcI}^* : DC link reference voltage under Inverter-MPPT control mode.

V_{dcB}^* : DC link reference voltage under boost voltage regulation mode.

V_{OV}: Non-operational dc over voltage (ov, e.g. 1000Vdc).

The PV operating range of the string boost and inverter power ratings can be described through the following expression:

$$P_{inv}(V_{pv}) = \begin{cases} P_b(V_{pv}) = \begin{cases} I_{MP}V_{pv} & if \quad V_{uv} \le V_{pv} < V_{MPP} \\ P_{mbN} & if \quad V_{MPP} \le V_{pv} < V_{dcMax} \end{cases} \\ P_{mbN} \cdot \left(1 - \dfrac{V_{pv} - V_{dcMax}}{V_{ov} - V_{dcMax}}\right) & if \quad V_{dcMax} \le V_{pv} < V_{ov} \\ 0 \quad if \quad V_{pv} \ge V_{ov}. \end{cases} \tag{2.36}$$

The string boost is designed with an adaptive duty-ratio, function of the grid ac voltage and is expressed as

$$D\left(V_{pv}, V_{ac}\right) = 1 - \frac{V_{pv}}{V_{dc}\left(V_{ac}\right)}. \tag{2.37}$$

In this case, the inverter control establishes the dc bus regulation level (V_{dcI}^*, Fig. 2.25), which is adaptive to the grid voltage variations (e.g. line voltage 400V_{ac} +/- 15%). As a result, two immediate benefits are established: a) lower boost duty-ratio $D(V_{pv}, V_{ac})$ operation leads to higher efficiency and b) the inverter performs with higher efficiency at lower dc-bus voltage, as will be demonstrated by the measured efficiency in the experimental section.

Fig. 2.28 shows the boost and inverter operating range derived from (2.36), (2.37) and the PV current drawn from the PV array, $I(V_{pv}) = P_b(V_{pv})/V_{pv}$.
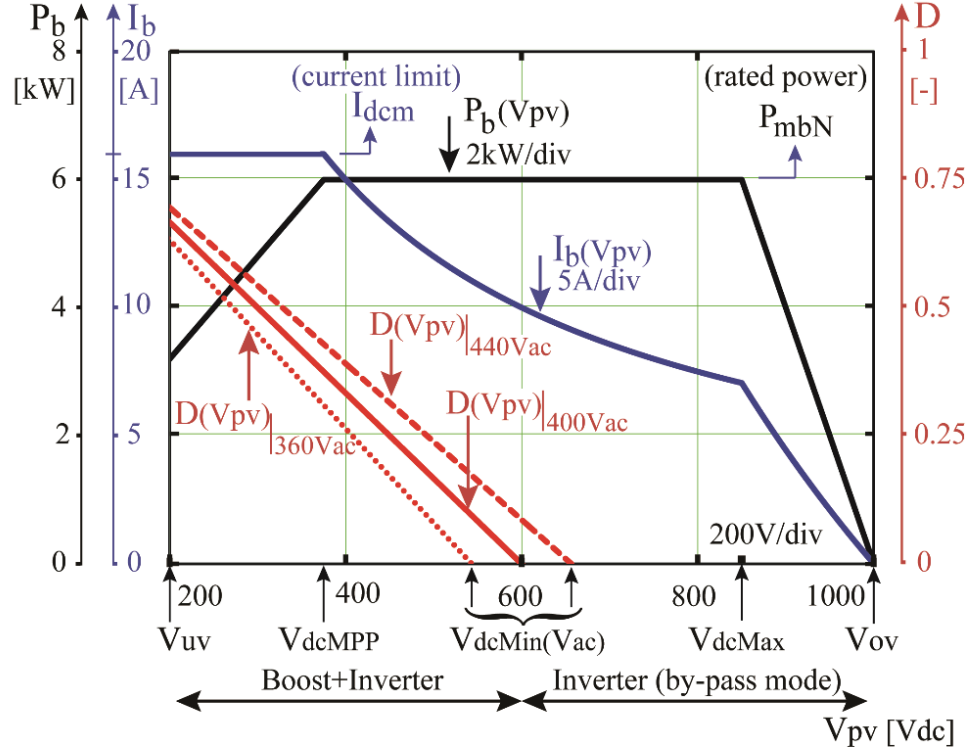
Figure 2.28: Grid-connected system operating range. Boost rated power (P_b), input current (I_b) and duty-ratio as a function of PV voltage V_{pv}.

B. Peak Power Envelope Optimization

An additional proposed optimization criterion is the power conversion system design selection at peak power envelope boundary operation. The inverter power stage is designed for operation over its rated power ($P_{dcMax} > P_{dcN}$). The P_{dcN} represents the inverter nominal MPPT power and is selected at maximum dc voltage (V_{dcMax}), where the inverter exhibits the higher conversion losses (due to increased power devices switching losses and core magnetics losses). The P_{dcMax} represents the maximum inverter MPPT power, operation at optimum dc input voltage (V_{dcm}) where the conversion losses are lower than at the maximum voltage V_{dcMax}.

The inverter MPPT power operation is designed for two intervals, given by

$$\begin{cases} m_{I1} = \dfrac{\Delta P_{I1}}{\Delta V_{pv1}} > 0 \\[3mm] m_{I2} = \dfrac{\Delta P_{I2}}{\Delta V_{pv2}} < 0. \end{cases} \tag{2.38}$$

During the first interval, the inverter operates with constant current,

$$I_{dcm} = \frac{P_{dcInv}}{V_{dcMin}} = \frac{P_{dcMax}}{V_{dcm}}, \tag{2.39}$$

and the dc power can increase linearly to P_{dcMax}

$$\begin{cases} \Delta P_{I1} = P_{dcMax} - P_{dcInv} \\[2mm] \Delta V_{pv1} = V_{dcm} - V_{dcMin}. \end{cases} \tag{2.40}$$

At the beginning of second interval, the dc power decreases linearly towards P_{dcN} due to increase in power losses

$$\begin{cases} \Delta P_{I2} = P_{dcMax} - P_{dcN} \\[2mm] \Delta V_{pv2} = V_{dcMax} - V_{dcm}. \end{cases} \tag{2.41}$$

The inclusion of this power gradients in the inverter operating area optimizes the utilization of the inverter power semiconductors. Instead of taking the conservative approach and defining the operating limit all through V_{dcMin} to V_{dcMax} as P_{dcN} (which is only true at V_{dcMax}) a more realistic approach is presented that has the benefit of being shaped as the P-V curve of the panel, adding operating region where it is most needed.

2.5.5. PV System Operation Case Study

A. PV String Mini-boost Stage Design Considerations Using P-V Characteristics

A solar array power installation is designed with PV modules connected in series-parallel configuration in order to ensure the desired working voltage and current within the power system.

The PV array maximum open-circuit voltage is calculated at lowest daily minimum temperature (with PV module voltage temperature coefficient β_V) and maximum-power point voltage (V_{mp}) for the PV array string is determined at the daily PV cell temperature (T_c), with the consideration of standard test conditions (STC) of 1000W/m^2 irradiance and $T_{stc} = 25°C$ reference temperature,

$$\begin{cases} V_{oc} = V_{oc.stc} \left[1 + \beta_{V_{oc}} \left(T_c - T_{stc} \right) \right] \\ V_{mp} = V_{mp.stc} \left[1 + \beta_{V_{mp}} \left(T_c - T_{stc} \right) \right]. \end{cases} \tag{2.42}$$

As per (2.28) - (2.29) and (2.42), the selection of number of series (N_s) connected PV modules is maximized up to the V_{ocAdm} (with the constraint of $V_{oc.max} = 1000\ V$) calculated at the lowest ambient temperature ($e.g.\ T_{min} = -20°C$). The selection of parallel (N_p) connected PV modules is selected based on grid-tie converter availability, cable sizing and maximum short-circuit switch-gear capability. Using (2.28) and (2.42), the series- and parallel-connected PV modules are $N_s = 19$, respectively $N_p = 2$.

In this case, the proposed string mini-boost design considers the use of up to two strings in parallel ($N_{Pmax} = 2$) for the balance-of-systems cost reduction due to fuse elimination (cost reduction), the higher MPPT granularity, and the arc-fault detection that can use the same current sensors used in the mini-boost control.

The over-sizing power ratio selection (e.g. $P_{pv}/P_{dcN} = 1.25$) between PV array and electronic converter (i.e. boost, inverter) is dependent on project location including tilt angle, orientation, dc switchgear, wiring losses.

Safety regulations and standards imposes design margins, in addition to over-sizing ratio, for cables, bus bars, switchgear which further leading to increased system cost. Therefore, the over-

sizing power ratio is practically limited and the proposed string mini-boost stage provides an improved and optimized solution.

The PV array strings are prone to non-uniform solar irradiance, the cases considered in this analysis are shown in Table 2.5. The I-V and P-V characteristics under different irradiation (two- and three-step change) and temperature conditions, as explained in Table 2.5, are shown in Figs. 2.29 and 2.34.

Table 2.5: Case study: series- and parallel connected PV modules with step-change irradiance.

Case	Irradiance distribution				Converter topology	
	N_s/G_1 [PV modules/ $(W/_{m^2})$]	N_{s1}/G_{21} [PV modules/ $(W/_{m^2})$]	N_{s2}/G_{22} [PV modules/ $(W/_{m^2})$]	N_{s3}/G_{23} [PV modules/ $(W/_{m^2})$]	Inverter without boost power stage	Inverter with mini-boost power stages
C1 (Fig. 2.29)	19 / 1000	13 / 1000	6 / 600	-	Limited power production. Shade intolerant.	MPPT power production. Shade tolerant.
C2 (Fig. 2.30)	19 /1000	13 / 1000	6 / 400	-		
C3 (Fig. 2.31)	19 / 1000	13 / 800	6 / 600	-		
C4 (Fig. 2.32)	19 / 1000	13 / 800	6 / 400			
C5 (Fig. 2.33)	19 / 1000	7 / 1000	6 / 600	6 / 200		
C6 (Fig. 2.34)	19 / 1000	7 / 800	6 / 400	6 / 100		

$N_s, N_{s1}, N_{s2}, N_{s3}$ - numbers of PV modules connected in series.

PV module characteristics:
$V_{oc.stc}$=44.8V, $V_{MPP.stc}$=36.3V, $I_{MPP.stc}$=8.41A, $I_{SC.stc}$=8.97A, $\beta = -0.34\%/°C$, P_{max}=305W (Canadian Solar CS6X-305P) with surface cell temperatures $T_c = -20, 0, 25, 50, 65, 80°C$ at $1kW/m^2$. The 1000V system has 2 parallel strings of 19 PV modules in series.

G1) Np=2; Ns/G1=19/1000W/m²
G2) Np=2; Ns1/G21=13/**1000**W/m², Ns2/G22=**600**W/m²
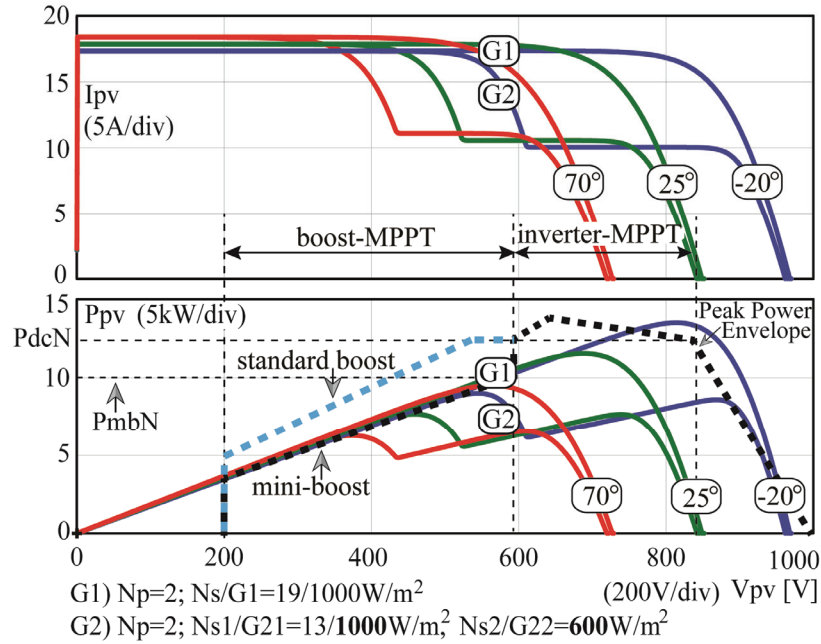
Figure 2.29: Case C1: Comparison between uniform irradiance G1=1000W/m² and partially shaded G2={G$_{21}$=1000 (Ns1=13), G$_{22}$=600 (Ns2=6)}W/m². The solution with mini-boost is able to successful cover the inverter operating regions.

G1) Np=2; Ns/G1=19/1000W/m²
G2) Np=2; Ns1/G21=13/**1000**W/m², Ns2/G22=**400**W/m²
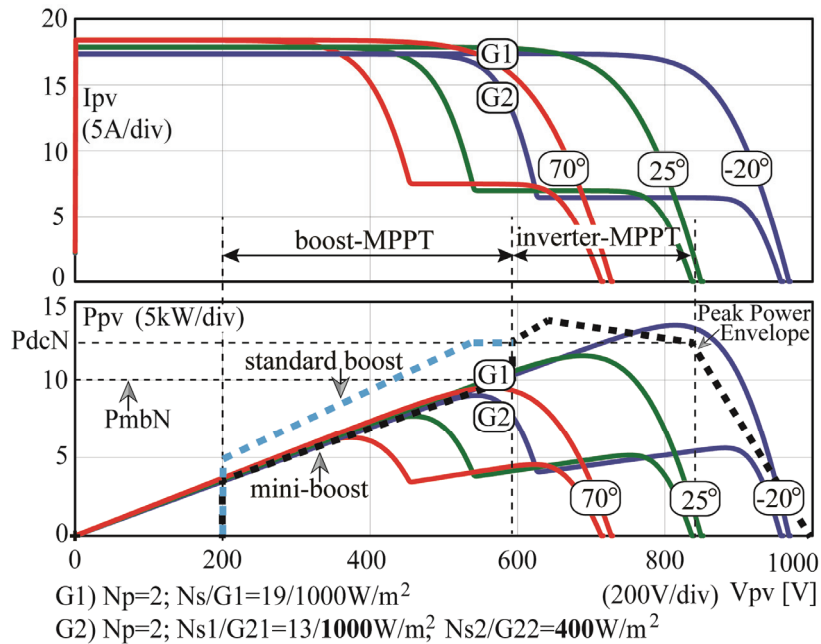
Figure 2.30: Case C2: Comparison between uniform irradiance G1=1000W/m² and partially shaded G2={G$_{21}$=1000 (Ns1=13), G$_{22}$=400 (Ns2=6)}W/m². The solution with mini-boost is able to successful cover the inverter operating regions.
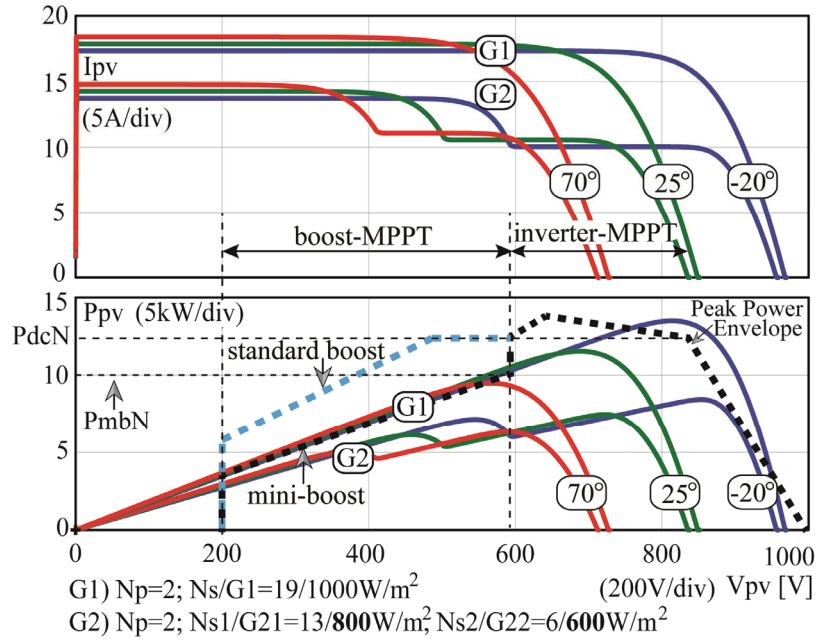
Figure 2.31: Comparison between uniform irradiance G1=1000W/m² and partially shaded G2={G_{21}=800 (Ns1=13), G_{22}=600 (Ns2=6)}W/m². The solution with mini-boost is able to successful cover the inverter operating regions.
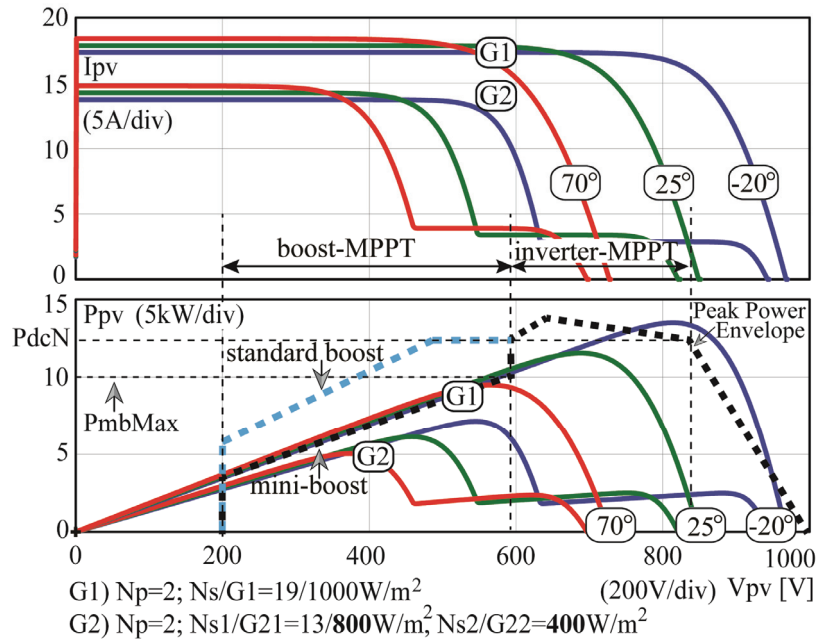
Figure 2.32: Comparison between uniform irradiance G1=1000W/m² and partially shaded G2={G_{21}=800 (Ns1=13), G_{22}=400 (Ns2=6)}W/m². The solution with mini-boost is able to successful cover the inverter operating regions.

G1) Np=2;Ns/G1=19/1000W/m^2
G2) Np=2;Ns1/G21=7/**1000**W/m^2; Ns2/G22=6/**600**W/m^2;Ns3/G23=6/**200**W/m^2
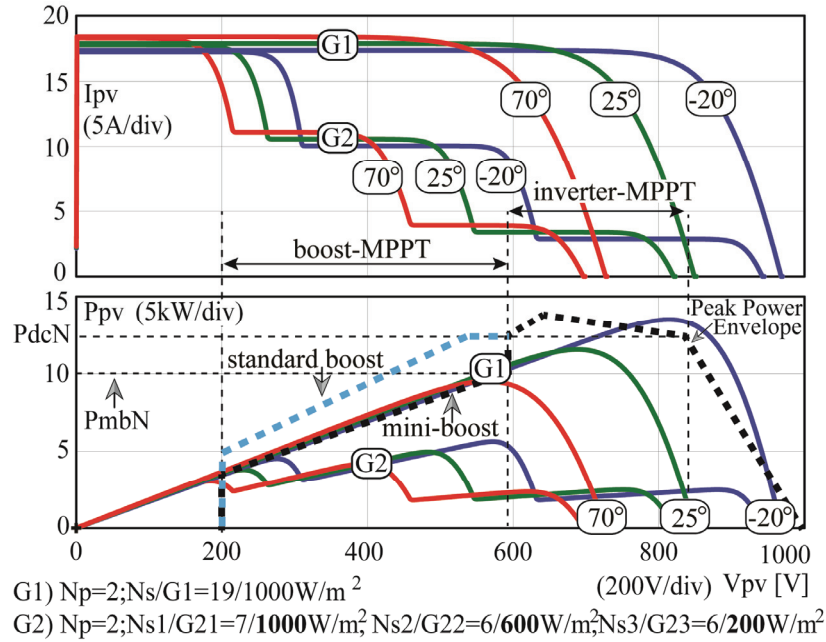
Figure 2.33: Case C3: Comparison between uniform irradiance G1=1000W/m^2 and partially shaded G2={G$_{21}$=1000 (Ns1=7), G$_{22}$=600 (Ns2=6), G$_{23}$=200 (Ns3=6)} W/m^2. The solution with mini-boost is able to successful cover the inverter operating regions.

G1) Np=2; Ns/G1=19/1000W/m^2
G2) Np=2; Ns1/G21=13/**800**W/m^2; Ns2/G22=**400**W/m^2;Ns2/G22=**100**W/m^2
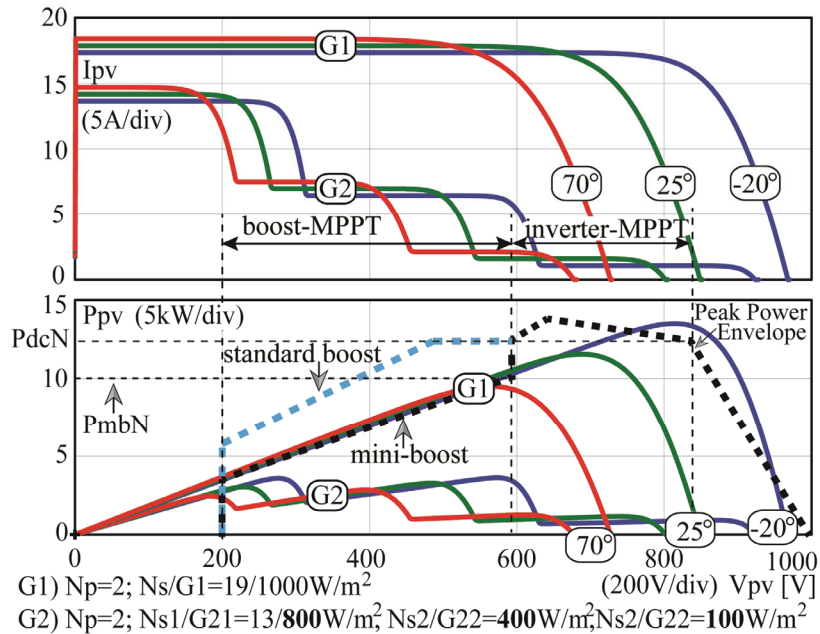
Figure 2.34: Case C4: Comparison between uniform irradiance G1=1000W/m^2 and partially shaded G2={G$_{21}$=800 (Ns1=7), G$_{22}$=400 (Ns2=6), G$_{23}$=100 (Ns3=6)} W/m^2. The solution with mini-boost is able to successful cover the inverter operating regions.

The optimization of the mini-boost size is based on practical shading and lower irradiance profile, components cost and PV modules aging resulting in performance degradation. The mini-boost component cost reduction aims for design optimization in cooling, magnetics, current sense transducer and power semiconductor devices, as it can be seen in Table 2.6.

Table 2.6: Boost design comparison.

Parameter	Standard Boost	String Mini-boost
Boost boundary maximum power, P_{Bmax} [p.u.]	1 (12.5kW)	0.48 (6kW)
Power gradient m_B [W/V]	26.7	17.5
Maximum operating current (I_{dcm}) [p.u.]	1 (26.5 A)	0.64 (17A)
Power semiconductor devices (Q, D_b) sizing [p.u.]	1	0.6
Inductor (L_b) size [p.u.]	1	0.7
Current sensor ratings [p.u.]	1 (40A)	0.625 (25A)

The proposed peak power envelope operation provides optimal inverter operation by maximizing the utilization of the power components. The use of the proposed new methodology allows the PV inverter to operate at high efficiency while extending the operating range and keeping the system cost down.

The MPPT algorithm implemented is a Perturb and Observe (P&O) with capabilities for detecting the global maximum using a periodic sweep. Other algorithms can be included to target specific needs given by the situation.

The sizing concept can be applied to a cost-performance optimization design, applicable to any PV system installation. Experimental results of the proposed architecture are presented in the following section to validate the system design.

B. Common-mode Circulating Current Issues and Improvement Solutions

Transformer-less grid-connected PV systems are susceptible to leakage current generation above the required safety limits. The stray capacitance between the PV array positive and negative terminals and grounded frame provides a current circulation path between the PV source, converter and ac grid port. In three-phase neutral-point clamped (NPC) topology, the neutral-point can be bonded to grid neutral in order to suppress the leakage current [132]. Modulation techniques have been proposed in three-phase systems for leakage current reduction [133] - [135]. However, with these methods, the modulation index is limited and maximum dc bus utilization cannot be achieved. In this work, three methods are discussed that minimize current leakage while maintaining the maximum dc bus utilization.

The inclusion of zero-sequence (ZS) triple harmonics components in three-phase converter's modulation ($m_{max} = 2/\sqrt{3}$) provides extended dc bus utilization that is 15% higher than the sinusoidal PWM ($m_{max} = 1$). As a result, the operation can be performed at a lower dc bus voltage range, which leads to two advantages in terms of efficiency: lower switching losses (dc-ac inverter stage) and a lower conversion ratio between dc-dc boost and dc-ac inverter power stages. In order to benefit from the above advantages, the three-phase 3L-TNPC considered in this work is designed with a neutral-point floating potential, i.e. the mid-point between top and bottom capacitors (C_{zT}, C_{zB}, Fig. 2.25). However, due to the nature of non-galvanic isolation between the PV modules and the grid, leakage currents are generated and propagated through the stray impedance (e.g. capacitance $C_{pv.p}, C_{pv.n}$ and resistance $R_{pv.p}, R_{pv.n}$, Fig. 2.25). The variability of the stray capacitance between the grounded PV module frame and the floating positive and negative terminals is mainly influenced by cell construction and weather conditions. In this case study, the stray capacitance is considered to have a value of $100 \ nF/kW$.

The common-mode (CM) voltage is the sum of the phase voltages at each filter inductor terminal with respect to a common point (e.g. neutral-point (z) point, negative (n) and positive (p) dc terminals). The 3-phase balanced voltage system and the CM voltage of the inverter output with respect to grid neutral (N) and neutral-point (z) is expressed:

$$\begin{cases} V_{aN} + V_{bN} + V_{cN} = 0 \\ V_{cm.z} = \dfrac{V_{az} + V_{bz} + V_{cz}}{3}. \end{cases} \tag{2.43}$$

The voltage fluctuation at the dc positive and negative terminals becomes the generator source for the CM current. The circulation path formed through the PV stray capacitance and resistance (C_{pv}, R_{pv}) leads to CM current generation:

$$\begin{cases} \displaystyle\sum_{x=a,b,c} I_x = I_{cm} \neq 0 \\ \left. \left(I_x = I_{x.d} + \dfrac{I_{cm}}{3} \right) \right|_{x=a,b,c}. \end{cases} \tag{2.44}$$

The phase output current contains the differential term ($I_{x.d}$), and one third of the CM current (I_{cm}). The CM current magnitude is influenced by the PV stray impedance elements (e.g. C_{pv}, R_{pv} – where the leakage resistance provides a damping effect), the system components (L_f, $L_{cm.dc}, L_{cm.ac}$), the dc voltage operation (V_{dc}), the modulation strategy and the switching frequency impact on $dV_{Cpv}(t)/dt$:

$$i_{cm}(t) = C_{pv} \dfrac{dV_{Cpv}(t)}{dt}. \tag{2.44}$$

The duration and magnitude of the leakage current above certain limits presents a safety hazard by allowing the current to flow through the human body or to create fire hazards. The conditions for a current leakage and residual fault must occur when its value (RMS, average and sudden

change) is above a permissible threshold (e.g. 300mA, P <30kVA and 10mA per kVA, P >30kVA), which is usually determined by standards. The issue of CM (leakage) current reduction is addressed in this work using three different techniques: common mode inductors, capacitive filtering and modulation strategy.

The first technique reuses the dc and electromagnetic compliance (EMC) components ($L_{cm.dc}$, $L_{cm.ac}$, Fig. 2.25), which now are designed for a dual purpose: electromagnetic emissions (e.g. EN61000-6-3) and current leakage (e.g. IEC62109-2, VDE-AR-N-4105) compliance. This technique introduces high impedance in the leakage current path. Furthermore, and an inductor (L_{gnd}, Fig. 2.25) can be placed between the grid ground bonding and protective earth (PE) of the PV system. However, the ground inductor L_{gnd} has the disadvantage of increasing the cost of the system.

The second technique involves adding relatively low cost film ac capacitors(C_z), between the inverter output and neutral-point (z). In this way, a fraction of I_{cm} is returned to its source and the leakage current circulation through the grid conductors is reduced.
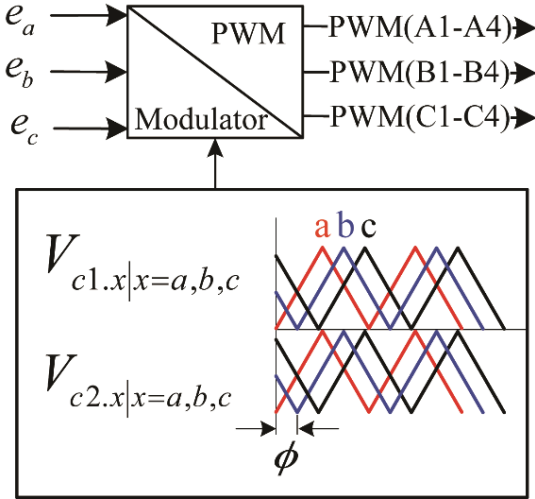
Figure 2.35: Modified Phase-disposition phase-shift modulator for common-mode circulating current reduction.

The third technique is implemented at the three-phase inverter modulator level: while maintaining the ZS, the three-phase carriers are shifted as shown in Fig. 2.35. The concept introduced is a modified phase disposition (PD) modulation with a phase-shift (PS) angle (φ) between the inverter's three phases. Using this technique, the $dV_{Cpv}(t)/dt$ term from (2.44) is reduced in magnitude, and the end result is a lower CM voltage spectrum, with significant reduced leakage current, as it will be demonstrated in the simulation and experimental section.

2.5.6. Photovoltaic and Wind Mini-boost System

An interesting expansion of the mini-boost architecture is to wind energy generation. The wind turbine (WT) converts the wind kinetic energy into mechanical energy. The mechanical energy is further converted into electrical power and generates a three-phase ac output at the generator (e.g. permanent magnet synchronous generator, PMSG) stator windings. The ac voltage amplitude and frequency depends on the angular speed of the WT.
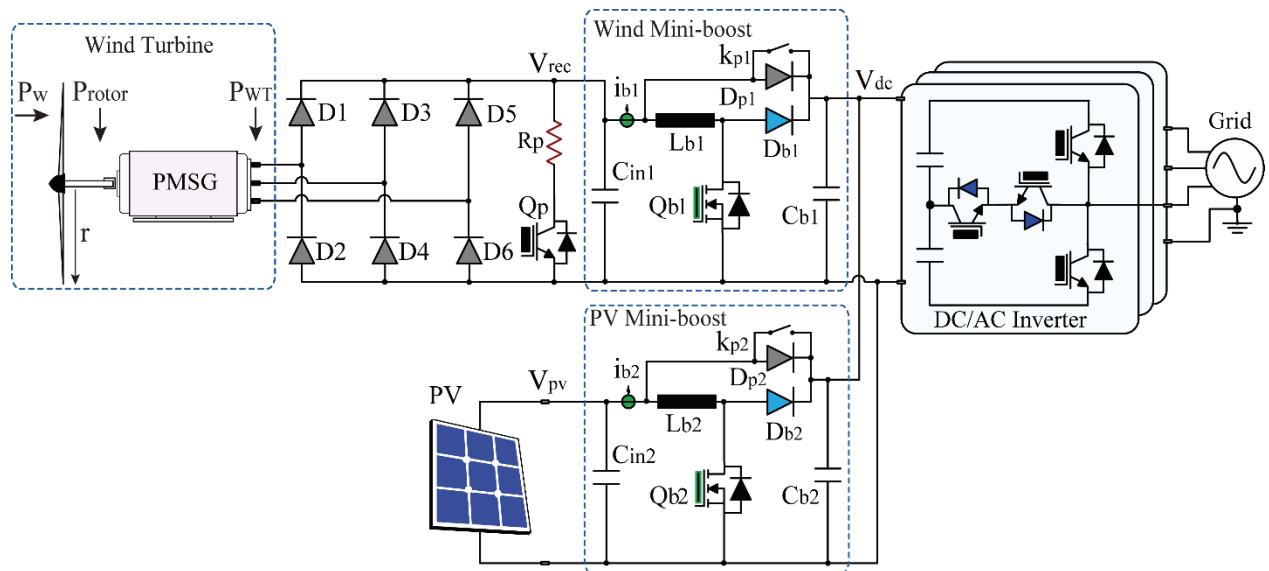
Figure 2.36: Photovoltaic and wind turbine using the mini-boost architecture.

Fig. 2.36 shows an integration of PV and wind, interfaced with two mini-boost converters. The combined output power is transferred to the grid port through the dc/ac inverter stage.

A wind turbine solution (mini-wind) employs a synchronous generator, a passive rectifier bridge $D_1 - D_6$ and the diversion load protection circuit $(R_p - Q_p)$. The resistance value R_p shall be designed to dissipate (e.g. for few minutes at maximum overvoltage limit of rectified voltage V_{rec}) the energy produced by the WT in emergency scenarios. The diversion load is activated by switch Q_p under very strong wind conditions, grid disconnect or not available, at the scenarios where the dc voltage V_{dc} exceeds a safe operation limit (e.g. 1000V).

The wind power P_w (Betz' law) and the wind turbine electrical output power P_{WT} can be expressed as

$$\begin{cases} P_w = \dfrac{1}{2}\rho_a \cdot A_w \cdot C_p(\lambda, \beta) \cdot v_w^3 \\ P_{WT} = \eta_{rotor} \cdot \eta_{gen} \cdot P_w, \end{cases} \tag{2.45}$$

where

ρ_a - air density ($\rho_a = 1.225\ kg/m^3$, at 15°C sea level).

A_w – WT swept area ($A_w = \pi r^2$, r is turbine blade length)

$C_p(\lambda, \beta)$ – WT power coefficient (Betz coefficient, $C_{pmax} = 16/27$)

$\lambda = v_{tip}/v_w = (\omega_w \cdot r)/v_w$ – WT tip speed ratio

ω_w – WT angular frequency

β - WT blade pitch angle

v_w - wind velocity

η_{rotor} – WT rotor efficiency ($\eta_{rotor} = P_{rotor}/P_w$)

η_{rotor} - electrical generator efficiency ($\eta_{gen} = P_{gen}/P_{rotor}$).
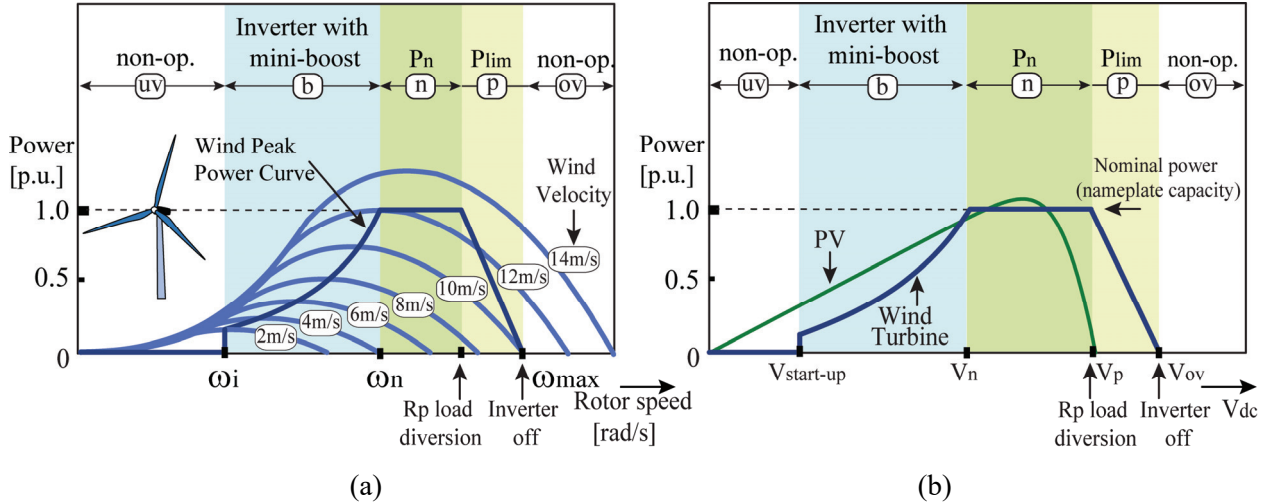
Figure 2.37: Photovoltaic and wind turbine using the mini-boost architecture. (a) Wind power characteristics and optimal wind peak power curve. (b) Wind peak power curve fit and PV characteristic for mini-boost design and control.

Fig. 2.37 (a) shows the WT power characteristics with respect to wind velocity and angular rotor speed. The polynomial curve section ($\omega_i - \omega_n$, respectively $V_{start-up} - V_n$) of the wind peak power curve (Fig. 2.37 (b)) is used for the mini-boost design and control algorithm. Using a similar methodology as explained in previous section, the mini-boost components can be optimized for ratings as per polynomial function characteristics. In addition, the WT maximum power point control algorithm is designed using the polynomial locus of the power curves. The WT rotor speed is adjusted proportional to the wind velocity by torque control, where the aerodynamic power harvested is maximal. The mini-boost controls the wind-MPPT by tracking the WT angular frequency (e.g. 0 - 500 rad/s) from the rectified ac voltage pulsations. In this way, it is no necessary for other complex communications interfaces with the WT generator.

In scenarios of wind velocity exceeds the rated values (e.g. $> 12m/s$, $\omega_n - \omega_{max}$, respectively $V_n - V_p$), it is required that the rotor mechanical torque (active power) to the generator should be kept as constant as possible to reduce the electrical power fluctuation. When the dc rectified voltage (V_{rec}) supplied to the input of the mini-boost, exceeds the voltage protection limit (V_p, Fig. 2.37 (a)) the diversion load resistive bank is engaged, while the dc/ac inverter curtails the

power production. Above the overvoltage limit (V_{ov}, Fig. 2.37 (a)) all system control turns off the power production to grid in order to avoid operation outside the safe operating ratings.

The performance of the mini-boost architecture is evaluated in the next section.

2.6.   Simulation and Experimental Results

An experimental set-up was developed in order to evaluate the proposed architecture design for energy production on a three-phase 25-kVA inverter with dual string PV system. The characteristics of the experimental set-up are presented in Table 2.7.

Table 2.7: Boost and PV inverter main characteristics.

Power stage	Nominal power P_{dcN}, P_n [kW]	Switching frequency f_s [kHz]	Power Inductor [mH]	DC operation range $V_{dcMin} \div V_{dcMax}$ [V]
Mini-boost1	6	20	1	200÷850
Mini-boost2	6	20	1	200÷850
3-phase PV inverter	25	20	0.8	575÷1000

As it can be observed, each mini-boost stage is sized to 1/4 of the total rated power of the PV inverter, using components that are much smaller and more economical than the corresponding full-rated components for a 25 kW boost.

The grid-connected photovoltaic inverter with dual mini-boosts hardware prototype layout configuration, used for experimental evaluation, is shown in Fig. 2.38.

The sizing of the converter components was performed following the design procedure based on the optimized peak-power envelope in order to maximize the device power utilization.
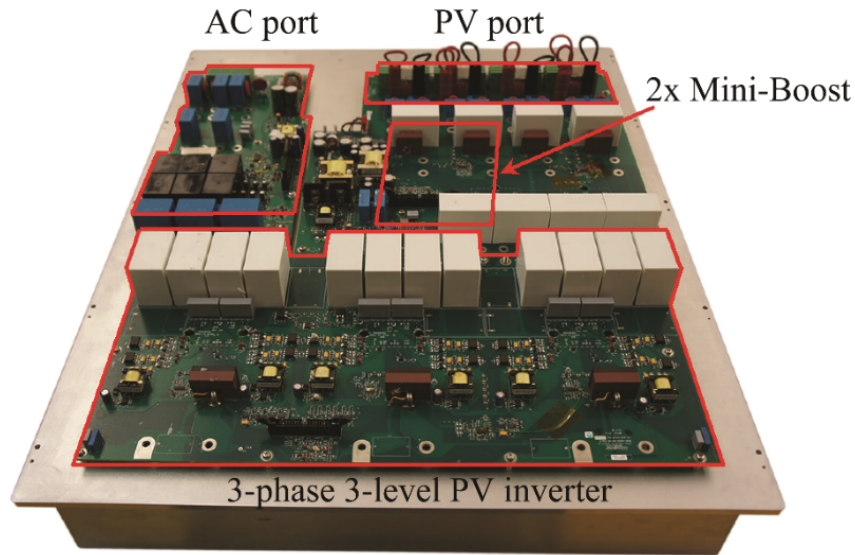
Figure 2.38: Three-phase grid-connected PV inverter with string mini-boosts prototype stage configuration for experimental evaluation.

Fig. 2.39 shows the key waveforms of PV inverter operation with dual mini-boosts using the proposed control structure from Fig. 2.25. During the first interval $(t_0 - t_1)$, both mini-boosts operate in independent MPPT mode, converting power from two separate and balanced PV arrays, $P_{pv1} = P_{pv2} = 2kW$. At moment t_1, an imbalance is produced (sudden difference jump in irradiance on PV1 array), and MPPT1 (mini-boost 1) detects an increase power available solely from PV1 array source and the total power generated is increased from 4kW to 7kW, which corresponds to the maximum power production available from PV arrays. Part of the effectiveness of the inverter's control structure of Fig. 2.25 is demonstrated in the dynamics evaluation tests from Fig. 2.39.
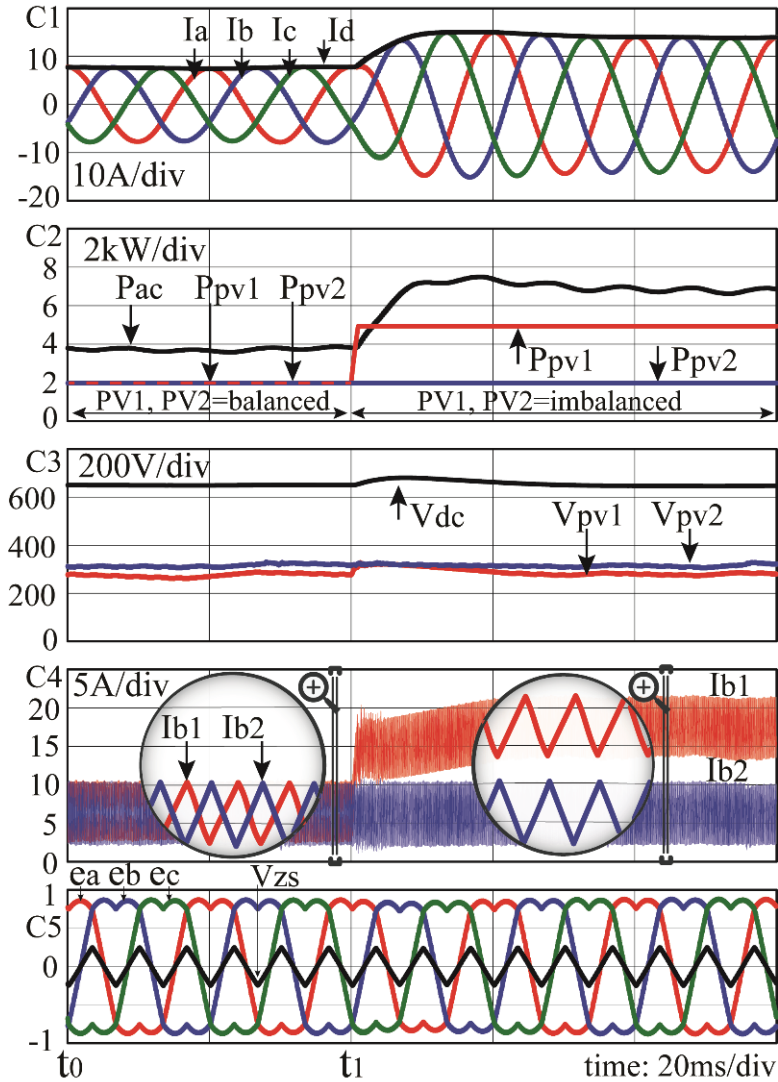
Figure 2.39: Grid-connected PV inverter power conversion with two mini-boosts under balanced and imbalanced test cases: key waveforms.

Y-axis: C1 - Inverter phase currents I_a, I_b, I_c and active current component I_d 10A/div. C2 - Boosts power P_{pv1}, P_{pv2} and inverter active power P_{ac}, 2kW/div. C3 - dc-link voltage V_{dc} and input voltages of two mini-boost stages V_{pv1}, V_{pv2} 200V/div. C4 - mini-boosts inductor currents I_{b1}, I_{b2}, 5A/div. C5 - 3-level 3-phase control signals e_a, e_b, e_c and zero sequence V_{ZS}, 0.5 p.u./div.

X-axis: 20ms/div.
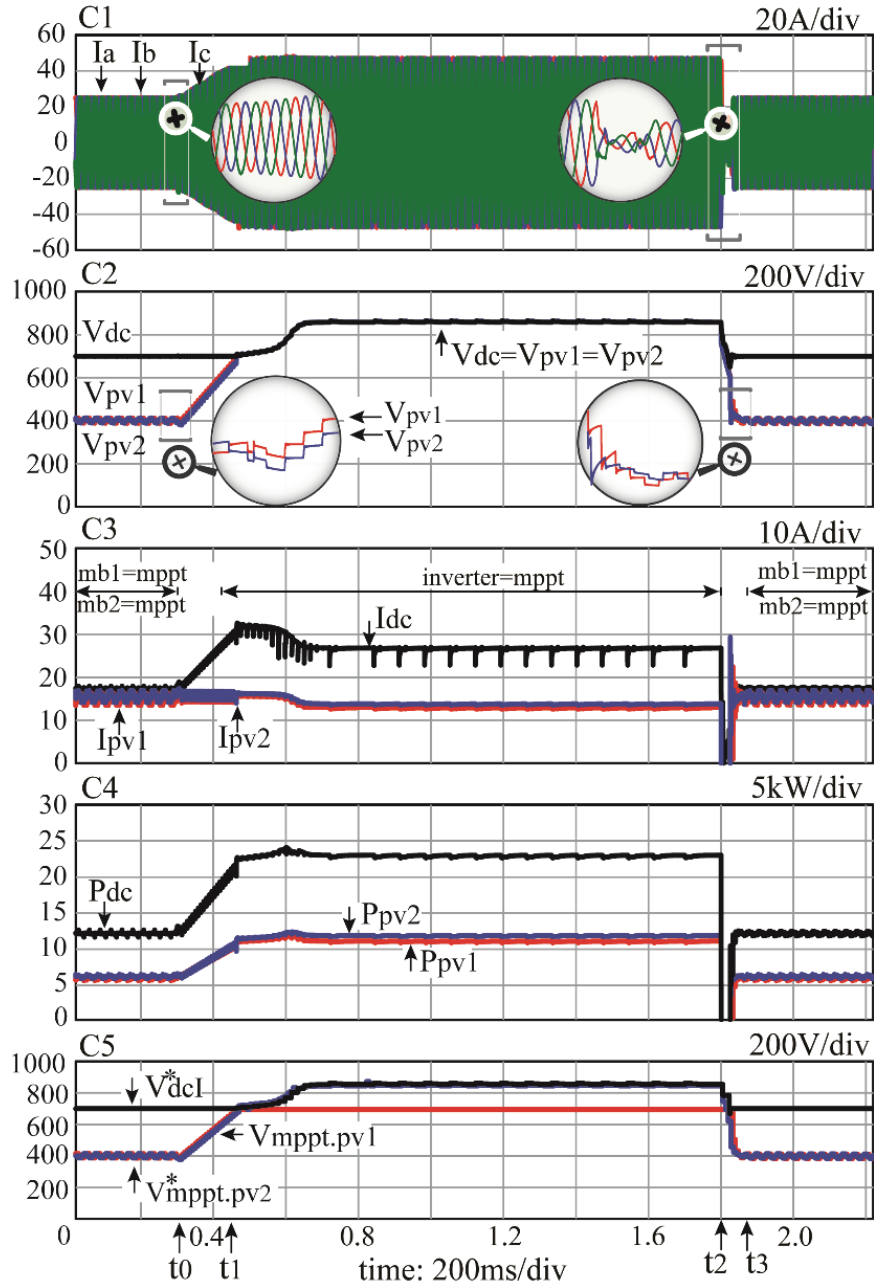
(a) System operation with MPPT transition from mini-boost1 and mini-boost2 to inverter stage. The PV1 and PV2 array characteristics are changed at t_0 as follows: $(I_{mp1}, V_{mp1}, P_{mp1}) = (15 \rightarrow 13A, 400 \rightarrow 850V, 6 \rightarrow 11kW)$ and $(I_{mp2}, V_{mp2}, P_{mp2}) = (15.5 \rightarrow 14.1A, 400 \rightarrow 850V, 6.2 \rightarrow 12kW)$. At t_2, PV1 and PV1 characteristics are returned to values prior to t_0.
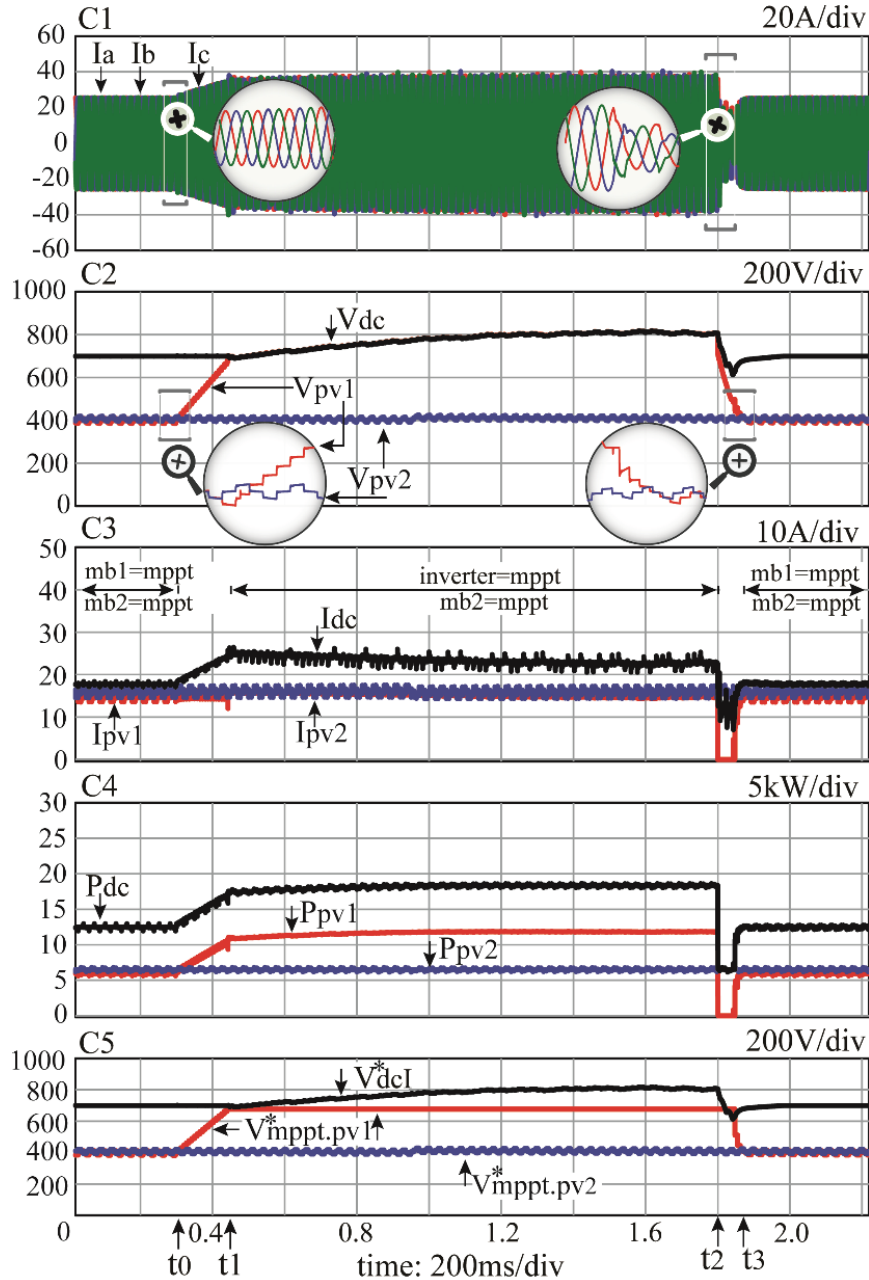
(b) System operation with MPPT transition from mini-boost1 to inverter stage: PV1 array characteristics change $\left(I_{mp1}, V_{mp1}, P_{mp1}\right) = (15 \rightarrow 14.8A, 400 \rightarrow 800V, 6 \rightarrow 11.8kW)$ while PV1 remains constant $\left(I_{mp2}, V_{mp2}, P_{mp2}\right) = (15.5A, 405V, 6.27kW)$. At t_2, PV1 characteristics is returned to values prior to t_0.

Figure 2.40: Grid-connected PV inverter power conversion with dual mini-boosts under two step-irradiance test cases:

Y-axis: C1 - Inverter phase currents I_a, I_b, I_c 20A/div. C2 – PV input voltages of two mini-boost stages V_{pv1}, V_{pv2}, dc-link voltage V_{dc} 200V/div. C3 - PV input currents I_{pv1}, I_{pv2} 10A/div. C4 - Boosts power P_{pv1}, P_{pv2}, and total dc power, P_{dc}, 5kW/div. C5 – MPPT control signals (Fig. 2.25), $V_{mppt1}^*, V_{mppt2}^*, V_{dcI}^*$ 200V/div. X-axis: 200ms/div.

Fig. 2.40 shows the grid-connected PV system's performance under step-load, i.e. PV array irradiance sudden profile change. In Fig. 2.40 (a), (b) prior to moment t_0, the two arrays PV1 and PV2 are exposed to a similar irradiance level. In this case, the mini-boosts execute the MPPT algorithms (V^*_{mppt1}, V^*_{mppt2}, Fig. 2.25) while the inverter regulates the dc-link voltage (V^*_{dcI} Fig. 2.25).

Fig. 2.40 (a) demonstrates the MPPT steady-state operation and transition of both mini-boosts, from step-up conversion to by-pass mode, where the MPPT is executed by the inverter stage. At the moment t_0, the available power at PV1 and PV2 ports suddenly approximately doubles. Consequently, the PV1 and PV2 voltages increase from $V_{mp1} = 400V$ (prior to t_0) until the MPP voltage is determined and settled by the inverter's MPPT algorithm. At t_1 the mini-boosts transition to by-pass mode and the task of tracking the maximum power is transferred to the inverter controls, regulating the dc-link voltage at $V_{dc} = 850V$. At t_2, the PV1 and PV2 characteristics return to their initial values prior to t_0 with stable transitions and, at t_3, the system resumes its initial operation.

Fig. 2.40 (b) demonstrates the system's ability to operate flexibly using independent MPPT controls, fulfilled by the mini-boosts and inverter conversion system. At the moment t_0, the available power at the PV1 port suddenly approximately doubles. As a result, the PV1 voltage increases from $V_{mp1} = 400V$ (prior to t_0) until the MPP voltage is determined and settled by the inverter's MPPT algorithm. At t_1, the mini-boost transitions to by-pass mode and the task of tracking the maximum power is transferred to the inverter controls, regulating the dc-link voltage at $V_{dc} = 800V$. At t_2, the PV1 characteristics returns to their initial values prior to t_0, while PV1 profile remains constant. The interchange of MPPT boosts-inverter functionality demonstrates the system's stability and robustness.

The experimental results of the inverter operation, with single- and two-stage, under dynamic and steady-state conditions for the MPPT arbitration are presented in figures 2.41 - 2.43.

(a)
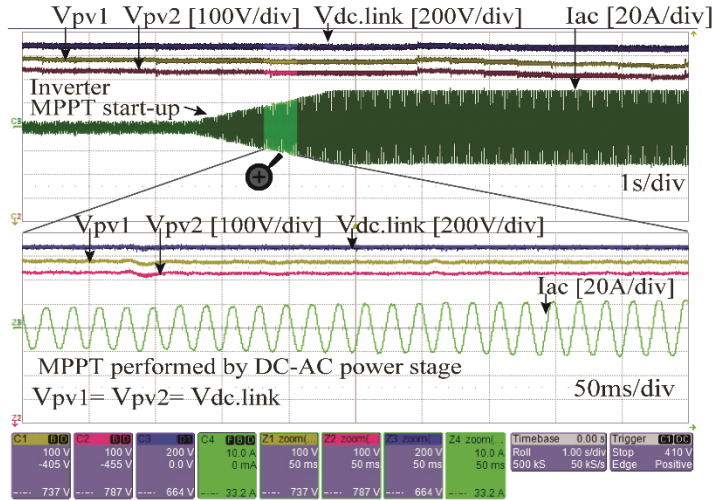
PV inverter operation: balanced PV loading.
DC: 2x MPPT, Pmp1=Pmp2=3.93kW
AC: 230V-50Hz, Pac=1→7.7kW

(b)
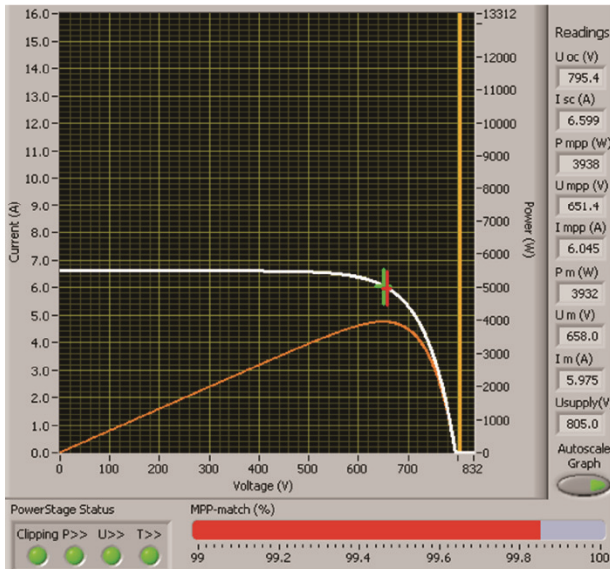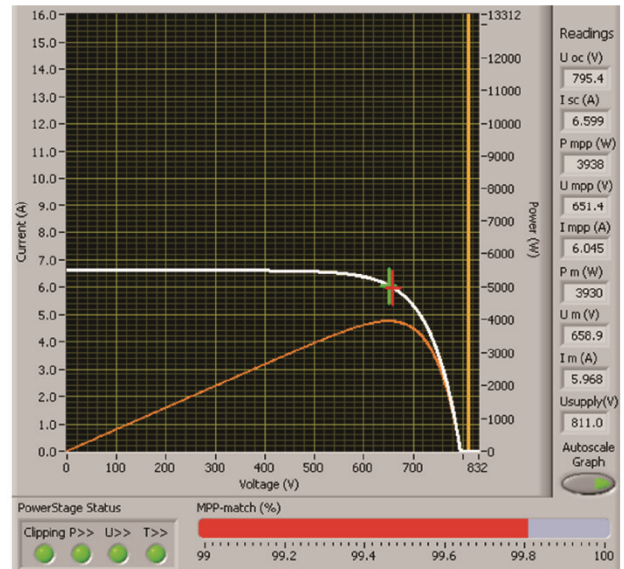
PV1:Vpv1=658V, Voc1=795V, Pmp1=3.93kW, Imp1=5.97A

(c)

PV2:Vpv2=658V, Voc2=795V, Pmp2=3.93kW, Imp2=5.97A

Figure 2.41: Single-stage PV inverter operation (mini-boosts are switched automatically off). The MPPT is performed by the inverter $(V_{pv1} \text{ and } V_{pv2}) > V_{dcMin}$.

Experimental results with inverter-MPPT control dynamics under irradiance-power change: 1kW to 8kW, grid connected 3-phase $230V_{LN}/400V_{LL}$-50Hz. PV1: I-V, P-V characteristics with Inverter-MPPT algorithm efficiency of 99.8%.

(a)
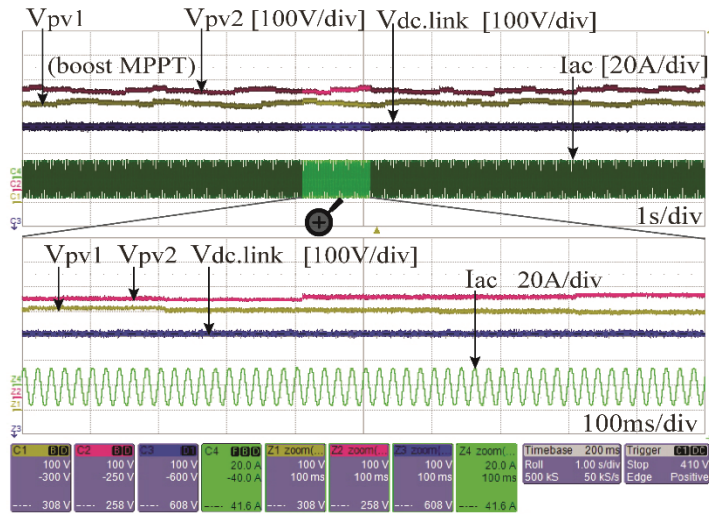
PV inverter operation: balanced PV loading.
DC: 2x MPPT, Pmp1=Pmp2=3.93kW
AC: 230V-50Hz, Pac=7.6kW
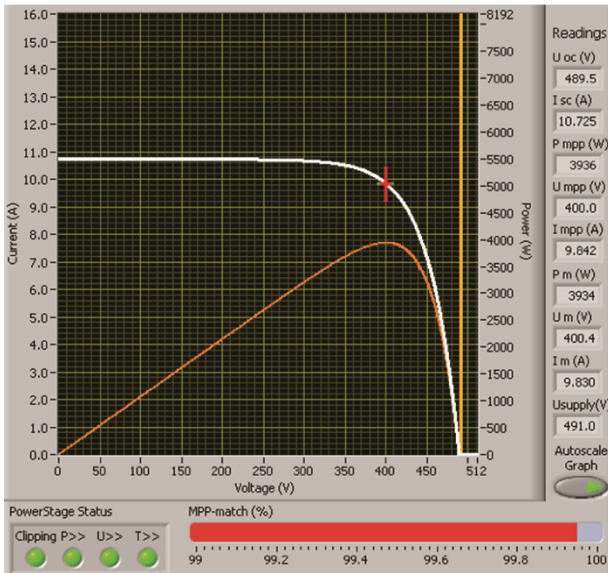
(b)	(c)
PV1:Vpv1=400V, Voc1=490V, Pmp1=3.93kW, Imp1=9.84A	PV2:Vpv2=400V, Voc2=490V, Pmp2=3.93kW, Imp2=9.84A
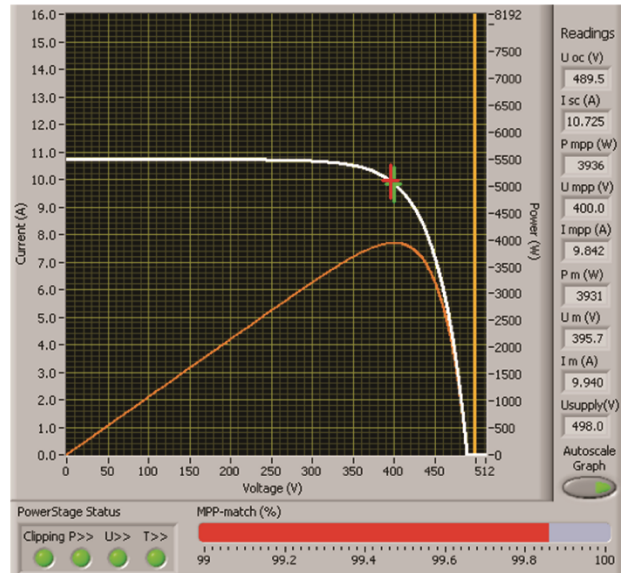
Figure 2.42: Two-stage PV inverter operation, with dual mini-boost engaged (PV1 and PV2). The MPPT is performed by two mini-boosts $\left(V_{pv1} \text{ and } V_{pv2}\right) < V_{dcMin}$.

Experimental results with string mini-boosts-MPPT under steady-state conditions with 7.6kW grid power production, with MPPT algorithm efficiency of 99.8%.

The single-stage inverter operation is shown in Fig. 2.41 since the PV voltages, $(V_{pv1}$ and $V_{pv2}) > V_{dcMin}$ are sufficient to by-pass the mini-boosts (case a, relation (2.29)). The MPPT tracking is performed by inverter stage, with two PV strings balanced at 3.93 kW for power production. The MPPT perturbation (voltage steps from the control set-point V_{dcI}^*, Fig. 2.25) is proportionally reflected in the dc components, V_{pv1}, V_{pv2} and V_{dcMin} as it can be noted in Fig. 2.41 (a). The inverter gradually increases the operating point of the converter until it reaches the 99.8% mark.

Fig. 2.42 includes the two-stage power conversion operation, with PV voltages $(V_{pv1}$ and $V_{pv2}) < V_{dcMin}$ (case b, relation (2.29)). The two mini-boost power stages are enabled due to low PV voltage operation. The MPPT perturbation (voltage steps voltage steps from the control set-points V_{mppt1}^*, V_{mppt2}^*, Fig. 2.25) is independently performed by the two mini-boosts as it can be observed in waveforms V_{pv1} and V_{pv2} in Fig. 2.42 (a).

A single stage PV inverter (without mini-boost) would not be able to operate under these conditions since the voltage is less than the required $V_{dcMin} = 575$ Vdc (e.g. 230/400V_{rms} ac grid).

Fig. 2.43 contains the experimental results with an imbalance of power between two independent PV input strings (Fig. 2.25, mini-boost 1 and 2 with conduction diodes D_{p1}, D_{p2}). This case corresponds for the case with different orientation of PV modules (e.g. rooftops angle) fixed typical position, without the capability to track the sun throughout the day. The inverter-MPPT algorithm performs periodic voltage sweeps in order to determine the global maxima for optimal energy production. The mini-boost is able to increase the dc voltage to the operating point for improved PV inverter energy production, with reduced size and power rating components.
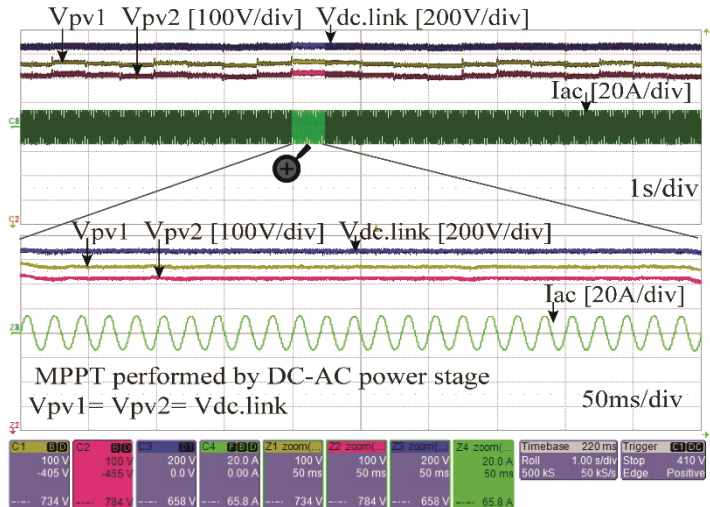
(a)
PV inverter operation: unbalanced PV loading.
DC: 2x MPPT, Pmp1=5kW, Pmp2=1.96kW
AC: 230V-50Hz, Pac=7.7kW
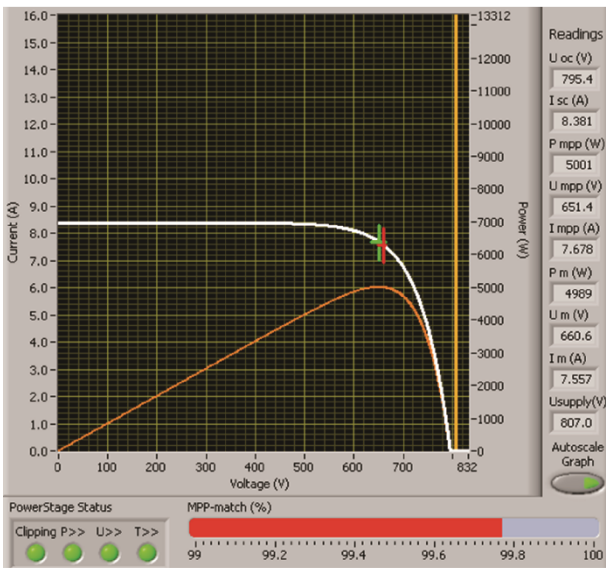
(b)
PV1:Vpv1=661V, Voc1=795V, Pmp1=5kW, Imp1=7.55A
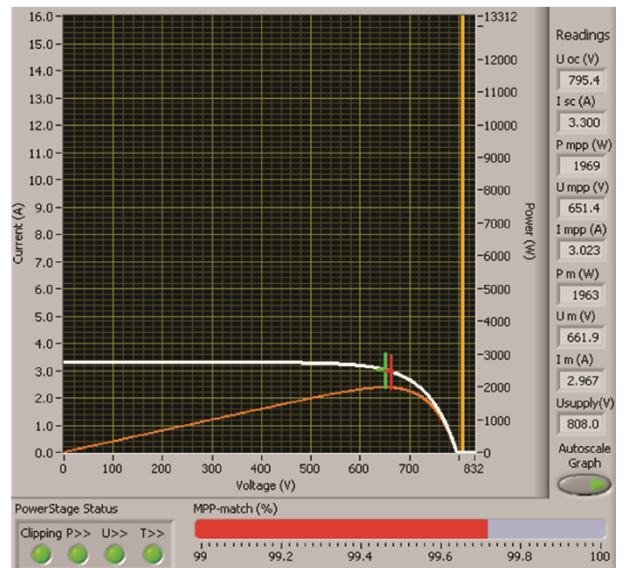
(c)
PV2:Vpv2=661V, Voc2=795V, Pmp2=1.96kW, Imp2=2.97A

Figure 2.43: Single-stage PV inverter operation (mini-boosts are switched automatically off)..
Inverter MPPT-control dynamics under imbalanced PV input strings loading: 5kW and 1.96kW,
grid connected 3-phase $230V_{LN}/400V_{LL}$-50Hz. PV1: I-V, P-V characteristics with Inverter-MPPT
algorithm efficiency of 99.7% (mini-boost=off with Dp1, Dp2=on, by-pass mode).

Fig. 2.44 shows the power conversion system's efficiency, where higher performance is
achieved when the boost stages are switched off, i.e. when using a by-pass switch and dc-ac
inverter, especially at higher modulation index (e.g. 620V, curve (1)) operation.
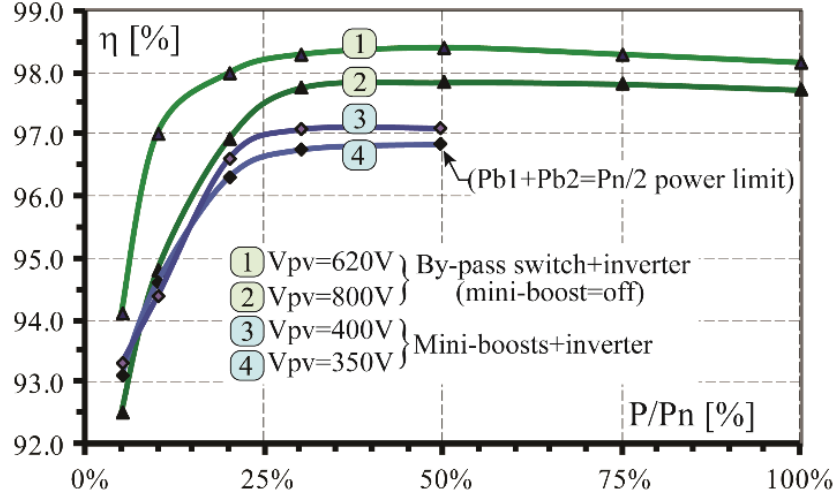
Figure 2.44. Power conversion efficiency measurements: (1), (2) are with by-pass switch and dc-ac inverter and (3), (4) are with two mini-boosts (each rated at $P_n/4$) and dc-ac inverter. Other auxiliary consumptions to the power system have been included: EMI filters, cooling fans, ac disconnect relays, signal conditioning.

Test conditions: unity power factor (PF=1), $230V_{LN}/400V_{LL}$, 50Hz, P_n=25kVA.

Table 2.8: System design parameters.

Description	Symbol	Value
Boost diode voltage drop ($I_f = 16A, T_j = 100°C$)	$V_f(D_{b1,2})$ (type: silicon carbide)	1.8 V ($P_{bp} = 2P_d = 57.6W$)
By-pass diode voltage drop ($I_f = 16A, T_j = 100°C$)	$V_f(D_{p1,2})$ (type: standard recovery)	0.825 V ($P_{bp} = 2P_d = 26.4W$)
By-pass switch resistance	$R_f(k_{p1,2})$ (type: relay)	10 mΩ ($P_{bp} = 2P_d = 5.12W$)
Rated power (PF=1)	P_n	25 kW
PV operating voltage	$V_{pv1} = V_{pv1} = V_{dc}$	800 V
PV Stray capacitance	$C_{pv} = \Sigma\, C_{pv.p,n}.$	2.5 µF
PV stray resistance	$R_{pv.equivalent}$	1 Ω
AC filter	C_f	10 µF
CM AC Neutral-point filter	C_z	4.7 µF
CM DC filter	$L_{cm.dc}$	2 mH
CM AC filter	$L_{cm.ac}$	1.5 mH
Differential ground filter	L_{gnd}	1 mH
Grid impedance	$Z_g = R_g + j\omega L_g$	[0.1+jω(0.1mH)] Ω
Maximum CM current (limits imposed by safety standards)	$I_{cm.max}$	300 mA_rms (detection time: 0.3 sec.)

Table 2.8 shows: the by-pass switch design comparison and the necessary design parameters for the CM current circulation reduction evaluation.

To present a practical and relevant example, when using a low voltage-drop diode $(D_{p1,2})$, the by-pass losses (P_{bp}) are 50% lower than the by-pass losses produced when the boost diode $(D_{b1,2})$ is used. Further improvement is obtained by using a low-cost relay $(k_{p1,2})$, which reduces the losses by 90%, as shown in Table 2.8. Evidently, the by-pass switch design has significant consequences for power dissipation (P_{bp}), which affects system cooling and efficiency.

The investigation of circulating CM current uses the design parameters from Table 2.8. The evaluation is considered at high dc operation voltage (e.g. 800V) where the leakage current attains maximum values (due to $dV_{Cpv}(t)/dt$ term from (19)).

Fig. 2.45 shows the inverter operating with (a) PD and (b) modified phase-disposition phase-shift (PD-PS) modulation strategies. In both modulation cases, the CM is measured under four identical test cases, as specified in Table 2.8. Prior to moment t_0, an ideal case is considered, without stray capacitance, where the CM current is zero, as per equation (21). At t_0, the stray capacitance C_{pv} is suddenly connected (Fig. 2.25) resulting in a leakage current of approximately 12% I_n (Fig. 2.45 (a)). The connection of the stray capacitance is also reflected in the inverter output current, as per equation (20). The modified PD-PS modulation provides a better performance, with a leakage current of 5% I_n. However, even this value is over the maximum continuous current limit (e.g. 300mA).

The test continues with the insertion (t_1) of EMC filter components, $L_{cm.dc}, L_{cm.ac}$, which dramatically reduces the CM current (e.g. 250% reduction). Under these conditions, the grid-connected PV system is standards-compliant only when using PD-PS modulation technique, as

can be seen in Fig. 2.45 (b) and Table 2.8. Using the standard PD modulation, the CM current is

still over the required limit, as shown in Fig. 2.45 (a) and Table 2.9.

Table 2.9: Parameters of the simulation evaluation.

Time interval	Improvement solution	Modulation strategy	I_{cm} [A_{rms}]	$I_{cm} < 300$ [mA_{rms}]
$t_0 - t_1$	None	PD	4.53	No
		PD-PS	1.78	No
$t_1 - t_2$	$L_{cm.dc} + L_{cm.ac}$	PD	0.357	No
		PD-PS	0.255	Yes
$t_2 - t_3$	C_z	PD	0.202	Yes
		PD-PS	0.158	Yes
$t_3 - t_4$	L_{gnd}	PD	0.186	Yes
		PD-PS	0.155	Yes

Further CM current improvement is achieved by connecting, at t_2, an impedance branch

(C_z) from the inverter output to the common neutral-point (z), as shown in Fig. 2.25. In this way,

a fraction (value dependent of C_z) of CM current circulates back to the source through this newly

inserted path. As a result, the leakage current is reduced and the PV system is compatible with

both modulation strategies. The last test occurs at t_3, where a ground inductor is enabled in the

CM current path for further leakage current attenuation.

The proposed PS-PD modulation leads to significant reduction (e.g. with 250%) in CM

RMS current than the traditional modulation scheme. The re-use of EMC components and the

capacitive network scheme provider additional system improvements in leakage current reduction

for hazards mitigation and safety compliance.

(a)

(b)
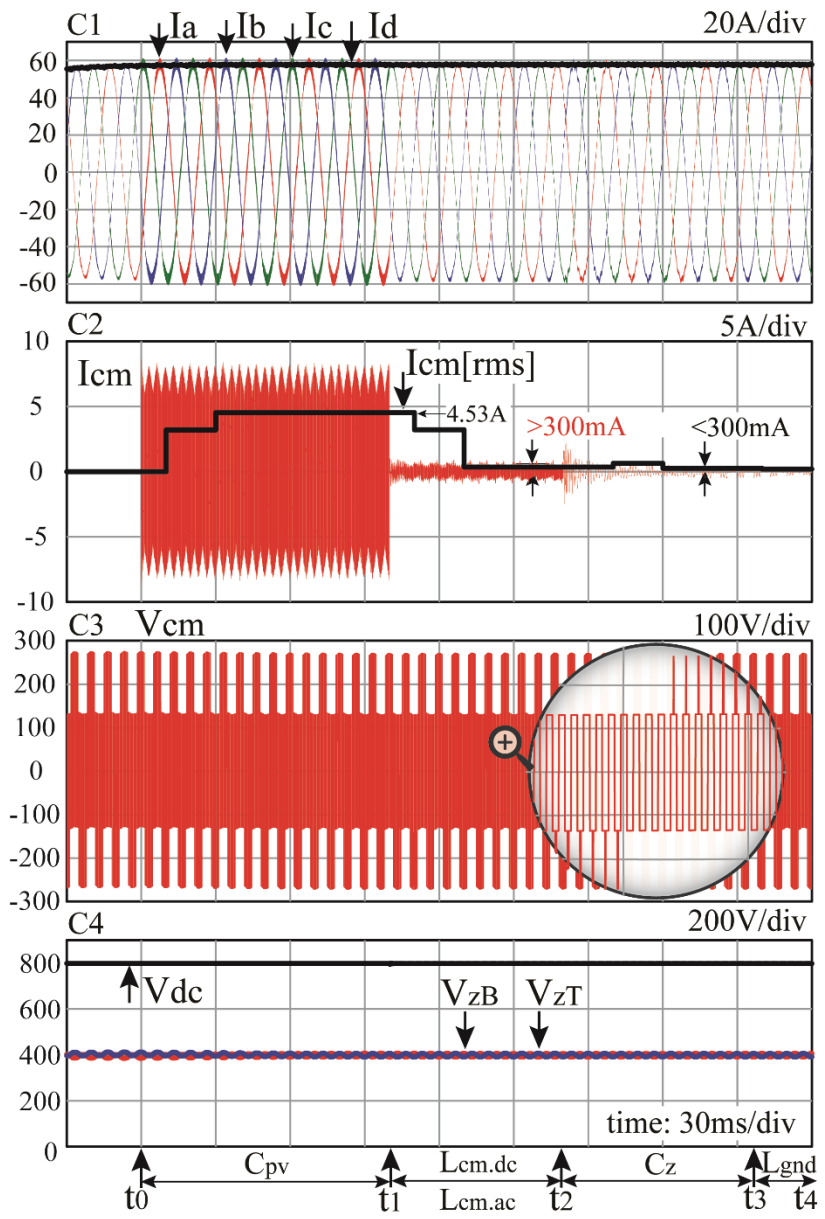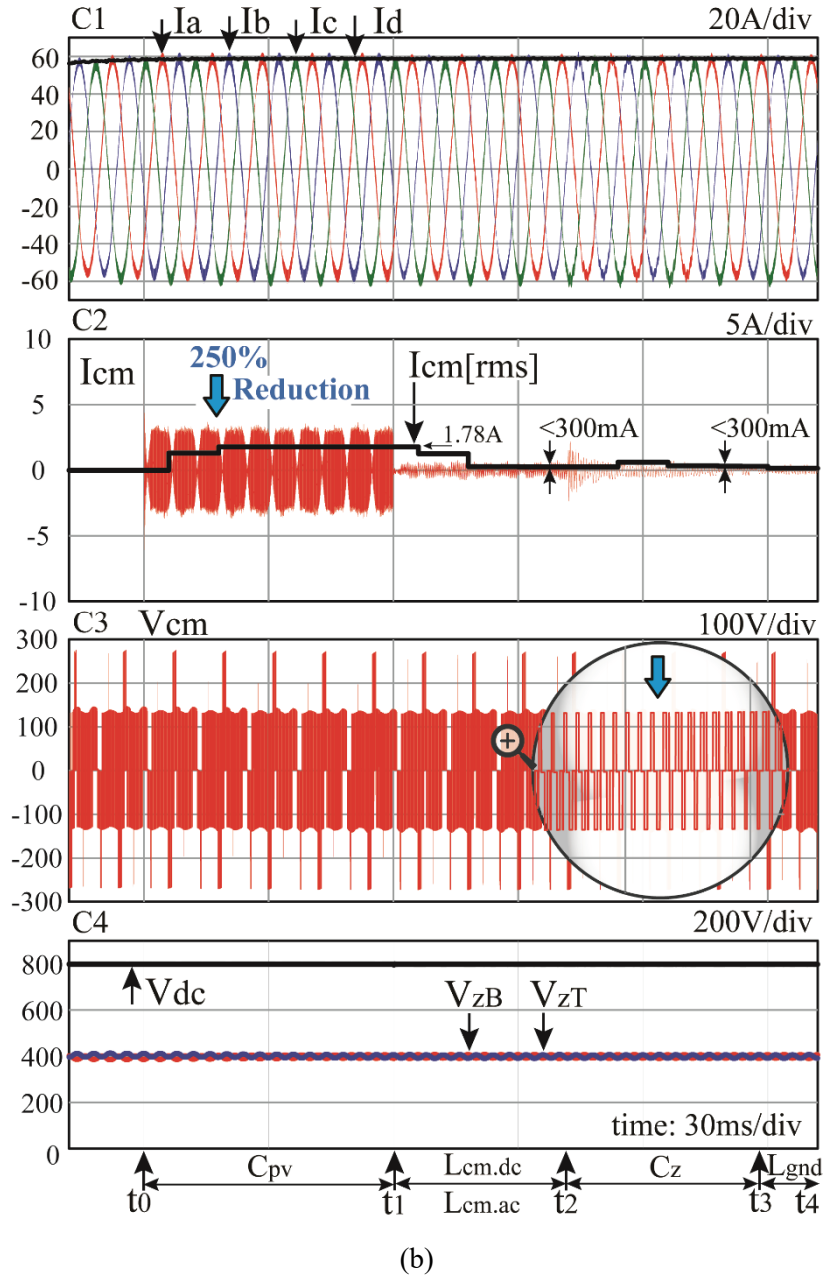
Figure 2.45: CM current reduction techniques: PD modulation (a) and modified PD-PS ($\varphi_A = 0, \varphi_B = \frac{\pi}{2}, \varphi_C = \pi$) strategies comparison.
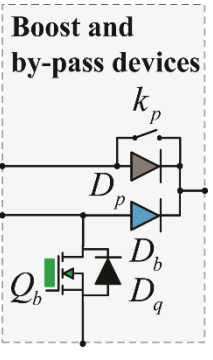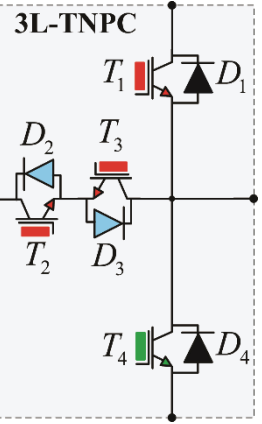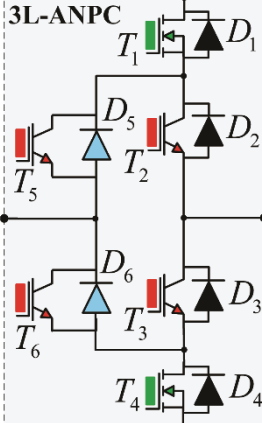
Y-axis: C1 - Inverter phase currents I_a, I_b, I_c and active current component I_d 20A/div. C2 - CM (leakage) circulating current, I_{cm} 5A/div. C3 - CM voltage waveform with respect to neutral-point (z) (equation (17), Fig. 2.25), V_{cm}, 200V/div.C4 - dc-link voltage V_{dc}, and bottom and top voltages with active neutral-point regulation control V_{zB}, V_{zT} 200V/div.

X-axis: 30ms/div.

Test conditions: $V_{pv1} = V_{pv2} = V_{dc} = 800V$ (by-pass mode), PF=1, $230V_{LN}/400V_{LL}$, 50Hz, $P_n = 25kVA$.

In this analysis, the typical ratings of power devices used in 1000V and 1500V PV systems are given in Table 2.10. The devices selection includes MOSFETs, IGBTs, WBG (silicon carbide, gallium nitride) and silicon fast recovery diodes for the desired cost-performance criteria.

Table 2.10: Voltage device ratings of power topologies used in the 1000V and 1500V PV systems analysis (current rating is dependent of the nominal power system design specification).

Power device	1000V PV system voltage ratings	1500V PV system voltage ratings	Topology for power conversion
Q_b	1200V	(*)	Devices: MOSFET; Switch; SiC Diode; Fast Recovery Diode; Standard Recovery Diode. **Boost and by-pass devices** — k_p, D_p, D_b, D_q, Q_b
D_q, D_b, D_p	1200V	(*)	
k_p	1200V	(*)	
Observations	k_p - low cost electromechanical relay or other low resistance devices.	(*): Not included for economics (low cost) reason.	
T_1, T_4	1200V	2200V (*)	**3L-TNPC** — Devices: IGBT; SiC Diode; Fast Recovery Diode. T_1, D_1, D_2, T_3, T_2, D_3, T_4, D_4
T_2, T_3	650V	1200V	
D_1, D_4	1200V	2200V (*)	
D_2, D_3	650V	1200V	
Observations		(*): 1700V can be only used as long the power devices provides sufficient voltage margin for terrestrial cosmic radiation.	
T_1, T_4	650V	1200V	**3L-ANPC** — Devices: MOSFET; IGBT; SiC Diode; Fast Recovery Diode. T_1, D_1, D_5, D_2, T_5, T_2, D_6, D_3, T_6, T_3, T_4, D_4
T_2, T_3	650V	1200V	
T_5, T_6	650V	1200V	
D_1, D_2, D_3, D_4	650V	1200V	
D_5, D_6	650V	1200V	
Observations	T_5, T_6 may not be used for cost reduction (3L-NPC)	T_5, T_6 can be used for providing flexibility in modulation strategies. (3L-ANPC)	

2.7. Summary

A graphical approach using I-V and P-V characteristics revealed remarkable insights into the PV-converter system interaction. This chapter analyzed and identified advantages of 1500V PV inverters (over 1000V) with a focus on the dc-bus extension range capabilities. The need for increasing both the lower and higher dc-bus limits was explained and based on fundamental motivations: 1) PV inverter operation at higher dc-bus voltage (i.e., 1500V) can save copper and switchgear costs; 2) Lower dc-bus limit extension allows energy capture under high PV temperatures (e.g., 70C) and low irradiation; 3) upper dc-bus extension allows for greater energy extraction under low temperatures (e.g., -20C) and high irradiation conditions.

The results demonstrated that 1500V systems have an MPPT dc range of +/-35%$V_{dc.n}$ (i.e. $V_{maxMPPT}:V_{minMPPT} = 2:1$), as compared to only +/-20%$V_{dc.n}$ (i.e. $V_{maxMPPT}:V_{minMPPT} = 1.7:1$) in 1000V inverters, providing a greater operational area to capture energy under wider temperature and irradiance ranges. As a result, with 30% wider MPPT dc voltage range is provided in 1500V systems, which represent a significant gain for grid power production maximization.

A novel VQ reactive injection strategy was proposed to further extend the lower dc-limit, showing further extensions in the range of 3% to 5%. This achievement is particularly important for operation under high temperature or low irradiance to maintain the inverter in MPPT operation with very low dc-bus voltage.

This chapter introduced a new modulation strategy, namely Quasi Space Vector (QSV) PWM to comply with 15% lower dc-bus extension while providing an accurate and robust Zero-Sequence employment for transients and paralleling inverter operation. The findings were validated with simulation and experimental results.

A new architecture for PV grid-tie inverters string-based mini-boost stage to increase the operating range of the inverter, as shown in Figs. 2.24-2.25, was introduced in this chapter. In essence, the mini-boost is a PV string boost converter equipped with an efficient by-pass switch element and an optimized boost design. The PV string boost concept is developed for design size optimization, of the typical PV modules used worldwide. The design optimization maximizes the utilization of the power components by using the proposed peak power envelope inverter operation and only engaging the mini-boost when necessary given the array conditions.

The proposed architecture kept the advantages of the current single-stage PV inverter (increased efficiency using a by-pass switch) when the PV voltage was high enough to avoid the use of the mini-boost and allowed the operation to continue when the PV array voltage dropped below the minimum voltage, likely due to partial shading phenomena. This proposed architecture is composed of one or more boost stages rated for a fraction of the nominal power of the PV inverter connected to each string of the PV array that could be bypassed if the PV string met the voltage requirements of the PV inverter by itself, avoiding the losses when the additional boosting is not needed and limiting the cost. Individual mini-boost stages could be used for multi-string PV arrays reducing the possibility of operation at local maxima and providing improved energy extraction capabilities. The extension of the mini-boost architecture has been discussed for a hybrid wind-solar energy generation solution.

Furthermore, a proposed inverter peak power envelope at boundary conversion operation provides design optimization for energy production maximization. Three methods of CM reduction for safety and standards-compliance were discussed. The PD-PS modulation strategy provides significant reduction (e.g. 250%) in leakage current circulation than the traditional modulation scheme.

The overall performance and the utilization of the PV array and converter capabilities were improved by the use of this topology and design methodology.

Simulation and experimental results using a three-phase 25-kVA inverter with dual string PV system and the same inverter with two mini-boost stages were presented showing the advantages for improved energy production, design guidelines and safety compliance of the proposed new topology approach.

Chapter 3. High Performance Islanding Detection Methodologies for PV Inverters under Grid Faults[3]

The previous chapter described novel techniques of dc voltage utilization extension, which lead to increased PV energy harvesting and design optimization for lower overall system cost. In addition to high performance system achievements, the grid-connected converters must comply to GCs and safety standards. Grid-connected converters require advanced controllers in order to achieve high performance and meet country specific anti-islanding standards, which is the focus of this chapter.

This chapter presents a novel, high performance Islanding Search Sequence (ISS) technique applied to four islanding detection (ID) methods. The salient aspects of the proposed determination technique reside in its fault tolerant safety redundancy with rapid unintentional ID integrated within: active-reactive power control, maximum power point tracking algorithm, and phase locked loop routine.

Section 3.1 presents the characteristics of the islanding elements and the parameters within which the AI schemes can be implemented. Section 3.2 describes the overall system architecture and the implementation of the control structures of the islanding search sequence methods within the DPG controls. Section 3.3 describes the experimental verification using a

---

[3] Part of this chapter has been published in [E. Serban, C. Pondiche, and M. Ordonez," Islanding Detection Search Sequence for Distributed Power Generators Under AC Grid Faults, *"IEEE Transactions in Power Electronics., vol. 30, no. 6, pp. 3106–3121, Jun. 2014.].

three-phase, multi-level, transformer-less converter developed for robust and rapid ID. The conclusions are provided in Section 3.4.

3.1. Control Methods for Islanding Detection

In this chapter, four ID methods are introduced, with an search sequence function, integrated within distributed power generation (DPG) converter at the following control levels: reactive power control (ISS-P), active power control (ISS-Q), integrated MPPT and ID control structure (ISS-MPPT), integrated PLL ID control structure (ISS-PLL). The main contributions in this chapter are:

- A novel, enhanced islanding search sequence (ISS) applied to P, Q, and PLL ID and the introduction of an integrated MPPT-ID method.

- The proposal of using a combination of two or more methods simultaneously with a safety redundancy feature to provide fault tolerant system compliance.

- Principles and practical design guidelines on the topic of search sequences for integrated control.

The advantages of the proposed ISS methods consist of its ability to integrate methods to support simplicity, robust controls for safety redundancy, fast and adaptive features for all operating DPG conditions and provide minimum impact on power quality.
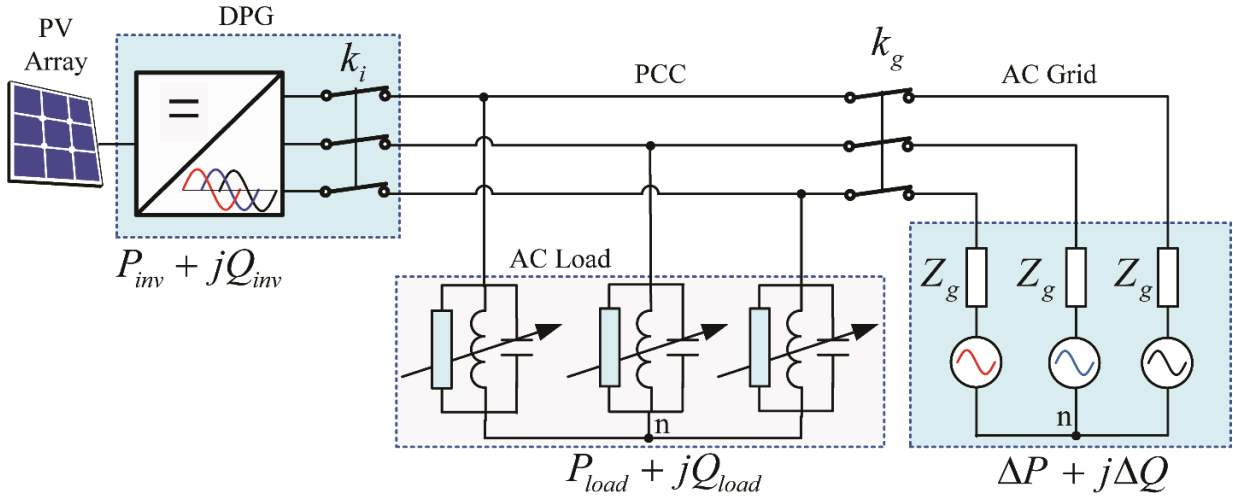
Figure 3.1: Generic anti-islanding test circuit for DPG under grid fault experiments.

Fig. 3.1 illustrates the simplified block diagram for DPG anti-islanding test evaluation. Based on Fig. 3.1, the background information and basic equations of islanding elements are reviewed and discussed, which will identify the parameters to implement the proposed islanding search sequence.
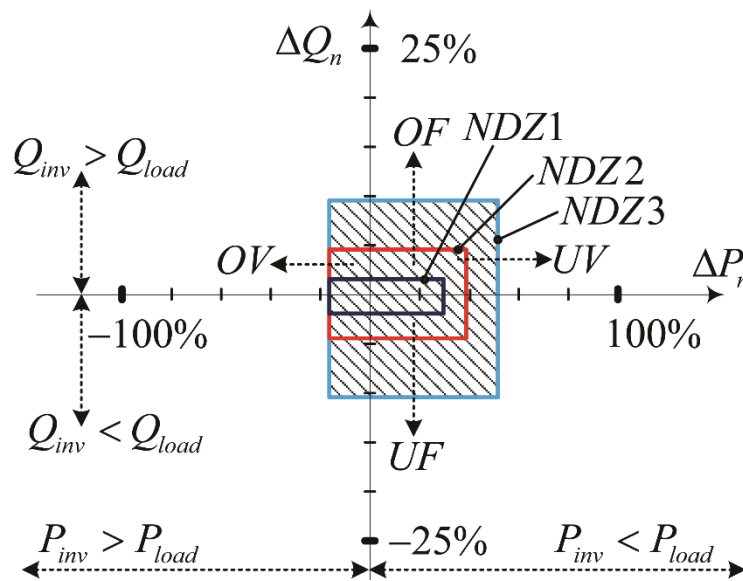
Figure 3.2: Non-detection zone definition is a function of the voltage and frequency standard specific limits: reactive with active power normalized variation.

Fig. 3.2 illustrates the normalized reactive versus active power variation employed in this chapter, indicating the non-detection zone (NDZ) for different under/over voltage/frequency and quality factors. The voltage at the point of common coupling (PCC) is represented by the grid voltage (V). In real conditions, there is a power exchange at the grid port, represented by power mismatch $\Delta P, \Delta Q$ between the inverter delivered power and ac load power:

$$
\begin{cases}
\Delta P = P_{inv} - P \\
\Delta Q = Q_{inv} - Q.
\end{cases}
\tag{3.1}
$$

In practical applications, the line impedances (e.g. grid impedance Z_g, Fig. 3.1) around PCC contribute to the power mismatch which during the ID evaluation can be compensated by the RLC load in order to achieve zero power exchange with the grid and capture the worst-case scenario time disconnect for DPG ID algorithm. The active and reactive power consumed by the ac load is represented by the elements of resistance (R), capacitance (C) and inductance (L), which can be modeled by the following expression:

$$
\begin{cases}
P = 3\dfrac{V^2}{R} \\[2mm]
Q = 3V^2(\dfrac{1}{\omega L} - \omega C).
\end{cases}
\tag{3.2}
$$

The DPG is represented by a converter which operates in inverter mode by exporting dc energy to the ac grid port. For ID test conditions, the values of reactive elements (L, C) are simply selected at the point where resonance (ω_0) is equal to grid frequency (ω). Another basic and important definition is the quality factor (Q_f) of the load at the resonance operation condition $(\omega_0 = \omega)$ of the L, C load elements:

$$\begin{cases} \omega_0 = \dfrac{1}{\sqrt{LC}} \\ Q_f = R\sqrt{\dfrac{C}{L}} = \dfrac{R}{\omega_0 L} = \omega_0 R C. \end{cases} \tag{3.3}$$

The reactive power is dependent on PCC frequency, active power and load characteristics. The voltage variation at PCC is proportional with active power delivered by the DPG and load resistance (R) value,

$$\begin{cases} Q = PR\left(\dfrac{1}{\omega L} - \omega C\right) \\ V = \sqrt{\dfrac{PR}{3}}. \end{cases} \tag{3.4}$$

After manipulation of (3.3) and (3.4) the angular frequency can be determined from the following quadratic equation:

$$\frac{1}{\omega_0^2}\omega^2 + \frac{Q}{\omega_0 Q_f P}\omega - 1 = 0. \tag{3.5}$$

The practical solution for the angular frequency derived from (3.5) reduces to:

$$\omega = \frac{\omega_0}{2}\left[\sqrt{\left(\frac{Q}{Q_f P}\right)^2 + 4} - \frac{Q}{Q_f P}\right]. \tag{3.6}$$

These parameters from relations (3.6), and later from (3.7), are considered for the experimental tests in order to tune the RLC load in order to evaluate the effectiveness of the proposed ID methods. During islanding tests, fine-tuning of RLC is required, since the passive elements are not ideal. As an example, the test inductance (L) is represented by an intrinsic built-in resistance, which should be compensated for during the anti-islanding tests.

The anti-islanding evaluation schemes can be represented by NDZ as a performance index. When the power differences between DPG and load represented in relation (3.4) are reduced, the PCC voltage and frequency undergo insufficient change to trigger a grid fault. The NDZ for under/over voltage and frequency (UV/OV and UF/OF) thresholds can be represented by the following relationships [136]:

$$\left(1 - \left(\frac{f_n}{f_{min}}\right)^2\right) Q_f \leq \frac{\Delta Q}{P_{inv}} \leq \left(1 - \left(\frac{f_n}{f_{max}}\right)^2\right) Q_f, \tag{3.7}$$

$$\left(\frac{V_n}{V_{max}}\right)^2 - 1 \leq \frac{\Delta P}{P_{inv}} \leq \left(\frac{V_n}{V_{min}}\right)^2 - 1, \tag{3.8}$$

where V_n, f_n represent nominal grid voltage and frequency (e.g. $230V_{LN}$-50Hz or $120V_{LN}/240V_{LL}$-60Hz).

The DPG system is evaluated as per the simplified diagram shown in Fig. 3.4. The *RLC* test load is tuned to the resonant frequency equal to line PCC frequency. The DPG power level is adjusted to equal the ac load demand while the power exchanged with the grid is minimized toward zero.

The normalized reactive versus active power variation is shown in Fig. 3.2, where the hatched areas represent the NDZ for different under/over voltage/frequency and quality factors. It should be noted from Fig. 3.2 that the larger area (e.g. NDZ3) has wider voltage/frequency limits for disconnection where the islanding disconnect time requirement is usually longer. The voltage and frequency operation limits and disconnect time requirements for the DPG are defined under country-specific standards.

From relation (3.4), the reactive power can be linearized by constructing a small-signal model with variance in converter power [69], and it can be approximated:

$$\Delta Q_{inv} = R(\frac{1}{\omega_0 L} - \omega_0 C)\Delta P_{inv} - P_{inv}R(\frac{1}{\omega_0^2 L} + C)\Delta\omega. \tag{3.9}$$

Based on relation (3.9), the PCC frequency variation can be expressed by:

$$\Delta\omega = \frac{(\frac{1}{\omega_0 L} - \omega_0 C)R\Delta P_{inv} - \Delta Q_{inv}}{P_{inv}R(\frac{1}{\omega_0^2 L} + C)}. \tag{3.10}$$

From the expression (3.10) and from similar observations [67], it can be noted that the measured PCC angular frequency variation relates directly to reactive power.

The general representation of the measured inverter active and reactive power for the three-phase balanced system on a synchronously rotating reference frame is expressed by the expression (3.11). The convention is selected such as that the grid phase voltage magnitude component V_d is aligned along d-axis and V_q voltage component is aligned along q-axis.

$$\begin{cases} P_{inv} = \frac{3}{2}(V_d i_d + V_q i_q) \\ Q_{inv} = \frac{3}{2}(V_q i_d - V_d i_q). \end{cases} \tag{3.11}$$

From the expression (3.11), it can be seen that the reactive power can vary based on the following variables:

- The reactive power relates directly to the quadrature-axis voltage component. The quadrature-axis voltage component is controlled for PLL frequency detection and generation; therefore, the AI can be implemented at the PLL level.

- Assuming the AI is not implemented within the PLL control, then the reference quadrature-axis voltage component is controlled to a constant value (e.g. $V_q^* = 0$) by the

PLL and the expression (3.11) can be simplified to the following small-signal approximation:

$$\Delta Q_{inv} = -\frac{3}{2} V_d \Delta i_q. \tag{3.12}$$

Relation (3.12) illustrates that the reactive power relates directly to quadrature-axis current component and opposite sign variation, with similar reports in the literature [67], [69], [71]. Since the DPG has direct control of quadrature-axis current, the ID can be based on this component. By employing the fundamental equations described in (3.4) – (3.12), the detection principles that will be employed by the proposed ISS are summarized as follows.

3.1.1. Islanding Detection Based on Reactive and Active Power Control Variation

Considering a worst-case islanding scenario, it can be assumed that the following parameters are constant: the DG active power and load resistance. From relation (3.7), the frequency variation can be approximated with:

$$\begin{cases} \Delta\omega = \dfrac{3}{2} \dfrac{V_d \Delta i_q}{P_{inv} R(\dfrac{1}{\omega^2 L} + C)} \\ \Delta\omega = \omega - \omega_n. \end{cases} \tag{3.13}$$

From relation (3.13) it can be observed that the PCC angular frequency has the same variation sign and direct relationship with reactive current component. The phase-locked loop detects the PCC frequency and continuously monitors the frequency deviation from the nominal frequency ($\omega_n = 2\pi f_n$).

From relation (3.4), the active power can be linearized and approximated to:

$$\begin{cases} \Delta V = \dfrac{1}{2\sqrt{3}} \sqrt{\dfrac{R}{P_{inv}}} \Delta P_{inv} \\ \Delta V = V - V_n. \end{cases} \tag{3.14}$$

As it can be observed from relation (3.14) and similar observations [63], [67], [69], the PCC voltage variation is proportional with DPG active power. Since the DPG has direct control of direct-axis current, ID can be based on active power variation.

3.1.2. Integrated Control of Islanding Detection and Renewable Energy Harvesting Algorithm

The following proposed control method enables the unification of ID and MPPT. Compared with systems that use separate controls, this control unification facilitates more predictable system behavior and increases simplicity by reducing firmware controls modules.

An example of the integrated control of ID with a renewable energy harvesting algorithm is realized with a periodic (proportional with grid fundamental line cycle T_L) function, implemented at the level of reactive power variation (ISS-Q) and maximum power point tracking (ISS-MPPT). The ISS-Q control is updated faster than the ISS-MPPT update routine for system stability reasons. The ISS-Q method's target is ID, while the mission of the ISS-MPPT is to achieve islanding safety redundancy and maximum energy harvesting algorithm. The ISS-Q is implemented with an adaptive behavior function for minimum overall system perturbance, and the redundancy within the ID can be combined as following:

$$ID = \begin{cases} ISS - MPPT, & V_{\min} < V < V_{\max}, & UV\,/\,OV \\ ISS - Q, & f_{\min} < f < f_{\max}, & UF\,/\,OF. \end{cases} \tag{3.15}$$
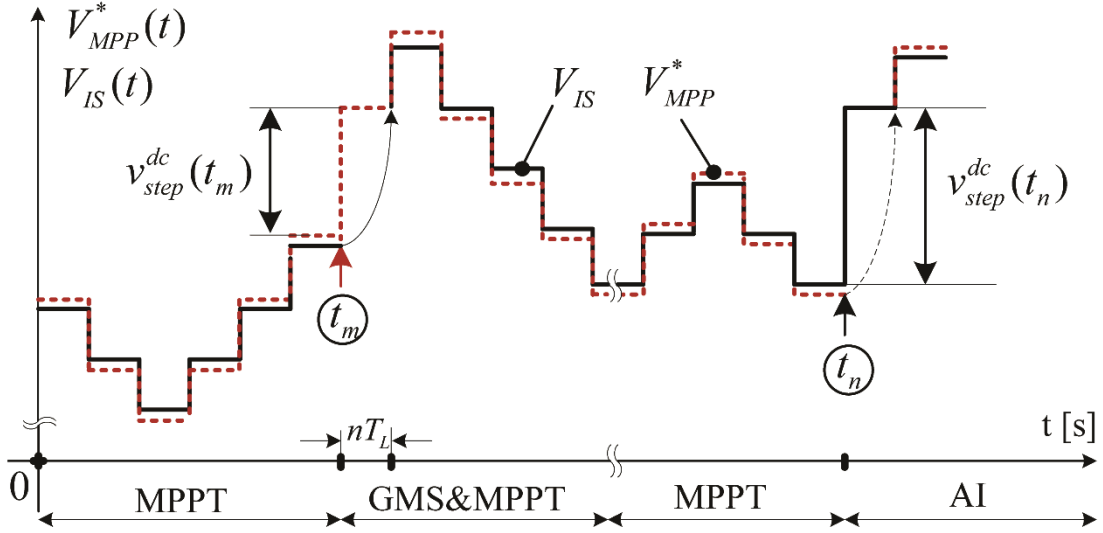
Figure 3.3: ISS-MPPT integrated controls for global maxima scanning and islanding detection.

Fig.3.3 illustrates the example of the ISS-MPPT flow-function: the input dc voltage reference V_{MPP}^* is controlled by the MPPT algorithm, which is continuously compared with the ID value function V_{IS}. The ID V_{IS} value is determined from the deviation of the ac grid voltage from its nominal level amplified on the search sequence function of active power variation.

The MPPT routine is updated at the rate nT_L ($n > 0$), where the step size satisfies the relation $V_{MPP}^* > V_{IS}$ and where the MPPT leads the ISS direction. At the moment t_m, the algorithm performs a global maxima scan (GMS) [137], [138] by changing the step size v_{step}^{dc} in order to determine any PV module shading condition, as illustrated in Fig. 3.4.

During the voltage sweep, the active power injected into PCC is changed and the algorithm naturally resets and establishes the global maxima. The second benefit of the voltage sweep feature is that, it reduces the probability that the anti-islanding effect between paralleled connected renewable DPGs will be cancelled.
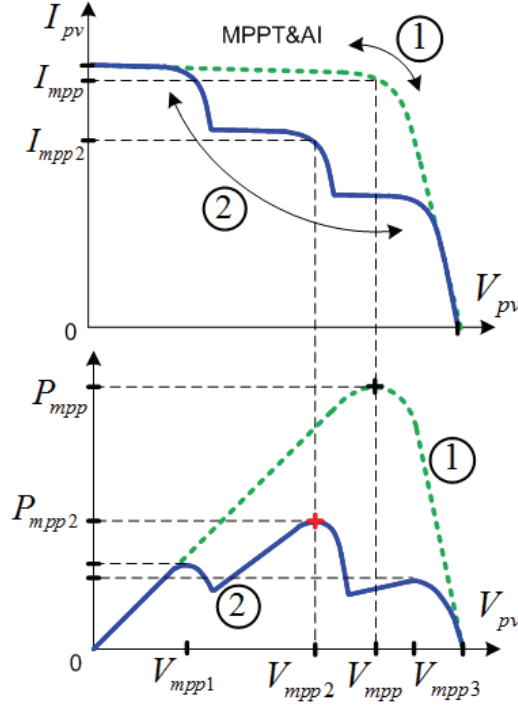
Figure 3.4: Example of a PV module I-V and P-V characteristics: case 1) uniform solar irradiance and case 2) partially shaded conditions.

Fig. 3.4 illustrates the I-V and I-P characteristics for a PV module in an ideal scenario (case1) and in a partially shaded situation (case2) where the PV inverter may not detect the global maxima, and may land instead on a local MPP (Fig. 3.4 - V_{mpp1}, V_{mpp3}). At the moment t_n (Fig. 3.3), the ID algorithm takes the control lead due to the detection of ac grid voltage variation. In this case, the ISS direction and step size v_{step}^{dc} updates the new value for PV loop voltage reference V_{MPP}^*. Therefore, the integrated control function takes the maximum deviation between the MPP V_{MPP}^* and islanding detection V_{IS} signals:

$$v_{step}^{dc} = \max\left(\frac{d}{dt}(V_{MPP}^*, V_{IS}) \right). \tag{3.16}$$

The implementation of ID at the MPPT level may represent an advantage for dc coupled (dc grids) systems where the active anti-islanding can be implemented at the dc-dc converter level. An additional cross-coupling signal is suggested between the controlled reactive current

and PCC voltage. While the PCC ac voltage varies, a proportional dc component is added to the search sequence function in order to increase redundancy ID, specifically for multiple DPGs connected in parallel. With a high penetration DPGs in the PCC network, the NDZ may increase due to the potential statistical cancelling effect of ID. The NDZ can be reduced through the following logic: during an islanding event, while the AI effect is considered to be cancelled between DPGs, a random GMS voltage sweep causes a reduction in active power. As a result, ac voltage droops and the ac variation signal updates both ISS-Q and ISS-MPPT. The ISS-Q has a faster response and is designed with an adaptive disturbance. The reactive current component is pushed in the opposite direction to the voltage support, e.g. in a case where the voltage droops, the injected reactive current lags the PCC network (under-excited inverter operation). During the implementation of any islanding method, the system stability has to be maintained during normal operation under grid disturbances (e.g. grid harmonics, high grid impedance) where the current regulators, PLL and AI controls play an important role. The ISS is designed with an adaptive step-size perturbation for increased margin system stability.

Renewable DPGs with separate AI and MPPT controls (traditional method) have inherently higher perturbation than the proposed method. Traditional methods have perturbation for AI and MPPT, while the proposed method combines both methods, thus reducing the overall system perturbation.

Table 3.1 illustrates a comparison between the traditional AI and the proposed ID with search sequence methods. As can be seen from the analysis and discussion, the integrated control of ID and renewable harvesting algorithms provide the advantages of adaptive controls, safety redundancy for a fault tolerant system and simplicity derived from the unification of control.

Table 3.1: Comparison between traditional AI and proposed method.

Criterion	Traditional AI method	Proposed AI method
Integrated controls (e.g. with MPPT)	No	Yes
Fault tolerant controls for safety redundancy	No	Yes
DC coupled systems	No	Yes
Adaptive AI	No	Yes
Perturbation to the system	Yes	Improved
AI cancellation effect under multiple DPGs paralleled connected	Possible	Improved
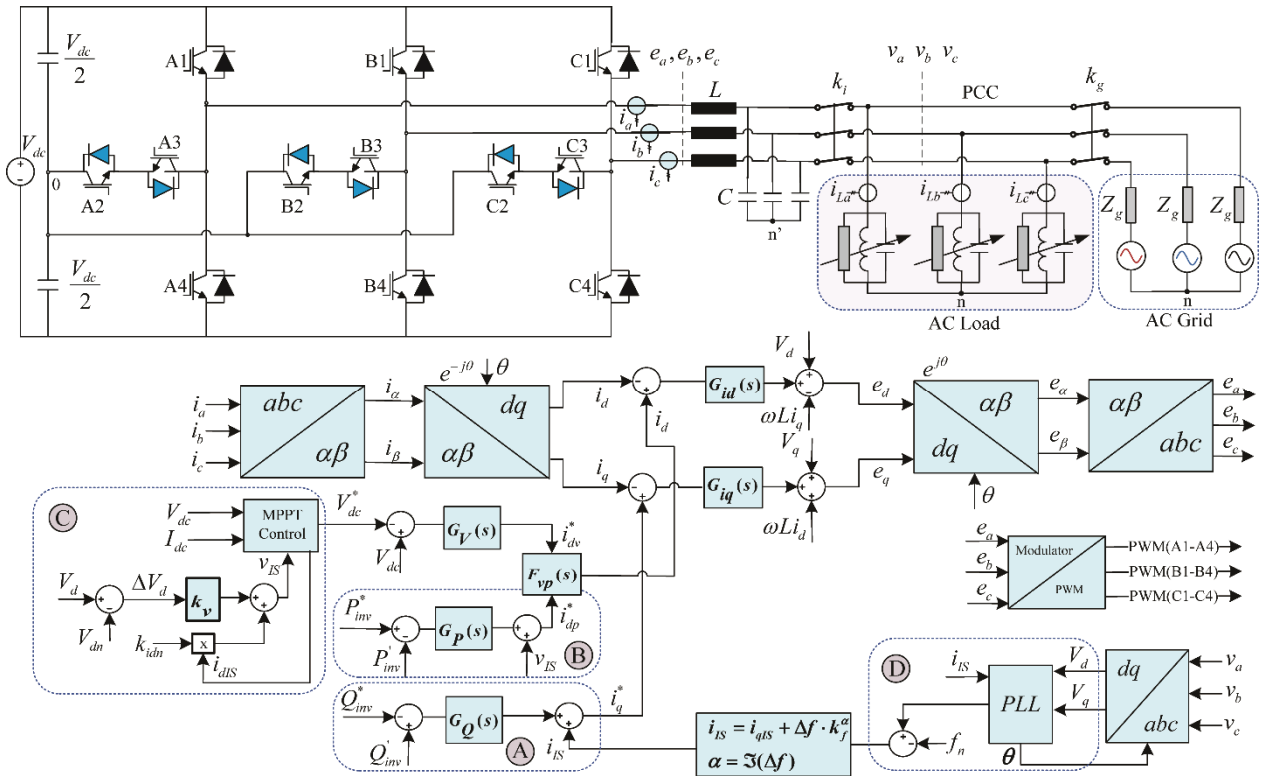
Figure 3.5: PV inverter with frequency detection function control block diagram. Four implementation options are indicated: A) reactive power controller, B) active power controller, C) the MPPT controller, and D) PLL controller.

3.2. Proposed Detection Methods: Islanding Search Sequence

The intended application for the DPG illustrated in Fig. 3.5 is for harvesting the renewable energy from dc and transferring it to ac three-phase utility grid port.
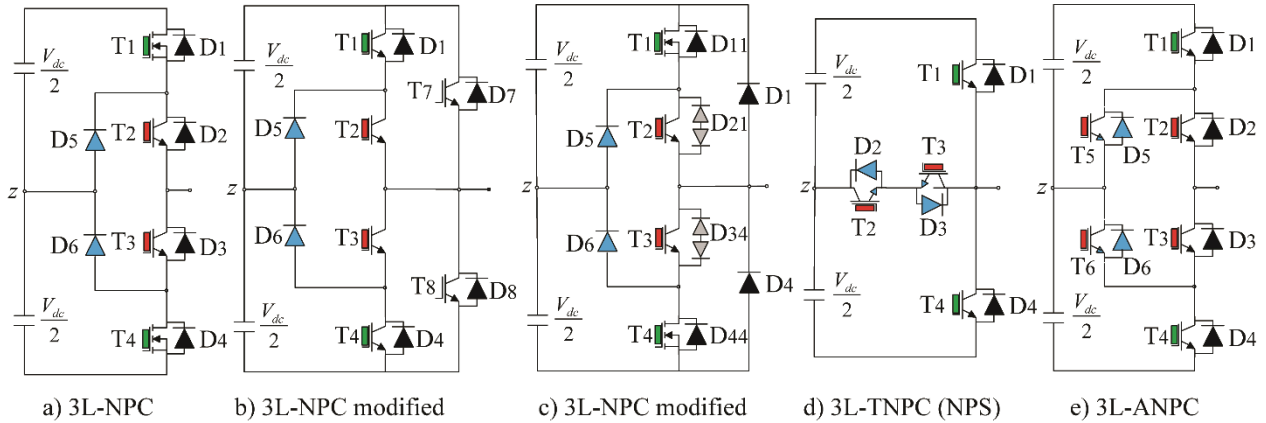
Figure 3.6: Three-level NPC-type topologies examples: (a), (b), (c) NPC, (d) TNPC (TNPC, BSNPC) and (e) ANPC.

In Fig. 3.6 the three-level topologies with different structure combinations is shown. The standard NPC topology is illustrated in Fig. 3.6 (a) where all the power devices can be rated at lower than the dc bus (V_{dc}), due to two series devices combination during the off-state, each device blocks only half of the dc bus. The structure configuration presented in Fig. 3.6 (b) improves conduction losses (T1/T4, T2/T3) from Fig. 3.6 (a), (b) where a single element (A7, A8) conducts the current during power transfer. The higher component count and component voltage rating (full dc bus) of A7/D7, A8/D8 devices represent a disadvantage. Fig. 3.6 (c) illustrates a derivation topology derived from the standard NPC structure. In the rectifier mode of operation, the two series diodes (D11/D44, D21/D34) are replaced by D1/D4 for lower conduction losses, but the diodes have to be rated for full dc bus. A similar advantage for improved conduction loss can be achieved with Fig. 3.6 (d) TNPC structure and with an additional advantage of requiring less count power semiconductors.

The high/low side devices (T1/D1, T4/D4) have to be full dc bus rated. The active NPC structure is illustrated in Fig. 3.6 (e) where the extra active switch devices (T5, T6) provide higher degree of freedom in modulation selection. The lower switching and conduction power loss is achieved with selection of wide bandgap (WBG) devices for the operation at higher switching frequency (e.g. >20kHz, depending of the power level): silicon carbide (e.g. SiC-MOSFET), gallium nitride (GaN), silicon carbide Shottky barrier diodes (SiC-SBD). The immediate benefit resides in reduction in system size and overall cost optimization.

The selected power conversion topology is T-type NPC (TNPC) three-level topology (Fig. 3.6 (d)) derived from neutral-point clamped (NPC). In the literature, it can be found under different descriptions: NPC2, neutral-point shorted (NPS) T-type NPC, bidirectional switch NPC, and it has several advantages over the classical structure:

- lower conduction losses due to single element in conduction during the power transfer
- lower voltage overshoots and switching losses due to the short/long commutation elimination problem [139] of the structure symmetry
- reduction of the gate drives power supply numbers, since the inner power semiconductors (e.g. A2, A3, Fig. 3.6) can be driven by the same supply voltage

The multi-level converters can be designed for size reduction using coupled-inductors, while the ripple current is reduced [140], [141]. The pulse-width modulation control is implemented with space vector voltage oriented control and integrated controls in synchronous reference frame (SRF) with zero phase and magnitude error controller design [109], [142].
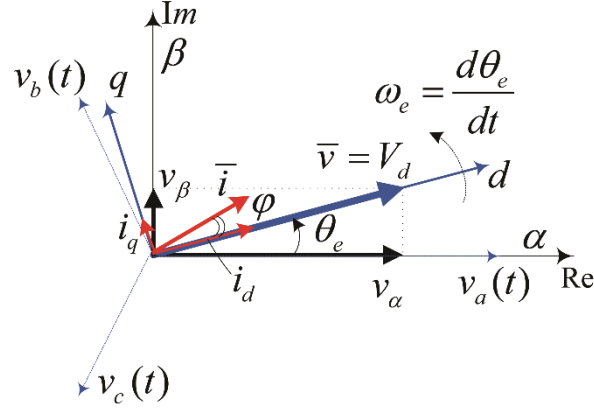
Figure 3.7: Graphical representation of the vector transformation: abc natural coordinates, stationary $\alpha\beta$ and rotating dq reference frame.

Fig. 3.7 illustrates the vector transformation diagram of grid phase voltages $v_a(t), v_b(t), v_c(t)$ to SRF voltages V_d, V_q and the current vector $\bar{\imath}$ with its dq components i_d, i_q, which are synchronously rotating with the angular grid frequency ω. The grid phase voltage magnitude ($V_d = V\sqrt{2}$) is aligned along d-axis with a phase shift φ from the current vector. The transformation of the three-phase system into the synchronous reference frame of grid voltage (V_d, V_q) and the inverter average voltages (e_d, e_q) relationship are given by:

$$\begin{cases} V_d = -L\dfrac{di_d}{dt} + \omega L i_q + e_d \\[2mm] 0 = -L\dfrac{di_q}{dt} - \omega L i_d + e_q. \end{cases} \tag{3.17}$$

The DPG converter is designed in a multi-loop structure control fashion. The dc input voltage regulation is controlled by the MPPT algorithm (with dc voltage reference $V_{dc}^*(V_{MPP}^*, V_{IS})$) where the voltage G_V and active power G_P controllers command the active current reference i_d^*, with the alignment on d-axis as per convention illustrated in Fig. 3.7. The grid-interactive converter active power regulation is achieved by the active current controller G_{id} with feedforward grid voltage d-axis component V_d and decoupling from d-axis with the cross-coupling term $\omega L i_q$. The grid-interactive converter reactive power regulation is achieved by the

reactive current controller G_{iq} with feedforward grid voltage q-axis component V_q and decoupling

from q-axis with the cross-coupling factor $\omega L i_d$; the equivalent inverter average voltages are

expressed as:

$$
\begin{cases}
e_d = V_d - \omega L i_q + (i_d^* - i_d)G_{id} \\
e_q = V_q + \omega L i_d + (i_q^* - i_q)G_{iq}.
\end{cases}
\tag{3.18}
$$

The converter three-phase currents from natural abc coordinates i_a, i_b, i_c are transformed to

stationary $\alpha\beta$-frame, i_α, i_β, which are then converted to synchronously rotating reference dq-

frame i_d, i_q as shown in Fig. 3.7. The power factor angle ϕ can be programmed by the converter

control in order to perform further grid support features.

The inverter operates as a current-controlled voltage source inverter where the search

sequence function is introduced within i_d and i_q current components, through the PCC voltage

SRF. Combining equations (3.17) and (3.18) to eliminate cross-coupling terms, the equation is

simplified to the following inverter dynamic current expression:

$$
\begin{cases}
L \dfrac{di_d}{dt} + (i_d - i_d^*)G_{id} = 0 \\
L \dfrac{di_q}{dt} + (i_q - i_q^*)G_{iq} = 0.
\end{cases}
\tag{3.19}
$$

From relation (3.19), it can be observed that the ISS can be controlled independently on d and q

axis through i_d^*, i_q^*.

As discussed in this chapter, the ISS can be implemented at different converter control

levels, as illustrated in Fig. 3.5. The options include implementation at the A) reactive power

controller, B) active power controller, C) the MPPT controller, and D) PLL controller. In

particular, implementation of this novel ISS within the MPPT controller present a new

mechanism for AI detection.

The ISS practical implementation and DPG response represents a disturbance factor within the ac grid network in order to determine an islanding condition. Therefore, the ISS has to be implemented with minimum system disturbance, negligible power factor displacement and current THD distortion under normal power conversion grid conditions.

The proposed islanding search sequence ISS is a periodic function with the following adaptive controlled parameters: angular frequency ω_{IS} and step amplitude y_S. Two examples of ISS periodic functions are:

The quasi-square single step waveform can be approximated with the following Fourier expression:

$$y_1(t) = \sum_{k=0}^{n} \left\{ \frac{4(2y_s)}{(2k+1)\pi} \left[\cos\left((2k+1)\frac{3\pi}{4} \right) \right] \cdot \sin\left(2k+1 \right)\omega_{IS}t \right\}. \tag{3.20}$$

Similar to the relation (3.20), the quasi-square two-step waveform can be expressed as:

$$y_2(t) = \sum_{k=0}^{n} \left\{ \frac{4y_s}{(2k+1)\pi} \left[\cos\left((2k+1)\frac{\pi}{8} \right) + \cos\left((2k+1)\frac{3\pi}{8} \right) \right] \cdot \sin\left(2k+1 \right)\omega_{IS}t \right\}. \tag{3.21}$$
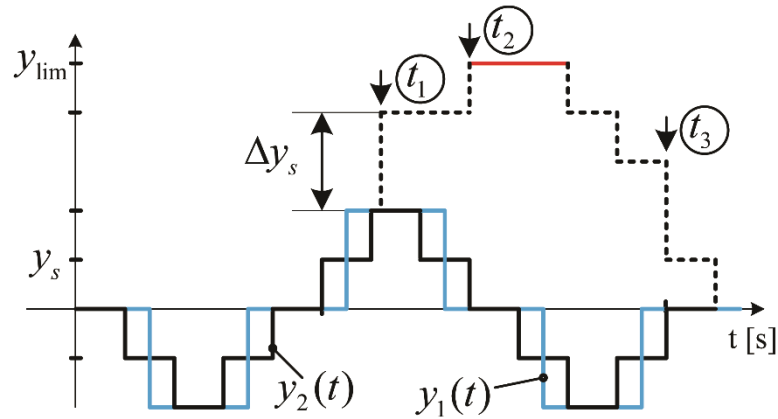
Figure 3.8: Example of active islanding search sequence with quasi-square based waveforms.

The quasi-square waveforms are represented in Fig. 3.8 and selected for the ID search method for the unintentional islanding conditions. For practical applications, the harmonics number can be selected up to $n = 40$.

Fig. 3.8 illustrates two periodic functions ($y_1(t)$ and $y_2(t)$) with adaptive features: at the moments shown, t_1, t_2, t_3, the ISS develops an adaptive step-size amplitude ($y_S \rightarrow \Delta y_S$), frequency ($\omega_{IS}$) and direction. The ISS rapidness and robustness for ID is achieved through:

▪ adaptive parameters: search sequence step-size amplitude, frequency and direction. While the ISS has a constant PCC perturbance, with line frequency or voltage variation detection the adaptive parameters are enhanced for AI. It is suggested that the search sequence parameters are selected, by design, adaptive to the normalized injected active power.

▪ implement the ISS at two or more control levels (A, B, C, D) as shown in Fig. 3.5.

The ac grid is subject to various disturbances (voltage dips, OV/UV/OF/UF, harmonic distortions, grid impedance) and the anti-islanding method has to be less sensitive to these numerous disturbances. The active ISS behavior within DPG may result in disturbances which might alter the overall system stability with consequences of unnecessary false anti-islanding trips or intermittent loss of renewable power production.
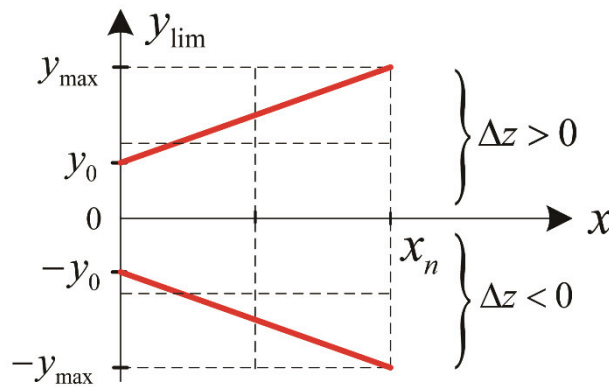
Figure 3.9: Islanding search sequence with adaptive disturbance limit.

In order to mitigate the overall effect on the system's stability, the ISS maximum disturbance function is limited. This limitation of disturbance is designed to have an adaptive behavior, as illustrated in Fig. 3.9, with minimum (y_0) and maximum (y_{max}) disturbance limits $[y_{lim}^-, y_{lim}^+]$, described by:

$$y_{\lim} = \begin{cases} y_{\lim}^+(x) = y_0 + (y_{\max} - y_0)\dfrac{x}{x_n} \ for \quad \Delta z > 0 \\ y_{\lim}^-(x) = -y_{\lim}^+(x) \qquad\qquad for \quad \Delta z < 0. \end{cases} \tag{3.22}$$

where the function limit y is introduced in ISS control for example as reactive current component (q-axis) or active current component (d-axis); the variable x represents the normalized active power and z represents the frequency or ac grid voltage magnitude limits related to the non-detection zone. Therefore, the proposed ID search methods have adaptive step-size (Δy_S) and limits (y_{lim}) for the controlled variables in order to contain the perturbations under dynamic system transients or false triggers.

By employing the search sequence function and the adaptive disturbance limits, the following proposed techniques can be enabled individually or integrated together:

A) ISS introduced on the q-axis reactive current component

B) ISS introduced on the d-axis active current component

C) ISS integrated within the MPPT controls

D) ISS integrated within the PLL controls

In order to provide enhanced ISS safety features, a combination of two or more techniques (A, B, C and D) shall provide AI system redundancy.

3.2.1. ISS Introduced on the Reactive Current Component (ISS-Q)

The first proposed AI method is based on the ISS implemented at the inverter control reactive current component level (Fig. 3.10) for Δi_q variation in order to determine the line frequency deviation as per relation (3.12).
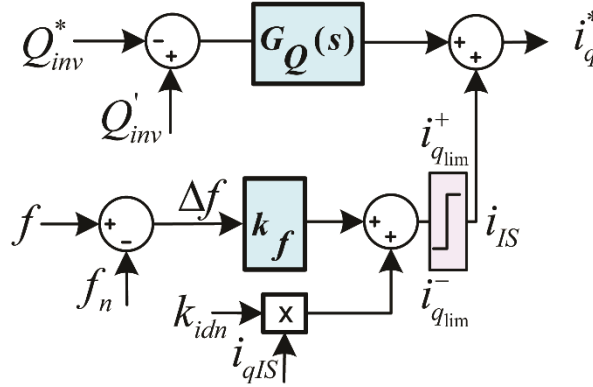
Figure 3.10: Method A: ISS with reactive power control.

The inverter reference reactive current component can be expressed as a function of the islanding search sequence:

$$i_q^*(s) = -Q_{inv}^*(s) + k_f \Delta f(s) + k_{idn} i_{qIS}(s). \tag{3.23}$$

It can be observed from relation (3.23) that the inverter can operate with a power factor different than unity if $Q_{inv}^* \neq 0$, where $Q_{inv}^*(s), k_f, i_{qIS}(s)$ represent the reactive power reference (usually configured for DPG grid support requirements), line frequency amplification factor and islanding search sequence.

The rapidness of the ISS is achieved with the line frequency amplification factor (k_f) introduced for an increased step-size amplitude action and faster ID, which has an exponential expression with grid frequency variation Δf (e.g. $k_f = e^{|\Delta f|}$).

In order to minimize the disturbance factor during normal conditions (i.e. without grid faults), the ISS perturbation is proportional to the momentary level of power operation. As such, the ISS

disturbance magnitude is directly influenced by the normalized active power: that is, by d-axis current component with the following normalized adaptive step-size parameter:

$$k_{idn} = i_d / i_{dn}.$$

(3.24)

The reactive power reference generated by the DPG is considered as per the following convention:

$$\begin{cases} Q^*_{inv} = Q^*_{cap} < 0 & i^*_q > 0 \\ Q^*_{inv} = Q^*_{ind} > 0 & i^*_q < 0. \end{cases}$$

(3.25)

As shown in Fig. 3.10, the reactive power controller $G_Q(s)$ compensates the reactive power error between the reference Q^*_{inv} and measured Q_{inv} value while the introduced reactive disturbance Q_{IS} is removed. The grid frequency error variation Δf is tracked from its nominal value f_n, multiplied with the amplification factor k_f and this quantity is added to the normalized ISS step-size amplitude. The nominal frequency f_n is tracked from the line frequency f through a low pass filter $f_n(s) = f(s) \cdot \omega_{fF}/(s + \omega_{fF})$. For system stability considerations, the search sequence function is limited to $\left[i^-_{qlim}, i^+_{qlim} \right]$ as previously explained in relation (3.22). This resultant value i_{IS} is summed further to the output of the reactive power controller to determine the reactive current reference i^*_q. The initial search sequence function introduced is described by the following relation:

$$i_{qIS}(t) = \sum_{k=0}^{n} \left\{ \frac{4I_s}{(2k+1)\pi} \cos\left((2k+1)\frac{\pi}{8} \right) + \cos\left((2k+1)\frac{3\pi}{8} \right) \cdot \sin\left(2k+1 \right)\omega_{IS}t \right\}.$$

(3.26)

where I_S represents the perturbance step amplitude introduced in the reactive current component. In the relation (3.23), it can be observed that the ISS does not affect the commanded reactive power due to the introduction of the cancellation term $Q_{IS} = (3/2)(V_d \cdot i_{qIS})$ as following:

$$Q'_{inv} = Q_{inv} - \frac{3}{2} V_d i_{qIS}. \tag{3.27}$$

The proposed ISS had the advantage of introducing an adaptive disturbance (k_{idn}) with minimum impact under normal grid operation, and the reactive power can be programmed independently of the ID method. Hence, from relation (3.22), the parameter controls are replaced with the following variables:

$$\{y \leftarrow i_q, x \leftarrow P_{inv}, z \leftarrow f\}. \tag{3.28}$$

In conclusion, in the case of islanding, the PCC frequency can be proportionally (α_f) changed by the inverter through the search sequence function $\Delta f = \alpha_f \cdot i_{qIS}$ - which is adapted from expression (3.13). The algorithm uses the positive feedback of the frequency variation; when it is sensed that the frequency has a tendency to increase/decrease, the control structure will command that the reactive component be further increased/decreased.
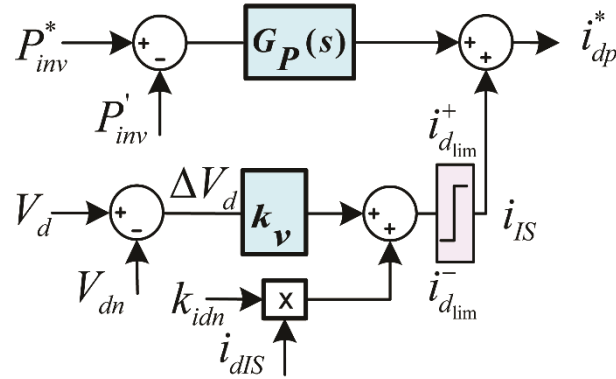
Figure 3.11: Method B: ISS with active power control.

3.2.2.　ISS Introduced on the Active Current Component (ISS-P)

The second proposed AI method uses ISS implementation at the inverter control active current component (Fig. 3.11) in order to determine the PCC voltage variations, (equation $\Delta V_d = V_d - V_{dn}$, as per relation (3.14)), for detecting a case of unsafe islanding.

The inverter reference active current component can be expressed as a function of the ISS:

$$i_{dp}^*(s) = P_{inv}^*(s) + k_v \Delta V_d(s) + k_{idn} i_{dIS}(s). \tag{3.29}$$

where $P_{inv}^*(s), k_v, i_{dIS}(s)$ represent the commanded active power, line voltage amplification factor and islanding search sequence. The line voltage amplification factor is introduced for an increased forcing function and faster ID, which may have an exponential expression of PCC voltage ΔV_d ($e.\,g.\,k_v = e^{|\Delta V|}$).

As shown in Fig. 3.11, the active power controller $G_P(s)$ compensates the active power error between the reference P_{inv}^* and measured P_{inv} value while the introduced active disturbance $P_{IS} = (3/2)(V_d \cdot i_{dIS})$ is removed:

$$P_{inv}^{'} = P_{inv} - \frac{3}{2}V_d i_{dIS}. \tag{3.30}$$

The grid amplitude variation ΔV_d is tracked from its nominal value V_{dn}, multiplied with the amplification factor k_v and this quantity is added to the normalized ISS function. This resultant value i_{IS} limited $[\,i_{dlim}^-, i_{dlim}^+]$ as per relation (3.22) is summed further to the output of the active power controller to determine the active current reference i_d^*. The expression for ISS $i_{dIS}(s)$ is similar to relation (3.26), where I_S represents the perturbance step amplitude introduced in the active current component. The PCC voltage V_d is processed by the PLL controls, and the nominal

voltage V_{dn} is expressed as $V_{dn}(s) = V_d(s) \cdot \omega_{fV}/(s + \omega_{fV})$. Under normal steady-state, non-islanding conditions, ΔV_d is zero.

From relation (3.22), the parameter controls are replaced with the following variables:

$$\left\{ y \leftarrow i_d, x \leftarrow P_{inv}, z \leftarrow V_d \right\}. \tag{3.31}$$

As can be observed in Fig. 3.11, the PCC voltage variation ΔV_d with respect to grid nominal value is quantified: if the voltage variation is increasing, then the converter programmed active power P_{inv}^* is increased. Conversely, if the ac voltage has a tendency to decrease, then the commanded active is reduced. Under islanding conditions, the PCC voltage variation is proportional (α_V) to the inverter's active power variation, $dP_{inv} = \alpha_V(V_d - V_{dn})$.

As a result, the PCC voltage will further drift out of the limits where the islanding condition is detected. Under normal grid operation, due to ac grid low impedance source, the voltage doesn't change during converter power production.

3.2.3.   ISS with Integrated MPPT Controls (ISS-MPPT)

In the case of renewable power systems - solar and wind converter applications - the advantage of this method is that it unifies the MPPT and AI control. The controller performs dc input voltage regulation with MPPT controls for maximizing the PV efficiency and energy harvesting by finding the global maxima, while performing the ID simultaneously. The MPPT algorithm determines the maximum energy harvest (e.g. PV array, wind turbine) input voltage operation point V_{MPP}. The control system is designed for stability and behavioral predictability where the control loop bandwidths ($f_{MPPT.ISS}^{bw}$, f_{Vdc}^{bw}, f_{id}^{bw}, f_{iq}^{bw}) should satisfy the following condition for MPPT execution time, search sequence function, dc voltage regulation and active/reactive power control loop:

$$f_{MPPT.ISS}^{bw} < f_{V_{dc}}^{bw} < f_{i_d,i_q}^{bw}.$$ (3.32)

All modern power converters have incorporated MPPT capability to operate the PV solar array at the level that maximizes power production. The solar array voltage operating point is dependent of illumination factor and temperature. The most widely used MPPT algorithms are based on hill-climbing methods, which can achieve greater than 99.0% harvesting efficiency (as it has been demonstrated in Chapter 2). Different MPPT techniques have been reported in the literature: P&O with its derivations [143] - [145], Incremental Conductance [146], sliding-mode control [147], [148], and other techniques [149].

The MPPT technique is implemented based on P&O with periodic local array sweeps for an increased energy harvest and return of investment under possible partial shading conditions. The $dP - P\&O$ method, with an interleaved sampling method for power calculation and algorithm determination [143], reports good MPPT performance. The three-level inverter with separate MPPTs can be controlled with asymmetrical dc-link regulation [150].
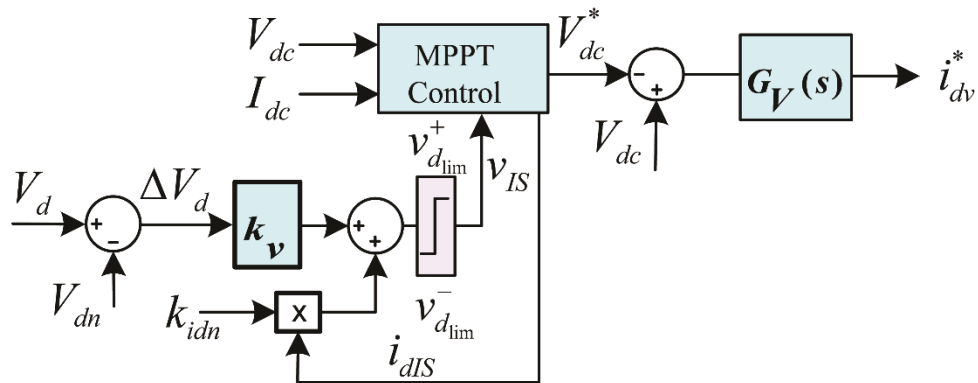
Figure 3.12: Method C: active power control loop with integrated MPPT and islanding search sequence (ISS).

The MPPT algorithm is designed with adaptive controls (e.g. dc voltage step size for global maxima determination) for performance improvement in non-ideal conditions: array

shading, mismatches between solar modules, different orientations of solar strings, low-irradiance conditions, and rapid changes in atmospheric conditions.

The proposed method integrates the ISS within any energy harvesting tracking algorithm. As illustrated in Fig. 3.12, the MPPT algorithm handles both renewable energy maximization and ID. The grid amplitude variation ΔV_d is tracked from its nominal value V_{dn}, multiplied with the amplification factor k_v and this quantity is added to the normalized ISS function. This resultant value V_{IS} (limited $[v_{dlim}^-, v_{dlim}^+]$ as per relation (3.22)) is augmented to the voltage reference V_{MPP}^* for finding the MPP global maxima and ID. The dc voltage controller G_V determines value for the reference active current i_{dv}^* for the current loop regulation control as shown in Fig. 3.5. The inverter reference active current component is provided by the dc input regulation loop, $i_{dv}^* = (V_{dc}(s) - V_{dc}^*(s))G_V(s)$, while the MPPT algorithm determines the dc input voltage reference, e.g. at the sampling instants $(k-1), (k)$: $V_{dc(k)}^* = V_{dc(k-1)}^* \pm v_{step}^{dc}$.

The ID is determined by the proportionality of $dV_{dc} = \alpha_{mppt}\, dP = \alpha_{inv}\, dP_{inv} = \alpha_V(V_d - V_{dn})$, where the MPP perturbation has a direct impact, with a positive feedback, on the grid voltage variation. Fig. 3.13 illustrates the ISS-MPPT method control structure and flowchart for MPP-ID algorithm. The DPG inverter samples the dc input voltage and current (v_k, i_k at the moment in time k), grid voltage variation ($V_{dc(k)}^* = \Delta v_k^{ac} = v_k^{ac} - v_{k-1}^{ac}$) and calculates the dc input power (p_k). The algorithm control continues the perturbation towards the MPP operating point by monitoring the relationship $dP/dV_{dc} > 0$ to a given direction, and the direction is reversed if $dP/dV_{dc} < 0$. The voltage step size (v_{step}^{dc}) is an adaptively changed function of: normalized dc voltage and current operating point and the ac grid voltage variation. The ISS is embedded and synchronized with the MPP tracking method and is represented with a similar

variation as per relation (3.20), with V_S representing the step amplitude voltage perturbance introduced in the MPPT algorithm.

$$v_{IS}(t) = \sum_{k=0}^{n} \left\{ \frac{4(2V_s)}{(2k+1)\pi} \left[\cos\left((2k+1)\frac{3\pi}{4} \right) \right] \cdot \sin\left(2k+1 \right)\omega_{IS}t \right\}.$$

(3.33)

Under normal ac conditions (e.g. $|\Delta v_k^{ac}| < k_{ac}$, where the voltage variation threshold k_{ac} can be a fixed value (e.g. 1%) or a dependent value of the momentary power level) the dominant control factor in the algorithm is the MPP tracking. Inherently, the MPPT algorithm has a constant variation of the active power injected to the grid, while ISS represents an augmentation which under grid faults produces PCC ac voltage variation as shown in relation (3.15).

In this case, the dominant control factor in the active power injection becomes the ISS by neglecting the energy harvest form dc sources. With this method, the overall DPG disturbance of the ac network grid is reduced while the MPPT algorithm inherently performs the perturbance required for ID.

This proposed ISS-MPPT technique is very attractive since it tackles two necessary functions (MPPT and ID) simultaneously with minimum disturbance on power quality.
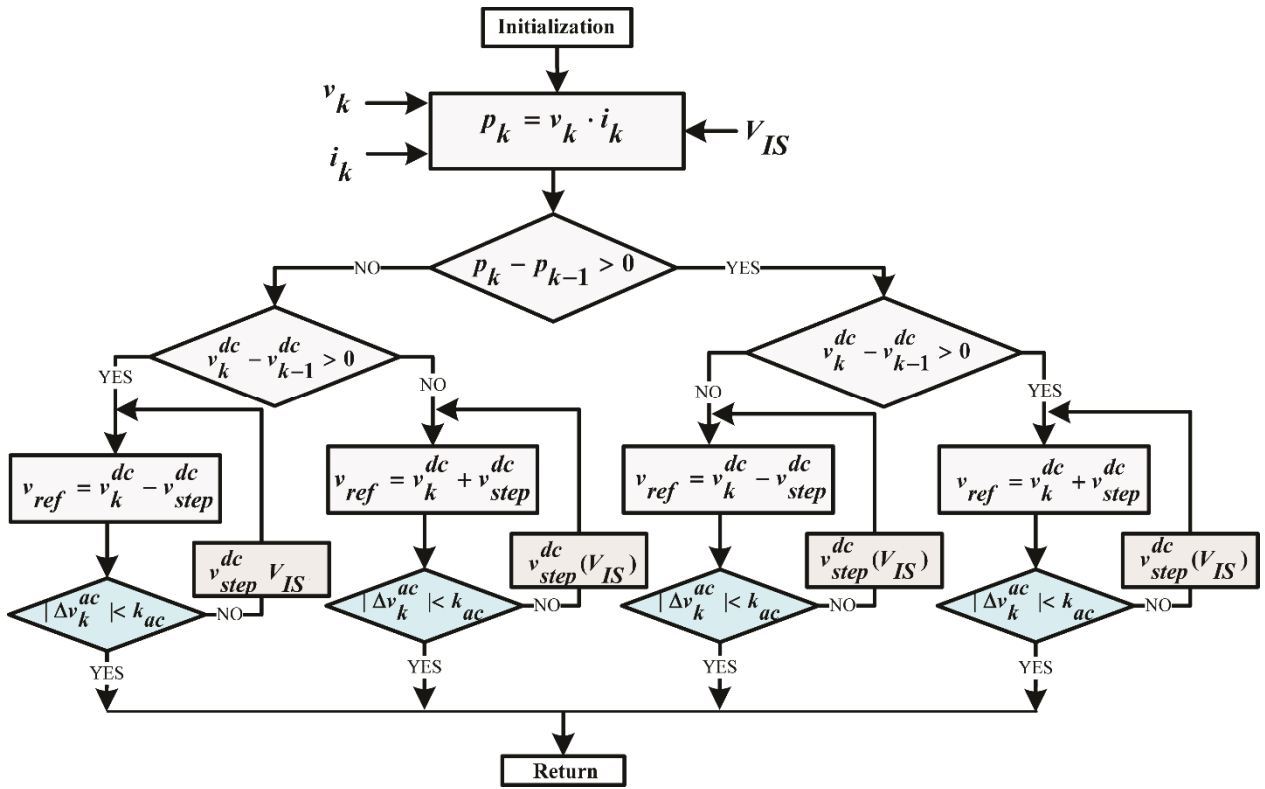
Figure 3.13: MPPT and ISS flowchart diagram.
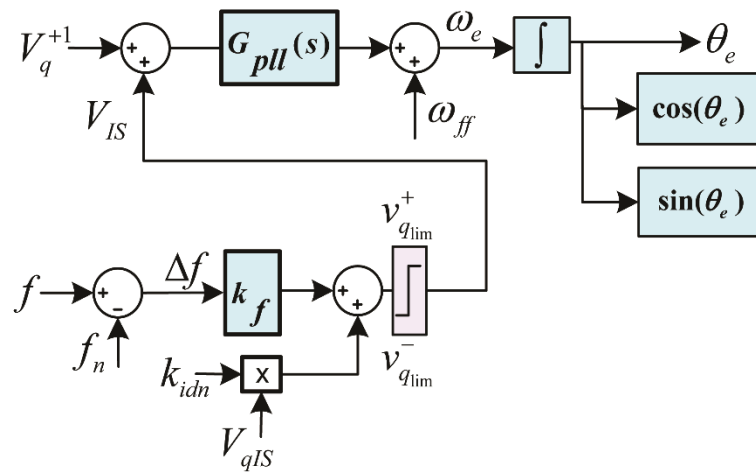
Figure 3.14: Method D: ISS integrated within SRF PLL control.

3.2.4.   ISS Integrated within PLL Control (ISS-PLL)

Another suggested anti-islanding method uses islanding search sequence (ISS) integrated within phase lock loop control with positive feedback on q-axis voltage component (as per convention from Fig. 3.7).

The ISS-PLL control is designed with the following features:

▪ Phase-locked loop grid synchronization $\omega_e = \omega$ is designed for high-order voltage harmonics rejection, three phase voltage space vector positive, and negative sequence components of the fundamental line frequency.

▪ The islanding search sequence is introduced within the PLL controls.

▪ Introduction of an automatic gain controller adaptation for fast PLL response under ac voltage dips: the ratio between the nominal grid voltage V_{dn} and measured value of the ac grid voltage positive sequence V_d^+ is part of the PLL loop filter, within the proportional-integral (PI) controller:

$$G_{pll}(s) = k_p \left(\frac{V_{dn}}{V_d^{+1}} \right) + \frac{k_i}{s}. \tag{3.34}$$

An example application is for voltage ride through under grid faults [151], when the ac phase voltage suddenly drops close to zero from its nominal value and the PLL dynamics are improved with the suggested adaptive gain feature, $k_{pv} = k_p \cdot (V_{dn}/V_d^+)$.

Fig. 3.14 illustrates the search sequence integration within PLL block diagram. The grid frequency error variation Δf is tracked from its nominal value f_n, multiplied with the amplification factor k_f and this quantity is added to the normalized ISS function. This resultant value V_{IS} is summed further to the fundamental q-axis component of three-phase voltage positive

sequence V_q^+. From the *dq*-transformation, the phase detection is represented by the following relation:

$$V_q^{+1} + V_{IS} = \sqrt{\left(V_d^{+1}\right)^2 + \left(V_q^{+1}\right)^2} \cdot \sin\left(\theta + \theta_{IS} - \theta_e\right), \tag{3.35}$$

where θ - grid phase angle, θ_{IS} - ISS phase disturbance and θ_e - PLL detected phase angle. Relation (3.32) can be rearranged with the voltage normalization:

$$V_q^{+1} + V_{IS} \approx \left(\theta + \theta_{IS} - \theta_e\right). \tag{3.36}$$

Under normal non-islanding conditions, the average value of the phase detection is zero (relation (3.35)), and the PLL tracks the fundamental positive-sequence component. In the case of islanding, the positive feedback principle introduced by the ISS phase disturbance is amplified and influences the inverter's fundamental phase current components:

$$\begin{bmatrix} i_a \\ i_b \\ i_c \end{bmatrix} = \begin{bmatrix} \cos\theta_{IS} & -\sin\theta_{IS} \\ \cos(\theta_{IS} - \dfrac{2\pi}{3}) & -\sin(\theta_{IS} - \dfrac{2\pi}{3}) \\ \cos(\theta_{IS} + \dfrac{2\pi}{3}) & -\sin(\theta_{IS} + \dfrac{2\pi}{3}) \end{bmatrix} \begin{bmatrix} i_d \\ i_q \end{bmatrix}. \tag{3.37}$$

The *dq* transformation to three-phase natural coordinates from relation (3.37) illustrates the inter-dependency between PLL phase angle disturbance and inverter output phase currents. The phase detection generated by the PLL continues to drift under an islanding condition, and the power mismatches $(\Delta P, \Delta Q)$ between the inverter and the load gradually increase, resulting in a proportional (α_Q) deviation of the line frequency (e.g. $\Delta\omega = -\alpha_Q \Delta Q$). Thus, the PCC frequency deviates due to the positive feedback mechanism outside of the permissible range of DPG's frequency operation. From relation (3.22), the parameter controls are replaced with the following variables:

$$\left\{ y \leftarrow V_q, x \leftarrow P_{inv}, z \leftarrow f \right\}. \tag{3.38}$$

This method is based on positive feedback of the q-axis voltage component variation. The periodic perturbance within q-axis component has an impact in the PLL detected frequency. As an alternative for ID, the controlled ISS perturbance can be implemented at the feedforward angular frequency ω_{ff}.

The ISS methods presented are constantly monitoring and injecting a negligible perturbation at the point of common coupling. The proposed methods are implemented within the inverter reactive current component (ISS-Q), active current component (ISS-P, ISS-MPPT) and phase-locked loop (ISS-PLL) in a positive-feedback fashion that enables the converter controls to distinguish a case of islanding from an non-islanding operation.

3.3. Simulation and Experimental Results

The islanding search sequence methods have been evaluated according to country specific standards (e.g. UL1741, IEEE1547, CSA107.1-01, VDE-AR-N 4105, AS4777). Table 3.2 represents three generic standards with different non-detection zones. Two of the standards (NDZ2 and NDZ3) have wider voltage-frequency disconnect limits, and as it can be observed in Fig. 3.2 and Table 3.2, the non-detect area is larger when the detection time is higher.

In general, with higher quality factor of the resonant RLC load, the AI algorithm detection time is increased. The experimental results are validated by a 20kVA power range solar inverter interfaced with ac network grid at 230Y400V-50Hz. The control firmware implemented uses a 32-bit CPU floating point DSP.

Table 3.2: Voltage and frequency disconnect limits examples (country specific standard) for protection under unintentional islanding.

Parameter	NDZ1	NDZ2	NDZ3
Quality factor (test)	1	2	2
Max. disconnect time	2 seconds	5 seconds	5 seconds
Over frequency disconnect	60.5Hz	50.5Hz	51.5Hz
Under frequency disconnect	59.3Hz	49.5Hz	47.5Hz
Over voltage disconnect	110% V_n	110% V_n	110% V_n
Under voltage disconnect	88% V_n	85% V_n	80% V_n
Reconnect time	300 s	30 s	60 s

The inverter switching frequency is $f_s = 20kHz$ with a 3-level topology, voltage oriented control space vector modulation in synchronous rotating reference frame controls (Fig. 3.5, and Fig. 3.15). The ac reactor inductance (L_f) and capacitance (C_f) filter values are at 2% per unit (p.u.). The ac resonant load tank elements are configured as per Table 3.3.

Table 3.3: Experimental test conditions and measurements for the DPG during simulated islanding (ISS-Q) introduced on the reactive current component).

Test Case	P_{inv} (total) [kW]	$I_{dcinput}$ (MPPT) [A$_{dc}$]	V_{PCC} (phase) [V$_{rms}$]	I_{Rload} (phase) [A$_{rms}$]	$I_{Lload} = I_{Cload}$ (phase) [A$_{rms}$]	Q_f -	R_{load} (phase) [Ω]	L_{load} (phase) [mH]	C_{load} (phase) [µF]	t_{dsim} [ms]	t_{dexp} [ms]	$\frac{\Delta i_{qstep}}{I_d}$ [%]
1	7.0	11.5	230.8	10.1	10.1	1	22.83	72.7	139.4	172	173	1.03
2	7.0	11.5	230.8	10.1	20.2	2	22.83	36.34	271	174	175	1.03
3	13.2	21.1	231.7	19.0	19.0	1	12.1	38.5	262	142	147	1.09
4	13.2	21.1	231.7	19.0	38.1	2	12.1	19.3	526.5	160	165	1.09
5	21.0	33.2	232.6	30.5	30.5	1	7.57	24.1	420	200	202	0.68
6	21.0	33.2	232.6	30.5	61.0	2	7.57	12.1	841	208	210	0.68

Table 3.3 shows DPG under different test cases at unity power factor for anti-islanding test. The dc input voltage is 640V$_{dc}$ and the ac output line voltage is 400V_{rms} at 50Hz. The ISS methods have been evaluated through both electronic simulation and laboratory test conditions. The ID de-energize time with simulation (t_{dsim}) vs. experimental (t_{dexp}) comparison is presented

in Table 3.3. The de-energize time is considered to be the period until the PCC voltage drops below a safe low voltage (i.e. $30V_{rms}$).

As can be seen from Table 3.3, the step change for the reactive current is on average 1% of the momentary active current component which represents a negligible perturbation effect to the normal DPG operation point.
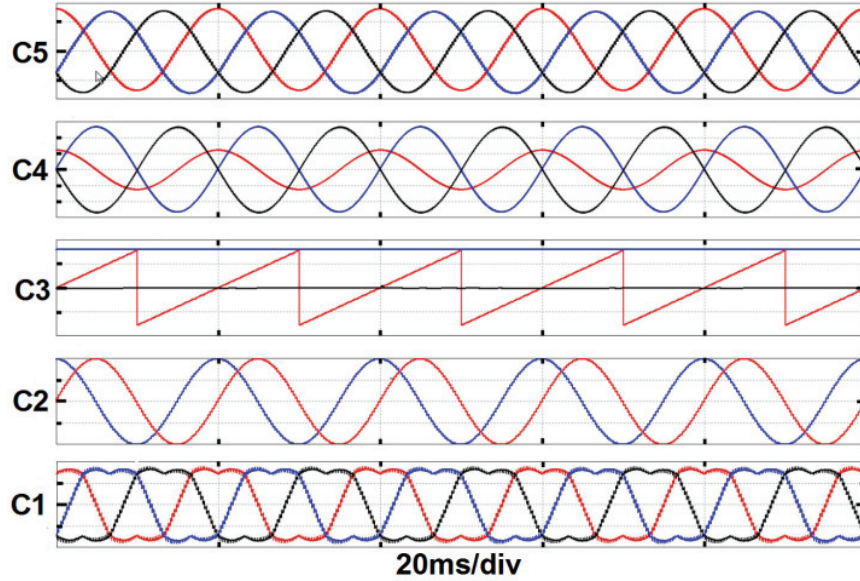
Figure 3.15: Simulation results performed at test case 4, Table 3.3.

Y-axis: C1 - abc-control signals e_a, e_b, e_c 200V/div, C2 - Voltage unit vectors 0.5V/div, C3 - PLL phase angle detection θ and grid voltage components V_d, V_q, 200V/div, C4 - Load phase currents $I_{La}(R), I_{La}(L), I_{La}(C)$ 20A/div, and C5 - DPG phase currents I_a, I_b, I_c 20A/div.

X-axis: 20ms/div.

Fig. 3.15 depicts the fundamental waveforms in natural coordinates (control signals e_a, e_b, e_c) DPG inverter phase currents I_a, I_b, I_c and ac load phase a currents $I_{La}(R), I_{La}(L), I_{La}(C)$, stationary (voltage unit vectors v_α, v_β) and rotating frame (PLL phase angle detection θ, grid voltage components V_d, V_q) of the DPG steady state operation upon which the ISS control structure is implemented.
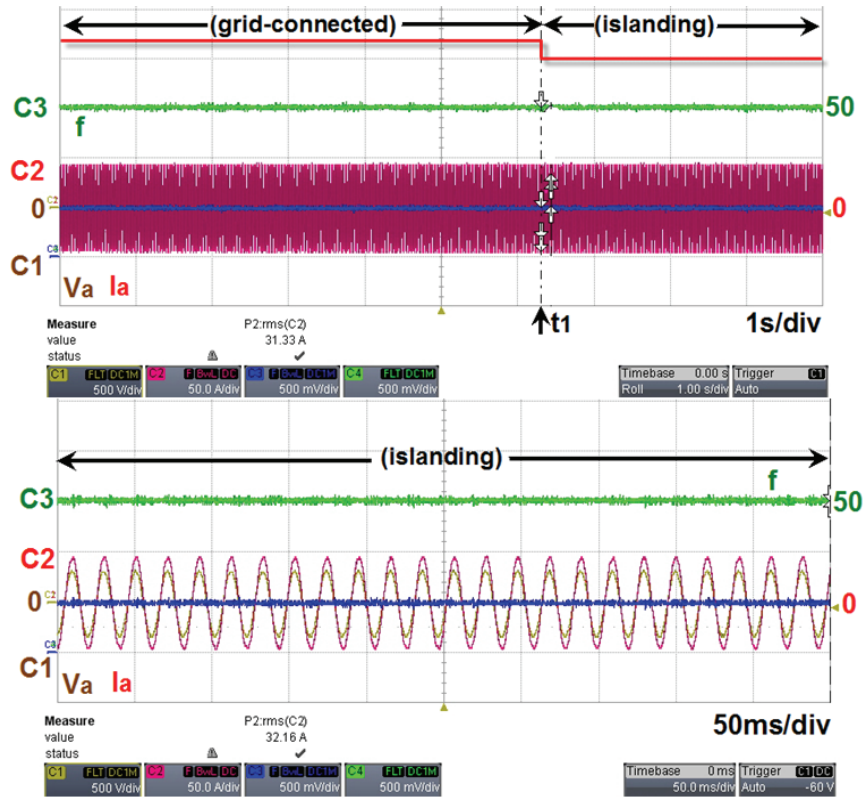
Figure 3.16: Experimental results with ISS disabled performed in test case 6, Table 3.3: the inverter fails to detect the islanding operating condition.

Y-axis: C1 - Phase voltage V_a (PCC) 500V/div, C2 - DPG Phase current I_a (DPG) 50A/div, and C3 - f (PCC) 0.34Hz/div.

X-axis: 50ms/div.

Fig. 3.16 demonstrates an islanding event, undesired DPG operation at the PCC, while the passive anti-islanding (AI) fails to disconnect from the electrical network. In this experimental case, the ISS methods were disabled and when the grid contactor (t_1, Fig. 3.16) is open the DPG continues to energize the PCC ac network. This case represents a safety hazard and this issue is addressed through the proposed ID methods. The islanding search sequence frequency considered for simulation and experimental verification is $\omega_{IS} = \omega_n/16 = 19.6$ rad/s.
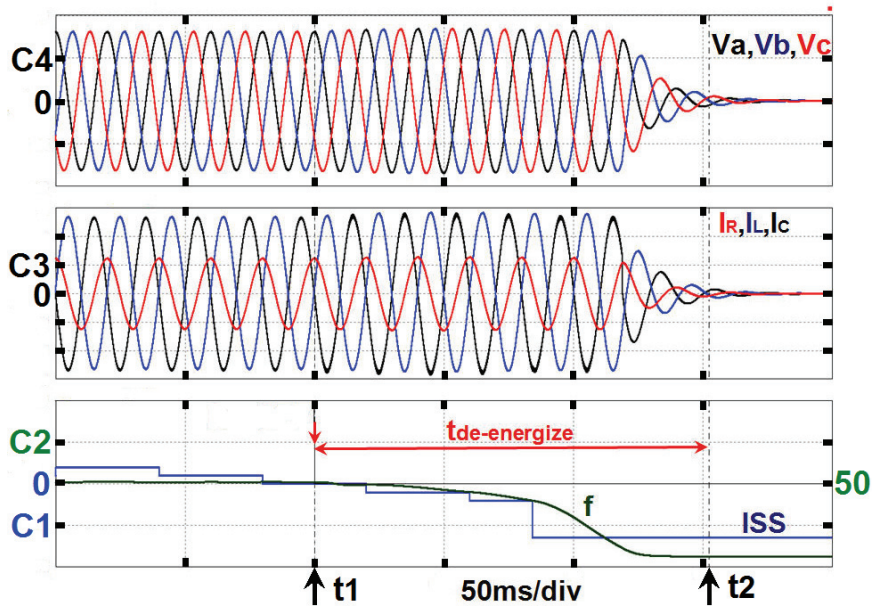
Figure 3.17: Simulation results performed with ISS-Q enabled in test case 4, Table 3.3.

Y-axis: C1 - ISS-Q 3A/div, C2 - f (PCC) 0.5Hz/div, C3 - Phase load currents $I_{La}(R), I_{La}(L), I_{La}(C)$, 20A/div, and C4 - Grid voltages V_a, V_b, V_c 200V/div.

X-axis: 50ms/div.
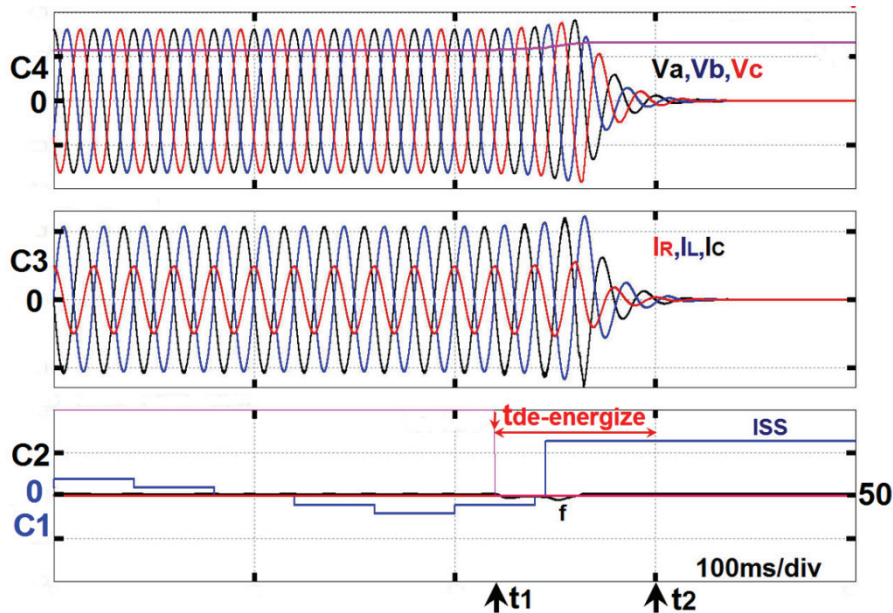
Figure 3.18: Simulation results performed with ISS-P enabled and similar test case 4, Table 3.3.

Y-axis: C1 - ISS-P 3A/div, C2 - f 0.5Hz/div, C3 - $I_{La}(R), I_{La}(L), I_{La}(C)$ 50A/div, and C4 - V_a, V_b, V_c 200V/div.

X-axis: 100ms/div.

Fig. 3.17 illustrates an anti-islanding test with the conditions from case 4, Table 3.3, where at moment t₁ the grid contactor opens ($k_g = off$, Fig. 3.5). The ISS with reactive power component variation method is capable of quickly detecting an islanding condition by decreasing the frequency (f) and DPG de-energizes the PCC at the moment t_2.

In Fig. 3.18, a similar anti-islanding test is demonstrated by enabling the ISS active power component variation method. At the moment t_1, the grid contactor opens and the ISS-P detects an islanding condition by increasing the active power component causing an increase of the PCC phase voltages V_a, V_b, V_c. At the moment t_2 DPG detects ac grid voltage out of the acceptable range and the ac network is de-energized to a non-hazardous voltage level.
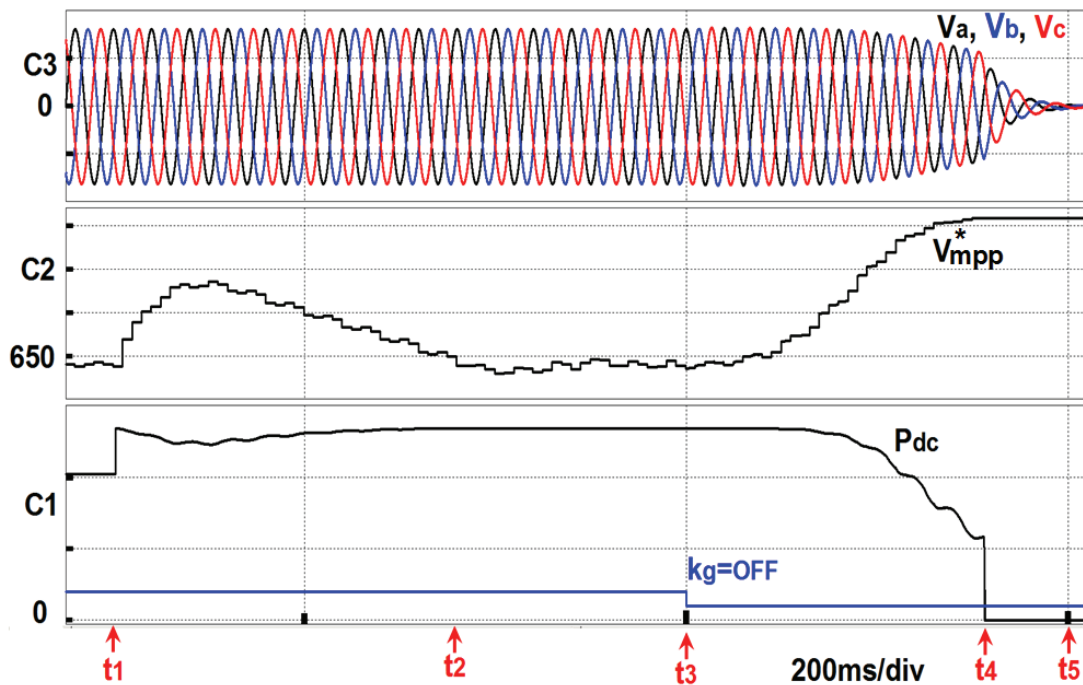
Figure 3.19: Simulation results performed with integrated MPPT controls, test case 4, Table 3.3.
Y-axis: C1 - P_{dc} 5kW/div and islanding switch (k_g) step-signal, C2 - V_{MPP}^* (MPPT) 50V/div, and C3 - V_a, V_b, V_c (PCC) 200V/div.
X-axis: 200ms/div.

Fig. 3.19 demonstrates an ID with ISS integrated in the MPPT algorithm. An advantage with this proposed method resides in the combined and optimized system operation for both

MPPT and ID. During the MPPT algorithm, with an updated time of $T_L/4$, the ISS is engaged only if the following relation is satisfied:

$$\Delta i_{d.step} > \Delta i_{MPPT.step}. \tag{3.39}$$

With this approach, the DPG continuously controls and monitors the active current component variation, and ISS is enabled only when relation (3.39) is true. With this method, the overall DPG disturbance of the ac network grid is reduced while the MPPT algorithm inherently performs the perturbance needed for ID; if the MPPT active current perturbance is not sufficient (relation (3.39)), then the ISS is engaged, as it can be seen on the Fig. 3.19. Prior to moment t_1, DPG exports power from the solar arrays (640V, 16A) to the ac grid. At the moment t_1, a sudden irradiance increase causes the input dc power (P_{dc}) to increase from 10.24kW to 13.5kW, which causes the dc input voltage to increase higher than the MPP voltage (V_{MPP}) for a few line cycles. At t_2, the DPG control algorithm stabilizes the dc input voltage and re-establishes the V_{MPP} and the desired new power level (13.5kW). At the moment t_3, the ac grid is disconnected, while during the $t_3 - t_4$ interval, the relation (3.39) is satisfied and ISS is enabled. The dc input reference continues to increase, and the MPPT algorithm is abandoned since an islanding condition is pursued. As a consequence, the active power reduces and at moment t_4, DPG ceases to convert energy from solar the array since an under-voltage event is triggered. The PV array voltage increases to its open voltage limit (Fig. 3.19). The total DPG time to de-energize the ac load (RLC resonant tank) is between t_3 and t_5 (approximately 200ms), which represents an order of magnitude less than some of the grid disconnect requirements (e.g. 2 s). In a comparison example with ISS-Q, the ISS-MPPT has a longer detection time (approximately with 50ms) due to the computational time, algorithm implementation and system stability (relation (3.32)) of

MPPT method since it has to control and monitor both, the energy harvesting maximization and the islanding detection.
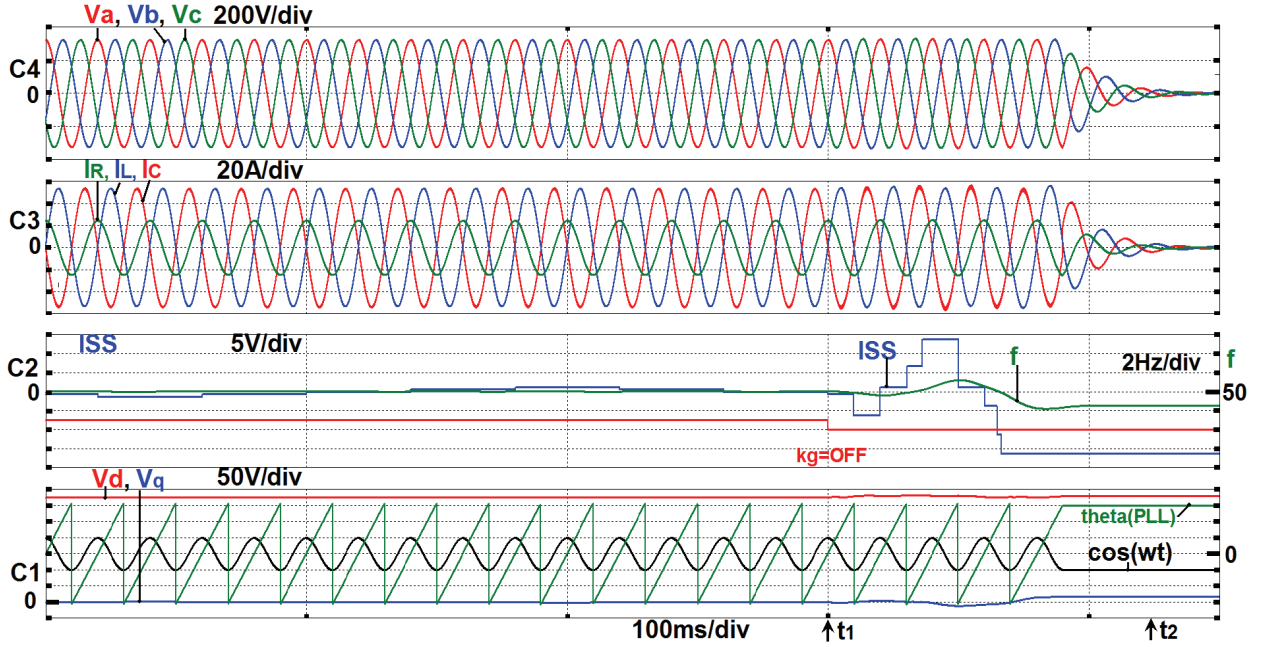
Figure 3.20: Simulation results performed with ISS-PLL enabled, test case 4, Table 3.3.

Y-axis: C1 - V_d, V_q 50V/div, PLL phase angle θ_e and unit vector $\cos(\theta_e)$, C2 - ISS-PLL 5V/div, f 2Hz/div, C3 - $I_{La}(R), I_{La}(L), I_{La}(C)$ 20A/div, and C4 - V_a, V_b, V_c 200V/div.

X-axis: 100ms/div.

In Fig. 3.20, an anti-islanding test with ISS-PLL is demonstrated under the test conditions from case 4, Table 3.3, where, at moment t_1, the grid contactor opens for an islanding simulation. The initial step size of $1[V/div]$ perturbation (V_{IS}, Fig. 3.14) is amplified within the q-axis grid voltage component due to a frequency Δf change, and parameter $k_{idn} = 0.63$ since it is adaptive (relation (3.24)) to the active power level operation from test case 4, Table 3.3. The ISS-PLL method detects an islanding condition by pushing the frequency (f) out of specified frequency range (e.g. Table 3.2), and the PCC is de-energized at moment t_2, with a total disconnection time of 125ms.
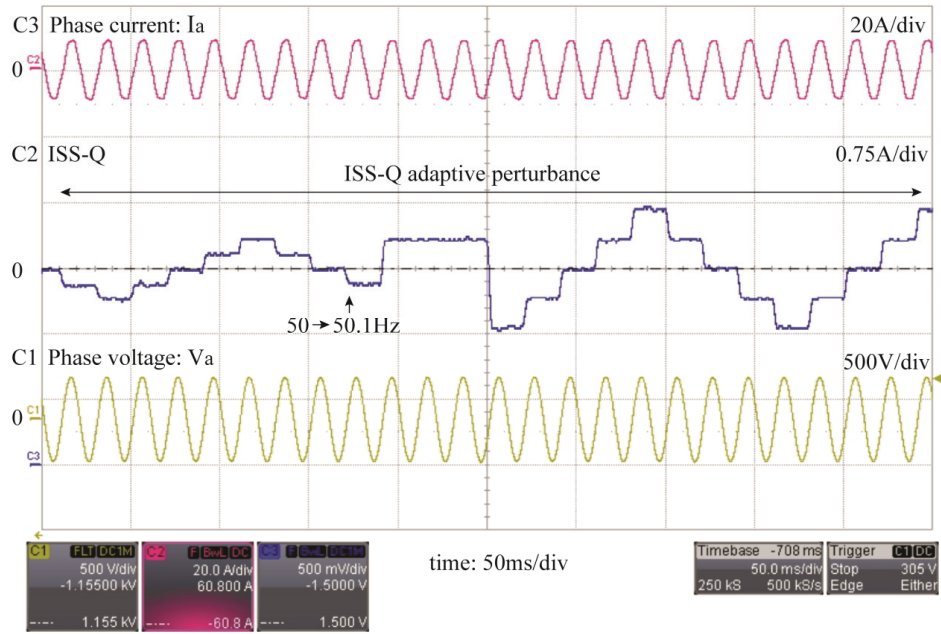
Figure 3.21: Experimental results performed with the adaptive feature of ISS-Q ($230V_{LN}/400V_{LL}$, 50Hz, $P_{ac} = 4.5kW$).

Y-axis: C1 - V_a (PCC) 500V/div, C2 - ISS-Q 0.75A/div, C3- I_a (DPG) 50A/div.

X-axis: 50ms/div.
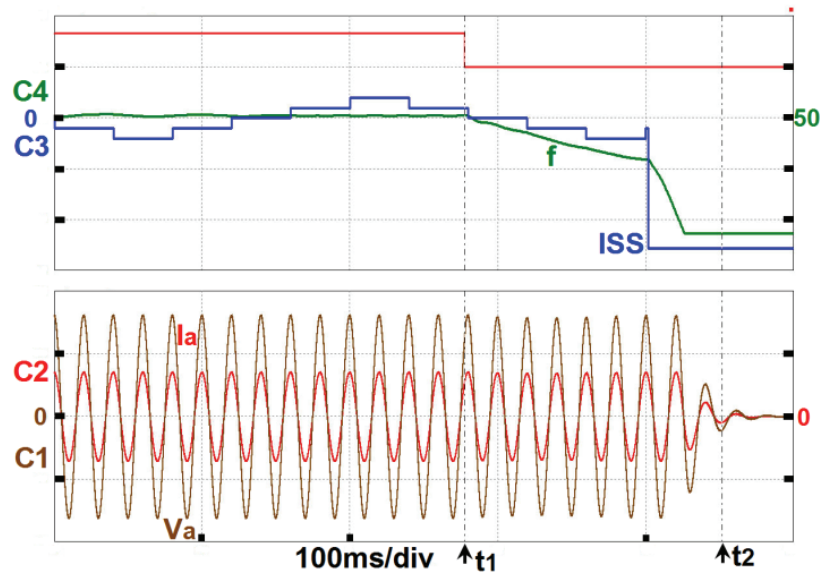
Figure 3.22: Simulation results performed with ISS-Q enabled in test case 2, Table 3.3.

Y-axis: C1 - V_a (PCC) 200V/div, C2 - I_a (DPG) 20A/div, C3 - ISS-Q 0.73A/div, and C4 - f (PCC) 0.5Hz//div.

X-axis: 100ms/div.
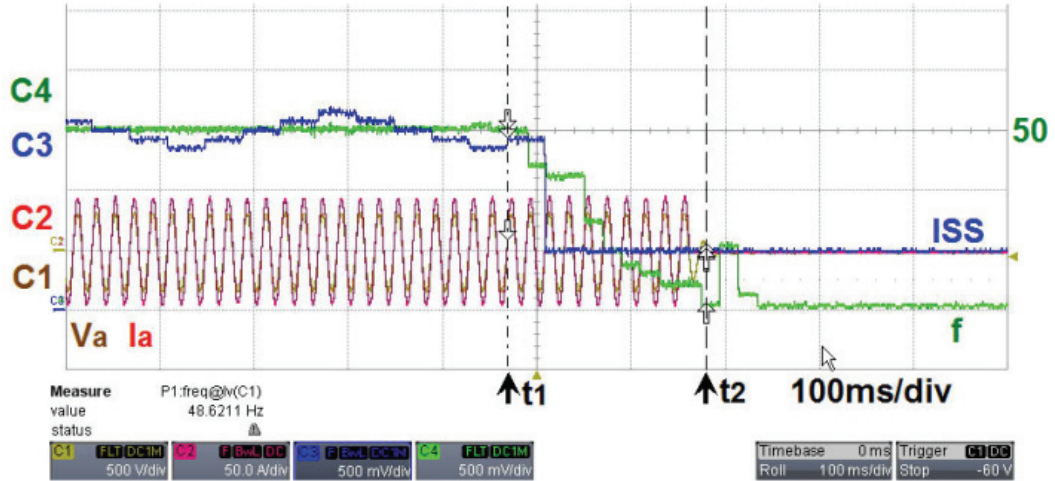
Figure 3.23: Experimental results performed with ISS-Q enabled in test case 2, Table 3.3.

Y-axis: C1 - V_a (PCC) 500V/div, C2- I_a (DPG) 50A/div C3 - ISS-Q 0.5A/div, and C4 - f (PCC) 0.34Hz/div.

X-axis: 100ms/div.

Fig. 3.21 shows the adaptive feature of ISS-Q method: the search sequence changes its perturbance step-size ($\Delta i_{q.step}/I_d$) as a consequence of grid frequency change (50 to 50.1Hz).

Figs. 3.22 - 3.29 represent the ISS behavior under different test conditions outlined in Table 3.3, such as power level and ac load quality factor. The moment t_1 represents the grid disconnect point, and t_2 is the moment when the ISS method de-energies the point of common coupling ac network.

The ISS perturbance has an adaptive behavior during DPG operation and ID: variable step-size (Δy_S) and maximum limit (y_{lim}). Under normal grid conditions, the search sequence is designed with an adaptive step-size change (I_S) as per relation (3.26) where at lower power level the variation of reactive current is only with 0.147A$_{pk}$/step (Fig. 3.22 - 3.23) and at nominal power level the step value is doubled (Fig. 3.24 - 3.27). During an ID, the limit function y_{lim} (relation (3.22) and Fig. 3.9) has an adaptive behavior: at DPG lower power level (e.g. <30% power, Fig. 3.22 - 3.23) the limit is set at 2A$_{pk}$, while at DPG nominal power the ISS is clamped

at $4A_{pk}$ (Fig. 3.24 - 3.27). The overall effect of the adaptive control is reported in Table 3.3 and quantified by parameter $\Delta i_{q.step}/I_d$. Without the adaptive feature, the ISS perturbation at lower power levels would be twice (e.g. 2%), while the aim for in this dissertation is to maintain it at less than 1% for all power levels.

Figs. 3.22 - 3.23 illustrates the ISS-Q method evaluation for ID through simulation and experimental results tested under test case 2, Table 3.3. After the islanding occurrence at moment t_1, the search sequence pursues the frequency negative change through its reactive current $(f \downarrow (i_{qIS} \downarrow, \& Q_{inv} \uparrow) \Rightarrow f \downarrow\downarrow)$ in agreement with relations (3.13), (3.25)) while the DPG phase current lags the phase voltage with a negligible phase shift, therefore has an insignificant impact on power quality. The PCC frequency continues to decrease until the DPG ceases the power conversion due the grid under frequency fault (e.g. Table 3.3, NDZ2 case).
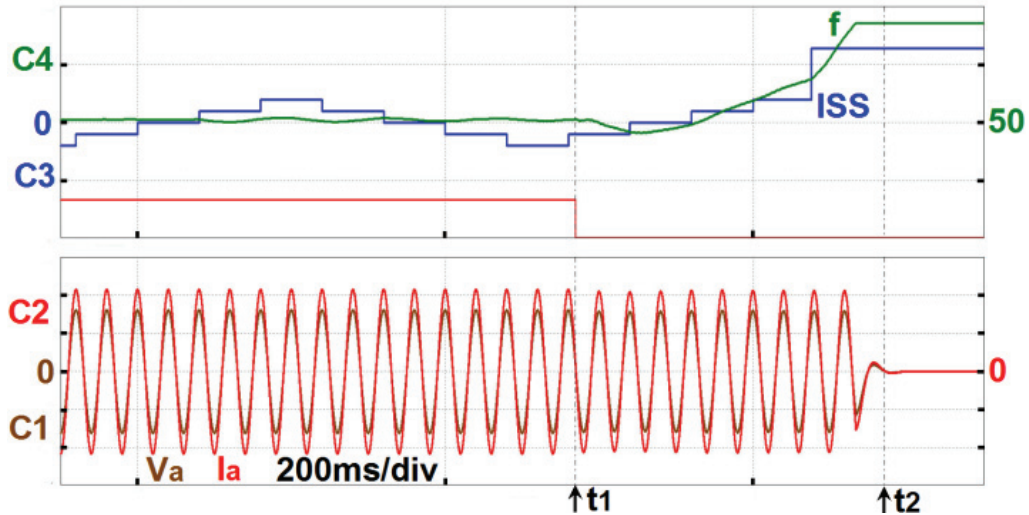
Figure 3.24: Simulation results performed with ISS enabled in test case 5, Table 3.3.

Y-axis: C1 - V_a (PCC) 200V/div, C2 - I_a (DPG) 20A/div, C3 - ISS-Q 3A/div, and C4 - f (PCC) 0.5Hz/div.
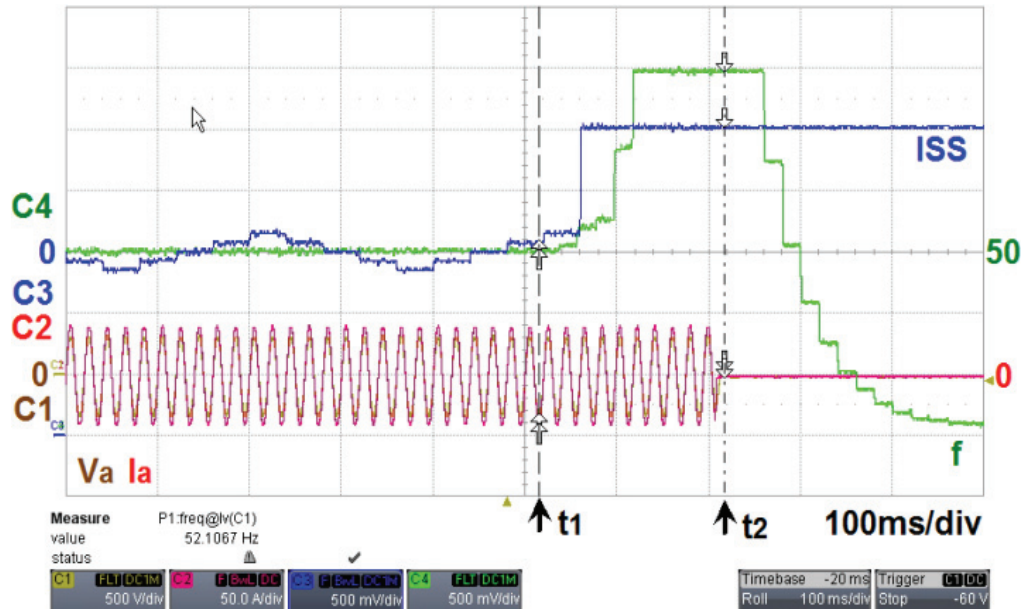
X-axis: 200ms/div.

Figure 3.25: Experimental results performed with ISS enabled in test case 5, Table 3.3.

Y-axis: C1 - V_a (PCC) 500V/div, C2 - I_a (DPG) 50A/div, C3 - ISS-Q 2A/div, and C4 - f (PCC) 0.34Hz/div.

X-axis: 100ms/div.

Figs. 3.24 - 3.25 illustrates the ISS-Q method evaluation under test case 5, Table 3.3, with similar simulation and experimental results. After the islanding occurrence at moment t_1, the search sequence pursues the frequency positive change through its reactive current component ($f \uparrow (i_{qIS} \uparrow, \& Q_{inv} \downarrow) \implies f \uparrow\uparrow$) while the DPG phase current leads the phase voltage with a negligible phase shift. In comparison with the previous case (lower power level), at nominal power the ISS step-size is perturbation is doubled (0.294A_{pk}/step) due to its adaptive capability.
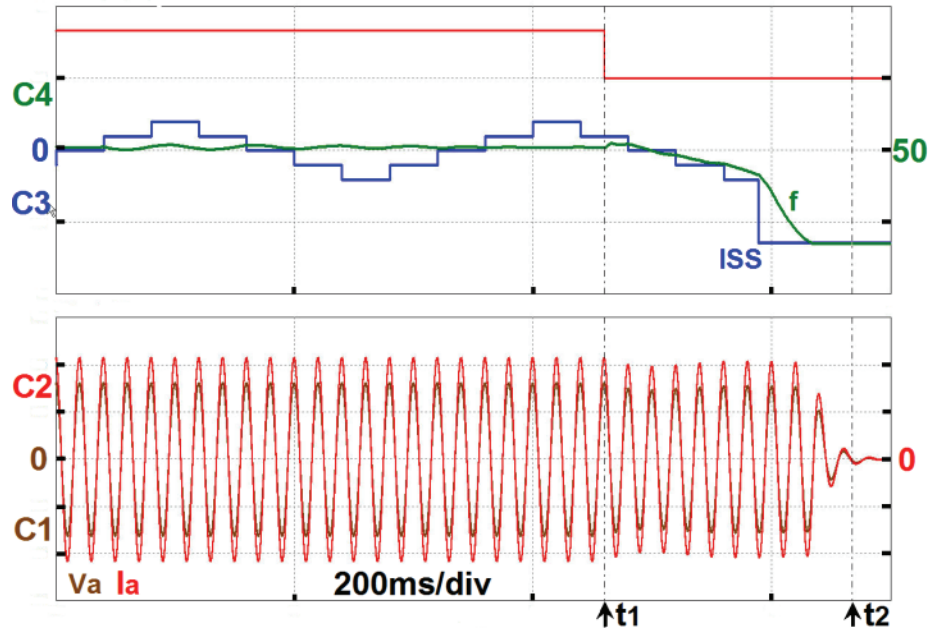
Figure 3.26: Simulation results performed with ISS enabled in test case 6, Table 3.3.

Y-axis: C1 - V_a (PCC) 200V/div, C2 - I_a (DPG) 20A/div, C3 - ISS-Q 3A/div, and C4 - f (PCC) 0.5Hz/div.
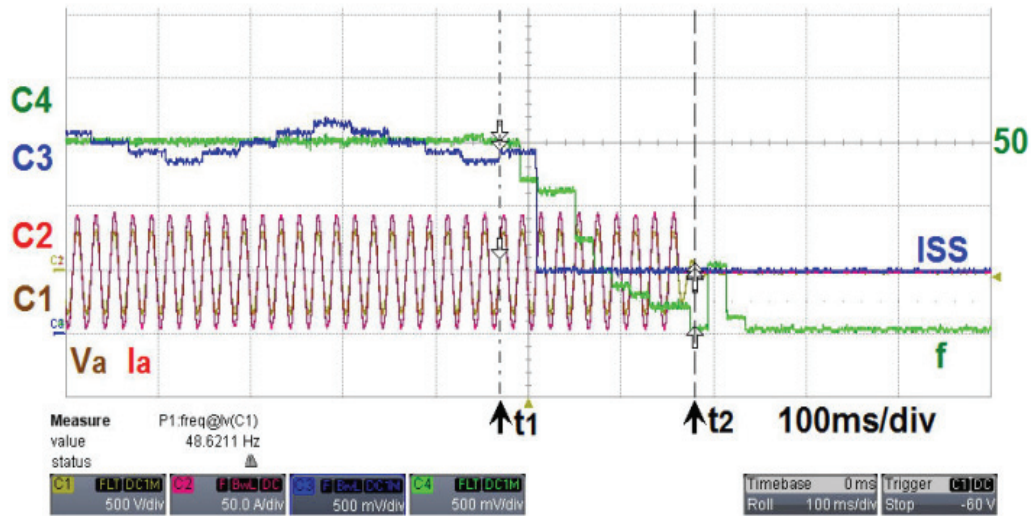
X-axis: 200ms/div.

Figure 3.27: Experimental results performed with ISS enabled in test case 6, Table 3.3.

Y-axis: C1 - V_a (PCC) 500V/div, C2- I_a (DPG) 50A/div, C3-ISS-Q 2A/div, and C4 - f (PCC) 0.34Hz/div.

X-axis: 100ms/div.

161

Figs. 3.26 - 3.27 illustrate the ISS-Q method evaluation for ID through simulation and experimental results tested under test case 6, Table 3.3. The bidirectional feature of search sequence is demonstrated, where it forces the PCC frequency for a continuous decrease (Figs. 3.22 - 3.23, 3.26 - 3.27) or increase (Figs. 3.24 - 3.25), where the DPG detects an under/over-frequency fault. It should be noted that the PCC frequency (f) measured in graphs is clamped within a range (e.g. +/-1Hz) in order to increase the digital to analog measurement resolution, while the frequency decays towards zero after the PCC network is de- energized.
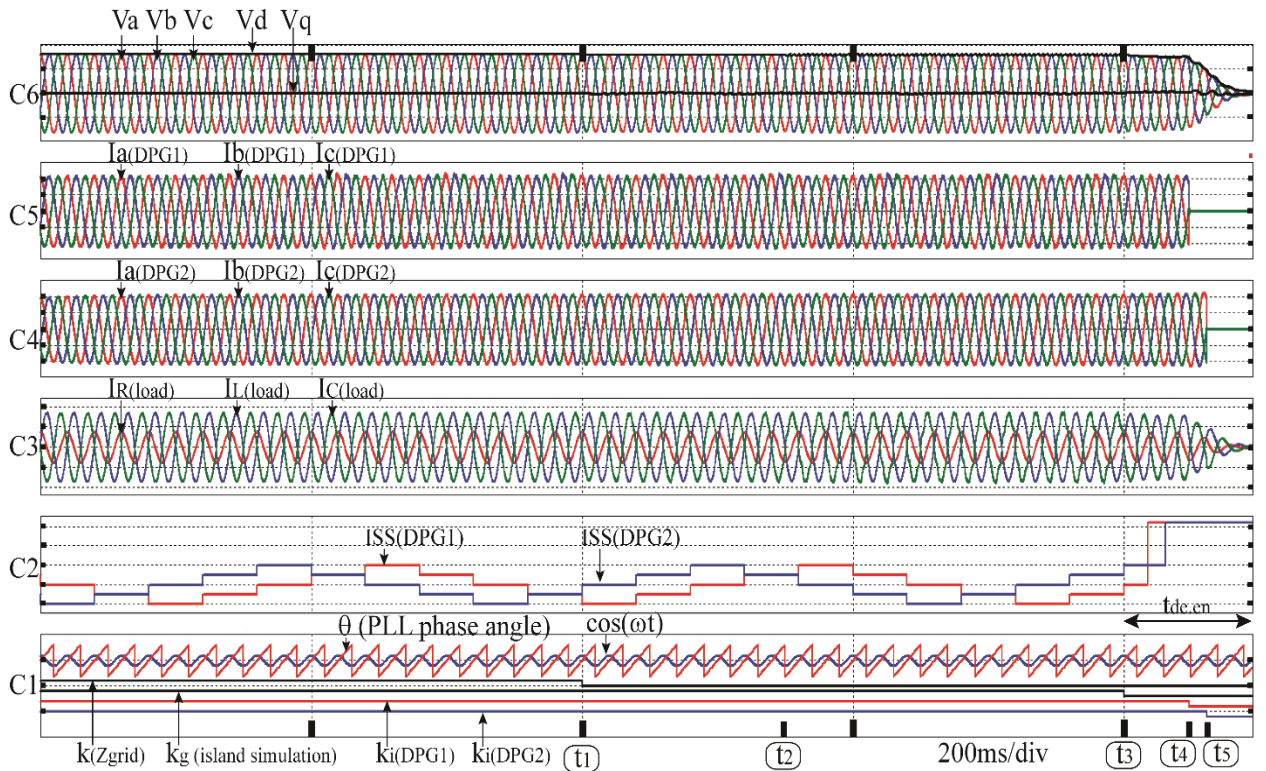
Figure 3.28: Islanding search sequence (ISS) method stability test under different grid conditions with two DPGs connected in parallel, case 6, Table 3.3 for each DPG1 and DPG2:

Grid impedance change t_1: from $Z_g = 0.1\Omega$ to $Z_g = [0.38 + j\omega(2.5mH)]\Omega$, grid harmonics at t_2: 10% of 5th +15% of 7th harmonics) and anti-islanding test at t_3.

Y-axis: C1 - Voltage unit vector, phase angle (θ), C2 - ISS-Q DPG1 and DPG2 0.3A/div, C3- $I_{La}(R), I_{La}(L), I_{La}(C)$ 100A/div, C4 - I_a, I_b, I_c (DPG1) 20A/div, C5 - I_a, I_b, I_c (DPG2) 20A/div, C6 - PCC V_a, V_b, V_c, V_d, V_q 200V/div.

X-axis: 200ms/div.

Fig. 3.28 demonstrates the method's stability as tested during normal operation, and its ID effectiveness. Two PV inverters are operated in parallel (DPG1 and DPG2) at the same PCC. At moment t_1, the grid impedance suddenly increases from $Z_g = (0.1)\Omega \rightarrow [0.38 + j\omega(2.5mH)]\Omega$. At moment t_2, the ac voltage grid becomes distorted with 10% of the negative sequence's 5th, and 15% of the positive sequence's 7th, components. Both DPGs units demonstrate stable operation under common grid disturbances. Finally, at moment t_3, the grid is disconnected and both DPGs quickly de-energize ($t_{d.en} < 100ms$) the PCC due to an ID event (DPG$_1$ at t_4 and DPG$_2$ at t_5).
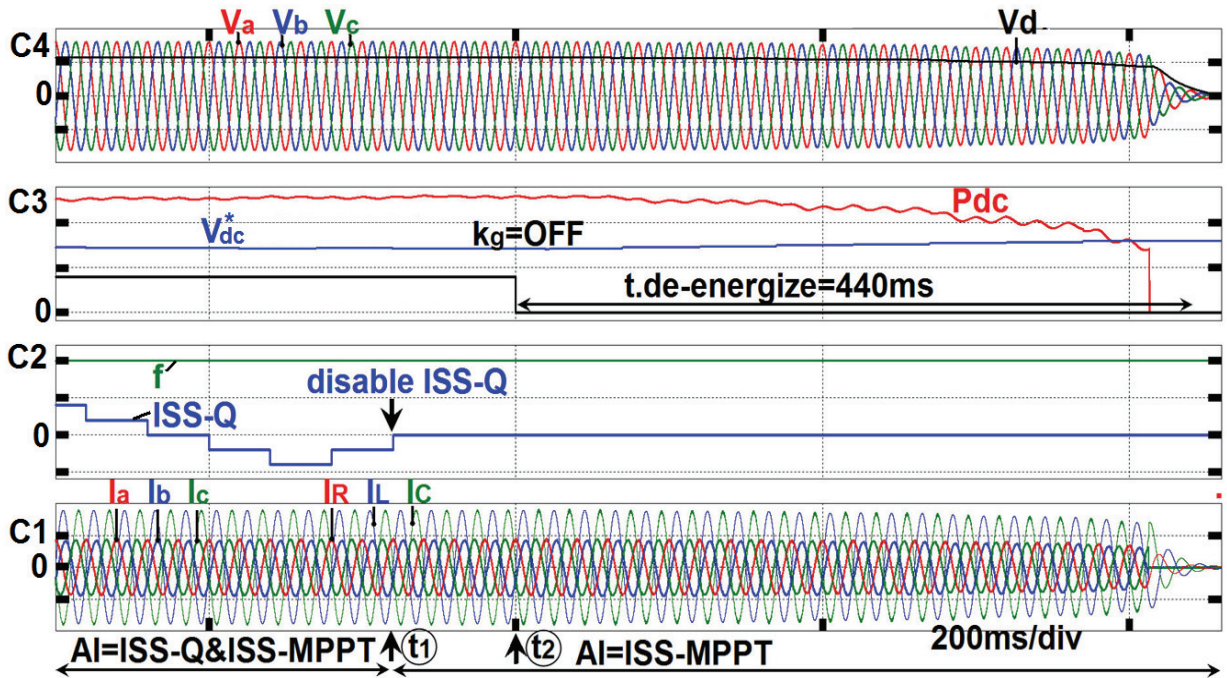
Figure 3.29: Fault tolerant simulation results performed with integrated ISS-Q and ISS-MPPT controls, test case 4, Table 3.3.

Y-axis: C1 - I_a, I_b, I_c (DPG), $I_{La}(R), I_{La}(L), I_{La}(C)$ 30A/div, C2 - ISS-Q 3A/div, f (PCC) 25Hz/div, C3 - V_{MPP}^* (MPPT) 500V/div, P_{dc} 5kW/div and C4 - $V_a, V_b, V_c, V_{LNa(RMS)}$ 200V/div.

X-axis: 200ms/div.

Fig. 3.29 demonstrates the safety redundancy of solar inverter operation with the integrated control methods, ISS-Q and ISS-MPPT. The fault tolerant feature provides a faster validation of the software algorithm, while the redundancy for safety critical functions provides

easier standard compliance. The ISS-Q control update is equal to $2T_L$ in order to accommodate both rapid ID and minimal system perturbation during normal DPG operating conditions.

The MPPT routine is selected at an update rate of $5T_L$ with integrated ID, which acts as a single, fault-tolerant watch-dog routine for safety and standards compliance (e.g. UL1998). Fig. 3.29 shows that, at the moment t_1, ISS-Q fails to function and, at the moment t_2, an anti-islanding test is simulated ($k_g = off$) with conditions per case 4, Table 3.3. The ISS-MPPT performs the routine as explained per Figs. 3.3, 3.12, 3.13, and disconnects with sufficient design margin compared with the standard requirements (e.g. Table 3.2). It should be noted that ID time can be reduced if it is decided to update the MPPT routine more quickly.

The MPPT control signal is equal to $\max\{dV^*_{mppt}, V_{IS})/dt\}$ and performs a frequent voltage sweep (e.g. every 30 seconds with a duration of $2T_L$) within a limited range (e.g. 50% of open circuit voltage) to minimize the impact on the MPP efficiency. Further refinement for an adaptive sweep frequency and voltage range is dependent on load and data logging statistical data. The frequent voltage sweeps provide the ability to harvest the maximum amount of energy possible from a PV array, over a wide range of shaded and non-shaded solar module characteristics.

Fig. 3.30 illustrates the I-V and P-V characteristics when the solar converter operates at the desired global maxima, ensuring the optimal PV system for a return on investment. The solar converter is comprised of dc-dc boost and dc-ac inverter power conversion stages in order to operate over a wide dc input voltage range: 200-1000V.
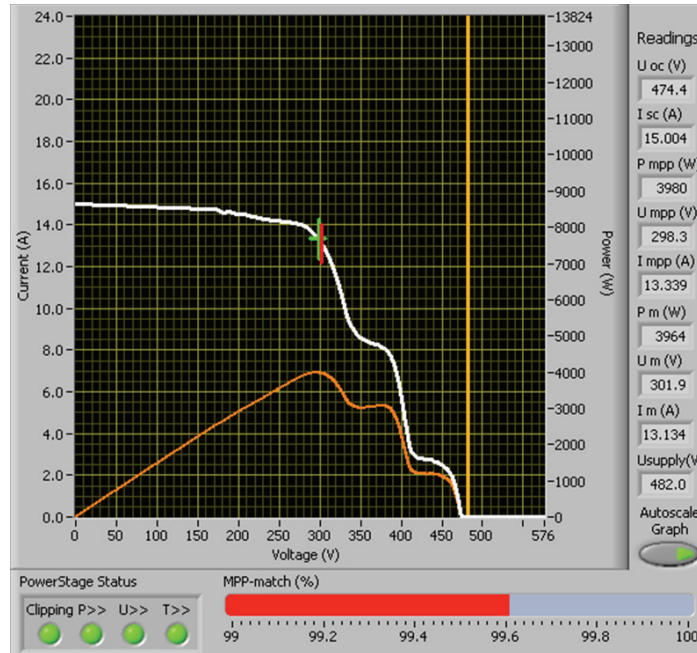
Figure 3.30: Solar converter with MPPT and AI control: experimental test with I-V, P-V characteristics under partially shaded conditions.

The MPPT algorithm is performed by the inverter power stage at higher dc input voltage (e.g. > 600V), while at lower dc voltage, the MPPT algorithm is performed by the boost converter, as illustrated in Fig. 3.30. Therefore, the MPPT algorithm unifies the controls of energy harvesting algorithms and ID with an average efficiency of 99.6%, as shown in Fig. 3.30.

Another interesting application of AI implementation at the MPPT control block level is in dc coupled system (dc grids) applications. The implementation control for dc coupled system configuration is explained in Fig. 3.12. For example, the dc-dc converters are responsible for the ID, while the dc-ac converters, without active AI controls, represent the conversion stage from the dc grid voltage line transmission to the ac grid.

In off-grid applications, the micro-grids may require different voltage and frequency ranges (usually extended) or with disabled anti-islanding protections. The micro-grid line frequency can be used as the agent for communication between the DPGs devices where the DPG

current source modules can automatically be reconfigured by re-adjusting the anti-islanding limits via a specific frequency pattern determined by the DPG voltage sources [124].

The advantages of the proposed ISS methods consist of its ability to integrate methods to support simplicity, robust controls for safety redundancy, fast and adaptive features for all operating DPG conditions and provide minimum impact on power quality.

Fig. 31 shows the laboratory and experimental islanding setup with user set-points interface of the three-phase RLC resonant tank.
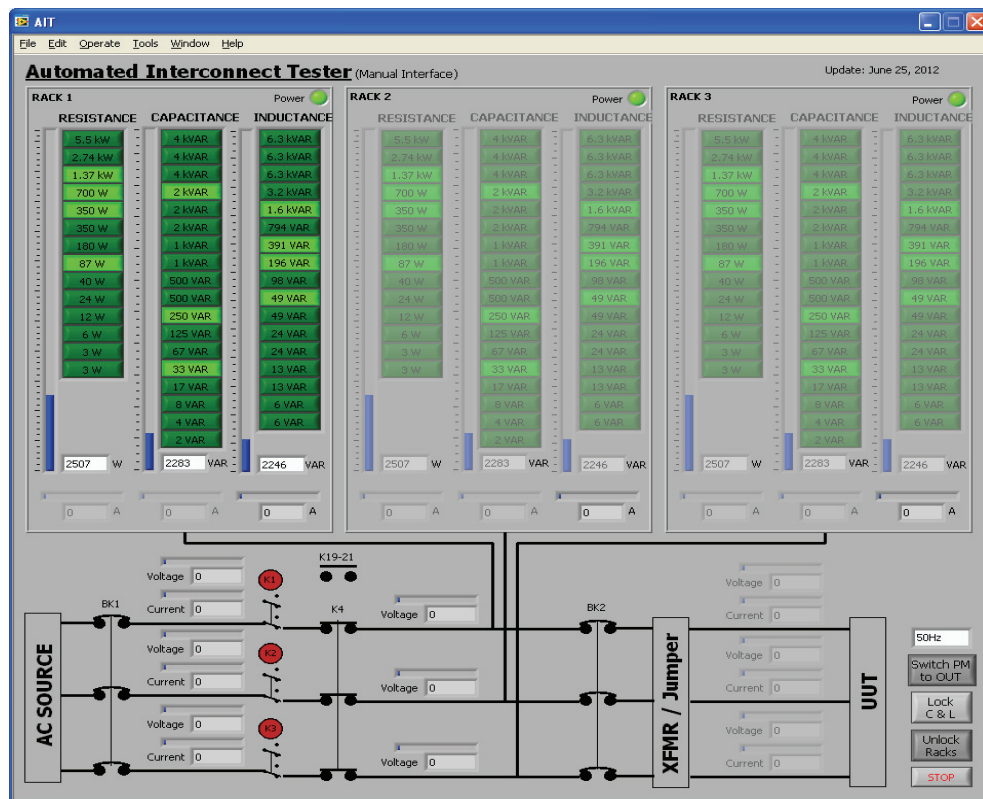
(a) Graphical user interface for controlling the resonant load.
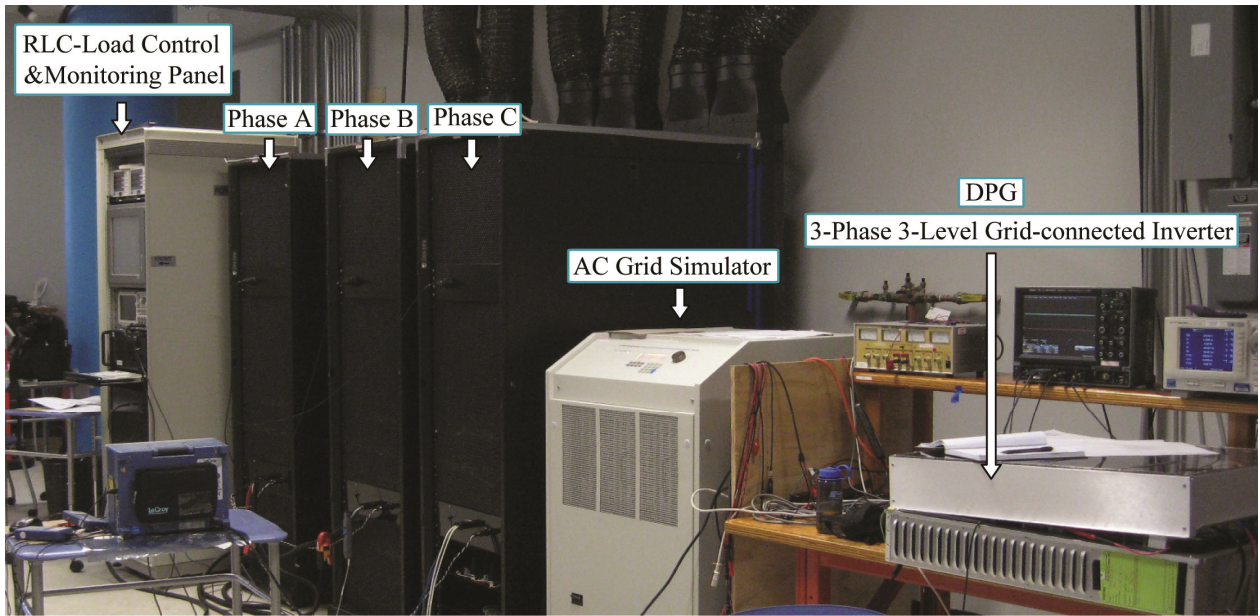
(b) Experimental setup.

Figure 3.31: Laboratory and experimental islanding setup:

(a) user configuration RLC software interface and (b) hardware setup. The resonant tank adjustment is performed within [-5%…+5%] of R, L, C values in order to capture different configured operating conditions.

3.4. Summary

Safety and electric grid requirements for the renewable distributed generation are permanently subject to change from different regulatory agencies. The DPG hardware and software architecture requires advanced controls in order to achieve high performance and meet country specific standards. In this chapter, a flexible architecture was presented in which an Islanding Search Sequence (ISS) technique can be easily implemented within four different methods: active power, reactive power, MPPT, and PLL. Principles and practical design guidelines are provided on the topic of search sequence for integrated power system control.

The ID concepts and methods presented are characterized by robustness in order to detect ac grid network faults while having a negligible impact on the quality of the renewable current

exported to utility grids during normal operation. The proposed islanding search sequence (ISS) techniques were implemented to control active and reactive current components, MPPT algorithms, and within PLL controls and validated with analysis and experimental results. The ISS detection and ac network de-energizing total action is rapid, while in normal DPG operation the impact on the normalized reactive and active power is negligible (approximately 1%). The mechanism explained above leads to rapid ID and can be used to further decrease the detection time with the ISS. An optimized detection time of less than 500 milliseconds is suggested (including the relay/contactor opening time, voltage collapse below 30Vrms - safe low voltage) while maintaining a small system perturbance overall (e.g. 1%).

The new ID synchronized within MPPT provides the advantage of an integrated solution and the possibility of implementing ID in dc-dc converters for dc coupled systems. The single-fault tolerant safety requirements can be achieved through the method's robustness for ID by enabling two or more ISS techniques. Thus, the proposed methods include the means of implementing redundancy within the firmware modules for the critical functions (e.g. islanding detection) required by the safety grid-interconnect standards.

Experimental results demonstrated the validity of the theoretical and electronic simulation models described in this chapter.

Chapter 4. Voltage and Frequency Grid Support Control Strategies Beyond Standards[4]

The previous chapter introduced a flexible architecture for ID, featured with redundancy for safety compliance and integrated within MPPT algorithm. This chapter continues the investigation of advanced grid support methods for standards compliance with results beyond standards requirements.

Once this grid support functionality is established, a grid-connected system is equipped with the proposed advanced controls which lead to high performance and exceeding the standards requirements.

4.1. Voltage and Frequency Grid Support

The utility grid standards mandate on-going requirements in interconnection, operating and metering requirements for distributed generators (DGs) to be connected to the distribution networks and transmission systems. Protective functions are required for voltage and frequency sensing with time-delay (e.g. < 2 seconds) functions to prevent DGs from energizing a de-energized distribution ac network.

The ID safety function to prevent the DGs from contributing to the formation of an unintended island and cease to energize ac network was presented in Chapter 2.

---

[4] Part of this chapter has been published in [E. Serban, M. Ordonez, C. Pondiche, "Voltage and Frequency Grid Support Strategies Beyond Standards," IEEE Transactions in Power Electronics, vol. 32, no. 1, pp. 298–309, Jan. 2017.].

The grid voltage and frequency protective functions requirement implementation in the DGs must be designed in a flexible fashion. When DG operation outside of voltage/frequency-limits (e.g. Table 3.1) is required, then momentary DG operation must support the grid.

In Fig. 4.1 is shown the voltage/frequency limits associated with the time requirements specified by the GCs for the distributed generators operation.

Modern grid-connected distributed generators are specified for design with the following grid-interconnect features during, considering excursions from nominal operating voltage and frequency ac system conditions:

- Anti-islanding grid disconnect.

- Low/High Voltage Ride-Through for grid network support.

- Ramp rate controls (e.g. power fluctuation control, connect/re-connect soft-start, $m_P = dP[\%]/df$, $m_{Pt} = dP[\%]/dt$ with increments between 1% to 100% per unit).

- Power factor configuration

    - Fixed power factor ($cos\varphi$) operation (based on a given AC network feeder location, ac system reactance to resistance X/R ratio)

    - Adjustable power factor function of active power ($cos\varphi(P)$)

- Dynamic grid-support functions

    - Frequency-active power control mode (Frequency-watt: $P(f)$)

    - Voltage-active power control mode (Volt-watt: $P(v)$)

    - Voltage-reactive power control mode (Volt-var: $Q(v)$).

- Load shedding.

- Communication support with ability to accept external commands and to perform advanced functionalities.
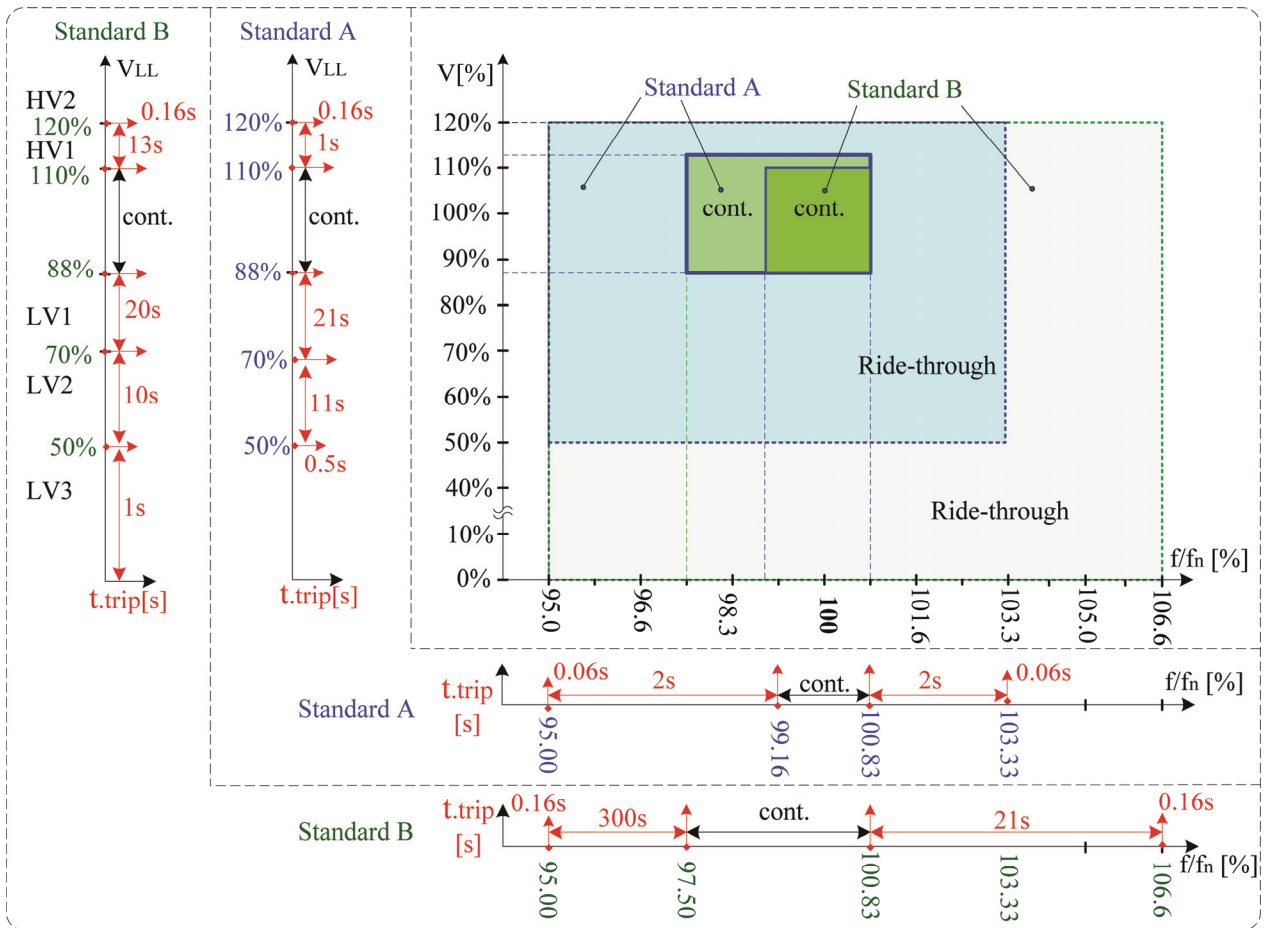
Figure 4.1: Converter settings example for grid limits of voltage vs. frequency.

Figs. 4.1 and Fig. 4.2 illustrate examples of voltage trip and ride-through settings for two different standards (e.g. similar with the following evolving standards, HECO and Rule21) with the following distributed generator (DG) behavior:

- The DG must stay connected in operation during the ride-through until voltage/frequency-time elapses.

- For voltage/frequency excursions beyond certain limits the DG must cease to energise within a specific timing (standard dependent).
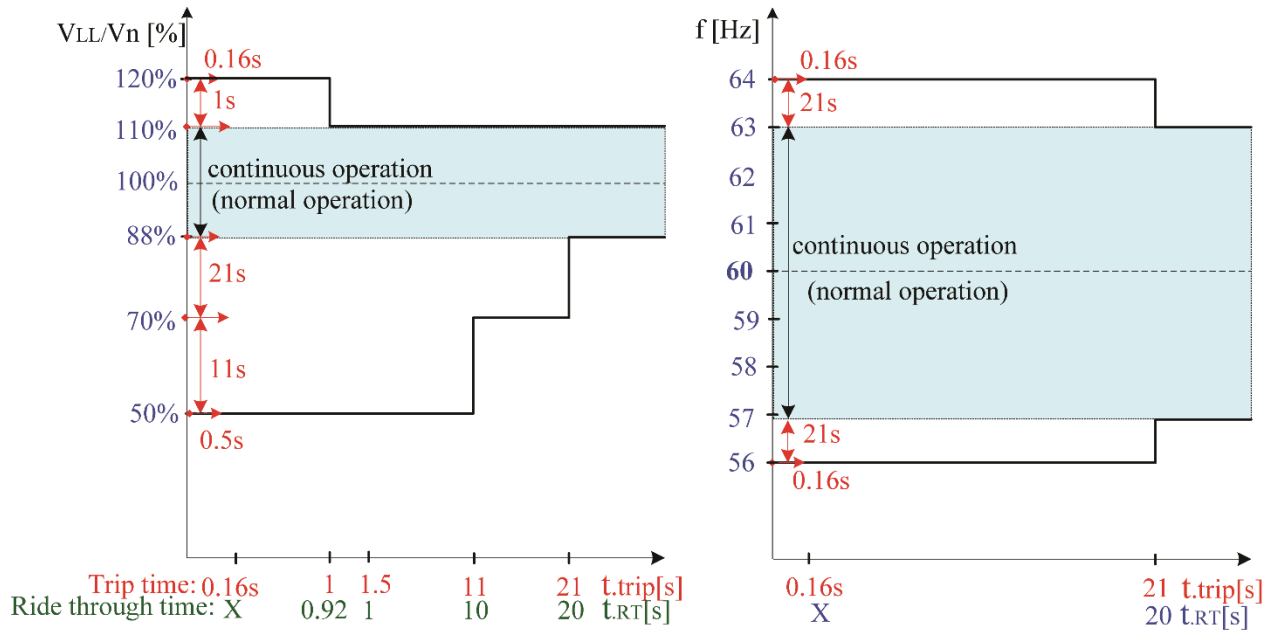
Figure 4.2: Voltage and frequency disconnect limits required by Standard A (e.g. similar with Hawaii Electric Company's grid interconnect standard requirements).

In recent years, with a higher penetration of renewable distributed generators into the ac grid network, the risk of grid instabilities and vulnerabilities has increased.

This chapter presents grid support strategies that can be used to alleviate the grid frequency-voltage variations, which are used in this research as the main indicators of the imbalance between power generation and consumption within an ac network. The proposed strategies to support grid stability in the event of frequency-voltage variation go beyond recent standards and provide extended functionalities.

The pre-configured set-points of active power-frequency $P(f)$ strategy features the control of the converter's power flow direction with an adjustable power gradient transition between grid-feeding and force charge as grid-loading, in response to grid frequency deviation. The proposed control strategy uses the generator reference frame convention illustrated in Fig. 4.3.

Grid-feeding

$q = Q/Sn$

S_n

II   I

$\overleftarrow{P} < 0$ (receives)

$\overrightarrow{Q} > 0$ (delivers)

GRF

PF leading
(over-excited)
PF > 0   (IEEE)
PF < 0   (IEC)

$\overrightarrow{P} > 0$ (delivers)

$\overrightarrow{Q} > 0$ (delivers)

GRF

PF lagging
(over-excited)
PF < 0   (IEEE)
PF > 0   (IEC)

C

L

R

$p\,(P/Sn)$

$\overleftarrow{P} < 0$ (receives)

$\overleftarrow{Q} < 0$ (receives)

GRF

PF lagging
(under-excited)
PF < 0 (IEEE/IEC)

L

III   IV

C

$\overrightarrow{P} > 0$ (delivers)

$\overleftarrow{Q} < 0$ (receives)

GRF

PF leading
(under-excited)
PF > 0 (IEEE/IEC)

$q = -Q/Sn$
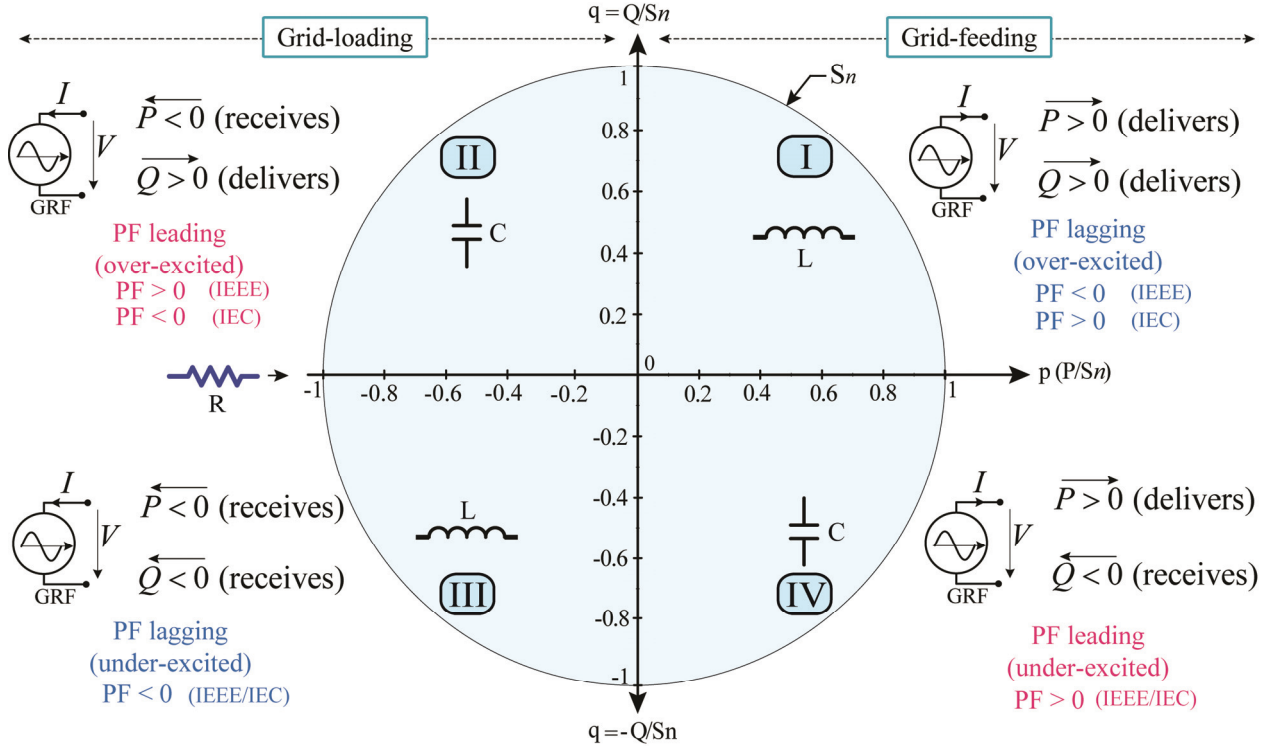
Figure 4.3: Generator Reference Frame (GRF) convention used for the proposed control strategy.

The grid support strategies $P(f)$ and $Q(v)$ are implemented and integrated within a bi-directional EES converter with the power exchange occurring between dc EES and ac grid port. The proposed strategies can be implemented in EES converters topologies used in both renewable energy storage and electric vehicles applications, due to the commonality of the ac grid and dc battery port.

The power converters must be designed to reliably provide active and reactive power to the grid. Typical PV inverter are designed to operate only in first and fourth quadrant (with limited capabilityy of reactive power Q_{limPF1}, Q_{limPF2} related to PF range, e.g. 0.8 lead/lag), as shown in Figs. 4.3 and 4.4. However, the EES converter can be designed to all four-quadrant operation (with increased limits of reactive power capability). In this way, fast-reacting with active and reactive power capabilities, the EES converter can provide enhanced grid support under difficult transient conditions.
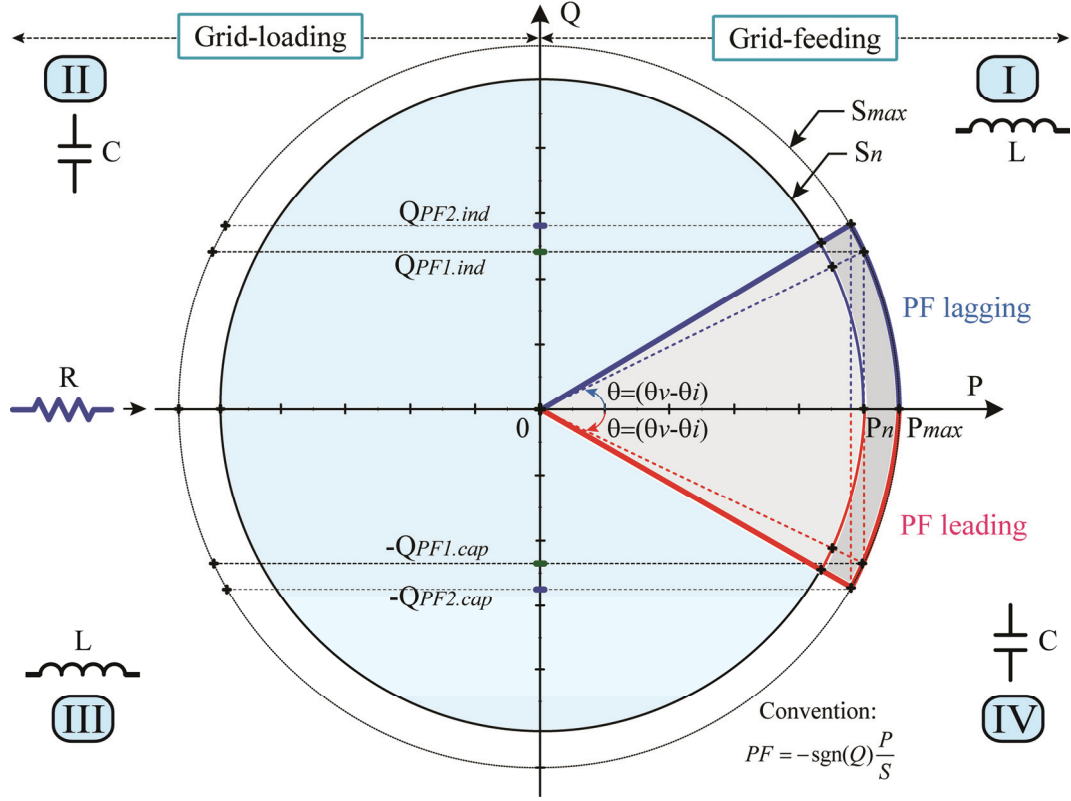
Figure 4.4: Active and reactive power capability example for grid-connected converters.

A fundamental limit for the converter operation's capability is the maximum apparent power (S_{max}), as shown in Fig. 4.4. The power factor (PF leading or lagging) can be controlled up to a maximum value of reactive power that the converter is designed for, $Q_{max}(t) = \sqrt{S_{max}^2 - P^2(t)}$. The nominal power ($S_n, P_n$) is tipically the nameplate of the converter ratings, specified over a certain operating conditions (e.g. $-25°C\ to + 50°C$ ambinent temperature range). The converter may be allowed to exceed it's nominal ratings to an extended power level (S_{max}, P_{max}) within a lower temperature range or for shorter duration in operation. Once the converter limits are established, then the active and reactive power capability can be used for grid-support purposes.

The proposed controller with ancillary supportive features is applicable for both low-voltage (mainly resistive, $X/R \ll 1$) and medium/high-voltage (inductive dominant, $X/R \gg 1$) grids.

The advantages of the proposed controller reside in the flexibility of the controller features (e.g. configuration and set-points for frequency- and voltage assist with $P(f)$ - $Q(v)$ strategies and energy management, Fig. 4.5 (b)) and in the power balancing with applications in both utility-grid and micro-grid systems. In this case, the distributed power generators are equipped with an energy storage converter, with the capacity to discharge and charge the Electrical Energy Storage (EES) element, primarily for grid support purposes.

The EES energy storage is configured for later usage when the grid requires active power support, under line frequency deviation, used under normal conditions, or during on-peak tariff high demand daytime hours (energy shifting for time of use (TOU), ac load shave). In addition to grid support enhancement, the $P(f)$ strategy is combined with reactive power-voltage $Q(v)$ control to attempt to correct frequency and voltage deviations in a collective impact of distributed generators operation for grid stabilization purposes. The $P(f)$ - $Q(v)$ strategy provides an automatic active/reactive power generate/receive pre-configured control, in response to frequency-voltage deviations, in order to support the grid and prevent network instabilities.

The proposed control strategy for local frequency- and voltage-assist is applicable for single and three-phase grid converters interfaced with energy storage systems. Simulations and experimental results, obtained using a single phase 6-kVA four-quadrant EES converter, are presented to validate the proposed $P(f)$ and $Q(v)$ grid support strategies.
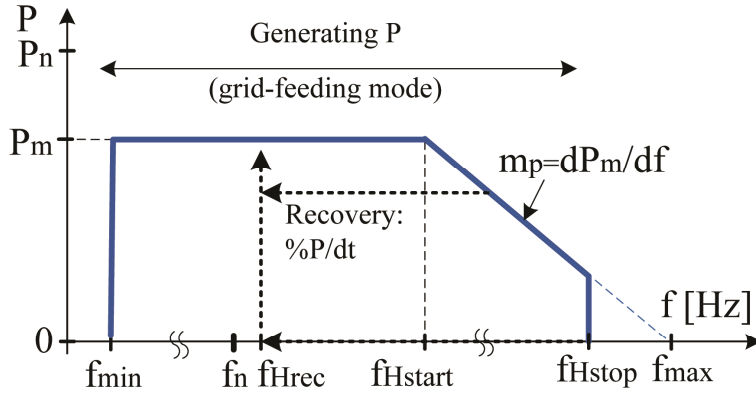
(a) Standard active power curtailment
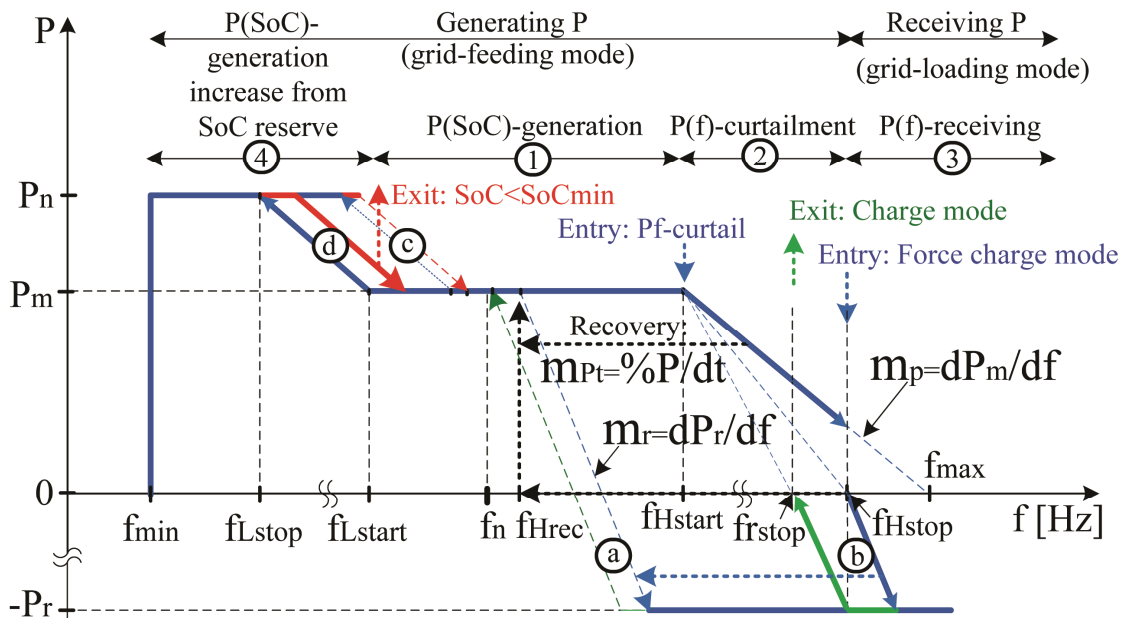
(b) P(f) grid support strategy

Figure 4.5: Active power control under grid line frequency variation.

(a) Standard requirement for the converter power curtailment.

(b) Proposed $P(f)$-strategy for grid support with the converter active power balancing for generation (P) and receiving (P_r) in response to line frequency variation.

This section presents an integration of PV and battery EES for grid-support controls with extended capabilities, beyond present GC standards. The specific GC requirement that converters cease operating beyond a certain frequency limit is implemented, in the existing methods, by suddenly disconnecting from the grid during power curtailing, which induces a local perturbance

in the grid network. Furthermore, this effect could be amplified in cases where there is high renewable PV/wind penetration in the grid network. In contrast, the proposed controller transitions the power flow from grid-feeding to force charge, using a grid-loading mode for ac network power balancing.

Table 4.1: Frequency configuration example (country specific standard) for grid support.

Configuration Parameter	Minimum limit	Default value		Maximum limit	Description
		50Hz-Grid	60Hz-Grid		
f_{Lstop} [Hz]	40	47.5	58.0	70	Low frequency deviation set-point for rated active power generation
f_{Lstart} [Hz]	40	49.5	59.7	70	Low frequency deviation set-point for start of rated active power generation
f_n [Hz]	-	50	60	-	Nominal grid line frequency
f_{Hrec} [Hz]	40	50.05	60.05	70	High frequency recovery limit for return to normal active power generation
f_{Hstart} [Hz]	40	50.2	60.2	70	High frequency start set-point for active power curtailment
f_{rstop} [Hz]	40	51.0	61.0	70	High frequency recovery limit for return to recovery to active power generation
f_{Hstop} [Hz]	40	51.5	61.5	70	High frequency start set-point for active power receive (storage)

Table 4.2: Power gradient configuration example (country specific standard) for grid support.

Configuration Parameter	Minimum limit	Default value		Maximum limit	Description
		50Hz-Grid	60Hz-Grid		
m_P, m_r [W/Hz]	0%	50%	40%	500%	Active power gradient with frequency
m_{Pt} [W/s]	0%	10%	10%	10000%	Active power gradient with time

Grid-loading charge mode represents the new transitional operational state used for the proposed control strategy. The controller commands the EES converter to transition from operating in grid-feeding, to operating in force charge grid-loading. The transition is implemented with adjustable ramps (m_P, m_r, Table 4.2) for overall power smoothing/balancing, which results in improvements to grid stability.

The typical application for the proposed controller relates to variable renewable PV/wind generation, which markedly affects the stability of the operation of utility-grid systems (e.g. Hawaiian Islands). The main contributions of this chapter are listed below and conceptually represented in Fig. 4.5 (b).

1) Extended $P(f)$ utility-grid support strategy: the converter's capacity to actively generate/receive power in response to frequency variation. The controller features an EES converter that operates in grid-feeding mode, while outside of the permissible GC frequency-voltage limits, commands the transition to force charge grid-loading in an attempt to gain stability through frequency-assist. The transition between grid-feeding and grid-loading is achieved using an adjustable power gradient, for smooth network power balancing.

2) Combined $P(f)$ - $Q(v)$ grid support strategy: the converter's active/reactive power manipulation for frequency- and voltage-assist in response to signs of grid instability. The $P(f)$ - $Q(v)$ control references follow pre-configured force charge/discharge set-points, for operation in the direction of frequency and voltage correction errors induced by variable PV/wind imbalances.

3) The $P - Q$ decoupled set-points are calculated from the pre-configured values of SoCmin, power gradient, energy shifting for TOU, voltage and frequency limits for immediate grid frequency- and voltage-assist in a network of DGs to achieve grid stabilization.

The $P(f)$ and $Q(v)$ grid support strategies are implemented and integrated within a bi-directional EES converter with the power exchange occurring between the dc EES and the ac grid port. The proposed strategies can be implemented in EES converters topologies used in both renewable energy storage and electric vehicles applications, due to the commonality of the ac grid and dc battery port. The proposed controller with ancillary supportive features is applicable for both low-voltage (mainly resistive, $X/R \ll 1$) and medium/high-voltage (inductive dominant,

$X/R \gg 1$) grids. The advantages of the proposed controller reside in the flexibility of the controller features (e.g. configuration and set-points for frequency- and voltage assist with $P(f)$ - $Q(v)$ strategies and energy management, Fig. 4.4 (b)) and in the power balancing with applications in both utility-grid and micro-grid systems.

This chapter presents the control architecture which describes the implementation of $P(f)$ - $Q(v)$ beyond standard grid support requirements, validated by the experimental results in Section 4.3.

4.2. Grid Support in Grid-connected Converters Using P(f) and Q(v) Strategies

EES converters will have a potentially great impact on renewable support, in energy smoothing/shifting, fossil generation support (e.g. diesel generators), contingency reserve, and power outage mitigation. An example of a PV smoothing application, is the use of EES converters designed with grid support features, in conjunction with the active and reactive power controls.

In this chapter, the EES converter monitors the grid frequency-voltage deviations for the active and reactive power flow manipulation in grid-feeding/loading mode, by using the following two proposed methods: $P(f)$ and combined $P(f)$ - $Q(v)$ grid support strategies.

4.2.1. P(f) Strategy: Active Power Control in Response to Line Frequency Variation

The grid power over-production results in line frequency increases, where the distributed generators cease to operate over a specified limit due to standard requirements. Instead, the proposed solution supports the ac network grid by reversing the active power flow of the EES

converter by loading the grid at upward frequency variation. The ac network distributed loading has a stabilizing effect on the overall power generation and consumption. The focus of this section is on the grid support control strategy, implemented at the local level of the distributed power generator (in the form of EES converter), while the power balancing effect on consumption vs. generation within the ac network, is not quantified.

To further enhance grid support under frequency response, this chapter proposes a solution that includes increasing active power generation/receiving for under/over frequency operation with automatic upward and downward ramp rate control. The recent standards for power curtailment are conceptually represented in Fig. 4.5 (a), indicating two operating regions. The proposed strategy is depicted in Fig. 4.5 (b), extending the operating modes well beyond existing standards.

Fig. 4.5 (a) shows the standard requirement for curtailing a converter's active power under grid frequency variation. If the grid frequency increases above f_{Hstart} limit, the converter must reduce its momentary output power P_m by a specified gradient (e.g. $m_P = 40\%$ of rated power per Hertz).

If the grid frequency is outside of $[f_{min}, f_{Hstop}]$, the converter must cease to generate power, as per GC requirements. The existing methods meet the grid requirement through grid-disconnection during the power curtailment, causing potential perturbance to the grid network. This undesirable effect could be amplified in applications with high PV/wind grid network penetration. The controller changes the operation from grid-feeding to charge grid-loading mode. The transition is implemented using flexible ramps (m_P, m_r) for overall power smoothing/balancing, which results in improvements to grid stability and, more importantly, in numerous renewable DGs within the ac network.

In comparison, Fig. 4.5 (b) illustrates the proposed $P(f)$ strategy, which provides the ability to charge and discharge the EES element for grid support purposes (frequency-assist with power balancing), and which has the following modes of operation:

① Normal operation $P(SoC)$-generation, in which the converter delivers active power from the state of charge (SoC) availability, under a controlled energy discharge from the EES element. While the converter operates at the nominal line frequency (f_n), the momentary active power (P_m) is supplied to the grid at a controlled SoC level. This specific mode of operation is usually used for load shaving, where the stored energy is supplied back to the grid during times when the price rate of electricity is higher in energy shifting for TOU.

② $P(f)$-curtail operation mode, where the active power reduces under frequency increase. In this case, the controller is designed with two modes of configuration based on the frequency range:

2.a) Immediate transition to grid-loading mode. The controller detects a rate of change in frequency increase ($f > f_n$ and $|\Delta f / \Delta t| > 0$) and commands force charge with adjustable gradient m_r in power receiving mode. This specific frequency-assist configuration provides fast and pro-active assistance in a network of DGs for grid stabilization purposes.

2.b) Standard $P(f)$ curtailment followed by grid-loading mode. This configuration is used when priority is given to power generation, and presents a reactive response to grid stabilization. The EES converter operates in generation mode, performs energy shifting for TOU or exports potential extra power received by the battery from another device. As the grid line frequency increase over a configurable threshold (f_{Hstart}), the grid-connected converter enters $P(f)$ −curtail mode by linearly decreasing the active power according to a configurable gradient (m_P). According to the current standards [73] - [77], the converter must stop operating (cease power generation) when the frequency exceeds the frequency limit f_{Hstop}. When the line

frequency returns below f_{Hrec}, the grid-connected converter recovers and starts supplying power to the grid with a time constant linear increase ($m_{Pt} = \%P/dt$, Table 4.2). These measures are imposed to avoid the 50.2Hz problem (e.g., reported as occurring in the low voltage distributed network in Germany), which can potentially lead to major grid disruption.

③ P(f)-receiving operation, in which the converter forces its operation mode to charge for grid-loading (active rectifier) mode beyond f_{Hstop}. The controller addresses the EES converter's operation outside of tolerable standard limits, since the GCs restrict the power generation only (cease export power). In this proposed strategy, the converters become a load for the grid by importing power (P_r) into the EES dc port. After the entry moment in grid-loading mode, the converter linearly increases active power receiving to the maximum limit P_r. If the line frequency starts to recover, the converter linearly decreases its receiving power and exits the rectification mode, while the frequency decreases below f_{rstop}, as illustrated in Fig. 4.5 (b). There are two immediate benefits to this suggested grid support strategy. First, the ac network loading contributes to a natural grid frequency recovery, compensating for the excess in power production. Second, during the line frequency increase, the energy is stored in the EES element and later used (energy shifting for TOU) when the grid frequency recovers at the nominal frequency (f_n), or when the frequency decrease below a critical value (f_{Lstart}).

④ $P(SoC)$-generation increases by drawing from the SoC power reserve as a result of the line frequency reduction. Like the over-frequency (e.g. > 50.2Hz) problem, the under-frequency (e.g. < 49.5Hz) problem represents a major risk to the stability of the ac network, and can lead to disruptions in the power supply. In the proposed strategy, the controller is designed with the following modes of configuration:

1) $P(f)$ active power generation (increase or curtail) and receive (grid loading with EES charge mode) arbitration with grid line frequency variation, Eq. (4.1).

2) $Q(v)$ reactive power generation under line voltage variation, Eq (4.3), (4.4).

$$p(f, P_m, m_P, SoC) = \begin{cases} 0 & if \quad f \leq f_{\min} \\ P_n & if \quad f_{\min} < f \leq f_{Lstop} \\ \left(P_n - \dfrac{P_n - P_m}{f_{Lstart} - f_{Lstop}}(f - f_{Lstop}) \right) & if \quad f_{Lstop} < f \leq f_{Lstart} \\ P_m & if \quad f_{Lstart} < f < f_{Hstart} \\ P_m \left(1 - m_P (f - f_{Hstart}) \right) & if \quad f_{Hstart} < f < f_{Hstop} \\ -P_r(SoC) & if \quad f \geq f_{Hstop}. \end{cases} \tag{4.1}$$

4.c) Immediate grid-support frequency-assist mode. The controller detects a rate of change in frequency decrease ($f < f_n$ and $|\Delta f / \Delta t| < 0$) and commands force discharge, with increased power generation.

4.d) Standard $P(SoC)$-generating mode. The converter supports the grid by increasing the level of power generated from the SoC reserve when the frequency falls below f_{Lstart} (force discharge). It should be noted that if the SoC reserve falls below a critical level (e.g. $SoC_{min} = 25\%$), the priority is changed and the EES element enters in conservation mode, where the converter ceases to operate, regardless of the status of the ac network.

The P(f) strategy illustrated in Fig. 4.5 (b) is programmed in response to line frequency variation and is described as per relationship (4.1).
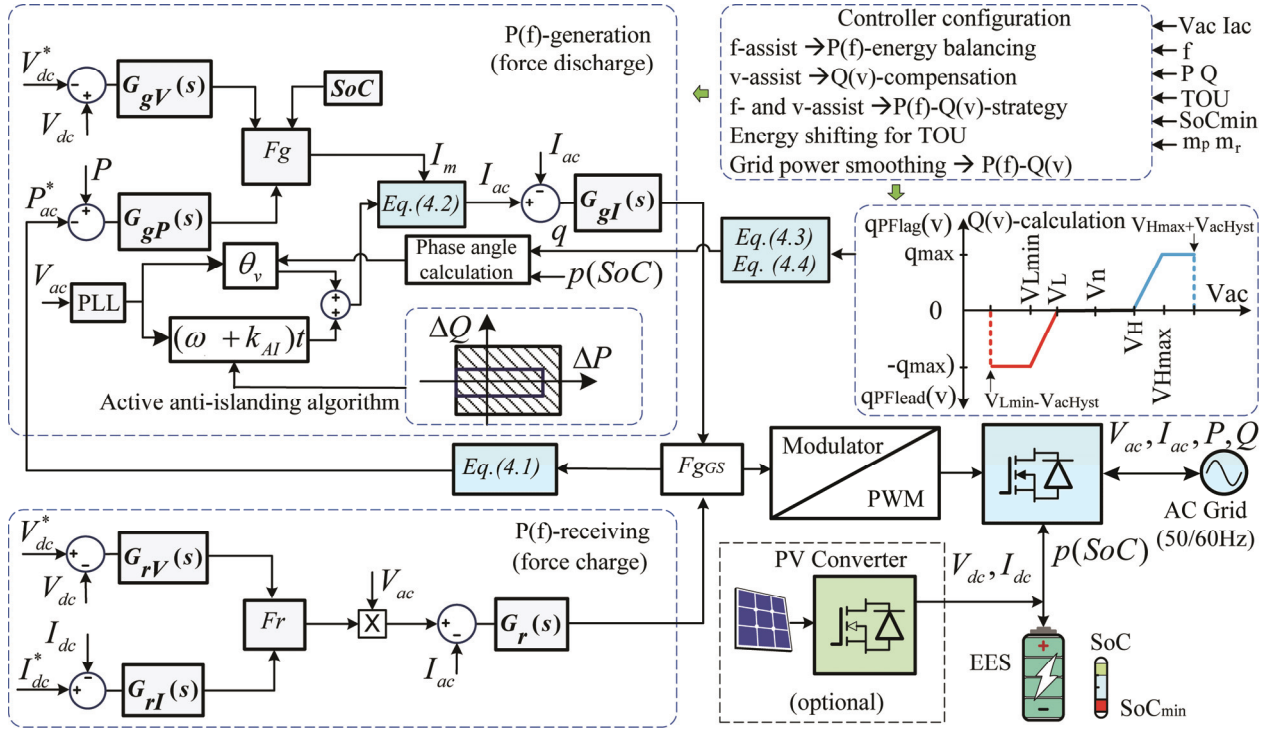
Figure 4.6: Single phase EES converter controller block diagram example: $P(f)$-generate/receive and combined $P(f) - Q(v)$ strategies for ac network power balancing.

Fig. 4.6 illustrates the single-phase converter control diagram for $P(f)$-generate/receive and combined $P(f)$ - $Q(v)$ strategies. The $P(f)$-generation strategy is achieved with the converter operating in current-controlled source inverter mode. The ac-current reference I_{ac}^* is a function of the dc voltage-loop controller G_{gV}, EES state of charge (SoC) and ac power-loop controller G_{gP}. The output of the selection function F_g is a normalized value of voltage, SoC or ac power, which controls the magnitude of the sine-wave generator I_m. The sine wave reference $I_{ac}^*(t)$ is generated by a look-up table with the amplitude scale reference I_m (function of EES voltage regulation, active power and SoC) and phase angle θ_v (function of the desired reactive power generation):

$$\begin{cases} I_{ac}^*(t) = I_m \sin[(\omega_0 + k_{AI}(t)) \cdot t + \theta_v] \\ I_m = f(V_{dc}, P, SoC) \\ \theta_v = f(Q). \end{cases} \tag{4.2}$$

The grid-connected converter current reference is designed with an islanding search sequence [78] at the PLL stage, where the anti-islanding algorithm (k_{AI}) detects the grid faults. The current controller G_{gI} output signal is further processed through the modulator in order to control the gate of the single-phase, two-level, full-bridge converter. The grid support function F_{gGS} selects the converter's mode of operation, $P(f)$-generate or receive, depending on the frequency variation obtained from equation (4.1). The $P(f)$-receiving strategy is represented by charge (active-rectifier) mode of operation, where the converter has three control loops. The inner power factor control loop (G_r) commands the input ac current to track the ac grid voltage (V_{ac}) with near unity power factor. Two low-bandwidth outer control loops are implemented for dc voltage regulation (G_{rV}) and dc current regulation (G_{rI}), for the EES charging phase. The $P(f)$ strategy has an automatic power generation/receive response to the frequency variation, and does not require an extra communication protocol between distributed EES converters and the transmission system operator of the main ac network generator. The mode of communication within the ac network is performed through the frequency or voltage variation [124].

4.2.2.   Combined P(f)and Q(v) Strategy for Enhanced Grid Support

The imbalance between power production and consumption within an ac power generation network can lead to grid frequency-voltage instability with the potential to disrupt power delivery. The $P(f)$ strategy forces the EES converter to generate/receive active power, when the grid frequency varies from its nominal value. The grid support $P(f)$ capability of distributed EES converters is enhanced with reactive power generate/receive $Q(v)$, at grid voltage deviation. The proposed grid support capability uses the $P(f)$ strategy combined with a reactive power $Q(v)$ controller (local voltage-assist mode).

When the ac grid network operates at a lower value voltage than the nominal (e.g. $V_n=230V_{rms}$) of ac grid network, the grid support $Q(v)$ controller uses relation (4.3), which is applicable in a case where the converter is controlled with power factor lead. Relation (4.4) is used by the grid support $Q(v)$ strategy at higher than nominal ac voltage, in a case where the converter is controlled with power factor lag.

The combined $P(f)$ and $Q(v)$ strategies provide a control option for active and reactive power grid support during deviations of both line frequency and voltage from the nominal values (local frequency- and voltage-assist). Fig. 4.7 shows a $P(f)$ - $Q(v)$ grid support flowchart with the states of EES converter operation.
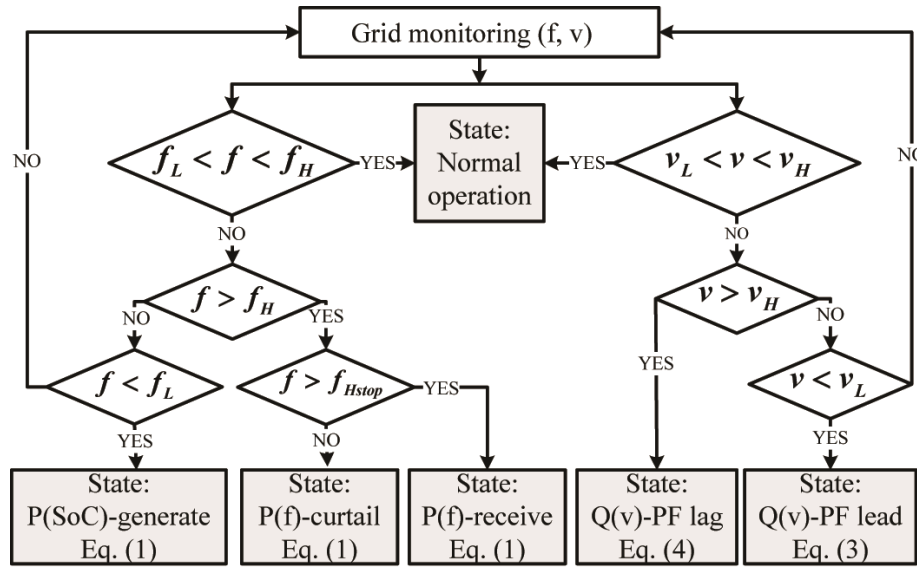
Figure 4.7: $P(f) - Q(v)$ grid support flowchart diagram.

Fig. 4.8 shows a typical dc-centric power system used in commercial and residential applications. The system consists of an EES battery (similar to line-interactive uninterruptible power supply) connected to a grid-connected bidirectional converter and an ac load port. The battery lifetime is a function of SoH and is dependent on charge/discharge rates, SoC swing operation ranges, DoD, number of cycles and operating temperature. Longer battery life can be achieved in the following two cases:

- As an alternative, an optional dc-dc PV converter is installed to increase the battery lifespan and the amount of renewable power generated. As can be seen in Fig. 4.8 (b), the battery bank is conditioned with a three-stage charge profile (bulk, absorption and float), while the PV energy surplus is exported to the ac load and grid port.

- When the PV converter is not part of the system, the active power set-point with SoC depth of discharge is limited to a minimum value (SoC_{min}), and if the critical level is reached, then the grid support is abandoned, based on a pre-configured priority to preserve EES. The complete EES re-charge process is programmed during the off-peak tariff (e.g. night time).

$$q_{PFlead}(v) = \begin{cases} 0 & if \quad 0 \le v \le \left(V_{L\min} - V_{acHyst}\right) \\ -\left|q_{\max}\right| & if \quad \left(V_{L\min} - V_{acHyst}\right) < v \le V_{L\min} \\ -\left|q_{\max}\right|\left(1 - \dfrac{v - V_{L\min}}{V_L - V_{L\min}}\right) & if \quad V_{L\min} < v \le V_L \\ 0 & if \quad V_L < v \le \dfrac{V_L + V_H}{2}, \end{cases} \tag{4.3}$$

$$q_{PFlag}(v) = \begin{cases} 0 & if \quad \dfrac{V_L + V_H}{2} \le v \le V_H \\ \left|q_{\max}\right|\dfrac{v - V_H}{V_{H\max} - V_H} & if \quad V_H < v \le V_{H\max} \\ \left|q_{\max}\right| & if \quad V_{H\max} < v < \left(V_{H\max} + V_{acHyst}\right) \\ 0 & if \quad v \ge \left(V_{H\max} + V_{acHyst}\right). \end{cases} \tag{4.4}$$

Table 4.3: Reactive power and ac voltage configuration example (country specific standard) for grid support mode.

Configuration Parameter	Minimum limit	Default value		Maximum limit	Description
		230V-Grid	240V-Grid		
q_{PFlead} [%]	0%	40%	40%	100% [*]	Capacitive reactive power set-point
q_{PFlag} [%]	0%	40%	40%	100% [*]	Inductive reactive power set-point
V_{Lmin} [%]	10%	90%	92%	100%	Low voltage deviation set-point for rated capacitive reactive power support
V_L [%]	10%	97%	98%	100%	Low voltage deviation set-point for start of capacitive reactive power support
V_n [%]	-	100%	100%	-	Nominal grid voltage
V_H [%]	100%	102%	102%	110%	High voltage deviation set-point for start of inductive reactive power support
V_{Hmax} [%]	100%	108%	106%	120%	High voltage deviation set-point for rated inductive reactive power support
V_{acHyst} [%]	0%	2%	2%	10%	AC voltage hysteresis set-point

(*) Note: Maximum limit for reactive power is given by converter's power capability (Fig. 4.4).
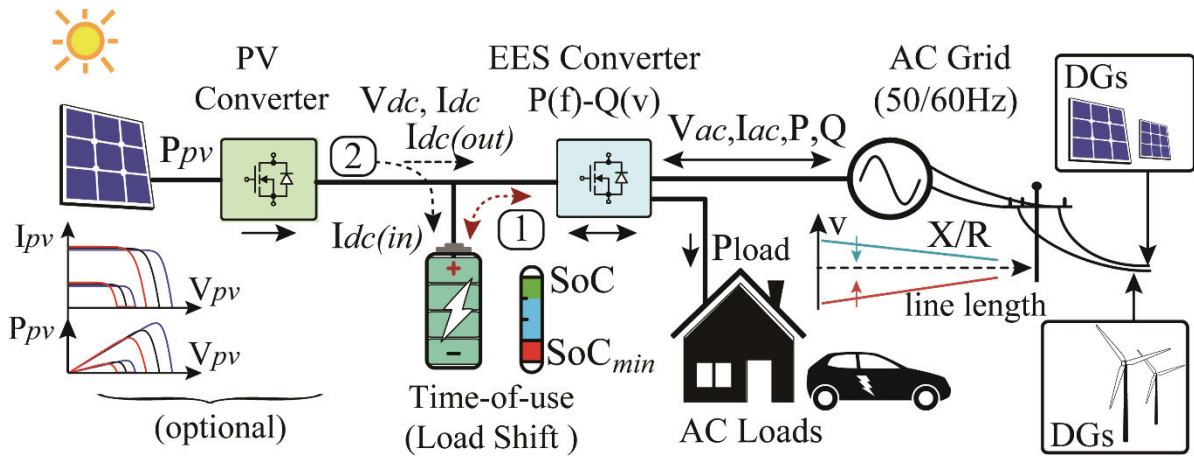
(a) Typical PV-ESS residential power system
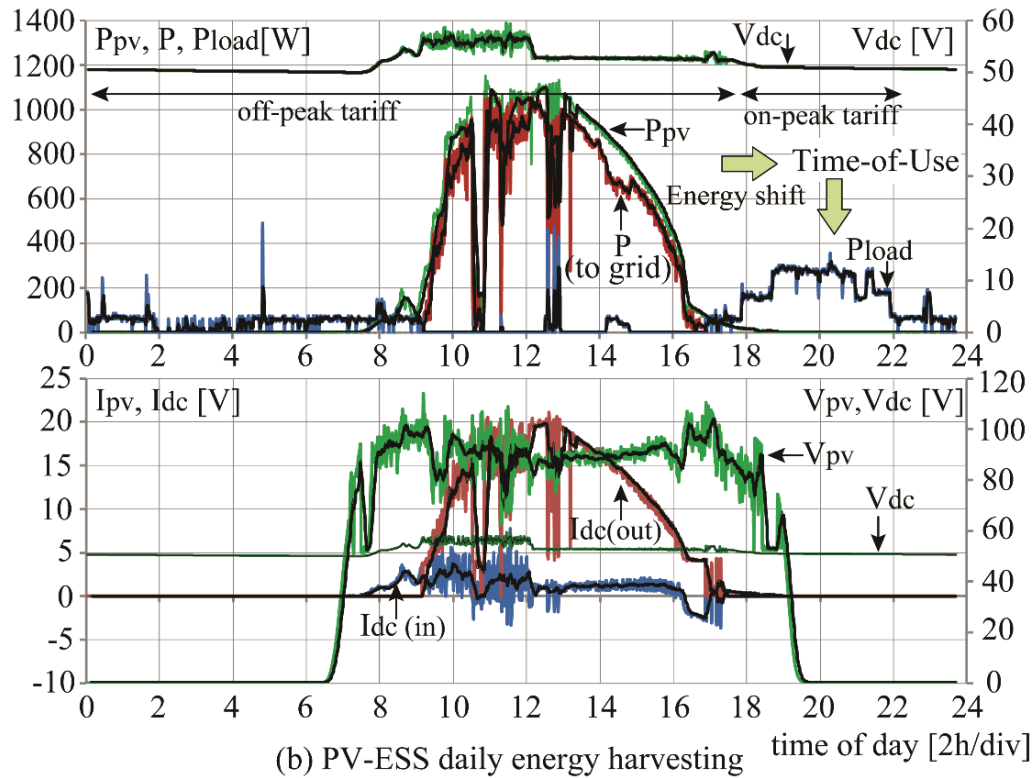
Figure 4.8: Grid-connected EES power system for energy management and $P - Q$ control strategies application.

(a) Typical dc-centric architecture: the battery EES can be charged and discharged (1) through bidirectional grid-connected converter. Optionally, for better battery SoC/SoH maintenance, the battery can be charged (2) through unidirectional dc-dc PV converter.

(b) Daily energy harvesting during a mixed sunny and overcast. Data collection: September 2015, Greater Vancouver area (New Westminster), Canada.

The variability of PV/wind power generation influences the grid system's stability. The controller can be configured using external forecast communication 'heads-up' data of PV/wind ramp events. Additionally, the EES converter's controller is designed with automatic pre-configured control settings and monitoring for frequency- and voltage-assist, time shifting for TOU and power smoothing.

The power balancing exchange with the grid is performed using the battery EES, which is a vital system component, and careful attention must be paid to battery sizing to ensure the maximum performance and longevity of the EES system. The battery EES system sizing is based

on the scheduled energy shifting for TOU, maximum allowable DoD, SoC swing range, frequency of charge/discharge rates and operation temperature range.

The metrics of dc to ac system conversion efficiency (η_{conv}) are also considered in system sizing in order to calculate the effective usable energy from EES to ac port, e.g. $E_{ac}[kWh] = E_{EES}[kWh] \cdot DoD[\%] \cdot \eta_{conv}[\%]$.

As shown in Fig. 4.8, the system controller can be designed to drive the EES converter operation in grid-forming (stand-alone UPS mode under grid fault), grid supporting (micro-grid), grid-feeding (utility-grid) and grid-loading charge mode.

The controller implementation provides a flexible architecture, with options and configurations for multiple operation modes, by using the same converter hardware, thanks to the presence of a battery energy storage system and the use of a four-quadrant selection converter topology. The EES converter designed and equipped with $P(f)$ and $Q(v)$ features, when distributed within an ac network, provides a balanced power generation/consumption ratio, to help stabilize the grid.
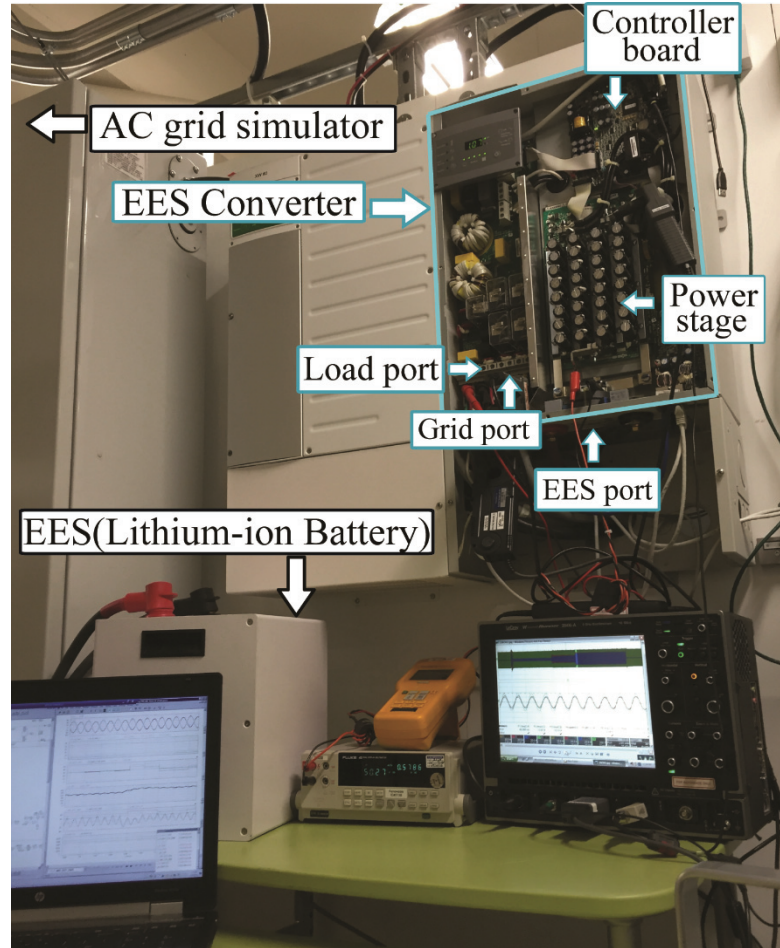
Figure 4.9: Experimental setup for $P(f) - Q(v)$ frequency- and voltage-assist control strategies evaluation.

4.3. Voltage and Grid Support Simulation and Experimental Results

The performance of the grid support strategy presented in this chapter was tested beyond the standard requirements by implementing and testing the strategy on a two-level, single-phase four-quadrant, 6-kVA, $230V_{rms}$/50Hz converter, 48V - 10kWh energy storage system (Fig. 4.9).

The 6-kVA EES converter, equipped with $P(f)$ and $Q(v)$ controllers, monitors the variation of the grid frequency-voltage from the nominal values and the generate/receive active/reactive power for grid support purpose.

Fig. 4.10 (a) shows the EES converter's response at frequency upward deviation: the active power curtails with unity power factor and automatically reverses its direction by receiving the power towards EES port, i.e. loading the grid (force charge mode for frequency-assist).
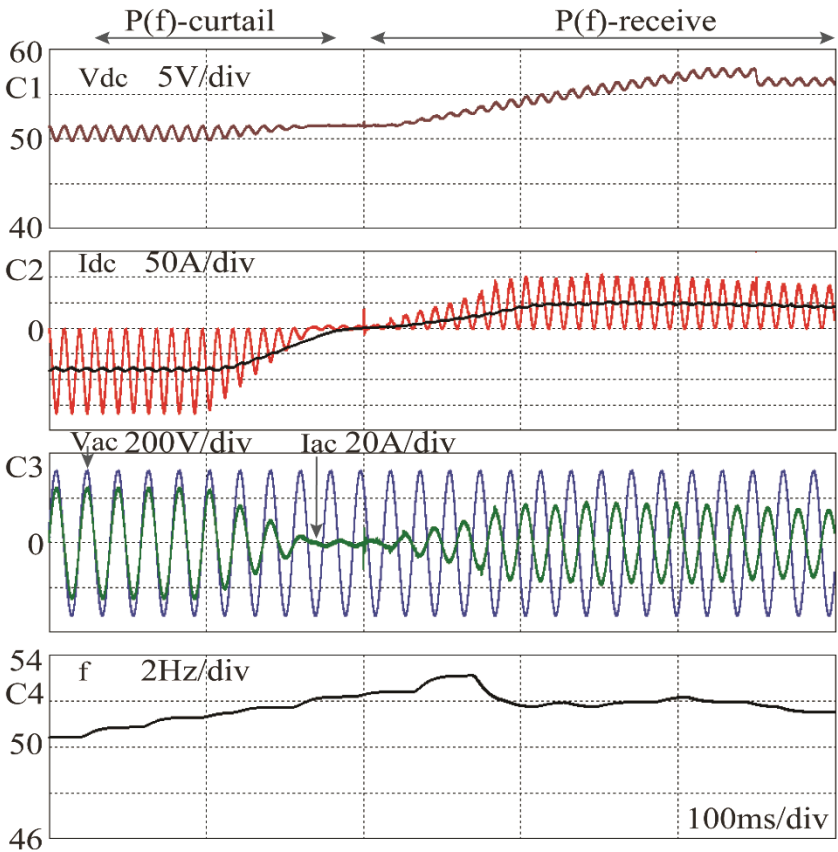
(a) Test performed with $P(f)$-controller enabled during upward frequency variation. $P(f)$ configuration: f_{Hstart}=50.2Hz, f_{Hstop}=51.5Hz, f_{Hrec}=50.05Hz.
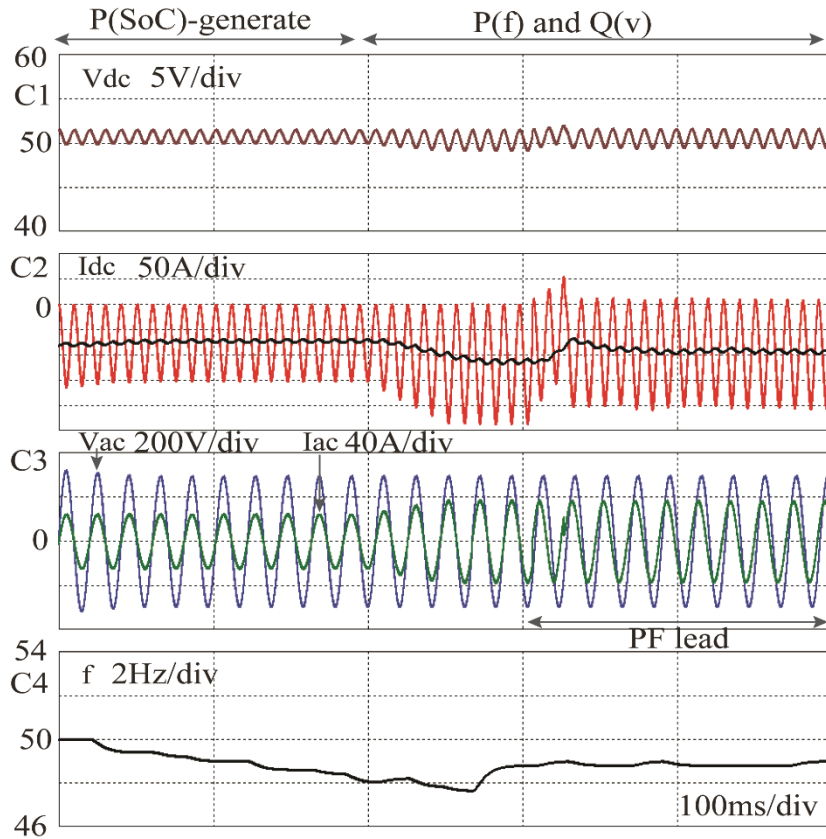
(b) Test performed with $P(SoC)$ reserve active power and reactive power $Q(v)$ during downward frequency variation (50 to 47.5Hz) and voltage reduction (230 to 210 V_{rms}).

Figure 4.10: Simulation results using $P(f)$ and $Q(v)$ grid support strategies.

Y-axis: C1 - V_{dc} EES battery dc voltage 5V/div, C2 – I_{dc} EES battery current 50A/div, C3 - V_{ac} grid phase voltage 200V/div, converter ac current 20A/div, C4 – f, grid line frequency, 2Hz/div. X-axis: 100ms/div.

The deviation of frequency and voltage below from their nominal values (50Hz and 230 V_{rms}) is shown in Fig. 4.10 (b). The converter operates with increased active power drawn from the SoC reserve of EES port in order to support the grid under low frequency operation. While the grid voltage magnitude reduces to $210V_{rms}$, the combined $P(f)$ - $Q(v)$ strategy uses equations (4.1) - (4.4). The converter operates with increased active power and power factor lead in order to stabilize grid frequency and voltage (frequency- and voltage-assist).

4.3.1. Experimental Results Using P(f) Grid Support Strategy
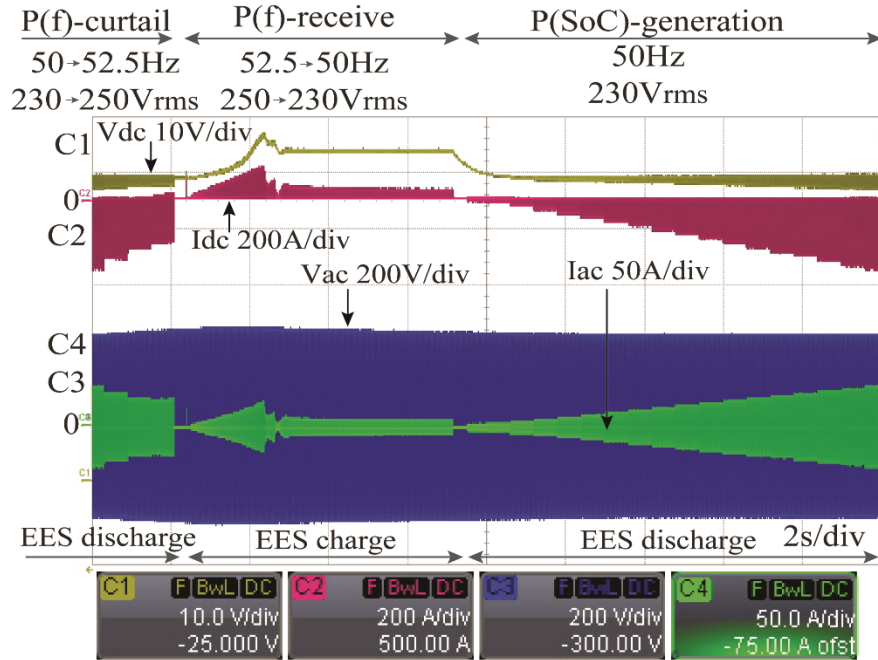
Figure 4.11: Experimental results with $P(f)$ control strategy.

Y-axis: C1 - V_{dc} EES battery dc voltage 10V/div, C2 – I_{dc} EES battery dc current 200A/div, C3 - V_{ac} grid phase voltage 200V/div, C4 – I_{ac} converter ac phase current 50A/div. X-axis: 2s/div.

Test conditions:

- $P(f)$ curtail operation mode: upward frequency-voltage variation (1Hz/s and $8V_{rms}$/s) from 50Hz to 52.5Hz and 230 to 250V_{rms}.

- $P(f)$ receive operation mode: downward frequency-voltage variation (0.25Hz/s and $2V_{rms}$/s) from 52.5Hz to 50Hz and 250 to 230V_{rms}.

- P(SoC) generation: normal operation under nominal grid conditions: 50Hz/230V_{rms}.

- Voltage and frequency settings for protection under unintentional islanding (configurable, based on country-specific standard): (205 - 262) V_{rms}, (47.5 - 51.5) Hz.

- $P(f)$ configuration: f_{Hstart}= 50.2Hz, f_{Hstop}= 51.5Hz, f_{Hrec}= 50.05Hz, m_P= (40%P_n)/Hz.

Fig. 4.11 demonstrates the $P(f)$ grid support strategy's performance during frequency-voltage variation. At the upward frequency variation, the EES converter curtails the power until

the frequency exceeds the set-point of 51.5Hz. While the grid frequency continues to increase (up to 52.5Hz), the controller changes the operation mode to $P(f)$ receive, by loading the grid. The controller's change in operation occurs at the high frequency limit, 51.5Hz, since the converter must only cease generating power to the grid, while receiving/loading power from the grid is permitted by the GCs. The converter performs a two-stage charge, receiving active power and maintaining the dc regulation voltage from bulk to absorption charge phase. Finally, the grid frequency and voltage returns to the nominal values ($50Hz, 230V_{rms}$) and the EES converter returns to $P(SoC)$ mode, actively generating power (discharge) from the available SoC available energy reserve.

4.3.2. Experimental Results Using P(f) - Q(v) Grid Support Strategy

(a) Test performed with $P(f)$-curtail.
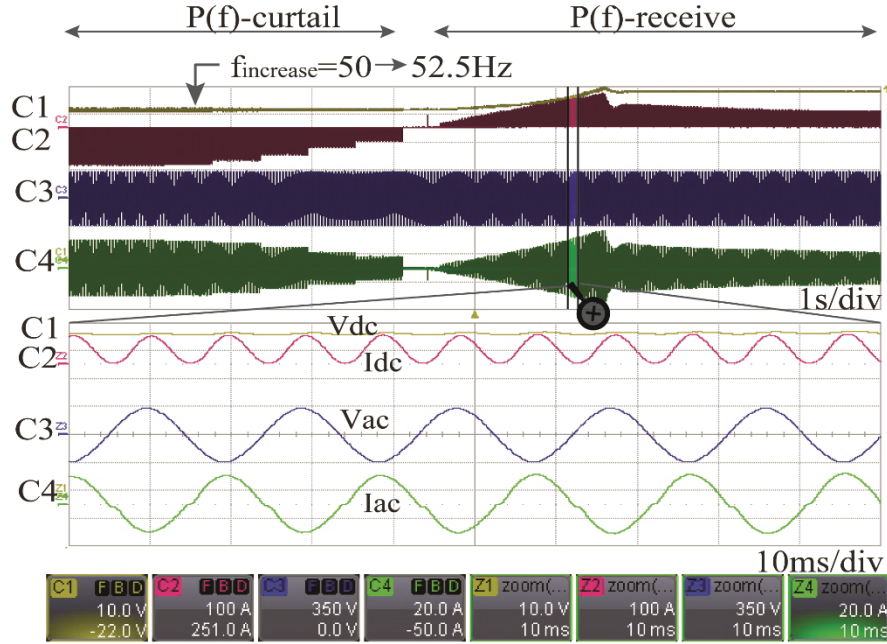
(b) Test performed with $P(f)$-receive.

Figure 4.12: Experimental results performed with $P(f)$ control strategy enabled during upward frequency variation (1Hz/s) from 50Hz to 52.5Hz at unity power factor and nominal grid voltage (V_n=230V_{rms}).

Y-axis: C1 - V_{dc} EES battery dc voltage 10V/div, C2 – I_{dc} EES battery dc current 100A/div, C3 - V_{ac} grid phase voltage 350V/div, C4 – I_{ac} converter ac phase current 20A/div. X-axis: 1s/div and 10ms/div.

Test conditions:

- $P(f)$ configuration: f_{Hstart}= 50.2Hz, f_{Lstop}= 51.5Hz, f_{Hrec}= 50.05Hz, m_P= (40%P_n)/Hz.

- Voltage and frequency settings for protection under unintentional islanding (configurable, based on country-specific standard): (205 - 262) V_{rms}, (47.5 - 51.5) Hz.

Fig. 4.12 (a) and (b) shows the experimental results with $P(f)$ strategy enabled, and with a higher degree of detail: the converter detects the grid frequency upward change from nominal 50Hz to 52.5Hz ($V_{ac} = 230V_{rms}$, $I_{ac} = 15A_{rms}$, unity power factor).

Using the control strategy shown in Fig. 4.6, the converter linearly decreases the current using the $P(f)$-generate strategy. While the frequency is above f_{Hstart}, the converter starts to

196

load the grid by receiving current using the $P(f)$-receive strategy. In this mode of operation, the grid energy is converted and stored in the EES element (48V lead-acid battery system, 10kWh).

Fig. 4.13 (a) shows the converter's operation while both frequency (50 to 52.5Hz) and voltage (230 to 250V_{rms}) are ramping upward. The $Q(v)$ strategy becomes active and linearly delivers reactive power ($Q > 0$) with power factor lag for grid support purpose. Fig. 4.13 (b) shows the converter's power flow reversal, at higher grid frequency operation ($f > 51.5$Hz). In this case, the energy is stored in the EES element for later use, while the grid is loaded in an attempt to balance the ac network's power generation and consumption.
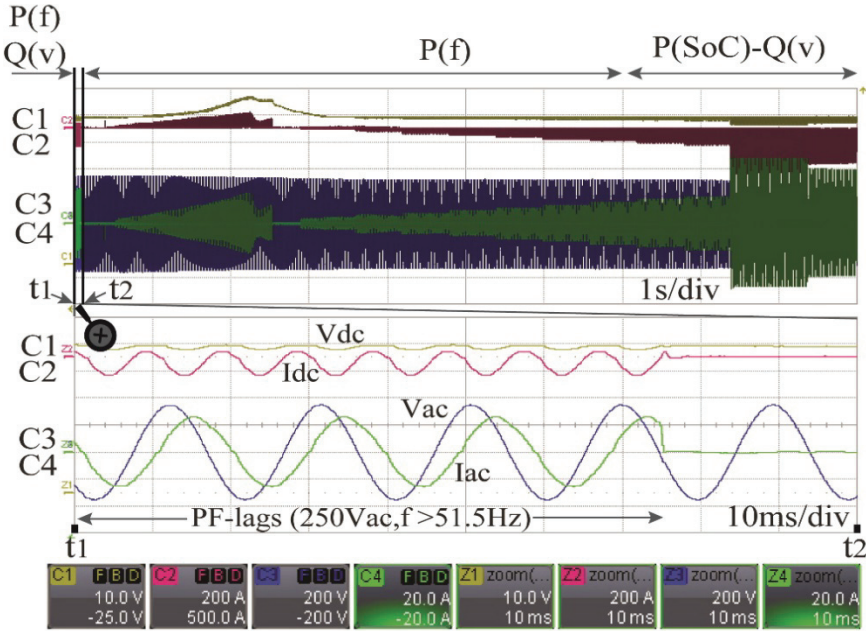
(a) Test performed with combined $P(f)$ and $Q(v)$ strategies at voltage-frequency variation: 230 to 250V_{rms} (8V_{rms}/s) and 50 to 52.5Hz (1Hz/s).
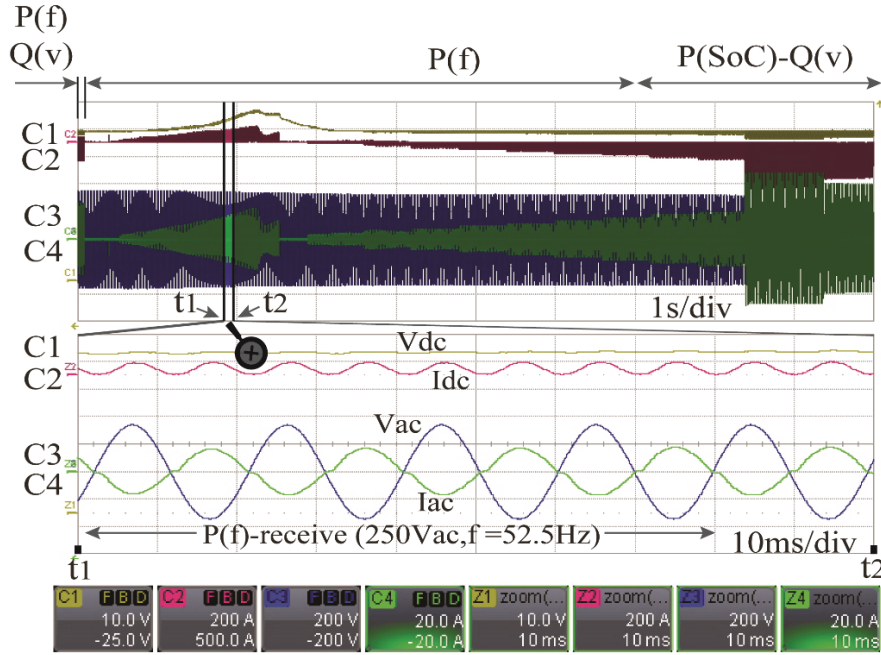
(b) Test performed with $P(f)$-receive strategy at voltage-frequency variation: 230 to 250V$_{rms}$ ($8V_{rms}$/s) and $f > 51.5Hz$ (1Hz/s).

Figure 4.13: Experimental results obtained through $P(f)$ - $Q(v)$ strategy test evaluation with frequency and voltage variation.

Y-axis: C1 - V_{dc} EES battery dc voltage 10V/div, C2 – I_{dc} EES battery dc current 200A/div, C3 - V_{ac} grid phase voltage 350V/div, C4 – converter ac phase current 20A/div.
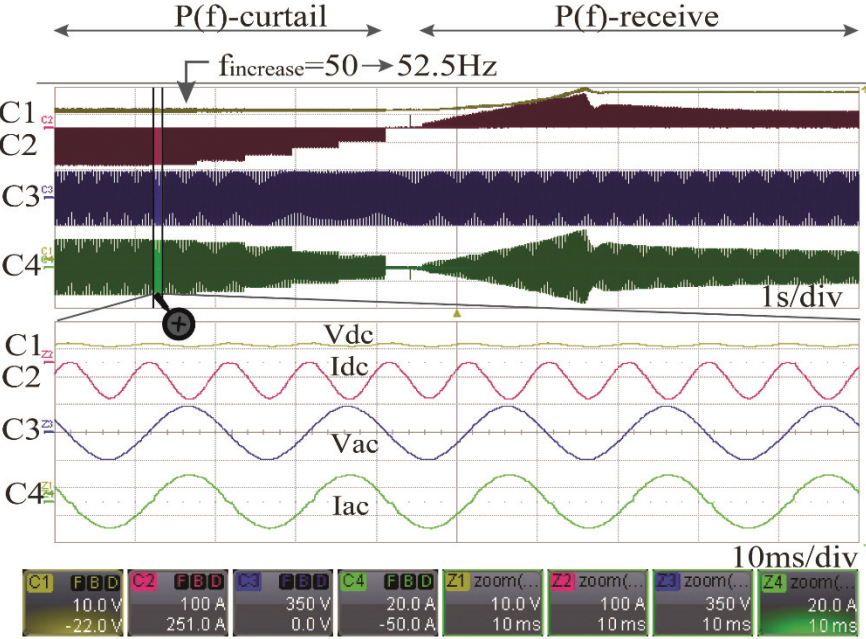
X-axis: 1s/div and 10ms/div.

Test conditions:

- $P(f)$ configuration: f_{min}=47Hz, f_{Lstop}=47.5Hz, f_{Lstart}=49.5Hz, f_n=50Hz, f_{Hrec}=50.05Hz, f_{Hstart}=50.2Hz, f_{Hstop}=51.5Hz, m_P=(40%P$_n$)/Hz.

- $Q(v)$ configuration: V_{Lmin}=210V_{rms} , V_{acHyst}=5V_{rms} , V_{Hmax}=250V_{rms}, q_{max}=60%.

- Voltage and frequency settings for protection under unintentional islanding (configurable, based on country-specific standard): (205 - 262) V_{rms}, (47.5 - 51.5) Hz.

(a) Test performed with $P(SoC)$ strategy at fast frequency (20Hz/s) downward ramp, 50 to 48Hz.
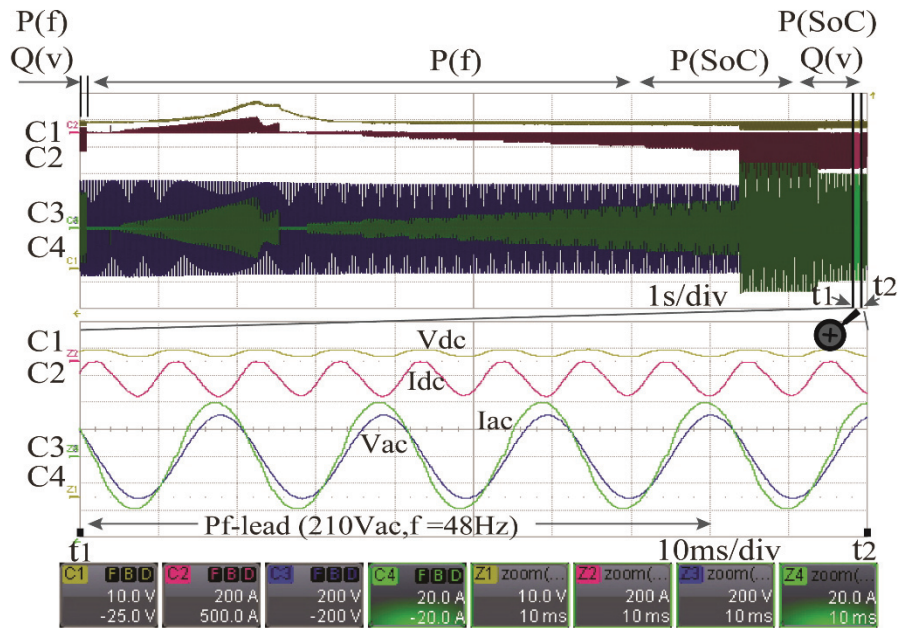
(b) Test performed with combined $P(SoC)$ and $Q(v)$ strategies under voltage-frequency variation: 230 to $240V_{rms}$ ($8V_{rms}$/s) and $f < 48Hz$.

Figure 4.14: Experimental results performed with $P(f)$ - $Q(v)$ strategy test evaluation with frequency and voltage variation.

Y-axis: C1 - V_{dc} EES battery dc voltage 10V/div, C2 – I_{dc} EES battery dc current 200A/div, C3 - V_{ac} grid phase voltage 350V/div, C4 – converter ac phase current, 20A/div. X-axis: 1s/div and 10ms/div.

Test conditions:

- $P(f)$ configuration: f_{min}=47Hz, f_{Lstop}=47.5Hz, f_{Lstart}=49.5Hz, f_n=50Hz, f_{Hrec}=50.05Hz, f_{Hstart}=50.2Hz, f_{Hstop}=51.5Hz, m_P=40%Pn/Hz.

- $Q(v)$ configuration: V_{Lmin}=210V_{rms}, V_{acHyst}=5V_{rms}, V_{Hmax}=250V_{rms}, q_{max}=60%.

- Voltage and frequency settings for protection under unintentional islanding (configurable, based on country-specific standard): (205 - 262) V_{rms}, (47.5 - 51.5) Hz.

Fig. 4.14 (a) shows the converter's operation under a fast-downward frequency ramp from nominal to 48Hz: the $P(f)$ strategy's fast response is reflected in the ac current (I_{ac}, Fig. 4.14) waveform. Fig. 4.14 (b) demonstrates the combined $P(SoC)$ - $Q(v)$ grid support strategy at low frequency and voltage operation (48Hz and 210V_{rms}). In this case, at low frequency operation (48Hz), the converter supplies active power from the SoC reserve. At the same time, under low voltage (210V_{rms}) operation, the converter receives reactive power ($Q < 0$) with power factor lead, for grid support purposes in frequency- and voltage-assist modes.

The EES converters that use $P(f)$ - $Q(v)$ strategy are able to smooth the frequency and voltage intermittencies caused by the effects of weather or other conditions on distributed PV generators.

Finally, the proposed strategies to support grid stability in the event of frequency-voltage variation go beyond recent standards and provide extended functionalities. The pre-configured set-points of active power-frequency $P(f)$ strategy features the control of the converter's power flow direction with an flexible power gradient transition between grid-feeding and force charge as grid-loading, in response to grid frequency deviation.

The distributed power generators are deployed in the form of energy storage converters, with the capacity to discharge and charge the Electrical Energy Storage (EES) element, primarily

for grid support purpose. The EES energy storage is configured for later usage when the grid requires active power support, under line frequency deviation, used under normal conditions, or during on-peak tariff high demand daytime hours (energy shifting for TOU, ac load shave).

In addition to grid support enhancement, the $P(f)$ strategy is combined with reactive power-voltage $Q(v)$ control to attempt to correct frequency and voltage deviations in a collective impact of distributed generators operation for grid stabilization purposes. The $P(f) - Q(v)$ strategy provides an automatic active/reactive power generate/receive pre-configured control, in response to frequency-voltage deviations, in order to support the grid and prevent network instabilities.

The proposed concepts can be implemented in the single and three-phase distributed EES converters, with no extra communication protocols needed in the transmission system operator of the ac network.

4.4. Summary

The utility GC requirements for the grid-connected power conversion systems are permanently subject to change from different regulatory agencies, in order to ensure the stability and quality of power delivery from distributed generators.

This chapter has presented a flexible grid support architecture strategy, where the proposed $P(f)$ and $Q(v)$ strategies are easily implemented within EES converters for active/reactive power generation (grid-feeding) and receiving (grid-loading). The $P(f) - Q(v)$ grid support strategy implemented in local EES distributed converters, monitors the grid frequency and voltage. The grid frequency-voltage deviation from the nominal values is a valuable indicator of the imbalance between power generation and consumption within the ac

grid network. During upward and downward frequency-voltage variations, the presented strategies control power generation and reception in real-time, providing automatic grid support. The proposed controller is designed with ancillary supportive frequency- and voltage-assist features for ac network stability and energy management. The active and reactive power flow control is performed using an adjustable gradient controller to command the transitions between grid-feeding (generate/export power) and grid-loading (receive power). The proposed strategy is primarily intended for grid networks with a high penetration of renewable energy (PV, wind), where the mechanism described is designed to achieve grid stability with power balancing.

The effectiveness of the proposed grid support strategies has been demonstrated through simulation and experimental validation in grid-connected converters, with outcome results beyond the present standards and GCs requirements.

Chapter 5. Conclusions

5.1. Conclusions and Contributions

When designing PV systems, the most important specifications include high efficiency, low cost, increased reliability, and safety standard compliance for a complete power conversion system design. To attain these design goals in a grid-connected PV system, it is extremely important that the PV operation voltage is optimized for maximum power production, that it is controlled in the most stable and efficient way possible, and that its protection detection mechanisms keeps the public safe.

The dissertation explored new research contributions related to PV/EES grid-connected converters. The contributions presented in this thesis were described through theoretical analysis and validated through experimental results. For future work, safety and control strategies investigation and design implementation are suggested, which would extend the applicability of grid-connected converters to islanded mode.

The following specific contributions were made in this dissertation.

5.1.1. DC-bus Extension Strategies in PV Energy Harvesting for Improved System Utilization

Chapter 2 focused on improving the power production of the entire grid-connected PV system through extending the dc bus voltage range. In particular, control strategies of grid-connected operation over a wider dc range for higher energy harvesting were provided.

The new proposed design concepts aid further to a higher system performance and system cost reduction over the traditional approach. Through analysis, essential key concepts were emphasized leading to important following insights of PV-converter system findings:

- Higher voltage inverter operation (e.g. 1500V) allows greater energy harvesting under low PV cell ambient temperatures (e.g. -20°C) and high irradiance conditions. In addition, from the comparison analysis, it was found that system installation cost is reduced, with savings in cables, and switchgear with less labor in system commissioning.

- Lower voltage dc-bus extension allows improved energy harvesting under high PV cell junction temperature (e.g. 70°C) and low irradiance.

The analysis and experimental work showed that, 1500V systems can provide with 30% larger dc range compared to 1000V inverters, which leads to significant operational area to capture energy under wider temperature and irradiance ranges.

In addition, a new concept of VQ reactive injection strategy was proposed and implemented to further extend the lower dc-limit, showing further extensions in the range of 3% to 5%. The proposed strategy becomes enabled under high temperature or low irradiance PV operation, forcing the inverter in MPPT operation mode, even at lower dc-bus voltage limit. In this way, the PV energy harvesting for power production is increased over the traditional method.

The inverter design was enhanced by using a new proposed modified modulation Quasi Space Vector (QSV), introduced to comply with 15% lower dc-bus extension gain and robust behaviour under dynamic conditions.

The single-stage conversion was extended to a two-stages, by using a mini-boost rated for a fraction of the nominal power of the PV inverter. Through the I-V and P-V graphical analysis, the concept of the inverter peak power envelope at boundary conversion operation provides

design optimization for energy harvesting maximization. The overall system performance and the utilization of the PV array and PV inverter were improved by the use of this architecture and design methodology.

5.1.2. Islanding Detection Strategies of PV Converters for Safety and Grid Codes Compliance

In Chapter 3, grid-connected PV systems were further improved through the use of proposed control functionalities for safety and grid network protection, using a modified MPPT algorithm to perform both, global maxima detection and islanding detection (ID). Therefore, the new concept leads to design simplification using a unified ID-MPPT functionality.

The proposed novel islanding search sequence (ISS) technique was implemented to control active and reactive current components, to synchronize ID-MPPT algorithm, and to maintain a small anti-islanding grid perturbance. The objective was to design the ISS methods with fast detection, robust operation and reduced reactive and active power injection. The investigation was carried out to develop a search sequence technique with an adaptive behavior (frequency, step-size amplitude and direction of the perturbance) in order to improve the ac network stability while it searches for unsafe, islanding conditions.

The proposed ID strategy allows to enable the combination of two or more methods simultaneously with a safety redundancy feature to provide fault tolerant system compliance.

5.1.3. Advanced Grid Support Operation of Grid-connected Converters for Network Stabilization with Power Balancing

Chapter 4 continues with the power conversion system exploration, by using new control functionalities intended to achieve network grid stability by using a newly proposed controller, designed with ancillary supportive frequency- and voltage-assist features. The characteristics of

frequency-voltage deviation from the nominal values provides an indication of the imbalance between power generation and consumption within the ac grid. As a result, controller is designed, with the detection of the upward and downward frequency-voltage grid variations, providing through controls, the necessary power generation and receiving in real-time, for an automatic grid support method.

The converter's active and reactive power flow control is performed using a flexible gradient controller to command the transitions between grid-feeding (generate power) and grid-loading (receive power). The intended application with the proposed new strategy is for grid networks with a high penetration of PV and wind distributed generators, where the control functionality is designed to achieve grid stability with power balancing, beyond the current standard requirements.

The system control strategies and advanced functionalities introduced in all chapters of this work were validated with electronic simulation and experimental measurements. The proposed functionalities implemented in grid-connected converters contribute to an improved PV and energy storage system performance.

5.1.4. Specific Academic Contributions

The work in the power electronics field of application, with advanced control functionalities for PV and energy storage systems culminated in the publications summarized below.

[1] E. Serban, M. Ordonez, and C. Pondiche, "DC-bus voltage range extension in 1500 V photovoltaic inverters," *IEEE J. Emerg. Sel. Topics Power Electron.,* vol. 3, no. 4, pp. 901–917, June 2015.

The major contributions covered in above-mentioned publication are:

- A novel VQ-control strategy for dc extension range for improved energy harvesting in 3-phase grid-connected systems.

- A new modified modulation strategy (QSV) for 3-phase systems which comply to 15% dc utilization range with robust behavior under dynamic conditions.

- A graphical analysis approach, using I-V and P-V characteristics, reflects remarkable insights into the PV-converter system behavior. This results to an optimized solution (e.g. 1500V systems) investigated for a higher system energy harvesting subsequent to 30% increase in dc extension range.

[2] E. Serban, F. Paz, and M. Ordonez, "Improved PV Inverter Operating Range Using a Miniboost," accepted for publication at IEEE Transactions in Power Electronics, Dec. 2016.

[3] E. Serban, F. Paz, and M. Ordonez, "PV Array Voltage Range Extension for Photovoltaic Inverters Using a Mini-Boost," in *Energy Conversion Congress and Exposition (ECCE),* 2016, pp. 1-8.

The major contributions resulted from above-mentioned publications are:

- A new architecture approach using a string mini-boost rated at a fraction of the nominal PV inverter for improved energy harvesting and cost optimization.

- Peak power envelope at the PV boundary conversion operation for system power production maximization. Increased system efficiency using an optimized by-pass element of the proposed string mini-boost architecture.

- Three methods of common-mode (leakage) circulation current reduction for safety and standard compliance.

[4] E. Serban, C. Pondiche, and M. Ordonez, " Islanding Detection Search Sequence for Distributed Power Generators Under AC Grid Faults*, "IEEE Trans. Power Electron.*, vol. 30, no. 6, pp. 3106–3121, Jun. 2014.

The major contributions resulted from the above publication are:

- A novel islanding detection method integrated in the MPPT algorithm as a unified control.

- Enhanced islanding search sequence (ISS) with an adaptive step-amplitude and time pattern applied to active/reactive power, phase locked-loop and MPPT.

- Islanding detection using a combination of two or more methods simultaneously enabled with a safety redundancy feature to provide fault tolerant system compliance.

[5] E. Serban, M. Ordonez, C. Pondiche, "Voltage and Frequency Grid Support Strategies Beyond Standards*," IEEE Trans. Power Electron.,* vol. 32, no. 1, pp. 298–309, Jan. 2017.

The major contributions resulted from above-mentioned publication are:

- Novel controller design for grid-support with active/reactive power balancing in grid-feeding and grid-loading mode.

- P(f) - Q(v) grid support strategy under frequency-voltage variation for grid network stability and energy management.

During the course of this work, the following additional conference scientific IEEE proceedings paper has been published:

[6] E. Serban, M. Ordonez, C. Pondiche, K. Feng, M. Anun, P. Servati, "Power Management Control Strategy in Photovoltaic and Energy Storage for Off-Grid Distributed Generation", in *Proc. IEEE 7th International Symposium on Power Electronics for Distributed Generation Systems (PEDG)*, pp. 1-8, Jun. 2016.

The major contributions covered in above-mentioned publication are:

- Power management controller design in off-grid (islanded mode) systems using frequency/phase angle as variables for the proposed EES charge algorithms in lead-acid and lithium-ion battery types.

- Controller design for power balancing and EES energy conservation using the principle of line frequency variation. At insufficient energy levels available from the EES, the line frequency is reduced, which determines an ac load-shedding effect. As a result, merely higher priority ac loads are maintained while the EES system is preserved.

5.2. Future Work

This work exposes several power conversion system areas of research which can build upon its findings, in which Engineers, Masters and PhD students could expand further system control functionalities.
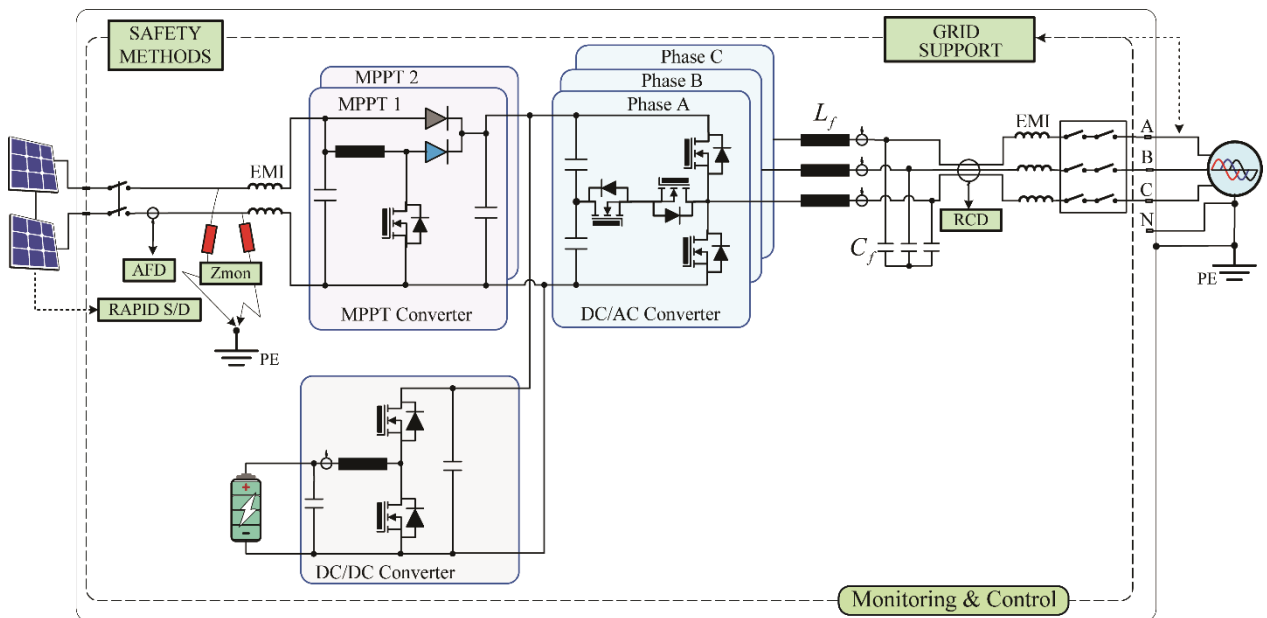
Figure 5.1: PV/EES converter system with safety means of protection and grid supporting/forming controls.

In Fig. 5.1 is shown the PV/EES system block diagram with grid-supporting/forming controls and integrated safety protections. The future research and development in continuation of the system control functionalities are suggested as follows:

- Grid-supporting/forming controls for the converters operation in islanded-mode intended for micro-grids applications [152]. Therefore, this new functionality will extend Chapter 4, for converter operation in grid-connected and islanded mode. Future work in the area will include aspects of modularity for scalability in single- and three-phase ac systems.

- Accurate safety detection methods for protection: Impedance monitoring (Z_{mon}) and arc-fault detection (AFD) for transformer-less non-galvanically isolated converters. Hazardous leakage currents to ground must be prevented by applying methods to avoid injuries and property losses. As a result, safety methods for system protection will complement the methods described in Chapter 3.

- System control coordination between three integrated converters using the architecture shown in Fig. 5.1. A complete model is required with extensive use cases with PV/EES and Grid/AC Loads for a stable and reliable system operation. With a continuation of the methods covered in Chapter 2, new controls are further required for achieving robust coordination and seamless transitions under different modes of operation, subsequent to the inclusion of the multi-port architecture proposal: PV, EES, AC loads and grid.

Bibliography

[1] T. Kerekes, E. Koutroulis, D. Sera, R. Teodorescu, and M. Katsanevakis, "An optimization method for designing large PV plants," *IEEE J. Photovoltaics*, vol. 3, no. 2, pp. 814–822, Apr. 2013.

[2] M. Schweizer and J. W. Kolar, "Design and implementation of a highly efficient three-level T-type converter for low-voltage applications," *IEEE Trans. Power Electron.*, vol. 28, no. 2, pp. 899–907, Feb. 2013.

[3] T. B. Soeiro and J. W. Kolar, "The new high efficiency hybrid neutral point-clamped converter," *IEEE Trans. Ind. Electron.*, vol. 60, no. 5, pp. 1919–1935, May 2013.

[4] N. C. Sintamarean, F. Blaabjerg, and H. Wang, "Real field mission profile oriented design of a SiC-based PV-inverter application, in" *IEEE Trans. Ind. Appl.*, pp. 4082-4089, Nov.-Dec. 2014.

[5] R. Teodorescu, M. Liserre, P. Rodriguez, "Grid Converters for Photovoltaic and Wind Power Systems", New York: Wiley, 2011.

[6] J. Rodriguez, S. Bernet, P. K. Steimer, and I. E. Lizama, "A survey on neutral point clamped inverters," *IEEE Trans. Ind. Electron.*, vol. 57, no. 7, pp. 2219–2230, Jul. 2010.

[7] D.O. Neacsu, E. Wagner, B. Borowy, "A Simulation Benchmark for Selection of the PWM Algorithms for Three-Phase Interleaved Converters", *IEEE Trans. Ind. Electronics*, April 2008, vol.55, pp.1628-1636.

[8] S. Zhangping, Z. Xing, W. Fusheng, C. Renxian, "Modeling and Elimination of Zero-Sequence Circulating Currents in Parallel Three-Level T-Type Grid-Connected Inverters ", *IEEE Trans. Power Electron.*, vol. 30, no. 2, pp. 1050–1063, Feb. 2015.

[9] T. P. Chen, "Zero-sequence circulating current reduction method for parallel HEPWM inverters between ac bus and dc bus," *IEEE Trans. Ind. Electron.*, vol. 59, no. 1, pp. 290–300, Jan. 2012.

[10] X. Zhang, J. Chen, Y. Ma, Y. Wang, D. Xu, "Bandwidth Expansion Method for Circulating Current Control in Parallel Three-phase PWM Converter Connection System", *IEEE Trans. Power Electron.*, vol. 29, no. 12, pp. 6847–6856, Dec. 2014.

[11] Y. D. Yoon and S. K. Sul, "Carrier-based modulation technique for matrix converter," *IEEE Trans. Power Electron.*, vol. 21, no. 6, pp. 1691–1703, Nov. 2006.

[12] J. Pou, J. Zaragoza, S. Ceballos, M. Saeedifard, and D. Borojevic, "A carrier-based PWM strategy with zero-sequence voltage injection for a three-level neutral-point-clamped converter," *IEEE Trans. Power Electron.*, vol. 27, no. 2, pp. 642–651, Feb. 2012.

[13] A. Mehrizi-Sani and S. Filizadeh, "An optimized space vector modulation sequence for improved harmonic performance," *IEEE Trans. Ind. Electron.*, vol. 56, no. 8, pp. 2894–2903, Aug. 2009.

[14] T. Ghennam, E. M. Berkouk, and B. Francois, "A novel space-vector current control based on circular hysteresis areas of a three-phase neutral point-clamped inverter," *IEEE Trans. Ind. Electron.*, vol. 57, no. 8, pp. 2669–2678, Aug. 2010.

[15] W. Song, X. Feng, and K. M. Smedley, "A carrier-based PWM strategy with the offset voltage injection for single-phase three-level neutral point-clamped converters," *IEEE Trans. Power Electron.*, vol. 28, no. 3, pp. 1083–1095, Mar. 2013.

[16] A. Choudhury, P. Pillay, and S. S. Williamson, "DC-link voltage balancing for a three-level electric vehicle traction inverter using an innovative switching sequence control scheme," *IEEE J. Emerg. Sel. Topics Power Electron.*, vol. 2, no. 2, pp. 296–307, Jun. 2014.

[17] S. Sirisukprasert, J.-S. Lai, and T.-H. Liu, "Optimum harmonic reduction with a wide range of modulation indexes for multilevel converters," *IEEE Trans. Ind. Electron.*, vol. 49, no. 4, pp. 875–881, Aug. 2002.

[18] J. Napoles, J. I. Leon, R. Portillo, L. G. Franquelo, and M. A. Aguirre, "Selective harmonic mitigation technique for high-power converters," *IEEE Trans. Ind. Electron.*, vol. 57, no. 7, pp. 2315–2323, Jul. 2010.

[19] Y. Zhang, Z. Zhao, and J. Zhu, "A hybrid PWM applied to high power three-level inverter-fed induction-motor drives," *IEEE Trans. Ind. Electron.*, vol. 58, no. 8, pp. 3409–3420, Aug. 2011.

[20] A. M. Hava, R. J. Kerkman, and T. A. Lipo, "Simple analytical and graphical methods for carrier-based PWM-VSI drives," *IEEE Trans. Power Electron.*, vol. 14, no. 1, pp. 49–61, Jan. 1999.

[21] L. Hadjidemetriou, E. Kyriakides, F. Blaabjerg, "A new hybrid PLL for interconnecting renewable energy systems to the grid," *IEEE Trans. Ind. Appl.*, pp. 1-9, Nov./Dec. 2013.

[22] N. R. N. Ama, F. O. Martiz, L. Matacas Jr., and F. Kassab Jr., "Phaselocked loop based on selective harmonics compensation for utility applications," *IEEE Trans. Power Electron.*, vol. 28, no. 1, pp. 144–153, Jan. 2013.

[23] K.-J. Lee, J.-P. Lee, D. Shin, D.-W. Yoo, and H.-J. Kim, "A novel grid synchronization PLL method based on adaptive low-pass notch filter for grid-connected PCS," *IEEE Trans. Ind. Electron.*, vol. 61, no. 1, pp. 292–301, Jan. 2014.

[24] A. V. Timbus, M. Liserre, F. Blaabjerg, R. Teodorescu, and P. Rodriguez, "PLL algorithm for power generation systems robust to grid faults," in *Proc. IEEE PESC*, 2006, pp. 1360–1366.

[25] M. Reyes, P. Rodriguez, S. Vasquez, A. Luna, R. Teodorescu, and J. M. Carrasco, "Enhanced decoupled double synchronous reference frame current controller for unbalanced grid-voltage conditions," *IEEE Trans. Power Electron.*, vol. 27, no. 9, pp. 3934–3943, Sep. 2012.

[26] J. T. Boys and P. G. Handley, "Harmonic analysis of space vector modulated PWM waveforms," *Proc. Inst. Elect. Eng. Elec. Power Appl.*, vol. 137, no. 4, pp. 197–204, July 1990.

[27] S. Bowes and Y. S. Lai, "The relationship between space-vector modulation and regular-sampled PWM," *IEEE Trans. Ind. Electron.*, vol. 44, pp. 670–679, Sept./Oct. 1997.

[28] E. Levi, D. Dujic, M. Jones, and G. Grandi, "Analytical determination of DC-bus utilization limits in multiphase VSI supplied AC drives," *IEEE Trans. Energy Convers.*, vol. 23, no. 2, pp. 433–443, Jun. 2008.

[29] L. Zarri, M. Mengoni, A. Tani, J.O. Ojo, "Range of the Linear Modulation in Matrix Converters," *IEEE Trans. Power Electron.*, vol.29, no.6, pp. 3166-3178, June 2014.

[30] E. Gkoutioudi, P. Bakas, A. Marinopoulos, "Comparison of PV systems with maximum DC voltage 1000V and 1500V ", *Proc. 39th IEEE Photovoltaic Spec. Conf.*, pp. 2873-2878, 2013.

[31] K.-N.D. Malamaki, C.S.Demoulias, "Analytical Calculation of the Electrical Energy Losses on Fixed-Mounted PV Plants", *IEEE Trans. Sustain. Energy*, vol. 4, no. 1, pp. 145–153, Jan. 2013.

[32] E. Romero-Cadaval et al., "Grid-connected photovoltaic generation plants: Components and operation," *IEEE Ind. Electron. Mag.*, vol. 7, no. 3, pp. 6–20, Sep. 2013.

[33] E. Roman, R. Alonso, P. Ibanez, S. Elorduizapatarietxe, and D. Goitia, "Intelligent PV module for grid-connected PV systems," *IEEE Trans. Ind. Electron.*, vol. 53, no. 4, pp. 1066–1073, Jun. 2006.

[34] N. Femia, G. Petrone, G. Spagnuolo, and M. Vitelli, Power Electronics and Control Techniques for Maximum Energy Harvesting in *Photovoltaic Systems*, 1st ed. Boca Raton, FL: CRC Press, 2012.

[35] F. Spertino and J. S. Akilimali, "Are manufacturing – mismatch and reverse currents key factors in large photovoltaic arrays?" *IEEE Trans. Ind. Electron.*, vol. 56, no. 11, pp. 4520–4531, 2009.

[36] Y.-J. Wang and P.-C. Hsu, "Analytical modelling of partial shading and different orientation of photovoltaic modules," *IET Renewable Power Generation*, vol. 4, no. 3, pp. 272–282, 2010.

[37] C. Konstantopoulos and E. Koutroulis, "Global maximum power point tracking of flexible photovoltaic modules," *IEEE Trans. Power Electron.*, vol. 29, no. 4, pp. 2817–2828, Jun. 2014.

[38] D. Sera, R. Teodorescu, J. Hantschel, and M. Knoll, "Optimized maximum power point tracker for fast-changing environmental conditions," *IEEE Trans. Ind. Electron.*, vol. 55, no. 7, pp. 2629–2637, Jul. 2008.

[39] D. Sera, L. Mathe, T. Kerekes, S. Spataru, and R. Teodorescu, "On the perturb-and-observe and incremental conductance MPPT methods for PV systems," *IEEE J. Photovoltaics*, vol. 3, no. 3, pp. 1070–1078, Jul. 2013.

[40] M. A. G. de Brito, L. Galotto, L. P. Sampaio, G. de Azevedo e Melo, and C. A. Canesin, "Evaluation of the Main MPPT techniques for photovoltaic applications," *IEEE Trans. Ind. Electron.*, vol. 60, no. 3, pp. 1156–1167, Nov. 2013.

[41] M. Drif, P. Prez, J. Aguilera, and J. Aguilar, "A new estimation method of irradiance on a partially shaded {PV} generator in grid-connected photovoltaic systems," *Renewable Energy*, vol. 33, no. 9, pp. 2048 – 2056, 2008.

[42] A. Bidram, A. Davoudi, and R. S. Balog, "Control and circuit techniques to mitigate partial shading effects in photovoltaic arrays," *IEEE J. Photovoltaics*, vol. 2, no. 4, pp. 532–546, Oct. 2012.

[43] B. N. Alajmi, K. H. Ahmed, S. J. Finney, and B. W. Williams, "A maximum power point tracking technique for partially shaded photovoltaic systems in microgrids," *IEEE Trans. Ind. Electron.*, vol. 60, no. 4, pp. 1596–1606, Apr. 2013.

[44] N. Mutoh, M. Ohno, and T. Inoue, "A method for mppt control while searching for parameters corresponding to weather conditions for PV generation systems," *IEEE Trans. Ind. Electron.*, vol. 53, no. 4, pp. 1055–1065, 2006.

[45] G. Carannante, C. Fraddanno, M. Pagano, and L. Piegari, "Experimental performance of mppt algorithm for photovoltaic sources subject to inhomogeneous insolation," *IEEE Trans. Ind. Electron.*, vol. 56, no. 11, pp. 4374–4380, 2009.

[46] T. L. Nguyen and K.-S. Low, "A global maximum power point tracking scheme employing direct search algorithm for photovoltaic systems," *IEEE Trans. Ind. Electron.*, vol. 57, no. 10, pp. 3456–3467, 2010.

[47] Y.-H. Ji, D.-Y. Jung, J.-G. Kim, J.-H. Kim, T.-W. Lee, and C.-Y. Won, "A real maximum power point tracking method for mismatching compensation in PV array under partially shaded conditions," *IEEE Trans. Power Electron.*, vol. 26, no. 4, pp. 1001–1009, 2011.

[48] E. Koutroulis and F. Blaabjerg, "A new technique for tracking the global maximum power point of PV arrays operating under partial-shading conditions," *IEEE J. Photovoltaics*, vol. 2, no. 2, pp. 184–190, Apr. 2012.

[49] M. Ropp, D. Larson, S. Meendering, D. McMahon, J. Ginn, J. Stevens, W. Bower, S. Gonzalez, K. Fennell, and L. Brusseau, "Discussion of a Power Line Carrier Communications-Based Anti-Islanding Scheme using a Commercial Automatic Meter Reading System," in *Proc. Photovoltaic Energy Conversion*, pp. 2351-2354, May 2006.

[50] Xu W. Xu, G. Zhang, C. Li, W. Wang, and J. Kliber, "A power line signaling based technique for anti-islanding protection of distributed generators: Part I: scheme and analysis," *IEEE Trans. Power Del.*, vol. 22, no. 3, pp. 1758–1766, Jul. 2007.

[51] S. A. Saleh, A. S. Aljankawey, R. Meng, J. Meng, C. P. Diduch, and L. Chang, "Antiislanding protection based on signatures extracted from the instantaneous apparent power," *IEEE Trans. Power Electron.*, vol. 29, no. 11, pp. 5872–5891, Nov. 2014.

[52] J. Yin, C. P. Diduch, and L. Chang, "Islanding detection using proportional power spectral density," *IEEE Trans. Power Del.*, vol. 23, no. 2, pp. 776–784, Apr. 2008.

[53] N. Liu, C. Diduch, L. Chang and J. Su, "A Reference Impedance-Based Passive Islanding Detection Method for Inverter-Based Distributed Generation System", *IEEE J. Emerg. Sel. Topics Power Electron.*, vol. 3, pp. 1205-1217, 2015.

[54] N. Liu, A. S. Aljankawey, C. P. Diduch, L. Chang, M. Mao, P. Yazdkhasti, "Performance evaluation for grid impedance based islanding detection method", *Power Electronics Conference (IPEC-Hiroshima 2014 - ECCE-ASIA) 2014 International*, pp. 2156-2160, 2014.

[55] F. DeMango, M. Liserre, A. D. Aquila, and A. Pigazo, "Overview of anti-islanding algorithms for PV systems. Part I: Passive methods," in *Proc. EPE-PEMC*, 2006, pp. 1878–1883.

[56] Jang, S.-I. and Kim, K.-H.," An islanding detection method for distributed generations using voltage unbalance and total harmonic distortion of current" *IEEE Transactions on Power Delivery,* 19(2), April 2004, 745-752.

[57] M. E. Ropp, M. Begovic, A. Rohatgi, G. A. Kern, R. H. Bonn, and S. Gonzalez, "Determining the relative effectiveness of islanding detection methods using phase criteria and non detection zones," *IEEE Trans. Energy Convers.*, vol. 15, no. 3, pp. 290–296, Sep. 2000.

[58] A. Yafaoui, B. Wu, S. Kouro, "Improved Active Frequency Drift Anti-islanding Detection Method for Grid Connected Photovoltaic Systems," *IEEE Trans. Power Electron.*, vol. 27, no. 5, pp. 2367–2375, May 2012.

[59] L. A. C. Lopes and H. Sun, "Performance assessment of active frequency drifting islanding detection methods," *IEEE Trans. Energy Convers.*, vol. 21, no. 1, pp. 171–180, Mar. 2006.

[60] G. K. Hung, C. C. Chang, and C. L. Chen, "Automatic phase-shift method for islanding detection of grid-connected photovoltaic inverters," *IEEE Trans. Energy Convers.*, vol. 18, no. 1, pp. 169–173, Mar. 2003.

[61] Bower, W. and Ropp, M., "Evaluation of islanding detection methods for utility-interactive inverters in photovoltaic systems", *SANDIA Report SAND2002-359I*, Albuquerque, NM: Sandia National Labs, November 2002.

[62] L. Asiminoaei, R. Teodorescu, F. Blaabjerg, and U. Borup, "A digital controlled PV-inverter with grid impedance estimation for ENS detection," *IEEE Trans. Power Electron.*, vol. 20, no. 6, pp. 1480–1490, Nov. 2005.

[63] A. V. Timbus, R. Teodorescu, and P. Rodriguez, "Grid impedance identification based on active power variation and grid voltage control," in *Conf. Rec. 42nd IEEE IAS Annu. Meeting*, Sep. 2007, pp. 949–954.

[64] M. Ciobotaru, R. Teodorescu, P. Rodriguez, A. Timbus, and F. Blaabjerg, "On-line grid impedance estimation for single-phase grid-connected systems using PQ variations," in *Proc. PESC*, 2007, pp. 2306–2312.

[65] M. Ciobotaru, V. Agelidis, R. Teodorescu, and F. Blaabjerg, "Accurate and less-disturbing active anti-islanding method based on pll for grid connected converters," *IEEE Trans. Power Electron.*, vol. 25, no. 6, pp. 1576–1584, Jun. 2010.

[66] D. Velasco, C. Trujillo, G. Garcera, and E. Figueres, "An active anti-islanding method based on phase-PLL perturbation," *IEEE Trans. Power Electron.*, vol. 26, no. 4, pp. 1056–1066, Apr. 2011.

[67] Z. Ye, R. Walling, L. Garces, R. Zhou, L. Li, and T. Wang, "Study and development of anti-Islanding control for grid-connected inverters," Nat. Renewable Energy Lab., Golden, CO, Rep. NREL/SR-560-36243, May 2004.

[68] G. Hernandez-Gonzalez and R. Iravani, "Current injection for active islanding detection of electronically-interfaced distrusted resources," *IEEE Trans. Power Del.*, vol. 21, no. 3, pp. 1698–1705, Jul. 2006.

[69] S.-K. Kim, J.-H. Jeon, J.-B. Ahn, B. Lee, and S.-H. Kwon, "Frequency shift acceleration control for anti-islanding of a distributed-generation inverter," *IEEE Trans. Ind. Electron.*, vol. 57, no. 2, pp. 494–504, Feb. 2010.

[70] J. Zhang, D. Xu, G. Shen, Y. Zhu, N. He, and J. Ma, "An improved islanding detection method for a grid-connected inverter with intermittent bilateral reactive Power variation" *IEEE Trans.Power Electron.*, vol. 28, no. 1, pp. 268–278, Jan. 2013.

[71] Y. Zhu, D. Xu, N. He, J. Ma, J. Zhang, Y. Zhang, G. Shen, C. Hu, "A Novel RPV (Reactive-Power-Variation) Antiislanding Method Based on Adapted Reactive Power Perturbation," *IEEE Trans. Power Electron.*, vol.28, no.11, pp. 4998-5012, Nov. 2013.

[72] P. Du, Z. Ye, E. Aponte, J. Nelson, and L. Fan, "Positive-feedback-based active anti-islanding schemes for inverter-based distributed generators: Basic principle, design guideline, and performance analysis," *IEEE Trans. Power Electron.*, vol. 25, no. 12, pp. 2941–2948, Dec. 2010.

[73] H. Berndt & M. Hermann, H.D. Kreye, R. Reinisch, U. Scherer, & J. Vanzetta, "Network and system rules of the German transmission system operators 2007". VDN, Berlin, Germany, 2007.

[74] "Generating Plants Connected to the Medium Voltage Network," BDEW Technical Guidelines, Germany, Jun. 2008, Berlin.

[75] Technical Requirements for the Connection to and Parallel Operation With Low-Voltage Distribution Networks, VDE-AR-N 4105, 2011.

[76] T. N. Preda, K. Uhlen, D. E. Nordgård,." An Overview of the Present Grid Codes for Integration of Distributed Generation", *CIRED Workshop 2012*, May 2012, pp 1-4.

[77] E. Troester, "New German grid codes for connecting PV systems to the medium voltage power grid," in *Proc. 2nd Int. Workshop Concentrating Photovoltaic Power Plants: Opt. Design, Prod., Grid Connection*, 2009, pp. 1–4.

[78] E. Serban, C. Pondiche, and M. Ordonez, " Islanding Detection Search Sequence for Distributed Power Generators Under AC Grid Faults*, "IEEE Trans. Power Electron.,* vol. 30, no. 6, pp. 3106–3121, Jun. 2015.

[79] Y. Yang, F. Blaabjerg, and H. Wang, "Low voltage ride-through of single-phase transformerless photovoltaic inverters," *IEEE Trans. Ind. Appl.*, vol. 50, no. 3, pp. 1942–1952, May/Jun. 2014.

[80] H. Geng, C. Liu, and G. Yang, "LVRT capability of DFIG-Based WECS under asymmetrical grid fault condition," *IEEE Trans. Ind. Electron.*, vol. 60, no. 6, pp. 2495–2509, Jun. 2013.

[81] F. K. A Lima, A. Luna, P. Rodriguez, E. H. Watanabe, and F. Blaabjerg, "Rotor voltage dynamic in the doubly fed induction generator during grid faults," *IEEE Trans. Power Electron.*, vol. 25, no. 1, pp. 118–130, Jan. 2010.

[82] A. Calle-Prado, S. Alepuz, J. Bordonau, J. Nicolas-Apruzzese, P. Cortes, J. Rodriguez, "Model Predictive Current Control of Grid-Connected Neutral-Point-Clamped Converters to Meet Low-Voltage Ride-Through Requirements," *IEEE Trans. Ind. Electron.*, vol. 62, no. 3, pp. 1503–1514, Mar. 2015.

[83] A. Camacho, M. Castilla, J. Miret, R. Guzman, and A. Borrell, "Reactive power control for distributed generation power plants to comply with voltage limits during grid faults," *IEEE Trans. Power Electron.*, vol. 29, no. 11, pp. 6224–6234, Nov. 2014.

[84] X. Guo, X. Zhang, B. Wang, W. Wu, and J. M. Guerrero, "Asymmetrical grid fault ride-through strategy of three-phase grid-connected inverter considering network impedance impact in low-voltage grid," *IEEE Trans. Power Electron.*, vol. 29, no. 3, pp. 1064–1068, Mar. 2014.

[85] M. Castilla, J. Miret, A. Camacho, L. G. de Vicuna, and J. Matas, "Modeling and Design of Voltage Support Control Schemes for Three-Phase Inverters Operating Under Unbalanced Grid Conditions," *IEEE Trans. Power Electron.*, vol. 29, no. 11, pp. 6139–6150, Nov. 2014.

[86] J. Matas, M. Castilla, J. Miret, L. G. Vicuna, and R. Guzman, "An adaptive prefiltering method to improve the speed/accuracy tradeoff of voltage sequence detection methods under adverse grid conditions," *IEEE Trans. Ind. Electron.*, vol. 61, no. 5, pp. 2139-2151, May 2014.

[87] M. Reyes, P. Rodriguez, S. Vasquez, A. Luna, R. Teodorescu, and J. M. Carrasco, "Enhanced decoupled double synchronous reference frame current controller for unbalanced grid-voltage conditions," *IEEE Trans. Power Electron.*, vol. 27, no. 9, pp. 3934–3943, Sep. 2012.

[88] P. Rodriguez, A. Timbus, R. Teodorescu, M. Liserre, and F. Blaabjerg, "Flexible active power control of distributed power generation systems during grid faults," *IEEE Trans. Ind. Electron.*, vol. 54, no. 5, pp. 2583–2592, Oct. 2007.

[89] M. Castilla, J. Miret, J. Sosa, J. Matas, and L. G. de Vicuna, "Grid fault control scheme for three-phase photovoltaic inverters with adjustable power quality characteristics," *IEEE Trans. Power Electron.*, vol. 25, no. 12, pp. 2930–2940, Dec. 2010.

[90] A. Camacho, M. Castilla, J. Miret, J. Vasquez, and E. Alarc´on-Gallo, "Flexible voltage support control for three phase distributed generation inverters under grid fault," *IEEE Trans. Ind. Electron.*, vol. 60, no. 4, pp. 1429–1441, Apr. 2013.

[91] Y. Bae, T.-K. Vu, and R.-Y. Kim, "Implemental control strategy for grid stabilization of grid-connected PV system based on German grid code in symmetrical low-to-medium voltage network," *IEEE Trans. Energy Convers.*, vol. 28, no. 3, pp. 619–631, Sep. 2013.

[92] B.-I. Craciun, T. Kerekes, D. Sera, R. Teodorescu, "Frequency Support Functions in Large PV Power Plants With Active Power Reserves," *IEEE J. Emerg. Sel. Topics Power Electron.*, vol. 2, no. 4, pp. 849–858, Dec. 2014.

[93] Y. Xue, L. Chang, S. B. Kjaer, J. Bordonau, and T. Shimizu, "Topologies of single-phase inverters for small distributed power generators: An overview," *IEEE Trans. Power Electron.*, vol. 19, no. 5, pp. 1305–1314, Sep. 2004.

[94] E. Serban, M. Ngosi, and T. Monk, "Parallel operation of multi-mode Voltage Source Inverter modules with equal load sharing in single phase AC systems," in *Proc. IEEE OPTIM Conf.*, Brasov, Romania, May 2008, pp. 319–326.

[95] J. M. Guerrero, L. G. Arcia de Vicuna, J. Matas, M. Castilla, and J. Miret, "A wireless controller to enhance dynamic performance of parallel inverters in distributed generation systems," *IEEE Trans. Power Electron.*, vol. 19, no. 5, pp. 1205–1213, Sep. 2004.

[96] J. M. Guerrero, J. Matas, L. G. de Vicuña, M. Castilla, and J. Miret, "Output impedance design of parallel-connected UPS inverters with wireless load-sharing control," *IEEE Trans. Ind. Electron.*, vol. 52, no. 4, pp. 1126– 1135, Aug. 2005.

[97] K. De Brabandere, B. Bolsens, J. Van den Keybus, A. Woyte, J. Driesen, and R. Belmans, "A voltage and frequency droop control method for parallel inverters," *IEEE Trans. Power Electron.*, vol. 22, no. 4, pp. 1107–1115, July 2007.

[98] J. M. Guerrero, J. C. Vasquez, J. Matas, M. Castilla, and L. G. de Vicuna, "Control strategy for flexible microgrid based on parallel line-interactive UPS systems," *IEEE Trans. Ind. Electron.*, vol. 56, no. 3, pp. 726–736, Mar. 2009.

[99] Y. W. Li and C.-N. Kao, "An accurate power control strategy for power-electronics-interfaced distributed generation units operating in a low-voltage multibus microgrid," *IEEE Trans. Power Electron.*, vol. 24, no. 12, pp. 2977–2988, Dec. 2009.

[100] Y. Xiaoxiao, A. M. Khambadkone, W. Huanhuan, and S. Terence, "Control of parallel-connected power converters for low-voltage microgrid—Part I: A hybrid control architecture," *IEEE Trans. Power Electron.*, vol. 25, no. 12, pp. 2962–2970, Dec. 2010.

[101] J. M. Guerrero, J. C. Vasquez, J. Matas, L. Garcia de Vicuna, and M. Castilla, "Hierarchical control of droop-controlled AC and DC microgrids—A general approach towards standardization," *IEEE Trans. Ind. Electron.*, vol. 58, no. 1, pp. 158–172, Jan. 2011.

[102] J. M. Guerrero, M. Chandorkar, T. L. Lee, and P. C. Loh, "Advanced control architectures for intelligent microgrids—Part I: Decentralized and hierarchical control," *IEEE Trans. Ind. Electron.*, vol. 60, no. 4, pp. 1254–1262, Apr. 2013.

[103] C. N. Rowe, T. J. Summers, R. E. Betz, D. J. Cornforth, and T. G. Moore, "Arctan power frequency droop for improved microgrid stability," *IEEE Trans. Power Electron.*, vol. 28, no. 8, pp. 3747–3759, Aug. 2013.

[104] T. L. Vandoorn, B. Meersman, L. Degroote, B. Renders, and L. Vandevelde, "A control strategy for islanded microgrids with dc-link voltage control," *IEEE Trans. Power Del.*, vol. 26, no. 2, pp. 703–713, Apr. 2011.

[105] I. Serban, C. Marinescu, "Control Strategy of Three-Phase Battery Energy Storage Systems for Frequency Support in Microgrids and with Uninterrupted Supply of Local Loads", *IEEE Trans. on Power Electron.*, vol.29, no.9, pp.5010-5020, Sept. 2014.

[106] M. A. Abusara, J. M. Guerrero, and S. M. Sharkh, "Line-interactive UPS for microgrids," *IEEE Trans. Ind. Electron.*, vol. 61, no. 3, pp. 1292–1300, Mar. 2014.

[107] T. L. Vandoorn, B. Meersman, J. D. M. De Kooning, and L. Vandevelde, "Transition from islanded to grid-connected mode of microgrids with voltage-based droop control," *IEEE Trans. Power Syst.*, vol. 28, no. 3, pp. 2545–2553, Aug. 2013.

[108] A. Micallef, M. Apap, C. Spiteri-Staines, J. M. Guerrero, "Single-Phase Microgrid With Seamless Transition Capabilities Between Modes of Operation," *IEEE Trans. Smart Grid*, vol.6, no. 6, pp. 2736–2745, Nov. 2015.

[109] A. Timbus, M. Liserre, R. Teodorescu, P. Rodriguez, and F. Blaabjerg, "Evaluation of current controllers for distributed power generation systems," *IEEE Trans. Power Electron.*, vol. 24, no. 3, pp. 654–664, Mar. 2009.

[110] K. Strunz, E. Abbasi, and D. N. Huu, "DC microgrids for wind and solar power integration," *IEEE J. Emerg. Sel. Topics Power Electron.*, vol. 2, no. 1, pp. 115–126, Mar. 2014.

[111] A. Urtasun, E. L. Barrios, P. Sanchis, and L. Marroyo, "Frequency-based energy management for stand-alone systems with distributed battery storage," *IEEE Trans. Power Electron.*, vol. 30, no. 9, pp. 4794–4808, Sep. 2015.

[112] Z. Zhang, Y. Cai, Y. Zhang, D. Gu, and Y. Liu, "A distributed architecture based on micro-bank modules with self-reconfiguration control to improve the energy efficiency in the battery energy storage system," *IEEE Trans. Power Electron.*, vol. 31, no.19, pp. 304–317, Jan. 2016.

[113] J. A. Gow and C. D. Manning, "Development of a photovoltaic array model for use in power-electronics simulation studies," in *IEE Proceedings - Electric Power Applications*, vol. 146, no. 2, pp. 193-200, Mar 1999.

[114] W. Xiao, W. Dunford, and A. Capel, "A novel modeling method for photovoltaic cells," in *Power Electronics Specialists Conference,* pp. 1950-1956 Vol.3, 2004.

[115] D. Sera, R. Teodorescu and P. Rodriguez, "PV panel model based on datasheet values," *2007 IEEE International Symposium on Industrial Electronics*, Vigo, Spain, 2007, pp. 2392-2396.

[116] D. L. King, W. E. Boyson, and J. A. Kratochvil, Photovoltaic Array Performance Model, Sandia National Laboratories, Albuquerque,NewMexico 87185-0752, 2004.

[117] D. Mayer, L. Wald: "Performance Prediction of Grid-Connected Photovoltaic Systems Using Remote Sensing", IEA-PVPS, Report Task2 IEA T2-07: 2008, March 2008.

[118] C. Newton and M. Summer, "Neutral point control for multi-level inverters: Theory, design and operational limitations," in *Conf. Rec. IEEE IAS Annu. Meeting*, 1997, pp. 1336–1343.

[119] A. Choudhury, P. Pillay, and S. S. Williamson, "Comparative analysis between two-level and three-level DC/AC electric vehicle traction inverters using a novel DC-link voltage balancing algorithm," *IEEE J. Emerg. Sel. Topics Power Electron*., vol. 2, no. 3, pp. 529–540, Sept. 2014.

[120] W. D. Jiang, S.W. Du, L. C. Chang, Y. Zhang, and Q. Zhao, "HybridPWM strategy of SVPWM and VSVPWM for NPC three-level voltage-source inverter," *IEEE Trans. Power Electron.*, vol. 25, no. 10, pp. 2607–2619, Oct. 2010.

[121] J. Shen, S. Schroder, B. Duro, and R. Roesner, "A neutral-point balancing controller for a three-level inverter with full power-factor range and low distortion," *IEEE Trans. Ind. Appl.*, vol. 49, no. 1, pp. 138 –148, Jan.-Feb. 2013.

[122] D. Sera, R. Teodorescu, J. Hantschel, and M. Knoll, "Optimized maximum power point tracker for fast changing environmental conditions," in *Proc. IEEE ISIE*, Jun. 2008, pp. 2401–2407.

[123] D. Sera, L. Mathe, T. Kerekes, S. Spataru, and R. Teodorescu, "On the perturb-and-observe and incremental conductance MPPT methods for PV systems," *IEEE J. Photovoltaics*, vol. 3, no. 3, pp. 1070–1078, Jul. 2013.

[124] E. Serban and H. Serban, "A control strategy for a distributed power generation microgrid application with voltage- and current-controlled source converter," *IEEE Trans. Power Electron.*, vol. 25, no. 12, pp. 2981–2992, Dec. 2010.

[125] A. G. Tapia, and J. X. Ostolaza, "Reactive power control of wind farms for voltage control applications," Renew. Energy, vol. 29, no. 3, pp. 377–392, Mar. 2004.

[126] D. O. Neacsu, "Power-Switching Converters - Medium and High Power," Ed. Taylor and Francis, 2006, Chap. 11.

[127] D. G. Holmes and T. A. Lipo, *Pulse Width Modulation for Power Converters*. New York: Wiley, 2003, Chap. 5, 6.

[128] E. R. C. da Silva, E. Cipriano dos Santos, and C. B. Jacobina, "Pulsewidth modulation strategies," *IEEE Ind. Electron. Mag.*, vol. 5, no. 2, pp. 37–45, Jun. 2011.

[129] C. Hou, "A multicarrier PWM for parallel three-phase active front-end converters," *IEEE Trans. Power Electron.*, vol. 28, no. 6, pp. 2753–2759, Jun. 2013.

[130] Z. Xu, R. Li, H. Zhu, D. Xu, and C. Zhang, "Control of parallel multiple converters for direct-drive permanent-magnet wind power generation systems," *IEEE Trans. Power Electron.*, vol. 27, no. 3, pp. 1259–1270, Mar. 2012.

[131] E. Serban, M. Ordonez, and C. Pondiche, "DC-bus voltage range extension in 1500 V photovoltaic inverters," *IEEE J. Emerg. Sel. Topics Power Electron.*, vol. 3, no. 4, pp. 901–917, 2015.

[132] T. Kerekes, R. Teodorescu, M. Liserre, C. Klumpner, and M. Sumner, "Evaluation of three-phase transformerless photovoltaic inverter topologies," *IEEE Trans. Power Electron.*, vol. 24, no. 9, pp. 2202–2211, Sep. 2009.

[133] M. C. Cavalcanti, K. C. de Oliveira, A. M. de Farias, F. A. S. Neves, G. M. S. Azevedo, and F. C. Camboim, "Modulation techniques to eliminate leakage currents in transformerless three-phase photovoltaic systems," *IEEE Trans. Ind. Electron.*, vol. 57, no. 4, pp. 1360–1368, Apr. 2010.

[134] M. C. Cavalcanti, A. M. Farias, K. C. Oliveira, F. A. S. Neves, and J. L. Afonso, "Eliminating leakage currents in neutral point clamped inverters for photovoltaic system," *IEEE Trans. Ind. Electron.*, vol. 59, no. 1, pp. 435–443, Jan. 2012.

[135] X. Guo, M. C. Cavalcanti, A. M. Farias, and J. M. Guerrero, "Single-carrier modulation for neutral-point-clamped inverters in three-phase transformerless photovoltaic systems," *IEEE Trans. Power Electron. lett.*, vol. 28, no. 6, pp. 2635–2637, Jun. 2013.

[136] Z. Ye, A. Kolwalkar, Y. Zhang, P. Du, and R. Walling, "Evaluation of anti-islanding schemes based on nondetection zone concept," *IEEE Trans. Power Electron.*, vol. 19, no. 5, pp. 1171–1176, Sep. 2004.

[137] H. Patel and V. Agarwal, "Maximum power point tracking scheme for PV systems operating under partially shaded conditions," *IEEE Trans. Ind. Electron.*, vol. 55, no. 4, pp. 1689–1698, Apr. 2008.

[138] B. Alajmi, K. Ahmed, S. Finney, and B. Williams, "A maximum power point tracking technique for partially shaded photovoltaic systems in microgrids," *IEEE Trans. Ind. Electron.*, vol. 60, no. 4, pp. 1596-1606, Apr. 2013.

[139] Z. Xi, U. Jansen, and H. Rüthing, "IGBT Power Modules Utilizing New 650V IGBT3 and Emitter Controlled Diode3 Chips for Three Level Converter" PCIM, Nuremberg, 2009.

[140] J. Salmon, J. Ewanchuk, and A. M. Knight, "PWM inverters using split-wound coupled inductors," *IEEE Trans. Ind. Appl.*, vol. 45, no. 6, pp. 2001–2009, Nov./Dec. 2009.

[141] J. Ewanchuk, J. Salmon, and B. Vafakhah, "A Five-/Nine-Level Twelve-Switch Neutral-Point-Clamped Inverter for High-Speed Electric Drives," *IEEE Trans. Ind. Appl.,* vol. 47, no. 5, pp. 2145- 2153, 2011.

[142] D. N. Zmood and D. G. Holmes, "Stationary frame current regulation of PWM inverters with zero steady-state error," *IEEE Trans. Power Electron.*, vol. 18, no. 3, pp. 814–822, May 2003.

[143] D. Sera, R. Teodorescu, J. Hantschel, and M. Knoll, "Optimized maximum power point tracker for fast changing environmental conditions, "*IEEE Trans. Ind. Electron.*, vol. 55, no. 7, pp. 2629–2637, Jul. 2008.

[144] W. Xiao and W. G. Dunford, "A modified adaptive hill climbing MPPT method for photovoltaic power systems," in *Proc. 35th Annu. IEEE Power Electron. Conf.*, Aachen, Germany, Oct. 3–7, 2004.

[145] N. Femia, D. Granozia, G. Petrone, G. Spagnuolo, and M. Vitelli, "Predictive and adaptive MPPT perturb and observe method," *IEEE Trans. Aerosp. Electron. Syst.*, vol. 43, no. 3, pp. 934–950, Jul. 2007.

[146] G. C. Hsieh, H. I. Hsieh, C. Y. Tsai, and C. H. Wang, "Photovoltaic Power-Increment-Aided Incremental-Conductance MPPT With Two-Phased Tracking", *IEEE Trans. Power Electron.*, vol. 28, no. 6, pp.2895–2911, June 2013.

[147] E. Bianconi, J. Calvente, R. Giral, G. Petrone, C. A. Ramos-Paja, G. Spagnuolo, and M. Vitelli, "A fast current-based MPPT technique based on sliding mode control," *IEEE Trans. Ind. Electron.*, vol. 60, no. 3, pp. 1168–1178, March 2013.

[148] Y. Levron and D. Shmilovitz, "Maximum Power Point Tracking Employing Sliding Mode Control", *IEEE Trans. Circuits and Sys.,* vol. 60, no. 3, pp.724–732, March. 2013.

[149] T. Esram and P. L. Chapman, "Comparison of photovoltaic array maximum power point tracking techniques," *IEEE Trans. Energy Conv.*, vol. 22, no. 2, pp. 439–449, Jun. 2007.

[150] Y. Park; S.-K. Sul; C.-H. Lim; W.-C. Kim; S.-H. Lee; "Asymmetric Control of DC–Link Voltages for Separate MPPTs in Three-Level Inverters," *IEEE Trans. Power Electron*, vol.28, no.6, pp. 2760-2769, June 2013.

[151] P. Rodrıguez, A. Luna, R. Munoz-Aguilar, F. Corcoles, R. Teodorescu, and F. Blaabjerg, "Control of power converters in distributed generation applications under grid fault conditions," in *2011 IEEE Energy Conversion Congress and Exposition (ECCE)*, pp. 2649–2656, Sept. 2011.

[152] E. Serban, M. Ordonez, C. Pondiche, K. Feng, M. Anun, P. Servati, "Power Management Control Strategy in Photovoltaic and Energy Storage for Off-Grid Distributed Generation", in *Proc. IEEE 7th International Symposium on Power Electronics for Distributed Generation Systems (PEDG)*, pp. 1-8, Jun. 2016.